Polarimetry in Bistatic Configuration for Ultra High Frequency Radar Measurements on Forest Environment

Etienne Everaere

École Doctorale de l'École Polytechnique

Thèse

présentée pour obtenir le grade de docteur de l'École Polytechnique
spécialité physique

par

Étienne Everaere

Polarimetry in Bistatic Configuration for Ultra High Frequency Radar Measurements on Forest Environment

Directeur de thèse : Antonello De Martino

Soutenue le 6 mai 2015 devant le jury composé de :

Rapporteurs :
François Goudail - *Professeur à l'Institut d'optique Graduate School*
Fabio Rocca - *Professeur à L'École Polytechnique de Milan*
Examinateurs :
Élise Colin-Kœniguer - *Ingénieur de recherche à l'ONERA*
Carole Nahum - *Responsable environnement et géosciences à la DGA*
Xavier Orlik - *Ingénieur de recherche à l'ONERA*
Razvigor Ossikovski - *Directeur de thèse au LPICM*
Lætitia Thirion-Lefevre - *Professeur adjoint au laboratoire SONDRA*
Lars Ulander - *Professeur, Swedish Defence Research Agency FOI*

UMR 7647

DEMR - TSI

ÉCOLE DOCTORALE DE L'ÉCOLE POLYTECHNIQUE

Abstract

Polarimetry in Bistatic Configuration for Ultra High Frequency Radar Measurements on Forest Environment

by Étienne Everaere

This manuscript deals with airborne or space borne radar remote sensing in the forested environment. It is devoted to the explanation of the methods that enable us to anticipate and understand polarimetric acquisitions in bistatic configurations. The Ultra High Frequency band is retained because of its penetration capabilities in the forest environment. The bistatic configuration has been sensed to increase the radar performances for civil and military application. The full polarimetry is a great source of information in radar, and to be able to test and to validate the simulation for this configuration, scaled down measurements are investigated. The methods were developed during the last three years and include electromagnetic propagation study, polarimetry for scaled down forest, simulation investigation and the use of polarimetric decompositions. Among conclusions, favorable polarizations, bistatic configuration retained and to improve contrast between forest types and new avenues for detection through the forest are proposed.

Acknowledgements

Cette thèse a été financée par la Direction Générale de l'Armement (DGA) conjointement avec l'Office National d'Étude et de Recherche Aérospatiale (ONERA) ainsi que le Laboratoire de Physique des Interfaces et Couches Minces (LPICM) et l'École Polytechnique. Je remercie ces organismes et en particulier Monsieur Pierre Touboul, directeur scientifique de l'ONERA et Monsieur Jean-Marc Boutry directeur du DEMR, Madame Carole Nahum ma référente DGA et Monsieur Pere Roca directeur du LPICM pour avoir financé ces recherches et m'avoir fait confiance pour l'avancée de ces travaux. Je remercie l'école doctorale de Polytechnique pour la disponibilité de Madame Alexandra Belus, Madame Audrey Lemarechal, Monsieur Fabrice Baronnet et Monsieur Emmanuel Fullenwarth et la qualité des formations proposées.

Je remercie les membres du jury pour le temps consacré à l'évaluation de cette thèse. Je suis tout particulièrement reconnaissant envers Messieurs Fabio Rocca et François Goudail pour les discussions passionnées et très approfondies sur le manuscrit. Je remercie très sincèrement Monsieur Xavier Orlik pour avoir présidé le jury de cette thèse et qui a même aidé pour l'installation de la salle pour le pot! Tous mes remerciements envers Monsieur Razvigor Ossikovski pour avoir repris la direction de ma thèse, pour son soutien et son aide précieuse pour la rédaction. My thanks to Mr. Lars Ulander for all his knowledge on the subject and for his kind advices. Thank you for your coming in Paris in spite of a long journey!

Tout ce travail n'aurait pas été possible sans la personne d'Antonello de Martino qui a dirigé mes recherches et dont je salue la mémoire. Je n'ai qu'aperçu tout son talent, j'ai pu observer en lui une intelligence, une lucidité et une passion jamais vues. Je suis très fier d'avoir eu un directeur de thèse de cette trempe et j'ai pu voir que cette force a été transmise à ses proches et ses collègues du LPICM.

Le trio Antonello de Martino - Élise Colin-Koeniguer - Nicolas Trouvé a été précurseur pour le projet: la polarimétrie optique et la mesures des nanotubes de carbone utiles pour le radar! Avec en plus Laetitia Thirion-Lefevre qui a été ma référente pour la simulation EM pour la forêt, avec le laboratoire SONDRA très sensible aux problématiques radars pour l'environnement forestier, avec l'inversion de la biomasse et la détection de cibles, j'avais toutes les clés pour mener à bien ses recherches. Je remercie d'ailleurs Monsieur Marc Lesturgie et le laboratoire SONDRA pour les moyens mis à ma disposition.

La collaboration avec Élise Colin-Koeniguer mon encadrante à l'ONERA avait déjà commencée lors de la thèse de Nicolas Trouvé soutenue en 2011. Ces travaux avaient commencé l'utilisation de la polarimétrie optique pour apporter de nouvelles informations pour des mesures radar sur des scènes mises à l'échelle. Ici nous avons pu poursuivre ces travaux et appliquer les premières observations au cas de la forêt en

bistatique grâce à l'outil du LPICM, le polarimètre résolu en angle, et qui a permis d'obtenir des résultats quantitatifs pour anticiper la mesure radar bistatique pour l'étude de la forêt et l'extraction de paramètres biophysiques et également la détection de cibles dans la forêt. Un grand merci à toutes les personnes avec lesquelles j'ai pu travailler au sein du LPICM : Jacqueline merci beaucoup pour avoir toujours été présente pour les mesures, les calibrations fastidieuses et les adaptations du banc de mesure. Merci à Martin pour les mesures spectrales, Bicher pour ses qualités humaines, son aide pour les mesures et la prise en main de "codiff ". Merci à Enric pour ces nombreux conseils et ses nombreuses explications, Stan, Marc, Fréderic, Ivan. J'ai quand même passé le plus clair de mon temps à l'ONERA dans l'équipe Traitement du SIgnal du Département électro Magnétisme et Radar. Toute ma gratitude envers Christian Riché chef de l'unité TSI, toujours un mot doux pour les doctorants ;) Un grands merci à Philippe Fargette, Olivier Rabaste, Alexandre Lepoutre, Flora Weissberger, Jean-Baptiste Poisson, Luc Vignaud, Dominique Poullin, Marc Flécheux, Jean-Philippe Ovarlez, Christèle Morisseau, Gilles Vieillard aussi pour ses bons conseils et le piment dans les discussions politiques enflammées, Jonathan Bosse, Éric Chaumette et Nicolas Trouvé pour les nombreux conseils et la transmission de ses connaissances, je te tire mon chapeau même si ça n'est pas facile de passer après une barre mise si haute niveau science et réalisation (http://www.dailymotion.com/video/xmhf2s_une-journee-au-radar_tech). Toutes les personnes autour de moi au cours de ces 3 ans m'ont fait énormément de bien. À l'ONERA je salue Élisabeth Bertheau pour sa disponibilité et sa proximité et également Françoise Ricci pour son dévouement. Mon parcours à l'ONERA a commencé par un stage dans l'équipe SFM. Je remercie Juan-Carlos, Béatrice, Go, Jérôme, Anil... Big up spécial à Sylvie, maintenant en retraite, pour le parfum si particulier signe d'un ménage tonitruant, rondement exécuté. Salut à l'équipe de choc pour l'organisation des JDD : Mathieu, Baptiste et Jessica. Salut à Azza, Panagiotis, Damien, Oana, Rata, Abi, Corinna, Nicolas, Jean-François et tous les doctorants et merci aux membres d'Echo pour les visites organisées. Je salue mes voisins du DOTA: Benjamin, Armande, Sébastien, Paul, Patrick. Grâce à toi Élise j'ai aussi pu rencontrer d'autres personnes formidables au DTIM. Toute ma gratitude envers Fabrice Janez, salut Hicham, Sémy et toute l'équipe. Je salue bien sûr tous les footeux du CSX et l'équipe de foot de l'ONERA pour le tournois: Nicolas, Olivier, Julien, Romain, Christophe, Rafaël, Florian, Olivier et Abigael! Et puis je remercie aussi mon vélo rouillé pour m'avoir trimballé sur le plateau de Saclay jusqu'au bout ><

Cette thèse a été pour moi une très belle aventure scientifique. Les épreuves humaines rencontrées n'ont uniquement pu être surmontées pour continuer le travail que grâce à mes encadrantes Élise et Laetitia, à ma famille, mes proches, les collèges de l'équipe TSI et du LPICM. Élise et Laetitia, vous avez été très présentes et très proches pour que le travail aille de l'avant. Vous avez tout mon respect.

Enfin merci à tous mes amis, à Émilie, Justine, Artémis, Corentin, Maman, Franco, Pascal, Louis et toute ma famille. Ce travail est dédié à la mémoire de mon père Jean-Michel Everaere et de mon directeur de thèse Antonello De Martino.

Contents

List of Figures

List of Tables

Abbreviations

ISAR	**I**nverse **S**ynthetic **A**perture **R**adar
BSAR	**B**istatic **S**ynthetic **A**perture **R**adar
AFM	**A**tomic **F**orce **M**icroscopy
SEM	**S**canning **E**lectron **M**icroscopy
MME	**M**ueller **M**atrix **E**llipsometry
ARMP	**A**ngle **R**esolved **M**ueller **P**olarimeter
CNT	**C**arbon **N**ano**T**ube
lidar	**li**ght **d**etection **a**nd **r**anging
SNR	**S**ignal to **N**oise **R**atio

Publications in peer reviewed journals

1. E. Everaere, E. Colin-Koeniguer, L. Thirion-Lefevre, A. De Martino, J. Tran, C. Cojocaru, "An optical scale device to characterize the forest in bistatic radar polarimetry," submitted in *JSTARS*.

Scientific conference proceedings

1. E. Everaere, E. Colin-Koeniguer, L. Thirion-Lefevre, A. De Martino, "Understanding and validation of the polarimetric scattering of a forest for bistatic P-band SAR measurements," in *Geoscience and Remote Sensing Symposium (IGARSS), 2014 IEEE International*, pp. 4556-4559, IEEE, 2014.

2. E. Everaere, E. Colin-Koeniguer, L. Thirion-Lefevre, and A. De Martino, "Influence of bistatic angle and forest structure description on classical polarimetric parameters," in *Geoscience and Remote Sensing Symposium (IGARSS), 2012 IEEE International*, pp. 6531- 6534, IEEE, 2012.

3. E. Everaere, E. Colin-Koeniguer, L. Thirion-Lefevre, "Polarimetric scattering model for the forest in bistatic configuration," in *3rd SONDRA Workshop*, 2013.

4. E. Colin-Koeniguer, N. Trouvé, E. Everaere, A. De Martino, "Bistatic polarimetric decompositions applied to depolarizing targets," in *Geoscience and Remote Sensing Symposium (IGARSS), 2012 IEEE International*, pp. 1429–1432, IEEE, 2012.

General Introduction

Forestry challenges in remote sensing

Due to penetration capabilities of electromagnetic waves and the possibility to cover large areas, radar is one of the most appropriate tools for remote sensing of forest. It can be used for both military and civil applications: detection of targets concealed by forest, or forest biomass estimation which is a key parameter in forestry. Accurate space observations of biomass can also help quantify carbon emissions resulting from deforestation and land-use changes. In the military context, the term FOPEN is often used. It is an acronym for FOliage PENetration, that refers to technical approaches to find and characterize man-made targets under dense foliage, as well as characterizing the foliage itself.

To use radar images for forestry, it is crucial to select and optimize the best configurations of acquisition. If the frequency is too high, no penetration occurs and only the top leaves will play a role in the scattering events. Large wavelengths used in radar are more able to penetrate within forest and to interact with the ground below. For this reason, we limit this thesis to the use of Ultra High Frequency (UHF), P-band and L-band that are defined on figure 1.

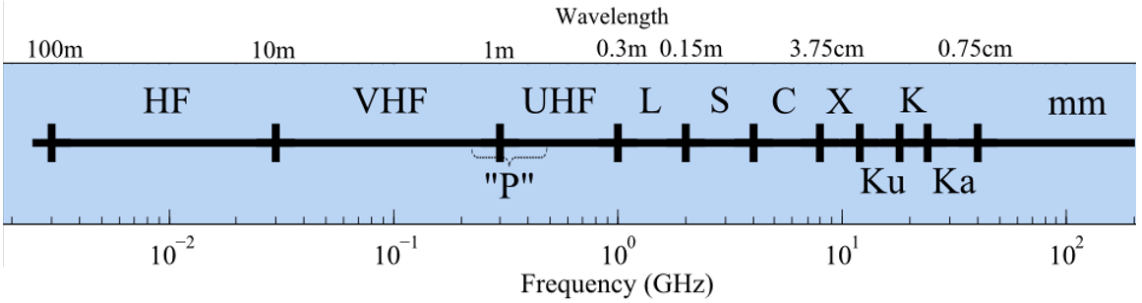

FIGURE 1: *Radar frequency bands.*

Toward the use of advanced modes: polarimetry and bistatic operation

In the case of a classical SAR image, the radiometric information can be used for physical parameters inversion [1]. Thus, several studies aim at linking the backscattering coefficients and the biomass. However, the link between the measured backscattering coefficients and the biomass in not obvious because their relation depends on the tree species, structure, acquisition configuration, etc. As the structure information is very important, any additional information can be useful to learn the characteristics of clutter, and the foliage scattering that affects the signal propagation.

The basic design of a SAR system can be enhanced to collect more information. By emitting and receiving several couples of polarizations, polarimetric images can be collected. The polarimetry is sensitive to the structure information and consequently, it can bring a diversity of information. Practically, the polarimetric SAR system measures four elements of the scattering matrix that describes the behavior of the scene under study. In a monostatic configuration, in which the transmitter and receiver are co-located, three out of the four elements are independent due to the reciprocity principle, which implies that the scattering matrix is symmetrical in this case. Numerous works have highlighted the utility of polarimetry in the forestry context. The polarimetric information is also important for target detection purpose as it enhances the contrast between the forest and hidden targets.

A radar system which comprises a transmitter and receiver which are spatially separated is an opportunity to supply additional information to a classical polarimetric radar, because it breaks symmetries observed in the monostatic case.

Bistatic radar is the name given to this configuration; this thesis proposes the study of polarimetric bistatic configurations for applications related to the forest.

Necessity to understand scattering phenomenology in polarimetric bistatic acquisitions

Since 2006 in ONERA, FOPEN studies were conducted in bistatic configurations [2]. Simulations have shown that trunks contribute more in the backscattering and in the specular scattering configuration, due to the strong response of the trunks coupled with a specular reflection on the ground in these both configurations [3]. The contribution of the branches coupled with the ground is also significant in the specular scattering region. However, their direct scattering is the most important contribution for these two geometric configurations. Given these results, it may be possible to determinate the

characteristics of each main forest component such as branches and trunks by modifying the bistatic angle of acquisition. For FOPEN studies, we could expect that bistatic configurations where the trunk response is very low is perfectly suited to improve target detection. Nevertheless, in all cases we still have to conduct an in-depth analysis of the scattering, and particularly on attenuation effects in bistatic configurations before concluding.

Having a reliable polarimetric bistatic modeling tool enables to better understand the phenomenology and to validate new processing algorithms. However, there is always a trade-off between the number of approximations made in simulation, and the computational complexity. The exact modeling tools are the only ones to solve Maxwell's equations by taking into account all the mechanisms, but they cannot handle too complex scenes. The predictions obtained through the application of approximated simulation tools have to be confronted with experimental data. However, the cost and complexity of a bistatic SAR campaign is a great difficulty in this context.

The lack of real data

A lot of previous campaigns have been conducted in monostatic configurations to study forests. For the future, the Biomass mission [4] was chosen by the European Space Agency (ESA) to help better understand and manage the Earth and its environment. It employs a new polarimetric Synthetic Aperture Radar and aims to take measurements of forest biomass to assess terrestrial carbon stocks and fluxes. This demonstrates that the interest of the low-band radar polarimetry to study the forest is well established.

However, the bistatic configurations are still very rare, and associated studies are still prospective studies:

- A collaboration between ONERA and FOI (Sweden aerospace lab) [2] was conducted in 2007 to study FOPEN at UHF and at P-band in bistatic settings. Several images were acquired by the respective SETHI and LORA facilities. Military vehicles were placed under the foliage, and change detection algorithms were investigated and compared on monostatic SAR images and bistatic SAR images. This study has demonstrated the potential of the bistatic configuration to increase the detection performances. Unfortunately, there were no full polarimetric acquisitions, and the number of geometric configurations was limited with low bistatic angle.
- A collaboration ONERA-DLR [5] led to X-band bistatic SAR campaigns, but not in the specific case of the forest environment.

- The tandem-X mission satellite [6] provides bistatic measurements at X-band. This mission is of prime importance because it proves the feasibility of the large scale bistatic SAR. However, the bistatic angle is very small, and the X-band is not suited to penetration in the forest. Consequently these data are not relevant for the foliage penetration study.

- In [7] a polarimetric bistatic X-band measurement is presented. An area of harvested crop is measured with a reception antenna fixed on a tower and a grazing airborne antenna. The correlations between polarization channels are investigated. Once again, the frequencies used in this study do not match the frequency range selected in this thesis.

Consequently, there are no full polarimetric bistatic measurement at the real scale adapted to forestry studies.

Overcoming the lack of real data

This thesis makes an original contribution to the studies of the forest by radar imagery.

To overcome the lack of data, reduced scale measurements can also be conducted. At ONERA the anechoic chamber BABI enables to produce full polarimetric scaled radar data. Measurements on dielectric cylinders were conducted in the framework of the LORAMBIS study. These data have helped understand the polarimetric bistatic behavior of elementary components of the forest: the cylinders. However, they are insufficient to quantify group effects such as multiple interactions, entropy (depolarization), and attenuation. In order to study non deterministic effects, a cloud of pins was measured in [8]. Geometrical effects on depolarization were analyzed. Meanwhile, other anechoic chamber measurements were conducted in [9] to validate an exact modeling tool for trees with few branches. In both cases, the main drawbacks of these measurements were that

- The number of descriptive parameters of the scene (dimensions, densities) that can be varied is very limited because it is difficult to construct controlled scaled forests with a great numbers of elements.

- The bistatic configurations that can be investigated are also limited by the possible relative positioning of antennas.

Meanwhile, simulation codes have been developed to understand the mechanisms that occur and to construct inversion models. The simulation of the propagation in

the forested environment has been a long time effort. Several bistatic and polarimetric models for the scattering of the forest have been proposed. Most often, the trees are modeled by set of cylinders. Then, the computation of scattering returns can be based on different approximations and different refinements. Among existing simulation codes, COBISMO has been proposed by Thirion-Lefevre [10]. COBISMO is a coherent scattering model dedicated to P- and L-bands in the bistatic case. A bistatic polarimetric validation was realized for a few cylinders [11]. In any case, at our knowledge, there is no bistatic simulation codes of forest that have been completely validated. Today, the major challenge of simulation tools are their validation.

The innovative solution proposed in this thesis: to measure the forest contribution at the optical scale

The aim of the thesis is to anticipate real measurements and to give keys to choose more appropriate configurations for a given application: physical parameters retrieval or target detection.

The solution we propose is to construct an optical scale device that is full polarimetric and that handles the bistatic configurations. With this device, we propose to measure scenes having a structure comparable to a real forest. Our ideal goal is to demonstrate that the optical scale measurements can be used to anticipate polarimetric behavior of forest and jointly to validate our simulation code.

In a first part, the specificities of bistatic configurations relatively to monostatic ones are reported. The differences concern the image processing and also the polarimetric theories. Considering the polarimetry, the understanding of the occurring mechanisms requires decomposition techniques. This work is based on [12] which aims at using multiplicative decompositions used in optics with the Mueller formalism and to apply them to radar data. The multiplicative decompositions seem to be particularly suited to forests described by successive horizontal layers.

Having identified the similarities and differences between the measurements and processings applied to different scales, the choice and the implementation of an optical scale device are described in the second part of this manuscript. We use nanotubes samples for which structure parameters can be controlled. The choice of the structures of investigation is also reported.

In the third part of the present thesis, the analysis of the resulting polarimetric images is conducted, jointly with the beginning of a cross validation of the simulation code COBISMO. This approach helps show off several densities of forest, for which the results of the electromagnetic code and the measurements agree. In cases of very

dense forest where differences are identified, hypotheses are proposed to explain the differences between simulation and measurements, and to make changes to the original code.

Once the code is validated by measurements, we can rely on it to investigate a number of questions. Thus the final part provides several kinds of applications of the simulation tool to forest parameters inversion, and for the detection of canonical metallic targets in the forest.

Part I

Tools to move from a monostatic polarimetric radar configuration to a bistatic configuration

Chapter 1

Bistatic Radar Image Processing

Since the goal of this thesis is to anticipate radar images with optical measurement, it is important to understand what differences exist between the different image processing at the radar scale in comparison to the optics scale.

Actually, it is possible to compare the measurement contained in the pixel of a radar image, or in the pixel of a classical optical image, but the information contained in this measurement may depend on the bandwidth used in the measurement or on the acquisition geometry, or, more generally, on the image resolution.

Optical resolution describes the ability of an imaging system to resolve detail in the object that is being imaged. In optics, an imaging system may have many individual components including a lens and recording and display components. Each of these contributes to the optical resolution of the system. The ability of a lens to resolve detail is ultimately limited by diffraction, and then the spatial resolution is proportional to λ/D where λ is the wavelength and D the lens diameter.

A radar image is not a classical image as our human eye can perceive. It results from an imaging algorithm, called SAR algorithm. Also, the resolutions obtained depend on parameters of the signal acquisition, such as acquisition duration and frequency bandwidth. Thus it is necessary to point out the differences with an optical system.

Traditional radar images are usually acquired in monostatic mode, where the transmitting antenna has the same position as the receiving antenna. Image resolutions in this case are well established. However in this thesis, we are interested in the bistatic mode, for which the expression of the resolutions is more complicated to derive.

This chapter has thus two purposes:

- The first is to understand what types of parameters determine the image resolution of a conventional radar image, compared to an optical image. This will allow

us to keep in mind the limitations of a generalization of a reasoning derived from an image acquired at the optical scale. This will be discussed in the first section.

- The second is to show how the expressions are generalized in the bistatic case. This will allow us to keep in mind that when we are choosing a geometric configuration in order to favor some electromagnetic mechanisms, the resolutions also depend on this choice. This will be discussed in the second section.

1.1 Synthetic Aperture Radar Resolution

1.1.1 SAR configuration: main parameters

The principle of a radar imaging system is to observe a scene through its interaction with an emitted electromagnetic wave. Synthetic-aperture radar (SAR) is the name of radar that is used to create images of the Earth surface. The emitted wave is characterized by its power, its wavelength λ, its incidence angle θ and its polarization. Polarization is described by the polarization state vector, as will be detailed in the next chapter. λ and θ are contained in the wave vector $\mathbf{k}$.

Radar is an active imaging system, that means it emits and control its signal by the transmitted electromagnetic field. The radar transmitter is an antenna. The antenna is traveled by an electric current of frequency $f = \frac{c}{\lambda}$ where c is the light velocity.

For the case of airborne or space borne radar system, the antenna is carried by an airplane or a satellite that sends the radio wave in the direction of the scene. Figure 1.1 illustrates an example of an antenna carried by an airplane. The scene re-emits the wave in a way that depends on this nature. The interaction changes the direction of the wave, the angular dispersion of the power (scattering), the total reflected power (linked with the transmission and absorption phenomenon) and the absolute phase of the wave that depends on the traveled distance. If the object reached by the wave is moving, the phase shift will be changed: this is linked to the well known Doppler effect.

An airborne measurement configuration is illustrated in figure 1.2. The footprint represents the surface on the scene that is significantly enlighten by the emitter. Considering a rectangular antenna of dimension $d_1 \times d_2$ the shape of the footprint is described by the function of angular coordinates θ_x, θ_y by equation 1.1

$$F(\theta_x, \theta_y) = d_1 d_2 sinc(\frac{\pi \sin\theta_x d_1}{\lambda}) sinc(\frac{\pi \sin\theta_y d_2}{\lambda}) \tag{1.1}$$

The azimuth aperture is defined by the width of the main lobe at $-3dB$ in the azimuth direction which is:

FIGURE 1.1: *Right pod of the SETHI facility of ONERA that carries a radar antenna*

$$\theta_{az,3dB} \approx 0.88\frac{\lambda}{d_1} \tag{1.2}$$

and the range antenna aperture is given by:

$$\theta_{range,3dB} \approx 0.88\frac{\lambda}{d_2} \tag{1.3}$$

That is why the larger is the antenna and smaller the wavelength, the more directive is the antenna.

1.1.2 Expression of the received signal

In order to create a SAR image, successive radio wave pulses are transmitted to illuminate the scene and the echo of each pulse is received and recorded. Signal processing of the recorded radar echoes enables the recordings from the multiple antenna locations to be combined to create the image. SAR processing is the way in which we obtain this SAR image from the recording of the pulse echoes.

A signal $s_0(t)$ is transmitted from each antenna position u, with a bandwidth B and a central wavelength λ. One of the main parameter in radar is thus the time delay between emission and reception. If we are able to measure this time delay τ, then we

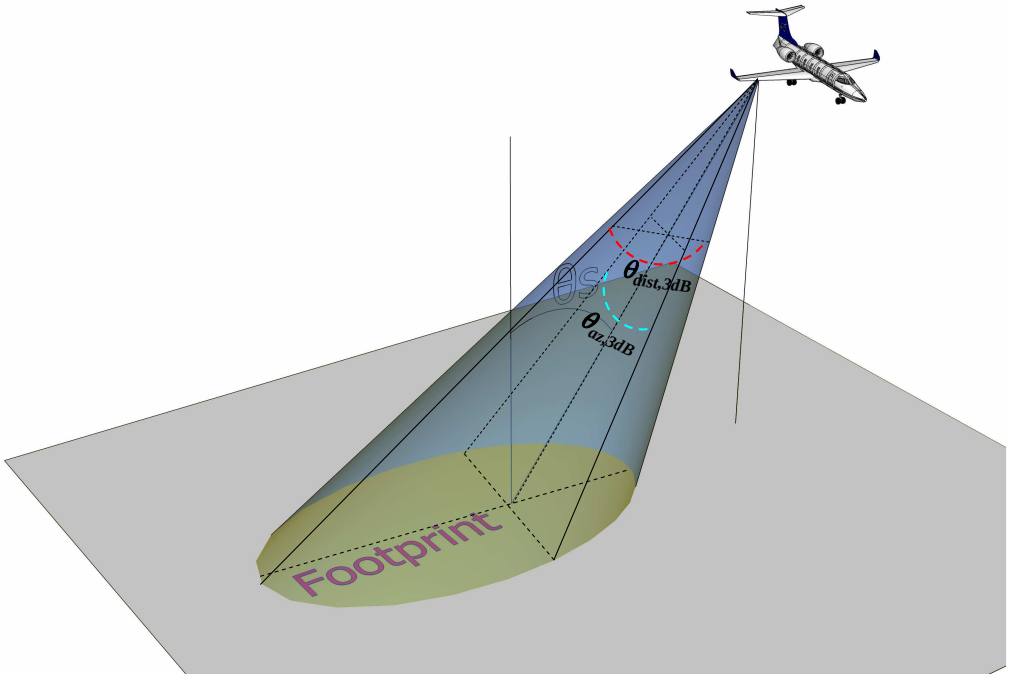

FIGURE 1.2: *View of an airborne SAR measurement configuration*

can deduce the distance R of the target from $R = c\tau/2$, c being the speed of light considered as a constant.

The signals collected are written $s(t, u)$ where t is called the short-time and u is a position of the antenna or long-time. The SAR image is synthesized from these acquisitions made during the path of the antenna, with a length L. L is also called the integration length.

The SAR image corresponds to a mapping of the ground reflectivity along two axes: the azimuth axis y, which corresponds to the axis of the trajectory, and the transverse axis x, or range axis.

The acquired signal $s(t, u)$ can be written as:

$$s(t,u) = \iint dxdyf(x,y)s_0(t - \frac{2}{c}d(x,y,u)) \tag{1.4}$$

where $d(x, y, u)$ is the distance between an elementary target located at a position (x, y) and the antenna at a position u, and $s_0(t)$ is the transmitted signal in each pulse. $f(x, y)$ is the reflectivity of the elementary targets. The purpose of the SAR algorithm is to deduce the image reflectivity $f(x, y)$ from the recorded signal $s(t, u)$.

In this modeling, each pixel of the image to reconstruct is considered as a point whose backscattering amplitude $f(x, y)$ is isotropic inside the angular range of view and uniform inside the frequency range: that means $f(x, y)$ does not depend on λ nor u or θ, the look angle.

In the next subsections, only the monostatic radar resolutions are detailed. Two resolution dimensions have to be distinguished in the radar, the azimuth resolution, along y axis that is collinear to the trajectory, and the range resolution, along x axis, in the perpendicular direction.

The resolutions are firstly described as they were obtained without processing and then the processing that consists in matched filtering and aperture synthesis is briefly explained to give the sustainable resolution in the context of SAR.

1.1.3 Range resolution: obtained by matched filtering

Pulse duration τ is the primary factor in range resolution. Considering two point targets distant from the emitter of R and $R + r$, the sensor must distinguish between the reception of two wave trains of duration τ. The difference between the two reception time being $2r/c$ it comes $2r/c > \tau$ and the range resolution is:

$$\delta_r = \frac{c\tau}{2} \tag{1.5}$$

To decrease δ_r a solution is to decrease τ. Matched filtering overcomes the technical limitation to do so with acceptable SNR for a given peak power. The principle is to use frequency modulation in the emitted pulse to illuminate two points at close time with two different frequencies.

Most often, the pulse emitted $s_0(t)$ is a linear chirp, as plotted in figure 1.3.

In a linear chirp, the instantaneous frequency varies linearly with time. Mathematically, a linear chirp with a duration τ, an amplitude A_0 and a central frequency f_0 can be written as:

$$s_0(t) = A_0 e^{2j\pi(f_0 t + \frac{K}{2}t^2)}, \qquad t \in [0, \tau] \tag{1.6}$$

with K the modulation factor. A matched filter is the optimal linear filter for maximizing the signal to noise ratio in the presence of additive noise. It is used in

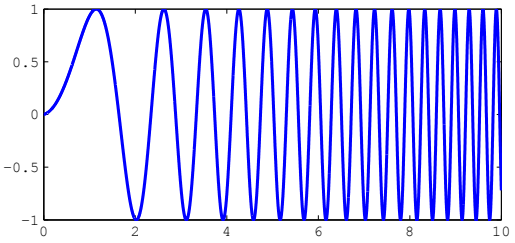

FIGURE 1.3: *Picture of a linear chirp signal*

radar systems where the transmitted signal $s_0(t)$ is used as a replica to be correlated with the received signal $s_r(t)$ to obtain:

$$s'_r(t) = \int_{-\infty}^{\infty} s_0^{\dagger}(\tau - t) s_r(t) \tag{1.7}$$

For a linear chirp $s_0(t)$ and for a target of backscattering level σ this filtering can be expressed as:

$$s'_r(t) = \sigma sinc(\pi K \tau t) * \delta\left(t - \frac{2R}{c}\right) \tag{1.8}$$

After matched filtering, the range resolution δ_{range} is then defined as the width of the *sinc* function at $-3dB$ in equation 1.9. It comes:

$$\delta_{range} = \frac{0.88c}{4K\tau} = \frac{0.88c}{2B} \tag{1.9}$$

where B is the frequency bandwidth, $B = 2K\tau$. In summary, in a classical monostatic radar, the range resolution depends only on the frequency bandwidth.

1.1.4 Azimuth resolution: obtained by aperture synthesis

In order to obtain a two-dimensional image, a first solution is to acquire several range profiles. This is what is done by Side-Looking Airborne Radar (SLAR) or Real Aperture Radar (RAR). In this case, the radar platform moves in the direction of the y-axis. The system uses an antenna that sends one pulse at a time and measures what is scattered back. The azimuth resolution (better known as the cross-range resolution) depends on the beam width of the radar antenna, see figure 1.2 . To be separated, the distance between two point targets in azimuth must exceed the azimuth width of the footprint

at distance R. As related in section 1.1.1, it comes:

$$\delta_a \approx 0.88 \frac{\lambda R}{d_1} \tag{1.10}$$

where d_1 is the dimension of the antenna aperture in the azimuth direction and R the distance between the antenna and the target. With this expression for classical radar designs, no acceptable resolution can be reached, as the distance R can be very large, especially for spaceborne systems where R can be higher than $500km$.

By using the coherent nature of the signal and the antenna platform displacement, the synthetic aperture technique enables to overcome this limitation. By using the entire set of recorded pulses for all antenna positions to synthesize the image, resolution depends on the integration length L. All parameter are depicted in figure 1.4. The distance that the SAR device travels over a target creates a large synthetic antenna aperture that plays the role of the size of the antenna.

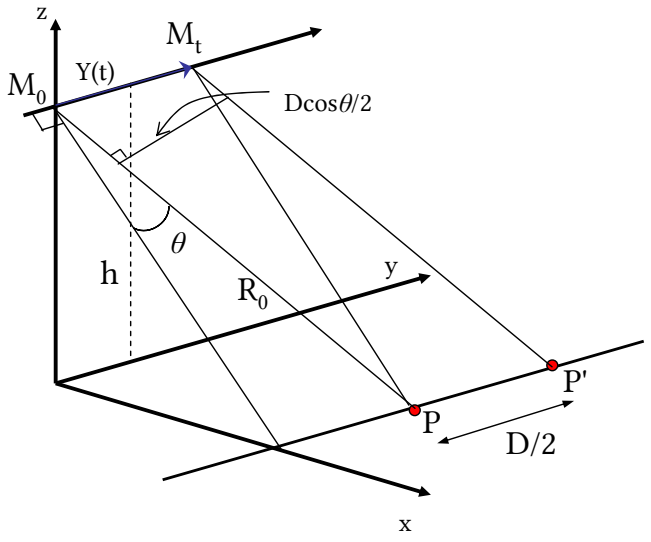

FIGURE 1.4: *Schematic of a synthetic aperture radar system in the monostatic configuration*

In order to express the azimuth resolutions in the monostatic case, one solution is to express the instantaneous phase of the point under consideration. For the notation M_0 is the carrier position at instant $t = 0$, M_t is the position of the carrier at instant $t \neq 0$. P is the position of the target. The antenna platform is set as $||\vec{M_0 M_t}|| = Y(t) = V_c t$, with V_c the constant velocity of the carrier. The distance between the target and the

carrier is then $M_tP = M_0P\sqrt{1 + \frac{Y(t)^2}{M_0P^2} - \frac{2Y(t)}{M_0P}\sin\theta}$, with θ the squint angle between the normal of the antenna and the vector $\vec{M_tP}$.

The instantaneous phase is related to the distance M_tP by equation 1.11.

$$\Phi(t) = 2\pi f_0 t + \frac{4\pi}{\lambda}M_tP \approx 2\pi f_0 t + \frac{4\pi}{\lambda}M_0P + \frac{2\pi V_c^2\cos^2\theta}{\lambda M_0P}t^2 - \frac{4\pi\sin\theta V_c}{\lambda}t \tag{1.11}$$

This variation of the Doppler frequency enables to localize the targets from the plane of sight and the Doppler frequency is the derivative of $\Phi(t)$:

$$F_d(t) = \frac{1}{2\pi}\frac{d\Phi}{dt} = f_0 + \frac{2V_c^2\cos^2\theta}{\lambda M_0P}t - \frac{2V_c\sin\theta}{\lambda} \tag{1.12}$$

In order to express the Doppler resolution the Doppler frequency for both targets is calculated [13]. We consider the distance $|PP'| = D/2$, as described in figure 1.4.

The time associated to the distance between them keeping the angle of view θ is $\Delta t = \frac{D\cos\theta}{2V_t}$ and consequently, the Doppler frequency of the both targets at a distance $R_0 = M_tP = M_{t'}P'$ but separated in azimuth by a distance $D/2$ is:

$$F_d(P) = f_0 + \frac{2V_c}{\lambda}\sin\theta \tag{1.13}$$

$$F_d(P') = f_0 - \frac{2V_c}{\lambda}\sin\theta + \frac{V_tD}{R_0\lambda}\cos\theta \tag{1.14}$$

The Doppler frequency shift is then $\Delta f_i = \frac{V_tD\cos\theta}{R_0\lambda}$. To be able to detect this frequency shift, data must be collected during a time T long enough, so $T > \frac{1}{\Delta f_i}$. It comes $\frac{D}{2} > \frac{R_0\lambda}{2V_tT\cos\theta}$.

The azimuth resolution can finally be approximated as follows:

$$\delta_a = \frac{R_0\lambda}{2V_tT\cos\theta} \tag{1.15}$$

As a conclusion, the synthetic azimuth resolution depends on the integration length and the central wavelength. The expression of the resolution is strongly related to the Doppler frequency separability of two close targets. That is why one can use the term Doppler resolution instead of the SAR azimuth resolution.

The description of the techniques of matched filtering and synthetic aperture showed that the radar imaging can achieve very good resolutions without being limited by the dimensions of the antennas.

The monostatic case is well mastered for radar imaging and resolution expression remains quite simple. A representation of the iso surfaces for the resolution is a convenient way to visualize the resulting resolution cells as in figure 1.5. In the figure, the iso Doppler surfaces are cones, and iso range surfaces are spheres. In bistatic, the question to describe the resolutions can be reduced to the question of what become these surfaces. In the general case there is no simple expression for the Doppler. We detail the problem in the following section.

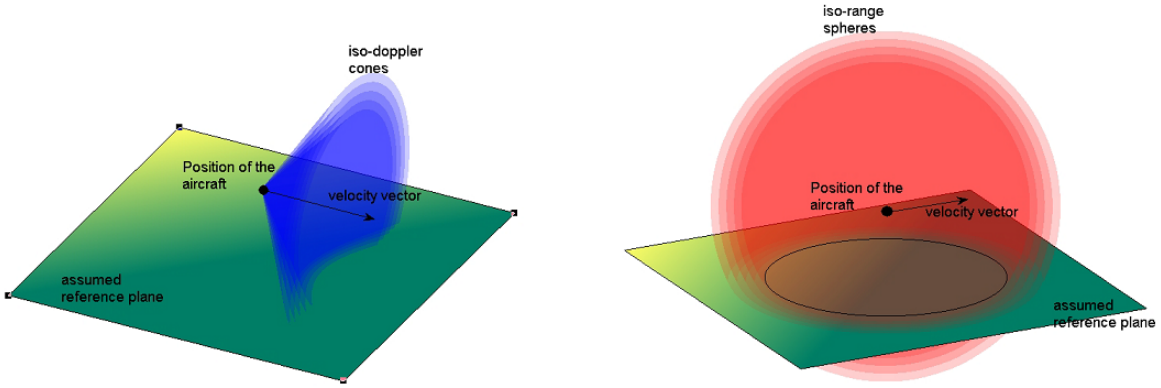

FIGURE 1.5: *Representation of iso range and iso Doppler surfaces in a classic monostatic configuration. The reference plane can be the ground.*

The general bistatic case leads to non-obvious formulations of the sustainable resolutions. Most of the time their expressions are derived for simplifying assumption cases.

1.2 Bistatic configuration

1.2.1 Introduction to bistatic SAR

The latter description is valid for the monostatic configuration where the transmitting antenna is at the same position as the receiving antenna. In this case, only the backscattering direction is considered. But it is possible to use a different position for the reception antenna and for the transmission antenna. If it is the case and if the reception antenna is carried by another platform such as a plane, a satellite or even a

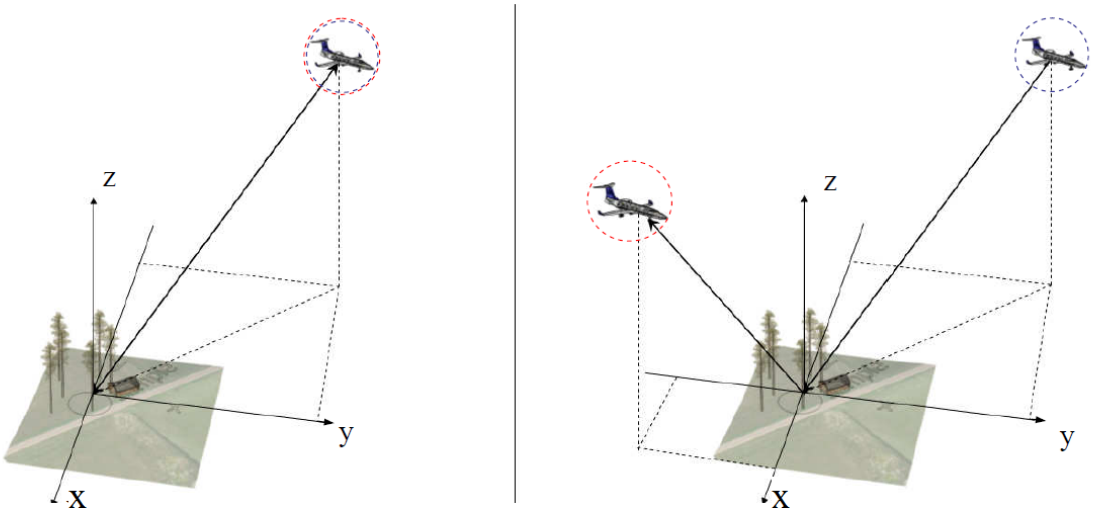

FIGURE 1.6: *Example of airborne radar configurations. Monostatic one the left and bistatic one on the right.*

fixed tower, the configuration is called bistatic. An example of such configuration is illustrated in figure 1.6.

Thus, several bistatic configurations exist:

- It is possible to use different moving platforms at the same time: one airborne and one spaceborne, two airborne, or two spaceborne. TanDEM-X is the first bistatic SAR system that has been set up [6], as represented in figure 1.7, using two spaceborne systems. TandEM-X setup enables to produce interferometric SAR measurements from which a Digital Elevation Model (DEM) can be computed, but it also enables to test bistatic capabilities, even if the bistatic angle is not much that 0.8 degrees [6]. The system works at X-band which corresponds to wavelength around 3 centimeters. Due to its poor penetration capabilities, it is out of the scope of this present work. In the same way, the European Space Agency (ESA) is exploring from 2014 the technical feasibility and the scientific value of the receive-only SAOCOM-CS satellite to be launched with Argentina's L-band SAR satellite SAOCOM. The two satellites would fly in formation, with SAOCOM acting as an emitter, enabling for the first time single-pass SAR interferometry and bistatic images at L-band.

- It is also possible to use an opportunity emitter, airborne or spaceborne one, with a hidden passive receptor on the ground.

These bistatic configurations suffer from numerous technological difficulties, such as the synchronization of the airborne clocks. Moreover, even with the assumption of

FIGURE 1.7: *Picture of the trace in the sky of the TanDEM-X facility in the close configuration.*

perfectly well controlled bistatic radar system, the SAR algorithms cannot be directly extended to the bistatic case. The image processing and the expression of the resolution remain generally different from the monostatic ones. Nevertheless, airborne bistatic SAR images already exist as the ones obtained during campaigns conducted at ONERA in 2006 during the LORAMBIS campaign [14].

Due to the complexity of the geometrical configurations, the ground resolution ability of bistatic SAR is more complex than that of the monostatic SAR. In a monostatic configuration, we have seen that the azimuth direction usually denotes the moving direction of the radar, while range direction denotes the beam pointing direction. However, in the case of bistatic SAR, since there are two antennas and they can move separately, the physical meaning of range direction and azimuth direction is no longer explicit. Hence, the understanding of bistatic resolution is more complex than that of monostatic SAR and the resolution calculation is more complicated.

In order to understand the resolutions in the bistatic case, the geometrical basis needs to be precisely defined. In the following, we have chosen definitions represented on figure 1.8.

The variables θ_e and θ_r are the incidence angles for emitted and received waves. φ_e and φ_r are the azimuth angles for emitted and received waves. The wave vector k_e and k_r are also represented.

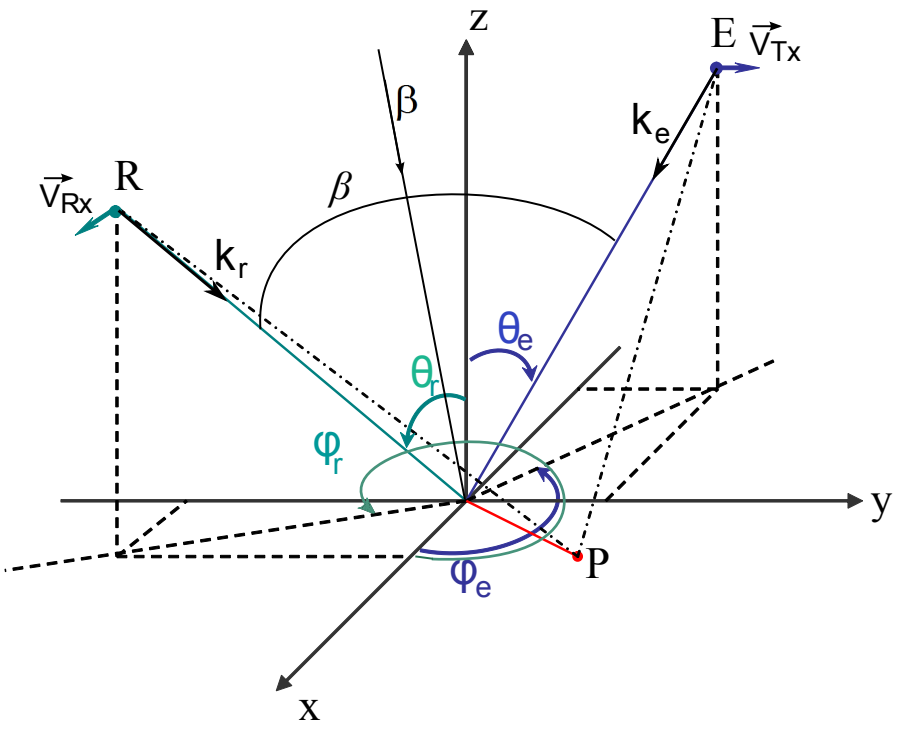

FIGURE 1.8: *Bistatic geometrical basis and convention vectors*

1.2.2 Resolutions for bistatic SAR

In a monostatic configuration the range axis is the main direction of the illumination beam. The points on the ground that are at a given distance of the antenna form circles on the ground. However, unlike monostatic case, the bistatic range includes distances in two directions, and the slant range defined by the bistatic range cannot be projected into the ground range through simple linear transformation. In bistatic configuration, points that are located at the same total distance from both antennas become ellipses as represented in figure 1.9.

Moreover, in the monostatic SAR, the azimuth direction is usually defined as the platform moving direction. The Point Spread Function has an elliptic shape, depending on the relative position of the transmitter and the receiver relatively to the target and to their velocity direction, as represented in figure 1.10. Thus, resolutions are linked to the dimensions of this elliptic shape for any direction, and more than two axis can play the role of preferred directions, as described in figure 1.10.

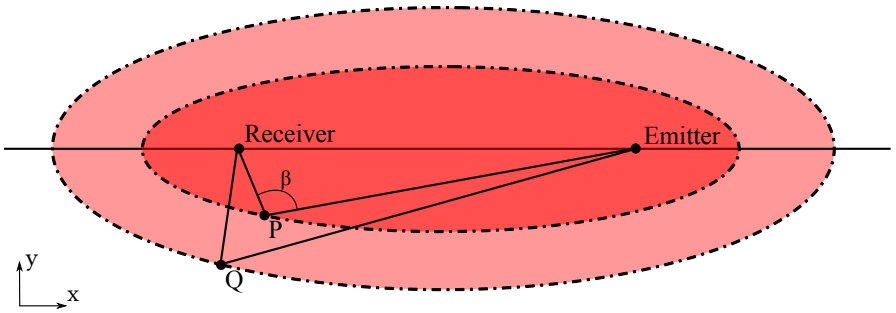

FIGURE 1.9: *Example of isorange lines (dashed lines) for a bistatic configuration.*

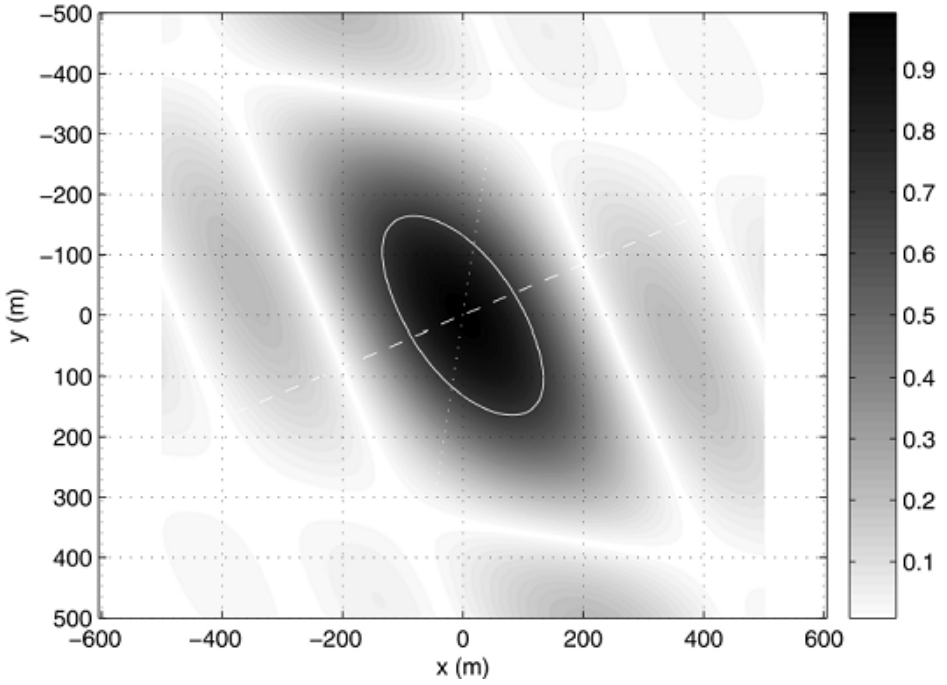

FIGURE 1.10: *Example of Point Spread Function given in [15].*

The expression of the resolutions is not as simple as in the monostatic case. There are no expression in the general case unless in cases where the configuration is limited to constant platforms velocities, constant height of the platforms and linear trajectories.

The range and azimuth resolutions can be defined as respectively minimum ground distance associated to the minimum detectable change of delay time and distance associated to the minimum detectable change of Doppler frequency. The azimuth resolution would be named more appropriately Doppler resolution. One can notice that the two

corresponding axis are not necessarily perpendicular and consequently the resolution cell is not necessarily rectangular.

Several methods enable to retrieve the theoretical bistatic SAR resolutions:

- the data projection in frequency domain [16], [17], [18] [19],
- the generalized ambiguity function [20], [15]
- the Gradient method [21] [22]. In [21] a complete study about the different bistatic resolutions is presented.

In any case,

- The range resolution δ_r is proportional to $(1/B)$, with B the chirp bandwidth and to $1/|\Delta t|$ gradient time delay. The direction of the range resolution is collinear to $\boldsymbol{\beta}$. $\boldsymbol{\beta}$ is the bisector of the bistatic angle. Along this axis, the distance resolution is equal to that of the monostatic case divided by the term $(\cos\beta)/2$. This term vanishes for $\beta = \pi/2$. This result has an important consequence: it shows in particular that resolution is very low with a mean bistatic angle of $\pi/2$.

  It is important to remark that the maximum delay time gradient involves the minimum resolution, and that the best ground range resolution is in the direction of the ground projection of the transmitter/receiver bisector vector.

- δ_a, the azimuth or Doppler resolution is proportional to $(1/T)$, with T the coherent integration time and to $1/|\Delta\mathbf{F}_g|$. $|\Delta\mathbf{F}_g|$ is the gradient of the Doppler frequency which depends on the relative velocity vector of the platforms. The direction of δ_a is collinear to $d\boldsymbol{\beta}/dt$. This direction is not necessarily perpendicular to $\boldsymbol{\beta}$.

Both resolutions cited above can be low while the resolution cell area remains large. That is why the angle μ between the two direction of δ_a et δ_r is also very important. Consequently, various criteria to report the resolution of the system are possible. Figure 1.11 synthesizes these parameters. The minimum and maximum resolutions, δ_{min} and δ_{max} respectively correspond to the minor axis and major axis of the ellipse. δ_x and δ_y can also be defined to match the reference coordinate system.

Finally, three resolution cell examples are given in figure 1.12 for three cases of antenna configuration: the monostatic case, the stationary case where velocities of emitter and receiver are equal, and a general case.

It is important to note that the bistatic area pixel is larger than the monostatic equivalent one, and can be very large when the flight directions of the platform are not parallel.

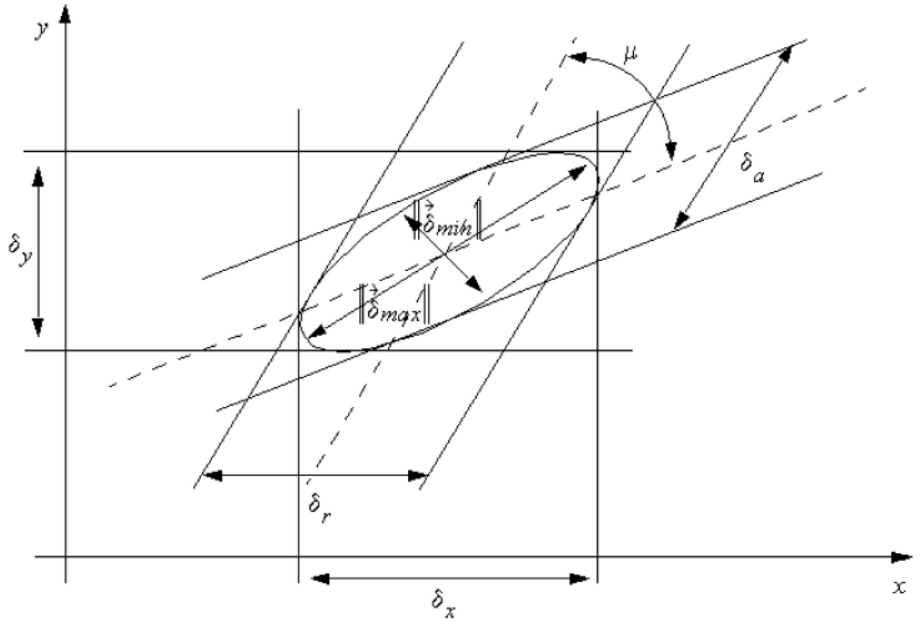

FIGURE 1.11: *The resolution ellipse can be defined by several preferred directions, extracted from [15].*

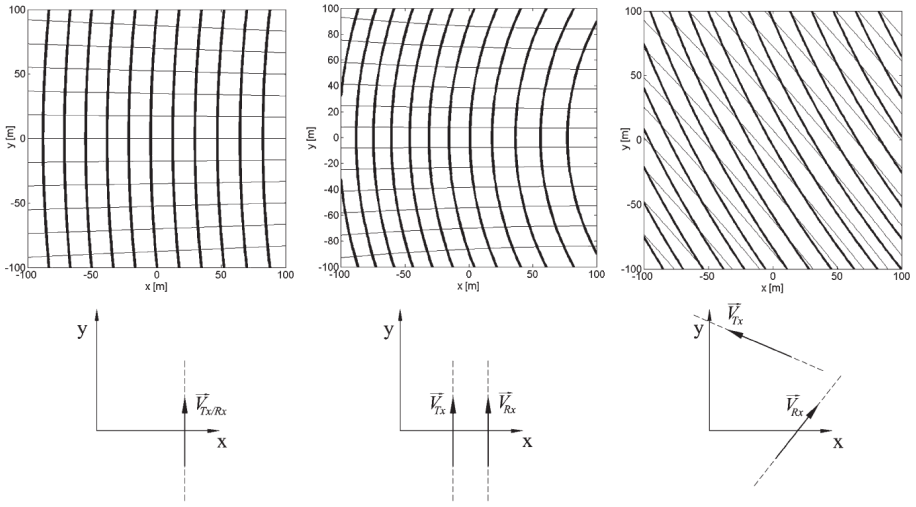

FIGURE 1.12: *(Top) Examples of (thick) isorange and (thin) iso-Doppler contours for different SAR geometries. (Bottom) (Left) Monostatic SAR, (center) parallel-track bistatic SAR, and (right) arbitrary geometry bistatic SAR. Same altitude and velocity moduli assumed for transmitting and receiving antennas. Extracted from [21].*

* * *

Summary

In this chapter, the main differences between bistatic and monostatic radar were described. They are crucial in order to keep in mind implication of the bistatic configuration in terms of resolution and also as soon as we want to perform a spatial estimation of our polarimetric parameters. Knowing this, in the following of the manuscript we do not consider the image processing but only the single signal obtained for a given frequency and a given viewing angle. Considering this base signal, a comparison will be drawn with signals obtained at other scale.
In the following, polarimetric optical scale devices are chosen to anticipate a bistatic and polarimetric radar signal. The next chapter draws the comparison of polarimetry and polarimetric decompositions in radar and in optics.

Chapter 2

Polarimetric tools

We have seen that the radar image has a resolution which depends on the wavelength, on the integration domain but also on the configuration of the antennas. The detected information also depends on the nature of the electromagnetic interactions. The polarimetry confers tools which allow diversifying the recorded information because this one varies generally strongly according to the state of polarization of the emitted field.

The various vocabularies depending on the application field will be detailed. Then the various formalisms from which we can estimate the non deterministic character of a target such as the forest will be compared. They are mainly the coherence matrix and the Mueller matrix formalisms.

Polarimetric decompositions are then used to extract the physical or discriminating information of the scene with regard to another scene. Several types of decompositions exist for either coherent or incoherent formalisms. This part aims at underlining the useful parameters for our case of study.

2.1 Characteristics of the considered electromagnetic field

The assumptions concerning the electromagnetic field are:

- It is totally, partially or even non polarized.
- It is stationary, that is the joint probability distribution does not change in time, and it is ergodic up to the second order
- The electromagnetic field is quasi monochromatic with a bandwidth B such as $1/B$ is negligible in comparison to the coherence time.

All these assumptions are reasonable approximations because even a chirp impulsion from a radar antenna is composed of different monochromatic fields separated in the time domain. Now the scattering regime and interactions can be considered.

2.2 Measured quantities and conventions

Polarimetry consists in the measurement and interpretation of the polarization of transverse waves, most notably electromagnetic waves. We use the term ElectroMagnetic field to deal with radio electromagnetic waves for radar, or light waves for optics.

The first section presents the different conventions and observed variables. Basically, in order to define the orientation of the polarization states of the waves, we need directions defined by a reference plane. Then, the primary description of how a radar target or surface feature scatters EM energy is given by the scattering matrix. The different conventions used to describe this scattering matrix will be thus presented.

In a second section, we present the formalisms used for the non deterministic behavior of waves and targets. This corresponds to the measurement performed by Mueller imaging systems.

In a last section, we present the different polarimetric decompositions that can be applied to polarimetric images.

2.2.1 Spatial reference planes

For a plane electromagnetic (EM) wave, polarization refers to the locus of the electric field vector in the plane perpendicular to the direction of propagation **k**. This perpendicular plane is called the **wave plane**.

In the wave plane, we need to define a privileged direction for the orientation ot the electric field. To this aim, in radar we use the **incidence plane** that is the plane that includes the wave vector **k** and the normal to the enlighten surface, assumed to be the horizontal earth surface. If the polarization is parallel to the incidence plane we speak about a transverse magnetic (TM) polarization or vertical polarization (v). In optics it is also called the p polarization (p stands for the first letter of *parallel*). The perpendicular polarization is the transverse electric (TE), also called in radar domain the horizontal polarization (h) and in optics s polarization (the first letter of the German name *senkrecht* which means perpendicular). An illustration of the reference plane is given in figure 2.1.

In optics, the reference plane can also be the transmitter-receiver-target plane. In [8], authors explain why they prefer the use of this convention in the case of a bistatic

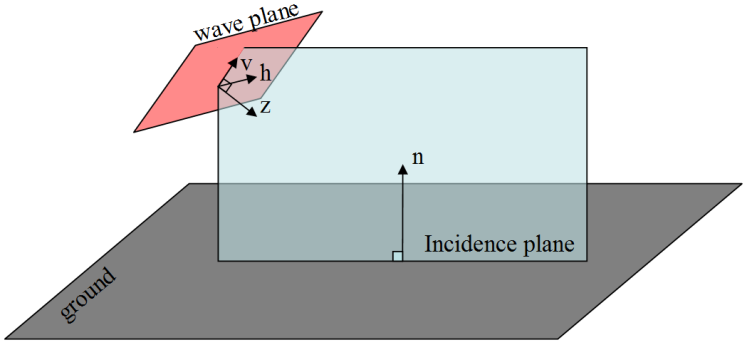

FIGURE 2.1: *Illustration of the reference planes.*

radar acquisition: it enables to make a polarimetric analysis according to a common orientation angle between receiver plane and transmitter plane. They also propose the formulas that allow to change conventions according to the reference planes.

Moreover, in order to completely describe the coordinate systems, once the orientation of the two polarimetric vectors have been chosen in the wave planes, we also have to choose the convention about the directions of the unit vectors relative to the sense of propagation. This leads to two different conventions: *Forward Scatter Alignment* FSA and *BackScatter Alignment* BSA.

In the FSA convention, the $z-$axis is defined by the direction of propagation of the wave. In the BSA convention, the $z-$axis is positive when pointing towards the target both before and after the wave is scattered. This BSA convention is less intuitive, but is generally chosen in SAR polarimetric images because in the particular case of backscattering (monostatic case), the coordinate systems are the same for the cases of the EM wave propagating from the antenna to the target and for the wave scattered from the target back towards the antenna.

2.2.2 Expression of a totally polarized wave

A given vector in the three dimensional space can be described by its three orthogonal components in the right handed system $(\mathbf{h}, \mathbf{v}, \mathbf{z})$. Because of the nature of the wave, the electric field has no component in the $\mathbf{z}$ direction so the vector can be limited to two orthogonal components:

$$E(z,t) = \begin{pmatrix} E_{oh}\cos(\omega t - kz - \varphi_h) \\ E_{ov}\cos(\omega t - kz - \varphi_v) \end{pmatrix} \tag{2.1}$$

To obtain the track of the electric field vector in the plane wave, the temporal parameter is eliminated in the preceding relation and we introduce the phase shift δ such as $\varphi_v = \varphi_h - \delta$. Then:

$$\left(\frac{E_h}{E_{oh}}\right)^2 + \left(\frac{E_v}{E_{ov}}\right)^2 - \frac{2E_hE_v}{E_{0h}E_{0v}}\cos(\delta) = \sin^2(\delta) \tag{2.2}$$

where $\varphi = \varphi_h - \varphi_v$. This equation describes an ellipse that is the general course of the electric field of a completely polarized wave. This course of the electric field is called the polarization state or even only the polarization. The parameters (α, ϵ) of a given polarization state is given in figure 2.2.

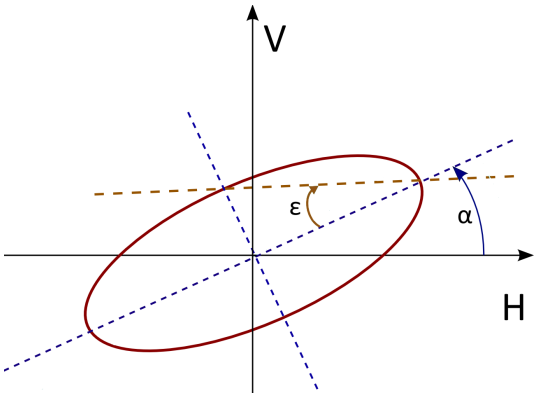

FIGURE 2.2: *Parametrization of the general elliptical polarization state by orientation α and ellipticity ϵ*

In the case of a monochromatic and completely polarized wave the notation can be simplified. R. Clark Jones proposed to represent the polarization state in this case by a complex column vector **E**, called Jones vector, that represents (relative) amplitude and (relative) phase of electric field in h and v directions.

$$\mathbf{E} = \begin{pmatrix} E_{0h} \\ E_{0v}e^{i\delta} \end{pmatrix} \tag{2.3}$$

This formalism deals with completely polarized wave, i.e. waves for which E_{0h}, E_{0v} and δ can be considered as constant over time. The relation between the different parameter are:

- $\tan(2\alpha) = 2\frac{E_{0h}E_{0v}}{E_{0h}^2 - E_{0v}^2}\cos\delta$
- $\tan(2\epsilon) = \sin(2\alpha)\tan\delta$

2.2.3 The scattering matrix

During the interactions of the electromagnetic field with the scene, the polarization state can be changed. In our case the types of interactions are the scattering through the forest and the reflection on the ground. The modification of the electromagnetic field can always be expressed in terms of a linear transformation of the Jones vector.

The polarimetric measurement behavior of a target can be described by a polarimetric 2x2 scattering matrix that connects two complex Jones vectors. In optics, the scattering matrix is defined using the FSA convention and is called the Jones matrix, whereas in the radar field it is defined using the BSA convention and is called the Sinclair matrix. The Sinclair matrix **S** and the Jones matrix **J** are related by:

$$\mathbf{J} = \begin{pmatrix} 1 & 0 \\ 0 & -1 \end{pmatrix} \mathbf{S}^*. \tag{2.4}$$

The Jones formalism that describes the transformation from a **totally polarized** input state into a totally polarized output state, can be written as:

$$\begin{pmatrix} E_h^s \\ E_v^s \end{pmatrix} = \mathbf{J} \begin{pmatrix} E_h^i \\ E_v^i \end{pmatrix}, \qquad \mathbf{J} = \begin{pmatrix} J_{11} & J_{12} \\ J_{21} & J_{22} \end{pmatrix} \tag{2.5}$$

The matrix **J** is a 2×2 complex matrix. This matrix can be parametrized in term of phase shifts Δ_{pq} and polarization ratios γ_{pq} $p, q \in [h, v]$:

$$\begin{pmatrix} J_{hh} & J_{hv} \\ J_{vh} & J_{vv} \end{pmatrix} = J_{vv} \begin{pmatrix} \gamma_{hh} e^{i\Delta_{hh}} & \gamma_{hv} e^{i\Delta_{hv}} \\ \gamma_{vh} e^{i\Delta_{vh}} & 1 \end{pmatrix} \tag{2.6}$$

The Jones matrix is a convenient tool to characterize the scene but most of the time non deterministic effect are produced and another formalism is needed to take these effects into account.

The first optical measurements were related to the measurements of the Jones matrix in order to characterize thin surfaces. As the optics measurements are incoherent, they are performed by intensity measurements, the Jones matrix can not be directly measured. Therefore, ellipsometry goes through a non-direct measure.

Spectroscopic ellipsometry measures Ψ and Δ, which describe respectively the output elliptical polarization state after that the linearly polarized light is reflected obliquely off of a thin film sample. The parameters Ψ and Δ are related to reflection coefficients r_p and r_s that are the Fresnel reflection coefficients for the p- and s- polarized light, respectively, according to:

$$\rho = \tan\Psi e^{j\Delta} = \frac{r_p}{r_s}.$$

Typically, ellipsometers do not measure Ψ and Δ directly. Instead, they measure several functions of Ψ and Δ that are intensities.

Moreover, these measures do not apply to non-deterministic effects. Gradually appeared in optical polarimetric imaging, a new range of measures: Mueller Polarimeters. That is those that have been investigated during this thesis, and we will now introduce tools for non-deterministic polarimetric parameters and measurements.

2.2.4 Partially polarized wave

In order to describe partial polarization that is a non-deterinitic state of polarization, the Stokes vector $\mathbf{g}$ can be introduced. It can be expressed from the covariance matrix of a Jones vector. After projection of this covariance matrix in the Pauli basis, real values that correspond to intensities can be obtained. They are parametrized as follows:

$$\mathbf{g} = \begin{pmatrix} I \\ Q \\ U \\ V \end{pmatrix} = \begin{pmatrix} \langle E_h^2 \rangle + \langle E_v^2 \rangle \\ \langle E_h^2 \rangle - \langle E_v^2 \rangle \\ 2\langle E_h E_v \cos\delta \rangle \\ 2\langle E_h E_v \sin\delta \rangle \end{pmatrix} = \begin{pmatrix} I \\ I \cdot DoP \cdot \cos 2\alpha \cdot \cos 2\varepsilon \\ I \cdot DoP \cdot \sin 2\alpha \cdot \cos 2\varepsilon \\ I \cdot DoP \cdot \sin 2\varepsilon \end{pmatrix} = \begin{pmatrix} I_H + I_V \\ I_H - I_V \\ I_{45^\circ} - I_{-45^\circ} \\ I_L - I_R \end{pmatrix} \tag{2.7}$$

, with $\delta = \varphi_h(t) - \varphi_v(t)$ and $<>$ representing the temporal average on the measurement time or the spatial averaging in the case of stationary multilook radar scenes. α is the orientation of the ellipse, and ε is the ellipticity. They are stated on figure 2.2. I_H and I_V stand for the horizontal and vertical polarization intensities, I_{45° I_{-45° are the linear polarizations for which $\alpha = \pm 45^\circ$ and $\varepsilon = 45^\circ$. I_L stands for the left circular polarization state ($\varepsilon = +45^\circ$) and I_R stands for the right circular polarization state ($\varepsilon = -45^\circ$). I is the total intensity and DoP is the degree of polarization of the Stokes vector [23], it is defined as:

$$DoP = \frac{\sqrt{Q^2 + U^2 + V^2}}{I} \tag{2.8}$$

The fact that one of the parameters U, Q or V has a non-zero value is due to the presence of a polarized component in the light wave, as represented in figure 2.3 on the right.

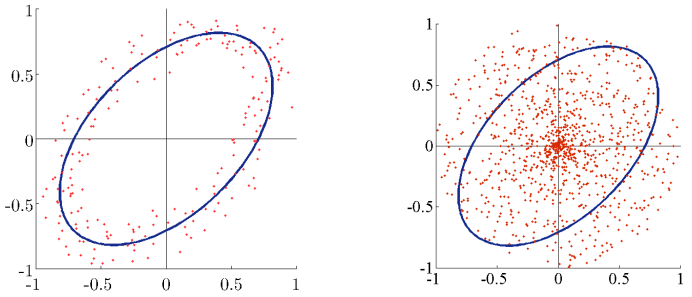

FIGURE 2.3: *In blue a totally polarized ellipse state. In red (a) realizations of a partially polarized state, (b) realizations of an unpolarized state.*

2.2.5 Transformation of a partially polarized wave

The Stokes formalism deals with partially polarized light. The Stokes vector that describes the polarization state that comes from an averaging and the transformation matrix includes transformations in the second order moments. Consequently, in the process of transformation of the polarization of the electromagnetic field the Stokes formalism can give the value of the capacity of the scene to *randomize* the incident polarization state. This important feature is denoted by the **depolarization**.

Definition 1. The depolarization is a process which transforms polarized light into unpolarized light. It can be considered as the action to increase the fluctuation in time and space of the polarization state of an incident wave.

The correspondence between the Stokes vector of the incident wave $\mathbf{g}_i$ and the received wave $\mathbf{g}_s$ is described by a real 4×4 matrix $\mathbf{M}$, called Mueller matrix of the object. More precisely, this transformation is written in equation 2.9:

$$\mathbf{g}_s = \begin{pmatrix} M_{11} & M_{12} & M_{13} & M_{14} \\ M_{21} & M_{22} & M_{23} & M_{24} \\ M_{31} & M_{32} & M_{33} & M_{34} \\ M_{41} & M_{42} & M_{43} & M_{44} \end{pmatrix} \mathbf{g}_i \tag{2.9}$$

The Mueller matrix is used to describe the polarization properties of any object whether depolarizing or not. In optics, one often uses the normalized Mueller matrix whose elements are divided by M_{11}, which exhibits the reflectivity. Given the generality of the description of the state of polarization Stokes vectors, the Mueller matrix is used to describe the polarization properties of any object whether depolarizing or not.

2.2.6 Coherency matrix

Optics measurements concern the Mueller matrices and the radar measurements concern only the first order Sinclair matrix. However, it is possible in radar to study also the statistical behavior of polarimetric information, by considering *second order polarimetric parameters* contained in the coherence matrix. The coherence matrix is defined as an expected value of the product of the scattering vector $\mathbf{k}$ with its complex conjugate $\mathbf{k}^\dagger$:

$$\mathbf{T} = \left\langle \mathbf{k}\mathbf{k}^\dagger \right\rangle \tag{2.10}$$

where the scattering vector $\mathbf{k}$ contains the components of the Sinclair matrix projected onto the Pauli basis as:

$$\mathbf{k} = \frac{1}{\sqrt{2}} \begin{pmatrix} S_{11} + S_{22} \\ S_{11} - S_{22} \\ S_{12} + S_{21} \\ -j(S_{12} - S_{21}) \end{pmatrix} \tag{2.11}$$

and $\langle\rangle$ corresponds to an averaging between several scattering vectors. Generally it is a spatial diversity of scattering vector. $\mathbf{T}$ is a 4×4 Hermitian matrix by definition, its eigenvalues are real, and its eigenvectors are orthogonal. In addition, since it is a variance-covariance matrix, its eigenvalues are positive or zero. These properties are interesting for decomposition purposes. This matrix is formed by complex elements but it contains the same information as the Mueller matrix. The linear link between the Mueller matrix and the Coherency matrix is given in equation 2.12.

$$\mathbf{T} = \frac{1}{2} \begin{pmatrix} M_{11} + M_{22} + M_{12} + M_{21} & M_{13} + M_{23} + i(M_{14} + M_{24}) \\ M_{13} + M_{23} - i(M_{14} + M_{24}) & M_{11} - M_{22} - M_{12} + M_{21} \\ M_{31} + M_{32} + i(M_{41} + M_{42}) & M_{33} - M_{44} + i(M_{34} + M_{43}) \\ M_{33} + M_{44} - i(M_{34} - M_{43}) & M_{31} - M_{32} + i(M_{41} - M_{42}) \end{pmatrix} \quad \ldots$$
$$\begin{pmatrix} M_{31} + M_{32} - i(M_{41} + M_{42}) & M_{33} + M_{44} + i(M_{34} - M_{43}) \\ M_{33} - M_{44} - i(M_{34} + M_{43}) & M_{31} - M_{32} - i(M_{41} - M_{42}) \\ M_{11} - M_{22} + M_{12} - M_{21} & M_{13} - M_{23} + i(M_{14} - M_{24}) \\ M_{13} - M_{23} - i(M_{14} - M_{24}) & M_{11} + M_{22} - M_{12} - M_{21} \end{pmatrix} \tag{2.12}$$

The table 2.1 summarizes the relations between the polarimetric formalisms.

TABLE 2.1: *Relations between polarimetric formalisms.*

Incident wave	⇒	Target	⇒	Scattered wave
Incident Jones vector $\mathbf{E}_E$	⇒	Deterministic target, Jones matrix $\mathbf{S}, \mathbf{J}$ ⇓ Scattering vector $\mathbf{k} = \frac{1}{2} trace(\mathbf{S}\Psi)$ $\Psi = \left[\sqrt{2}\begin{pmatrix}1 & 0\\ 0 & 1\end{pmatrix}, \sqrt{2}\begin{pmatrix}1 & 0\\ 0 & -1\end{pmatrix}, \sqrt{2}\begin{pmatrix}0 & 1\\ 1 & 0\end{pmatrix}, \sqrt{2}\begin{pmatrix}0 & -i\\ i & 0\end{pmatrix}\right]$	⇒	Scattered Jones vector $\mathbf{E}_R$
radar: statistical estimation (ex.: spatial averaging, looks averaging) optics: time averaging ⇓ Coherency matrix $\mathbf{T} = \langle \mathbf{k}\mathbf{k}^\dagger \rangle$ ⇕				
Incident Stokes vector $\mathbf{g}_E$	⇒	Muller $\mathbf{M}$ or Kennaugh $\mathbf{K}$ matrix General Case (used in practice in optics)	⇒	Scattered Stokes vector $\mathbf{g}_R$

2.2.7 Physically feasible Mueller matrix

Any four real component vector is not necessarily a feasible Stokes vector. It has to verify that the relation:

$$I \geq Q + U + V \tag{2.13}$$

and a real 4×4 matrix does not necessarily correspond to a Mueller matrix. Obviously a necessary condition is the following: any physical Stokes vector must be converted into another physical Stokes vector. This condition is not sufficient, and, moreover, it

is not very convenient to actually check the realizability of a measured matrix. The physical nature of a Mueller matrix is actually determined as follows:

1. From the matrix **M** investigated, the coherency matrix is formed using 2.12 relations.

2. Determine whether or not the **T** eigenvalues are positive or null. It is a necessary and sufficient condition for a matrix **T** to be a variance-covariance matrix of four complex random variables (the elements of the J_{ij} Jones matrix statistically defined). See table 2.1.

One can notice that reasons to obtain a non physical matrix can be a low SNR ratio, and measurement can be infected by over-polarization that characterize a non physical measured matrix.

2.2.8 Depolarizing or nondepolarizing character of a Mueller matrix

The coherency matrix also makes it easy to answer the question whether a Mueller matrix discloses a depolarizer system. Indeed, in the latter case, the Jones matrix **J** is given exactly, not statistically. The matrix **T** is then strictly equal to the $E_{ij}E_{kl}^{*}$ products: it is the orthogonal projection matrix, in the $\mathbb{C}^4$ space formed by the vector of the four components J_{ij} of the Jones matrix.

In other words, a necessary and sufficient condition for a Mueller matrix not to be depolarizing is that the associated coherency matrix has one **strictly positive eigenvalue**, and the other three zero.

In addition, the diagonalization of **T** provides the associated Jones matrix: its four elements are the four components of the eigenvector from **T** associated with the nonzero eigenvalue.

In addition, several proposal decompositions of the coherency or Mueller matrix exist to extract the polarimetric behavior of a material. Considering only the depolarization effect one can mention the work of Gil [23] and Lu and Chipman [24] with respectively that we will name here the parameters PI and Δ.

$$PI = 1 - \sqrt{\frac{1}{3}\frac{\sum_{i,j}(M_{i,j}^2) - M_{1,1}^2}{M_{1,1}^2}} \tag{2.14}$$

with $\mathbf{M}_{i,j},\ i,j = 1,2,3,4$ denoting the elements of the Mueller matrix. If $PI = 0$ the scene does not depolarize and if PI reaches 1, the scattered electromagnetic field is

totally depolarized.

$$\Delta = 1 - \frac{|Trace(M_\Delta - 1)|}{3} \tag{2.15}$$

with M_Δ being the depolarization factor of the matrix $\mathbf{M}$. In [25] the difference between these two indexes is detailed.

The statistical properties of partially polarized waves have been studied by Barakat in [26]. In the radar community, the depolarization component of the Stokes vector in the framework of the forest was studies as soon as the early nineties in [27]. In the next section the polarimetric decompositions are more deeply investigated.

2.3 Polarimetric decompositions

2.3.1 Visualization and Pauli basis decompositions in bistatic

In monostatic radar it is common to use a color representation of the polarimetric information. One parameter is assigned to a color channel: Red, Green or Blue, via the Pauli basis. In that way, the Red often corresponds to the $|hh + vv|$ contribution, the Blue to the $|hh - vv|$ channel and the Green to the $|hv|$, in BSA convention. Other assignations can be imagined, but the result of these colorful representations depends on a number of other choices too:

- It is possible to take into account the intensity as multiplying factor of each color channel. This one balances the intensity of the pixel and it gives more contrasted image. In all cases, the channels must have a common boundary. This can raise issue especially for decompositions that lead to unbounded parameters, such as for Yamaguchi decomposition [12]. In such cases, it may be necessary to threshold the parameters to avoid non-significant values. However the choice of the threshold remains arbitrary.

- Moreover the dynamics of these parameters often produced visually disappointing results if this dynamic is not adapted. One can therefore choose whether or not to make a histogram normalization, i.e. to transform the image such that each value is present in equal amount. The reason why histogram normalization is performed is to make maximum use of the range of values available. A low-contrast image can have a lot of details after equalization.

Depending on these choices, the resulting color image can actually be very different. A colorful representation of three polarimetric parameters is therefore not sufficient to demonstrate the relevance of the selected parameters.

Nevertheless, for the case of our bistatic study the high contrast between the pixels is not of prime importance, and when decomposition results will be presented in this manuscript, the total intensity will not be used.

Here, using the Stokes formalism the $|hh + vv|$, $|hh - vv|$ and $|hv|$ or $|vh|$ channels can be deduced from the Kennaugh matrix, considering the first 2×2 bloc matrix:

$$\begin{pmatrix} K_{11} & K_{12} \\ K_{21} & K_{22} \end{pmatrix} =$$
$$\begin{pmatrix} \frac{1}{2}(|J_{vv}|^2 + |J_{vh}|^2 + |J_{hv}|^2 + |J_{vv}|^2) & \frac{1}{2}(|J_{vv}|^2 - |J_{vh}|^2 + |J_{hv}|^2 - |J_{vv}|^2) \\ \frac{1}{2}(|J_{vv}|^2 + |J_{vh}|^2 - |J_{hv}|^2 - |J_{vv}|^2) & \frac{1}{2}(|J_{vv}|^2 - |J_{vh}|^2 - |J_{hv}|^2 + |J_{vv}|^2) \end{pmatrix}.$$

En example of the use of color representation of a polarimetric SAR image is given in figure 2.4

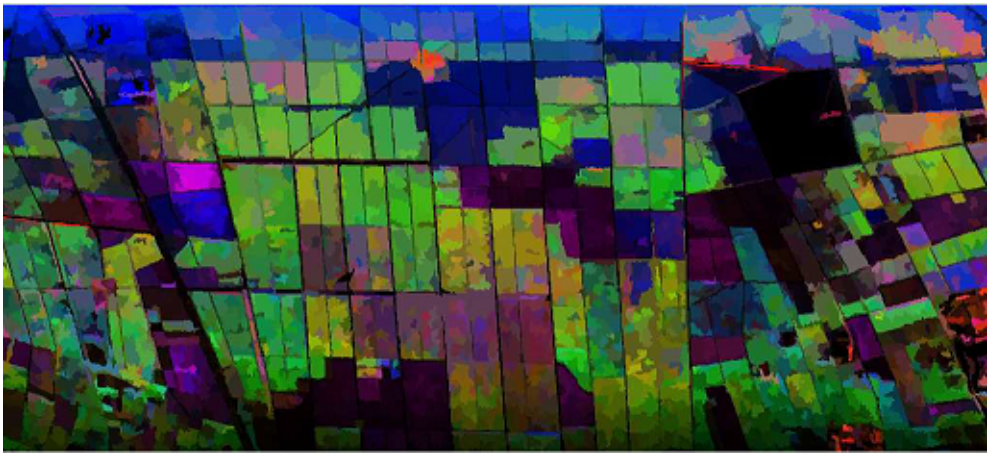

FIGURE 2.4: *Polarimetric SAR image of the Nezer forest using the color representation in the Pauli basis.*

The target behaviors are difficult to interpret directly from the scattering matrix coefficients. Consequently one uses polarimetric decompositions to try to describe targets as superpositions or series of canonical behaviors. Two categorizations of decompositions are possible:

- coherent and incoherent decompositions
- additive and multiplicative decompositions (or serial and parallel ones)

The incoherent and coherent decompositions of Jones and Mueller matrices are described in [28] and [23]. The incoherent decompositions serial and parallel are privileged for this work because incoherent decomposition can handle depolarization effect resulting from complex interaction.

2.3.2 Bistatic Cloude-Pottier parameters

The Cloude-Pottier decomposition uses the diagonalization of the coherency matrix $\mathbf{T}$ that is linearly linked to the Mueller matrix [28]. The entropy H is defined as follows:

$$H = -\sum_{i=1}^{n}(\hat{\lambda}_i \log_n \hat{\lambda}_i), \qquad \hat{\lambda}_i = \frac{\lambda_i}{\mathrm{tr}\mathbf{T}}, \tag{2.16}$$

where $n = 3$ for the monostatic case where $\mathbf{T}$ is a 3×3 matrix and $n = 4$ for the bistatic case where $\mathbf{T}$ is a 4×4 matrix. H represents the randomness of the scattering mechanisms. $\hat{\lambda}_i$ can be considered as being the probability for a scattering mechanism represented by λ_i to be present in the measurement.

Cloude [28] defines also the scattering anisotropies as:

$$A_{i,j} = \frac{\lambda_i - \lambda_j}{\lambda_i + \lambda_j}, \qquad 0 \leq A_{ij} \leq 1 \tag{2.17}$$

If an anisotropy parameter has a value near to 1, it means that there is subspace where the depolarization is low. The anisotropy often used is $A_{2,3}$.

Each eigenvector u_i can be parametrized as:

$$u_i = \begin{pmatrix} \cos\alpha_i e^{j\phi_1} \\ \sin\alpha_i \cos\psi_i e^{j\phi_2} \\ \sin\alpha_i \sin\psi_i \cos\gamma_i e^{j\phi_3} \\ \sin\alpha_i \sin\psi_i \sin\gamma_i e^{j\phi_4} \end{pmatrix} \tag{2.18}$$

So the α_i angle is characteristic of each eigenvector. Then, a synthetic parameter $\bar{\alpha}$ was introduced by Cloude and Pottier to extract information about the type of mechanism and it is defined as :

$$\bar{\alpha} = \sum_{i=1}^{4} \hat{\lambda}_i \alpha_i, \qquad 0 \leq \bar{\alpha} \leq 90° \tag{2.19}$$

The efficiency of the parameters H and $\bar{\alpha}$ has been proven for classification purposes in backscattering radar imagery but it remains to be tested in the general bistatic case.

2.3.3 Lu and Chipman decomposition

From the Mueller matrix, several optical decompositions exist that exhibit parameters describing optical characters of the sample. The essential role of decomposition is to distinguish elementary optical activities that the material induces [23].

The Lu & Chipman decomposition [24] is a multiplicative decomposition elaborated to outline the diattenuation, the retardance and the depolarization. Those three parameters summarize the polarization behavior of the scattering media.

This serial decomposition was originally developed to retrieve the behavior of the optical components (lenses, polarizer, retarder) that interact in cascade with the incident beam. In our case, the forest can be modeled in a layered manner with branches and then trunks and could then be linked to this serial decomposition. Lu and Chipman decomposition has been widely used and tested in bistatic configuration including specular configuration [29] and it is a way to simply exhibit the polarization transformation.

The basic polarization transformers are the partial diattenuator $\mathbf{M}_D$, the retarder $\mathbf{M}_R$ and the depolarizer $\mathbf{M}_\Delta$. $\mathbf{M}_D$ describes the changes in amplitudes, $\mathbf{M}_D$ describes the changes in phase and $\mathbf{M}_\Delta$ describes the reduction of the DoP of the incident Stokes vector. Any Mueller matrix $\mathbf{M}$ can be written in the form

$$\mathbf{M} = \mathbf{M}_\Delta \cdot \mathbf{M}_R \cdot \mathbf{M}_D, \tag{2.20}$$

with the following expressions:

$$\mathbf{M}_D = \mathbf{M}_{11} \begin{pmatrix} 1 & \mathbf{D}^t \\ \mathbf{D} & \mathbf{m}_D \end{pmatrix}, \mathbf{M}_R = \begin{pmatrix} 1 & \mathbf{0}^t \\ \mathbf{0} & \mathbf{m}_R \end{pmatrix}, \mathbf{M}_\Delta = \begin{pmatrix} 1 & \mathbf{0}^t \\ \mathbf{P}_\Delta & \mathbf{m}_\Delta \end{pmatrix}, \tag{2.21}$$

with $\mathbf{M}_{11}$ the transmission factor of the unpolarized electromagnetic wave. In [24] the expression for the different matrices are detailed as follows. T_u is the transmission factor of the unpolarized electromagnetic wave and,

$$\mathbf{m}_D = \sqrt{1-D^2}\mathbf{Id} + (1-\sqrt{1-D^2})\hat{\mathbf{D}}\hat{\mathbf{D}}^t, \quad \hat{\mathbf{D}} = \frac{\mathbf{D}}{||\mathbf{D}||} \tag{2.22}$$

$$(\mathbf{m}_R)_{ij} = \delta_{ij}\cos R + a_i a_j(1-\cos R) + \sum_{k=1}^{3} \epsilon_{ijk} a_k \sin R, \quad i,j = 1,2,3 \tag{2.23}$$

$$\mathbf{m}_\Delta^T = \mathbf{m}_\Delta \tag{2.24}$$

$\mathbf{D}$ is the 1×3 vector called the diattenuation vector of norm D, R is the retardance linked to the retardance vector $\mathbf{R}$

$$\mathbf{R} = R \cdot \begin{pmatrix} a_1 \\ a_2 \\ a_3 \end{pmatrix} = \begin{pmatrix} R_H \\ R_{45^\circ} \\ R_C \end{pmatrix}, \tag{2.25}$$

with δ_{ij} and ϵ_{ijk} the Kronecker symbol and the Levi-Civita permutation symbol. **Id** is the 3×3 identity matrix.

Here the calculus to retrieve these three matrices is briefly exposed. Firstly **D** can be extracted from the first line of **M**. $\mathbf{M}_D$ is created from **D** and then $\mathbf{M}' = \mathbf{M}_D^{-1} \cdot \mathbf{M}$. $\mathbf{P}_\Delta$ is extracted from $\mathbf{M}'$ and $\mathbf{m}_\Delta$ is calculated as follows:

$$\mathbf{m}_\Delta = sign(det(\mathbf{m}')) \left[\mathbf{m}'(\mathbf{m}')^T(\sqrt{\lambda_1\lambda_2} + \sqrt{\lambda_2\lambda_3} + \sqrt{\lambda_3\lambda_1})\mathbf{Id}\right]^{-1} \cdot \left[(\sqrt{\lambda_1} + \sqrt{\lambda_2} + \sqrt{\lambda_3})\mathbf{m}'(\mathbf{m}')^T + \sqrt{\lambda_1\lambda_2\lambda_3}\mathbf{Id}\right] \tag{2.26}$$

λ_1, λ_2 and λ_3 are the eigenvalues of $\mathbf{m}'(\mathbf{m}')^T$ such as $\mathbf{M}' = \begin{bmatrix} 1 & \mathbf{0} \\ \mathbf{P_\Delta} & \mathbf{m}' \end{bmatrix}$. Finally the retardance matrix is retrieved as $\mathbf{M}_R = \mathbf{M}_\Delta^{-1} \cdot \mathbf{M}'$

From $\mathbf{M}_D$,$\mathbf{M}_R$ and $\mathbf{M}_\Delta$ the vectors diattenuation **D**, retardance **R** and the scalar Δ are extracted. **D** represents the state of polarization that is less attenuated by **M**, it has the form of a Stokes vector from which parameter, the scalar value $D = |\mathbf{D}|$ represents the relative attenuation between **D** and its orthogonal state. Ellipse parameters $\alpha(\mathbf{D})$ and $\varepsilon(\mathbf{D})$ contain the other information about the diattenuation vector. Then, $\mathbf{m}_R$ is a 3×3 rotation matrix and **R** is the axis of rotation. From the vector **R** on can also extract a scalar parameter $R = |\mathbf{R}|$ and ellipse parameters $\alpha(\mathbf{R})$ and $\varepsilon(\mathbf{R})$.

Concerning the depolarization characteristics of the Mueller matrix the scalar Δ is extracted from the diagonal components of $\mathbf{M}_\Delta$. Another figure of merit called Purity Index was introduced by Gil and Bernabeu [30] that can be easily extracted directly from the Mueller matrix elements. It can be interpreted as the euclidean distance between the matrix **M** and an ideal depolarizer using equation 2.14

Figure 2.5 shows the depolarization parameter and the entropy parameter in the case of a SAR image of the Nezer forest (Landes, France). Forest stands present high depolarization and entropy. Both parameter exhibits similar behavior but with different dynamic range.

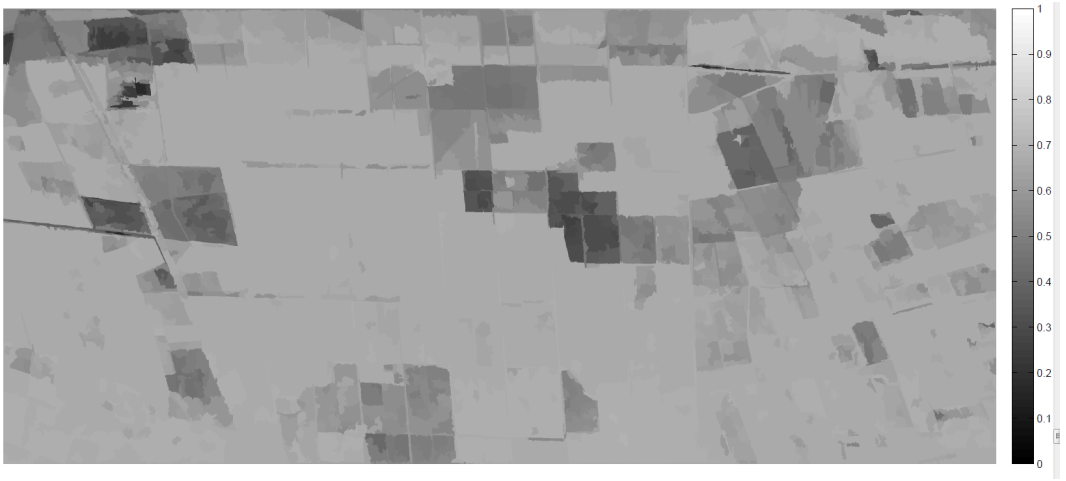

(a)

(b)

FIGURE 2.5: *Comparison example of application of the Lu and Chipman depolarization (a) and Cloude and Pottier entropy (b) decompositions for the case a the SAR image of the Nezer forest.*

2.3.4 Reverse decomposition

The decomposition proposed by Lu and Chipman is commonly used today in optics. However, it is non commutative and the order of the elements can affect the resulting diattenuation, depolarization and retardance parameters. This problem was addressed in [31]. Depending on the order of the matrices used in such a decomposition, six possible arrangements can be obtained. They are divided into two groups according to the relative positions of the diattenuator and the depolarizer. Each family has different values for the diattenuation, the retardance and the depolarization. The only modifications are the eigenstates of the elementary matrices but the two families have different properties. Indeed, it is possible to obtain non physical Mueller matrices in the case where the diattenuation matrix is before the depolarizer especially when diattenuation and depolarization are both high. To solve these problems in this second family of decomposition, [32] proposes to define the depolarizing element as follows:

$$M_\Delta = \begin{pmatrix} 1 & \mathbf{D}^t \\ 0 & \mathbf{m}_\Delta \end{pmatrix} \tag{2.27}$$

characterized by a zero polarizance vector $\mathbf{P}$ and nonzero diattenuation $\mathbf{D}$. Consequently when the diattenuation and the depolarization values are high this decomposition must be investigated.

2.3.5 Ossikovski decomposition

We have seen that the limitation of the decomposition of Lu and Chipman is highlighted for non-diagonal depolarization matrices. R. Ossikovski proposes an alternative solution in [33] which consists in decomposing the Mueller matrix in a symmetrical product of five matrices:

$$\mathbf{M} = \mathbf{M_{D1}}\mathbf{M_{R1}}\mathbf{M_{\Delta}}\mathbf{M_{R2}}\mathbf{M_{D2}} \tag{2.28}$$

The depolarization matrix $\mathbf{M}_\Delta$ is diagonal. It is surrounded by two pairs of diattenuator and retarder. As the Lu and Chipman decomposition it is both the re-setting and sub-setting of the polarimetric information. The advantage of this decomposition is that it allows to consider a return path in a medium that can be suited to what is happening physically for monostatic configuration or bistatic configuration. For the study of forest it is useful if we consider the wave penetration in the environment. Furthermore, this decomposition produces two pairs of retarder and diattenuators that are different for the inward and the outward path of the wave. In the monostatic case, the two produced matrices $\mathbf{R}_1, \mathbf{D}_1$ and $\mathbf{R}_2, \mathbf{D}_2$ are identical. Two limitations were encountered in [12]. The first occurs when the matrix decomposed by Lu and Chipman

already gives a diagonal depolarization matrix, and in practice the Lu and Chipman decomposition should first be trained to check if it produces a diagonal depolarization matrix. In this case, the depolarization matrix switches and thus it is possible to write the symmetric form of a matrix with null retarder and null diattenuation to the left and to the right of the decomposition and consequently the symmetric decomposition is unnecessary. Otherwise the symmetric decomposition correctly applies. The second problem is the non-uniqueness of the couple formed by the two retarders. Indeed a rotation angle $+\theta$ of the first retarder is equivalent to the $-\theta$ rotation of the second retarder. However, this ambiguity can be solved simply by the principle of minimum retardance which is arbitrarily set the first retarder to minimize the total retardance.

2.3.6 Choice of the parameters for the purpose of this work

From the precedent description, the Lu and Chipman decomposition seems more adapted for a bistatic configuration and non deterministic targets such as the forest. Nevertheless the bistatic Cloude and Pottier decomposition has not been deepen studied in the bistatic case, and it seems interesting to try it and to compare the results with the Lu and Chipman decomposition. Moreover, in case where the depolarization matrix computed through the Lu and Chipman decomposition is not diagonal, the reverse and symmetrical decomposition can also be considered.

* * *

Summary
In this chapter the polarimetry formalisms were introduced for radar measurement but also for the optical scale. The two research domains have been developed independently. Consequently, there are many differences in the two formalisms, even if it accounts for the same physical phenomenons. Nevertheless, the equivalences can be retrieved. What is more, the optical polarimetry has been developed in the bistatic context hic is common in optics. The formalism and the decompositions developed for optics seem very relevant for radar, especially for non-deterministic targets such as forest and in the bistatic configuration. In the next chapter, the correspondences are summarized.

Chapter 3

Comparative synthesis of the optical and radar polarimetric imaging

Our aim is to use alternative measurements at optical scale to extrapolate the results in radar even if we saw that for the formation of the images the data of the radar and the optics are to be distinguished. This section synthesizes changes between a polarimetric optical image and a polarimetric radar image. Concerning the radar domain, the bistatic radar does not lead to the same simplifications for the formation of image as the monostatic radar. The resolutions are not expressed simply and they are degraded when the bistatic angle increases. Moreover, the states of polarization are not produced and not detected in the same way for both scales. Nevertheless, the mathematical formalisms can be applied to the one or the other domain at the condition to master correctly the polarimetry coordinate system in the bistatic configuration. This one influences some parameters stemming from polarimetric decompositions. This is why it is important to specify here these differences. It is also useful to be able to make a warned custom of the measurements and to give recommendations for the acquisition campaigns and implementations.

3.1 Measured quantities

The measured signal in radar is deduced from electrical current sensed by the receiving antenna. The signature of the target is evaluated for the case of a delimited target by the Radar Cross Section (σ $[m^2]$) defined by:

$$\sigma = \lim_{R\to\infty} 4\pi R^2 \frac{|E_r|^2}{|E_e|^2} \tag{3.1}$$

where E_r and E_e denote respectively the received and the emitted electric field and R is the distance between the antenna and the target. In the case of a distributed scene, such as the forest, the parameter σ^0 is introduced in order to evaluate the reflectivity of the scene per unit area:

$$\sigma^0 = \lim_{R\to\infty} \frac{4\pi R^2}{A} \cdot \frac{|E_r|^2}{|E_e|^2} \tag{3.2}$$

with A the footprint area of the emitted signal on the scene in $[m^2]$. The terms sigma naught, differential scattering coefficient, normalized radar cross-section or backscatter coefficient are used for σ^0 [34]. The coefficient also depends on emitter and receiver linear polarizations. From four couples of E/R polarizations one can reconstruct the scattering matrix $\mathbf{S}$ of the target.

On another hand our implementation tool at optical scale consists in a Mueller polarimeter and this kind of system measures light intensities. Generally, a Mueller polarimeter consists of a first light source. This source can be monochromatic or spectral depending on applications and characteristics of the instrument. This source is followed by a polarization state generator (PSG) which modulates the polarization of the light and provides the initial polarization states. To measure a complete Mueller matrix, these states will form a part of the generator Stokes vector space and be therefore composed of at least four independent polarization states. The light whose polarization is controlled then interacts with the studied sample, as configured by transmission, reflection, diffraction. Modified polarization states are then projected on a known state basis, provided by the analyzer polarization state (PSA), before measuring intensity with a detector.

The Mueller matrix is obtained after inversion of the measured intensity matrix in the PSA and PSG basis matrices. It is worth noting that no absolute phase is measured and the system deals directly with the Mueller matrix formalism, linearly linked to the covariance matrix, see table 3.1. The table 2.1 gives relations between the formalisms.

TABLE 3.1: *Measured Quantities in polarimetry,* $\mathbf{W}$ *and* $\mathbf{A}$ *denote respectively the PSA and The PSG basis matrices.*

RADAR	*OPTICS*
Complex values	Intensities
$\mathbf{S} = \begin{pmatrix} \sigma^0_{hh} & \sigma^0_{hv} \\ \sigma^0_{vh} & \sigma^0_{vv} \end{pmatrix}$	$I_{i,j}$, $\mathbf{M} = \mathbf{W^{-1}}.\mathbf{I}.\mathbf{A^{-1}}$

It must be remarked that the PSA and PSG basis matrices are critical for the Mueller matrix retrieval which needs a special attention to their calibration. This calibration is made in a chosen coordinate system which is not always the same in radar or in optics.

3.2 Vocabulary

The terms used in both domains are summarized in Table 3.2.

TABLE 3.2: *Polarimetric vocabulary correspondence for radar and optics.*

RADAR	*OPTICS*
Monostatic measurement	Backscattering measurement
Sinclair matrix	Jones matrix
Kennaugh matrix	Mueller matrix
Kennaugh vector	Stokes vector
Non deterministic target	Depolarizing target
Deterministic target	Non depolarizing target
Man made object	Mueller-Jones media

It is important to note that the polarimetric tools can refer both to the description of the electromagnetic wave (scattered wave and incident wave) and description of the target (the behavior with respect to the incidence wave polarization).

3.3 Conventions and coordinate systems

3.3.1 Wave conventions

Here we present the three main polarimetry conventions that are used in both domains. The coordinated systems are the basis of polarization directions in the wave plane.

TABLE 3.3: *Convention for the polarization basis for radar and optics*

$(\mathbf{h}, \mathbf{v})$	$(\mathbf{s}, \mathbf{p})$	$(\mathbf{x}, \mathbf{y})$
The reference is the horizontal for the antenna	The reference is the incidence plane	It is independent on the azimuth angles φ_e, φ_r after projection in the horizontal plane

The emitted wave and the received wave have to be distinguished and the same wave convention can lead to opposite vectors depending on the target convention.

3.3.2 Target conventions

The existence of several target conventions for one coordinate system is due to implementation commodities. For example in radar when the same antenna is used as

emitter and receiver the same polarization directions are used for the transmission and the reception (Back Scattering Alignment or BSA). It disagrees with the convention which uses the wave vector as reference vector (Forward Scattering Alignment convention or FSA), as represented in figure 3.1.

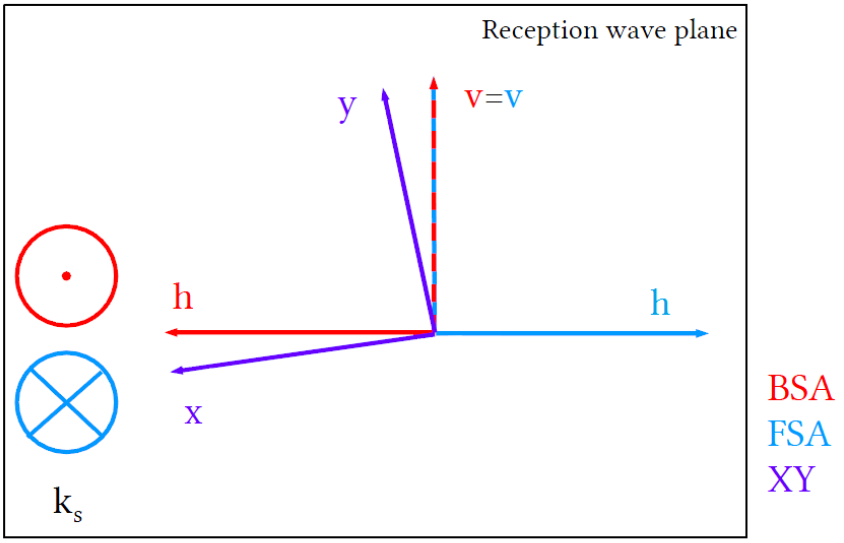

FIGURE 3.1: *Schematic of the wave conventions. In BSA,* $\mathbf{k}_s$ *does not correspond to a physical wave vector but to a wave vector in the opposite direction, such as* $(\mathbf{h}, \mathbf{v}, \mathbf{k})$ *is direct.*

3.4 Image properties

As stated in chapter 1 the main differences reside in the image processing principles. The table 3.4 relates several characteristic imaging dimensions for both domains. The resolution dimension cannot be simply expressed for bistatic radar, only monostatic SAR resolution is expressed here.

TABLE 3.4: *Comparison of image properties. λ denotes the central wavelength, λ_1 and λ_2 denote respectively the high and low limits of the radar frequency band. R_0 is the distance between the platform and the target (see figure 1.4) V_t is the platform velocity and T is the integration time, θ is the semi aperture angle of the optical objective, n is the refractive index of the optical objective.*

	RADAR	*OPTICS*
Spatial dimension order	1km	1mm
Resolution functions	$\frac{R_0\lambda}{V_tT} \times \frac{0.88\lambda_1\lambda_2}{2(\lambda_1-\lambda_2)}$	$\frac{\lambda}{2n\sin\theta}$
Image sampling	sample rate of the carrier	CCD camera grid

Images issued from polarimetric measurement are often created after a processing step. The Mueller matrix can be directly imaged because it is formed of real values but the Stokes formalism and the Mueller matrix includes an averaging of scattering matrices.

3.5 Averaging process

The averaging is included in the measurement at optical scale because intensity are measured on the CCD detector in order to reconstruct the Mueller matrix. The intensity are recorded along an integration time. This integration time is linked to the received power to have a sufficient SNR. Otherwise, in radar the antenna are moving and there is no averaging directly during the measurement to estimate the coherence matrix. Despite this problem, in practice neighbor image pixel coefficients are averaged in order to compute a Coherence or a Mueller matrix.

TABLE 3.5: *Stokes parameter estimation process.*

RADAR	*OPTICS*
Pixel based spatial estimation From the complex measurement of a scattering matrix	Fixed sensor and integration time from intensity measurements

3.6 Polarimetric decomposition categories

Usually, distinct decompositions are used depending on the application domain, see table 3.6, but as the polarimetric formalism can be adapted in both case the decomposition can be applied in both cases too. In [12], the use of optics decomposition for radar was investigated. It is very relevant especially in the bistatic case which is natural in optics.

TABLE 3.6: *Usually used decomposition types depending on the application domain.*

	RADAR	*OPTICS*
Coherent decomposition	ex: Pauli, Krogager [35]	ex: Polar decomposition (Ψ, Δ)
Incoherent decomposition	Parallel decomposition ex: Cloude-Pottier	Serial decomposition ex: Lu Chipman, Ossikowski, reverse

* * *

Summary
Distinctions must be realized between image formation techniques nd polarimetric formalisms at radar scale and optical scale. The main particularity of the radar is the use of the chirp signal in order to gain a Doppler resolution which avoid a 2D angular diversity for the acquisition. Nevertheless it is shown that comparison can be realized. The pieces of advice that can be pointed out from this chapter are

- the use of the $(\mathbf{x}, \mathbf{y})$ polarization coordinate system to be able to compare bistatic configurations,
- to avoid the specular position to be able to form a SAR resolved image,
- to use polarimetric decompositions from optics that are well adapted for the bistatic configuration.

In the following the similarities between the two scales enables to use an optical scale device for the anticipation of the radar scale measurement within the restriction domin given by the similitude principle.

Part II

Scaled down measurement on forests

Chapter 4

A forest at radar scale and a forest at optical scale

To be able to work out smaller scale measurements on forests, we need to understand what structure of forest must be kept and what forest parameters are essential for the polarimetric measurements.

In this chapter we justify via the scale invariant rule the use of optical tools, bistatic in essence, to go further to the anticipation of the real radar measurements on forests, whatever the bistatic angle. It leads to a proposal for forest structure samples with micrometer size elements, to be able to have an equivalent with radar measurements, exhibiting the same behavior. The choice of the scaled forest structure is also related to the sample elaboration know-how at LPICM.

4.1 Similitude principle

Scaled measurements using the similitude principle give the opportunity to validate simulation tool from which scenarios are used to predict full polarimetric and bistatic radar SAR measurements. Down scaled measurements are sustainable classically using anechoic chamber [11]. Some examples of the use of this device are the study of Sami Bellez [9], conducted in order to validate exact modelling tool and the one of Nicolas Trouvé [36], in order to study the influences of geometrical bistatic configurations on the polarimetric parameters.

The main problem that limits the use of this device is the creation of the scene playing the role of the forest at the other scale. Typically, for the bistatic anechoic chamber owned by ONERA, the bistatic frequency range is 0.4-40 GHz. It leads to a scale of 1/40 for the forest when the far field conditions are maintained with respect to

an airborne measurement. Dielectric cylinders are used as trunks but it is not feasible to reproduce experimentally an entire forest that would be actually needed to take into account all interactions that occur for the real SAR measurement. Facing this main difficulty, another scaling step was investigated in the Nicolas Trouvé's thesis [12]. The investigation of similar targets at the two scales leads to a structure correspondence between a tree forest at the radar scale and carbon nanotubes samples at the optical scale.

The similitude principle is developed in [37]. In[38] it is expressed in a simple manner as a scale invariant rule (**SIR**) for an isotropic, linear and possibly inhomogeneous material. What is called the microwave analog technique is also based on the same rule. The similitude principle is obtained by the way of the Lippmann-Schwinger equation in [38]. This rule can also be derived from the Helmholtz equation using appropriate boundary conditions, [39][40] or from the principle of electrodynamic similitude [41]. Using the Maxwell equations, let us consider two homogeneous, isotropic and lossy electromagnetic systems (A) and (A'). The fields are described in both systems by equations:

$$\nabla \times \mathbf{E} + \mu \frac{\delta \mathbf{H}}{\delta t} = 0, \qquad \nabla \times \mathbf{H} - \sigma \mathbf{E} = \varepsilon \frac{\delta \mathbf{E}}{\delta t} \tag{4.1}$$

and

$$\nabla \times \mathbf{E}' + \mu' \frac{\delta \mathbf{H}'}{\delta t} = 0, \qquad \nabla \times \mathbf{H}' - \sigma' \mathbf{E}' = \varepsilon' \frac{\delta \mathbf{E}'}{\delta t} \tag{4.2}$$

where $\mathbf{E}$, $\mathbf{H}$, $\mathbf{E}'$ and $\mathbf{H}'$ are the electric and magnetic fields of system (A) and (A'). σ, σ', ε, ε', μ and μ' are respectively the conductivities, the real permittivities and the permeabilities of the media. We consider that the system (A') is similar to the system (A) with a scale factor k_l such as $x = k_l x'$, $y = k_l y'$ and $z = k_l z'$. One can write equation 4.2 in term of the parameters of (A') via scale factors k_l if the scale factor for the other parameter are introduced:

$$k_l = \frac{l}{l'}, k_\mu = \frac{\mu}{\mu'}, k_\varepsilon = \frac{\varepsilon}{\varepsilon'}, k_\sigma = \frac{\sigma}{\sigma'},$$

$$k_t = \frac{t}{t'}, k_\lambda = \frac{\lambda}{\lambda'}, k_f = 1/k_\lambda, k_E = \frac{|E|}{|E'|}, k_H = \frac{|H|}{|H'|}$$

as in [42], with l and l' equivalent lengths in system (A) and (A') and t, f, t', f' equivalent times and frequencies in system (A) and (A'). To have the same solution in 4.1 and 4.2 and considering $k_f = k_t$ because the field's period is the inverse of the frequency it comes:

$$\frac{l^2\varepsilon}{\lambda^2} = \frac{l'^2\varepsilon'}{\lambda'^2} \tag{4.3}$$

$$\frac{l^2\sigma}{\lambda} = \frac{l'^2\sigma'}{\lambda'} \tag{4.4}$$

In order to have the same attenuation and distortion behaviors at the two scales, the real permittivities and the permeabilities are equal at two scales, $\varepsilon = \varepsilon'$ and $\mu = \mu'$. Consequently from equations 4.3 and 4.4:

$$k_\lambda = k_l, \qquad k_\sigma = 1/k_l, \qquad k_E = k_H \tag{4.5}$$

If we consider the complex refractive indexes of the system by $\tilde{n} = \sqrt{\tilde{\varepsilon}\mu}$, with $\tilde{\varepsilon} = \varepsilon - j\sigma\lambda/(2\pi c)$, the rule can be summarized in the following sentence:

> If the same ratio of elements size to wavelength is observed between two scenarios, the measurement result of one scenario is valid to the other provided that the refractive index remains the same.

We base ourselves on the **SIR** in measuring scaled down forest at a scaled down frequency. The refractive index is a critical parameter and same relative refractive index between the trunks and branches and a nanometric element is not obvious to obtain. In any case we use the simulation as a relay between the two scales for which proper permittivities are set. As stated in [42], in a geometric scaled model the relative power can differ and the solution can be calibrated afterward. It means that the absolute power of the source in our scaled model is not a key parameter as long as the SNR in our measurement is sufficient.

It is important to observe again that optical scale measurement cannot provide the SAR image for a down scaled scene as explained in chapter 3. But we want to look at the building block of the global image, that is the scattered signals for each frequency and each angle configuration. Optical scale devices exist and can provide evolution depending on the frequency thanks to spectrometric polarimeter and also to provide evolution depending on the angular configuration thanks to rotation of the standard polarimeter or angle resolved polarimeter.

4.2 Development of a target of interest at the right scale ratio

4.2.1 General remarks on the nanotube forests

The "Laboratoire de Physique des Interfaces et Couches Minces" (LPICM) has developed advanced research and technologies for the thin film creation and semiconductors. A wide variety of material are investigated for their creation with structural requirement. Our interest in these techniques is the possibility to have forest structure at the nano scale for which the scale ratio between the tree elements and the optical wavelength of the source remains the same as for the P-band radar. The carbon nanotube was for us the most interesting material for their tree like structure, as represented in the artistic view of figure 4.1.

FIGURE 4.1: *From the study of full scale forest to the study of carbon nanotube forests.*

At LPICM carbon nanotube creation techniques have been developed for applications in solar panels development or nanocathode for X-ray sources. In particular, the team directed by Costel Sorin Cojocaru developed a Chemical Vapor Deposition reactor.. One aim of the technique in the case of the nanotubes is to maximize the electron

emission from the CNT arrays. In Chemical Vapor Deposition (CVD) the growth process involves the use of fine particles of some transition metal catalyst (for instance Ni) on a heated substrate (typically $700°C - 900°C$) that is exposed to a gaseous carbon source such as methane, ethylene or acetylene.

4.2.2 The characterization of the substrate

The substrate is the material plane where the nanotube forest elements grow during the CVD process. From our standpoint, the structural parameters of the substrate act on the sample polarimetric measurements. Here the issues raised are:

- What are the characteristics of our sample substrate?
- Whether choices can be done on the substrate characteristics?

For the CVD creation technique the substrate is a silicon layer [43]. It also contains a nickel catalyst (7 nm thick) and a TiN diffusion barrier (10 nm thick) films which are deposited onto the doped silicon substrates. As depicted in [44] the thickness of the Ni film is around $10-50nm$. The thickness determines partially the diameter of the CNT. The latter also depends upon the size of the metal catalyst particles (Ni) [45]. The Nickel catalyst is removed after the CNT creation by CVD. That is why it is not taken into account for our study. Consequently it is possible to evaluate the refraction index of the Silicon substrate knowing its thickness. For our present study only $10nm$ thick substrate was possible. In any case Silicon substrate possess high reflection properties and act closely as a mirror surface.

4.2.3 The characterization of the carbon nanotubes

Carbon nanotubes (CNTs) are graphitic tubules with nanometer-size diameters and have a very large aspect ratio (length/radius). They exhibit highly anisotropic physical properties and excellent field emission properties. It is high local electric field due to nanometer-size radius of curvature at the CNT's apex and it makes them attractive as potential electron sources in various vacuum electronic applications. The CVD can afford for variable densities of small-diameter ($< 50nm$) multi-walled nanotubes (MWCNTs). You can see below in figure 4.2 pictures of different CNT structures. The sample can have random or ordered clutters distributions.

With FEG high resolution scanning electron microscope images, a good evaluation of the geometrical parameters and morphology of the forest can be realized. Recent techniques [45], [43] enable to control the diameter CNTs and their array position, but

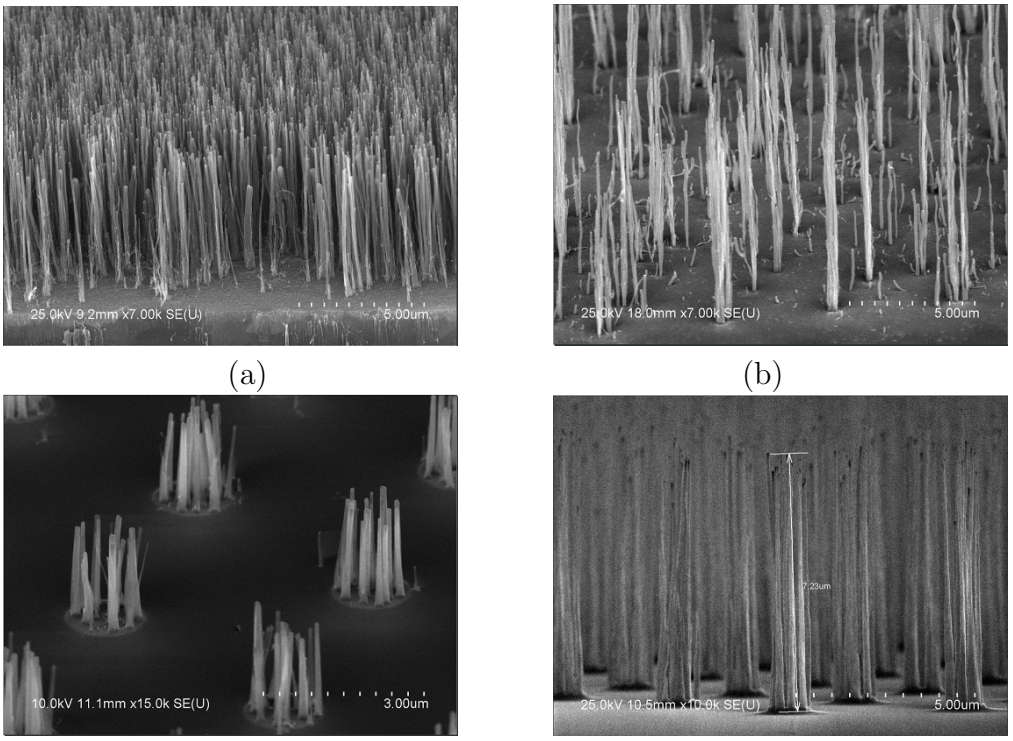

FIGURE 4.2: *Scanning electron microscope images of the carbon nanotube samples. (a) dense random forest (b) sparse random forest (c) small lithographed forest (d) high lithographed forest*

it is easier to create random positioned CNTs. The dc PECVD process favors growth of aligned CNTs. Here, the CNT diameter ranges from 30 to $100nm$ and the CNT length from 1.8 to $2.2\mu m$.

In figures 4.2 arrays of a few discrete and separate CNTs within a specified area are depicted and exhibit a density of $10^{11}cm^{-2}$. This kind of structure were originally developed to the field emission[46] but can be used by us for structure comparison purpose. The patterning techniques comes from optical UV lithography (with a resolution of $1\mu m$) and electron-beam lithography (with a resolution of $40nm$).

For the case of the permittivity, it is not possible to measure it directly. Only models for graphene can be extrapolated to our case. Globally, one can retain their high light absorption property and high electric conductivity. As explained in section 6.5.1 the complex retained permittivity value at $633nm$ is around $\varepsilon_{CNT} = 4.9 - j9.5$

* * *

Summary
Our scaled down scene is made of Carbon NanoTubes (CNT). Their position, structure and sizes are well controlled thanks to the PECVD technique managed at the LPICM. The Silica substrates have good reflection properties and finally the selected CNT samples represent well trunk forest structure. The large possibility of density level is interesting for us in order to validate the simulation model. In the next chapter the optical scale measurement devices are presented.

4.3 Investigated experimental tools

Once we have selected scenes that can be used with polarimetric tools at visible light, it is necessary to look at the possible tools and possible adaptations in order to get closer to the radar measurement. Data for specific bistatic configurations and specific frequencies are needed. All the tools investigated for this aim are totally polarimetric.

In [12] the use of a macroscopic imager on CNT led to qualitative measurements for several geometries. So the possibility to use optical devices and polarimetric decompositions in the purpose of radar applications was demonstrated. Several receiving positions were used and a increase in the depolarization parameter was observed when the receiver is more grazing. The results from this tool are presented in the first section.

From those observations, more specific measurements are needed to quantify the tendencies. The two possible types of polarimetric devices that can afford the measurement of the carbon nanotube samples are in the one hand a spectral polarimeter with a white source in the range $[450nm - 1000nm]$ and on the other hand an angle resolved microscope with a monochromatic laser source.

The spectral measurement enabled to examine the relations of the polarimetric behavior of the samples with the incidence light wavelength. The measurement made with the spectral polarimeter underline a low Signal to Noise ratio due to the lack of illumination power compared to the high absorbance of the carbon nanotubes. It constrained us to stay in the specular configuration. Nevertheless, the incidence angle is adjustable and the full Mueller matrix is workable.

The Angle Resolved Mueller polarimeter has been developed at LPICM and was the object of several development thesis [47], [48], [49] principally in the domain of bio medical polarimetry. It is not a fully mature device because it is a laboratory device, it is not totally stable and not fully compact but such a tool presents a very high potential. What is more, it presents a high progressiveness that enables adaptations needed for this present work. The angle resolved microscope performs measurements for a continuous positions of receiving angles. Our main idea here is to deepen the kind of measurements done in [12] adding geometrical control and sample diversity to be able to produce parametric comparisons.

All investigated measurement tools have limitations. In order to select the best one we will see that the ARMP is the one where there is a better signal to noise ratio and with wider possibilities of configurations. In parallel, the most adapted cases of scene have to be selected. We will see that forests of homogeneous configurations present advantages and exploitable results. Indeed if we consider the investigated nanotubes samples, the distributions are either in blocks, or homogeneous. The hemispherical measurement is continuous on the whole domain measured for the homogeneous case, with a good signal to noise ratio on the whole domain. They are going to be the object

of comparisons following their density. Then, the measurements on these forests are going to allow validating the tool of simulation for these measurements. It will lead also to validate the measurement tool in reproducing the polarimetric behavior which would be observed in airborne radar measurements on forests.

4.3.1 Imaging Polarimeter

Here we present a proof of principle that was investigated in [12]. This study was only qualitative because no information on the density and dielectric permittivities was owned and the used device was only an imaging polarimeter with no specific control of the incidence and reception position.

The measured CNT are $27\mu m$ in length and random positioned. Images of the sample are processed using a light source in the range $500nm - 650nm$. The scale ratio $M_L = \lambda_{radar}/\lambda_{laser} = 10^6$ thus corresponds to a L-band radar measurement on 20m trunks.

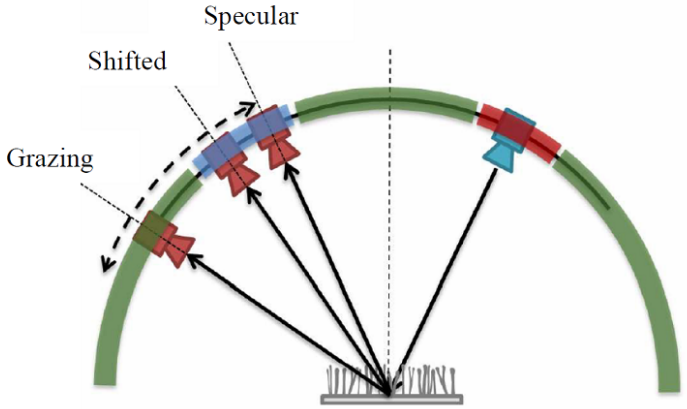

FIGURE 4.3: *Experimental setup for measuring the polarization of a carbon nanotube sample using a polarimeter.*

The sample is placed on a horizontal plane. The source is placed above the sample and the reception can be variably positioned as shown in figure 4.3. However in this experimental setup it is not possible to perform measurements for a regular angular pitch, or precisely control the position of the reception. Thus a reduced number of receiving positions were investigated, coming gradually from specular position ($\theta_e = \theta_r$). The gradient position is slightly away from the specular position, while the so called shifted position is much more grazing. These positions are described qualitatively and backscattering measurement is not feasible. Nevertheless, it is impossible to observe

similar "double-bounce" backscattering effects for the specular bistatic configuration case. Indeed, in this configuration, the specular scattering related to the ground is much higher than the volume scattering and as a consequence depolarization is low. A bistatic configuration that moves away from the specular configuration enables a higher relative level of the volume scattering (which tends to be less directive) and thus increases depolarization. This effect is illustrated on the right part of figure 4.4 where depolarization level is obtained via the Lu and Chipman decomposition (see chapter 2). We represent in figure 4.5 depolarization for the three positions of the reception for our Carbon Nanotube sample. A clear evolution of depolarization effects is observed depending on the angular configuration considered for the receiver. For the specular configuration, depolarization is zero, as expected the scattering via the ground silicon substrate is predominant and the volume scattering and thus depolarization is not observable. Away from this configuration, the specular scattering decreases, and there is a larger part of volume diffusion and depolarization appears although it remains quite low (around 0.2). Further away from the specular configuration, the volume diffusion becomes predominant, and a very significant depolarization is observed (around 0.9).

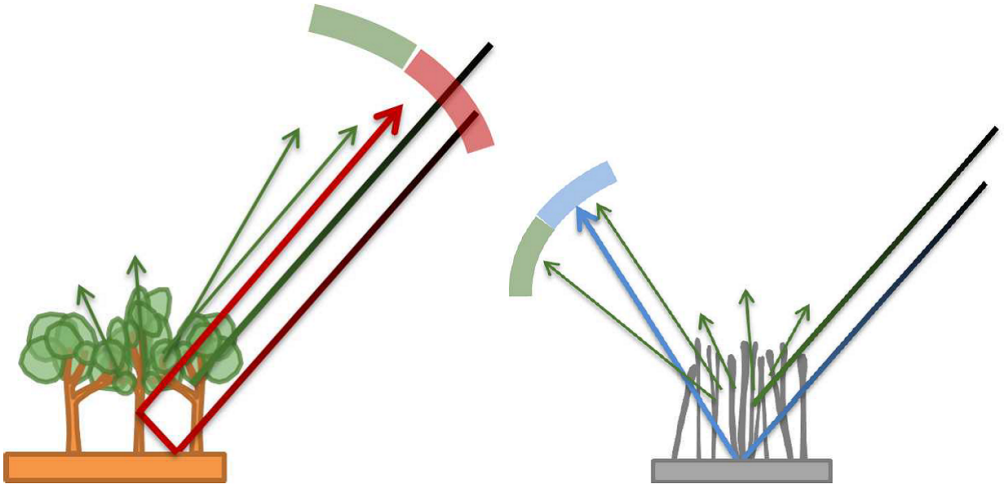

(a) (b)

FIGURE 4.4: *Backscattering radar (a) or specular optical (b) scattering configuration by the ground, or double bounce on the ground and the trunks, hide the depolarization related to the volume diffusion.*

From these preliminary measurements the following conclusions can be drawn:

- The impact of geometrical configurations for the observation of volume scattering in the context of the study of forest is illustrated experimentally.

- The specular scattering by the ground plays a similar role to the double scattering by the soil and trunks. It can be reduced, or canceled, by a suitable choice of the receiving position.

A more detailed analysis of the polarimetric signal is needed to extract bio physical parameters. The further exploitation of this idea requires more accurate modeling of scattering by a nanotube forest. We also want to provide a measuring tool capable of measuring precisely the set of angular positions, ideally including the backscattering.

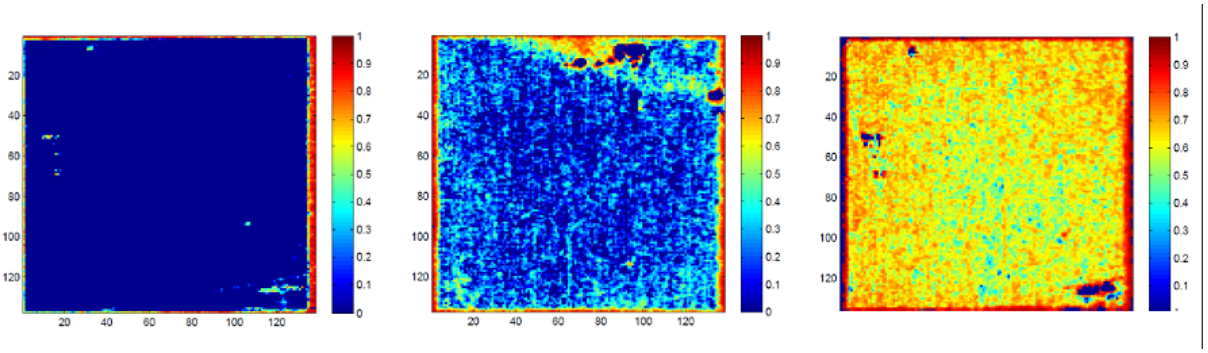

(a) (b) (c)

FIGURE 4.5: *Depolarization of the decomposition of Lu and Chipman for three positions: (a) Specular, (b) shifted and (c) grazing, with measurement wavelengths equal to 650 nm.*

4.3.2 Spectroscopic Polarimeter

During the first year of my thesis, the spectroscopic Mueller polarimetry was investigated for the measurement of the CNT. The device is a polarimeter conceived by Horiba Jobin-Yvon. It is a spectroscopic Liquid Crystal Mueller Matrix Polarimeter (MM16), see figure 4.6.

The measurement campaign was performed around the specular configuration and for an entire spectral range from $0.4\mu m$ to $1\mu m$.

With this spectral polarimeter the footprint of the beam in $500\mu m$. An integration time of 10 seconds is set for each configuration of emitter and receiver. The spectral resolution is $1.5nm$ can induce overestimation of the depolarization since the measured value rapidly change into the spectral domain.

Especially, a lithographed sample (figure 4.2, (d)) was measured with an incidence angle of 60°. This sample presents an important diffraction pattern and an high intensity order can be sensed in the specular direction. This phenomenon is linked to which is called a "Bragg" effect caused by constructive interference of the CNT clutters.

FIGURE 4.6: *Smart SE Spectroscopic Ellipsometer from HORIBA*

The Lu and Chipman decomposition was applied for several azimuth position of the receiver, keeping $\theta_r = \theta_e = 60°$. Nevertheless only the specular configuration induces sufficient SNR. Consequently only this measurement is retained. Analyzing briefly the decomposition issued parameters, one can notice the an important variation around the wavelength of $500nm$, see figure 4.7. This effect may corresponds to the relation between the wavelength and the average distance between each block of CNTs.

Focusing on the depolarization parameter that is evaluated with the Polarization Index (PI), see chapter 2, introduced by Gil [50] and is plotted in figure 4.7 (a). The increase of the depolarization level would be explain by this phenomena and by multiple bounce inside the CNT clutters.

For the diattenuation parameter (figure 4.7 (b)) the wavelength of $550nm$ corresponds to a regime modification. Below $550nm$ the diattenuation is low and this parameter increases for larger wavelength. The scattering regime change can be implied her because for $\lambda > 550nm$, the ratio radius versus wavelength is $\frac{r_{CNT}}{\lambda} < 1$. This evolution needs to be verified in the radar domain because it would means that relative attenuation between the polarization are lower at high frequencies (for example S band) that at lower frequencies (for example P band).

Investigating the retardance (figure 4.7 (c)), the evolution presents the minimum value of 90° at $\lambda = 550nm$ and then there is a smooth transition from 90° to 250°.

Finally, the confidence in the results for domain outside $450 - 650nm$ may be questioned. Indeed, looking at the decomposition parameters one can see that the parameters are not stable for wavelength outside $450nm - 650nm$ mainly because SNR is low for these wavelengths. The spectral source does not produce an high intensity, and only the low density and lithographed forest have been measured with a sufficient SNR. Moreover, only the specular configuration was measured on the retained samples. That is why it was important for us to move for another experimental setup with a intense source of light and the possibility to measure other bistatic configurations.

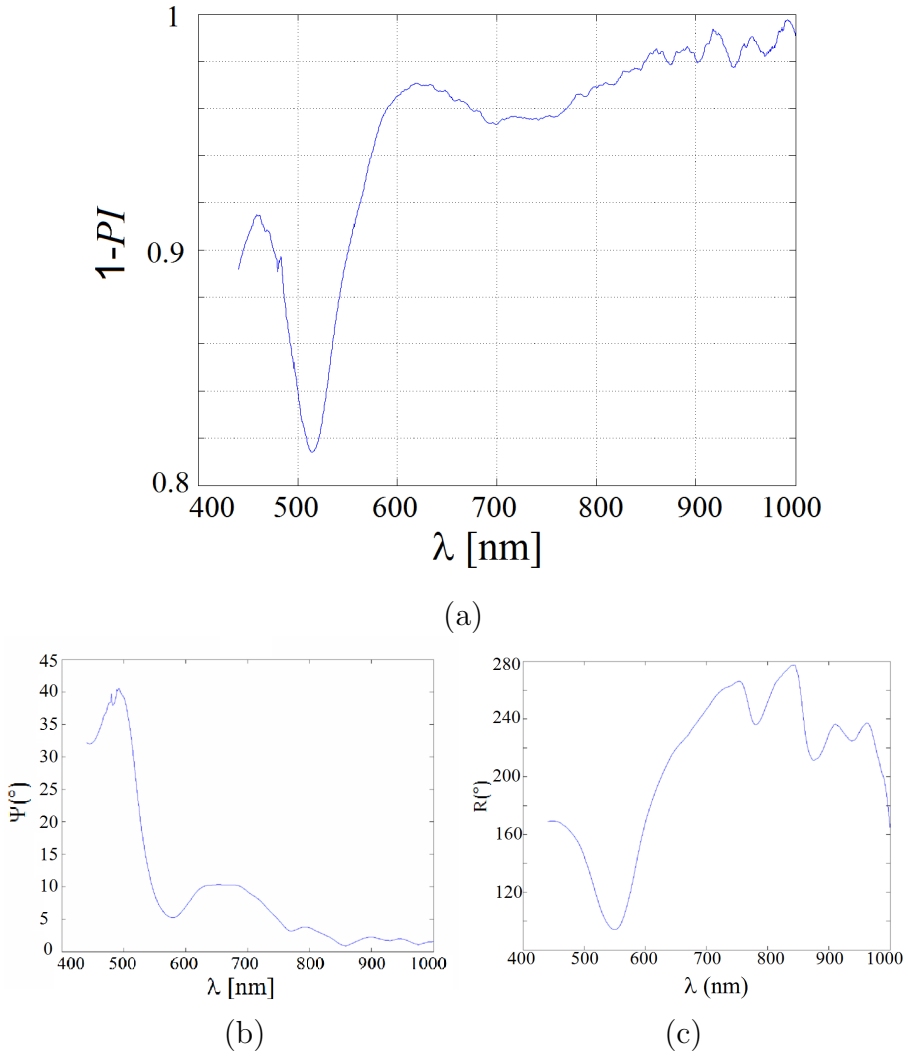

FIGURE 4.7: *Lu & Chipman decomposition applied to the spectroscopic measurement on lithographed Carbon Nanotube sample at* $60°$ *of incidence in the specular direction. (a) the PI, (b)* Ψ $[0° - 45°]$*which is related to the diattenuation via* $D = \cos(2\Psi)$*, and (c) the retardance* R $[80° - 280°]$*.*

4.3.3 Angle resolved Polarimeter

The spectral measurements does not allow to obtain a large diversity of bistatic angles. Another reflection polarimeter is chosen to be able to have the bistatic diversity. The one that is investigated here enables access to a wealth of information that we could never have had with real radar or even anechoic measurement.

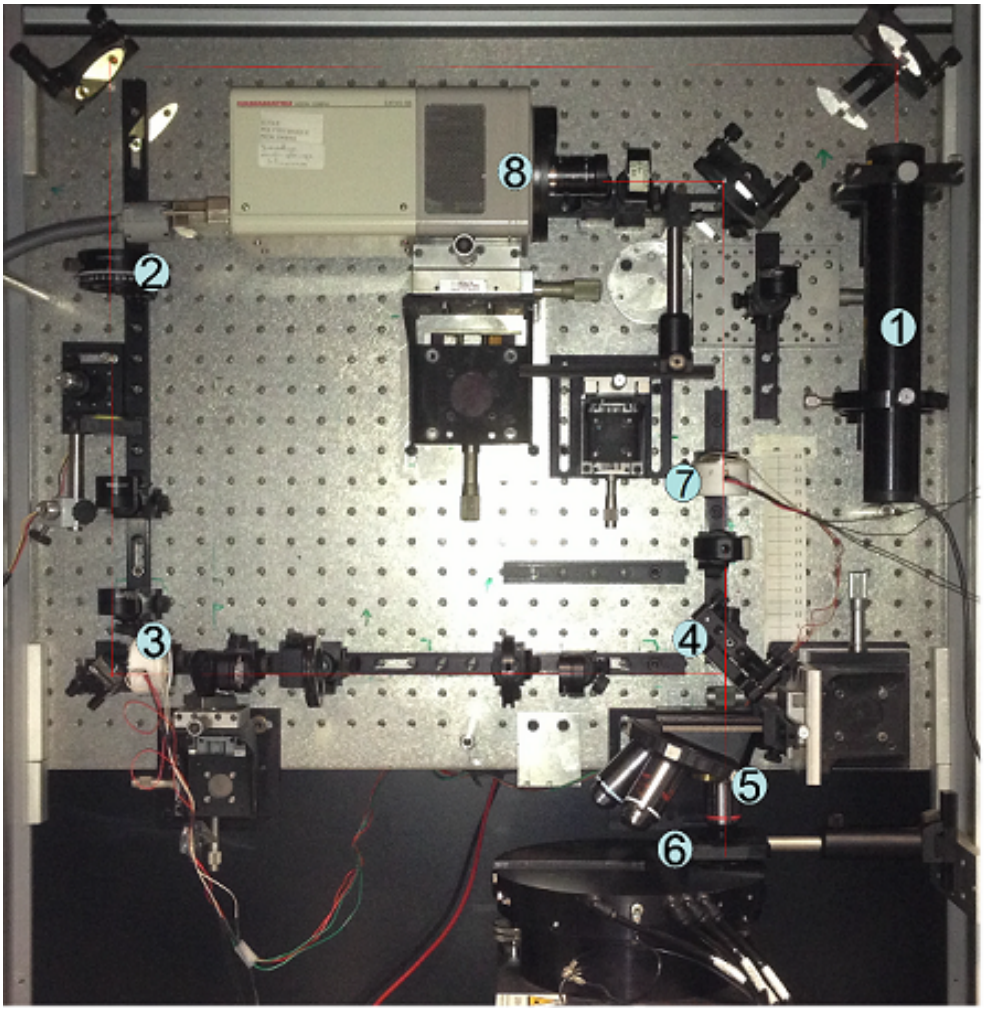

FIGURE 4.8: *Picture of the optical setup for the Angle Resolved Polarimeter. 1: laser source; 2: diffuser; 3: PSG; 4: splitter; 5: objective; 6: sample; 7: PSA; 8: camera*

The new optical device is an Angle Resolved Mueller Polarimeter (ARMP) and has been proposed in [49]. It can achieve both the polarimetric and the multi-angle configuration we are looking for. We propose here to use this device, that we describe now in the next section. The test bench pictures is depicted in figure 4.8.

The aim of the ARMP is to measure the Mueller matrix that describes the polarimetric behavior of the sample regarding to the reception angle. To explain the functioning of the device we start with the optical scheme of the setup presented in Fig. 4.9.

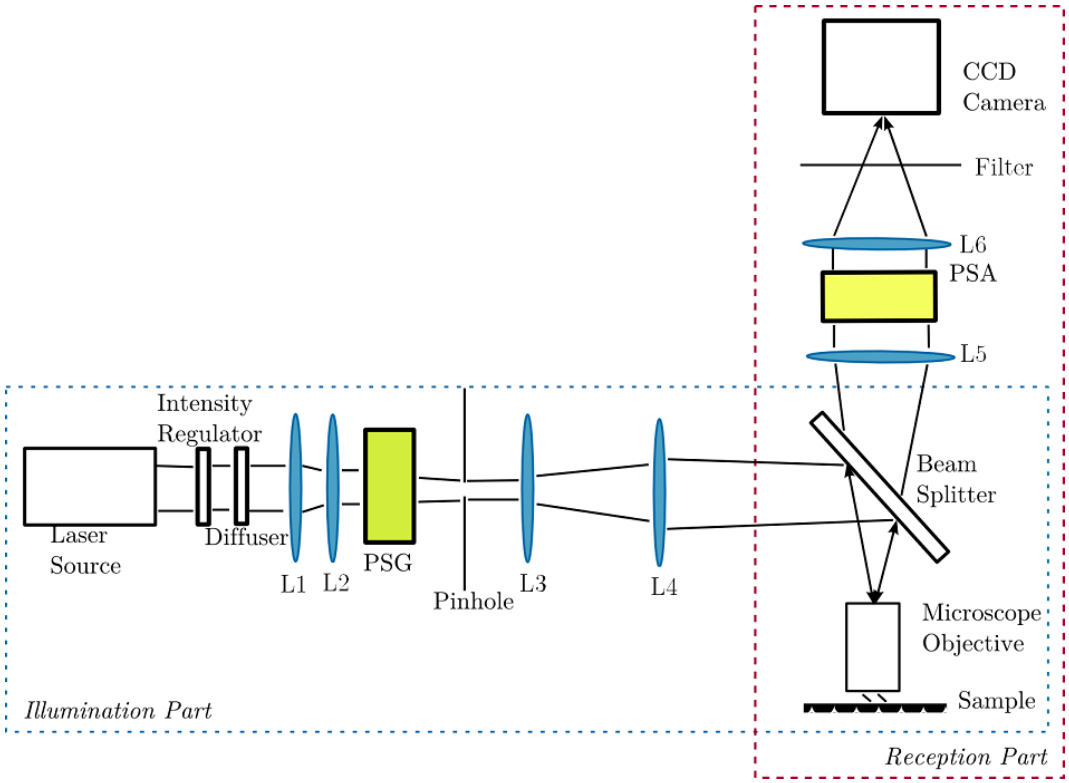

FIGURE 4.9: *Schematic description of the Angle Resolved Mueller Polarimeter. The illumination part, in the blue rectangle, adjusts the intensity emitted by the source using the intensity regulator, and suppresses the laser speckle using the diffuser. The incidence beam is controlled with the pinhole. The reception part, in the red rectangle, collects the beam reflected by the sample. A frequency filter is used to ensure the monochromaticity.*

The **illumination part** is designed following the Köhler Illumination Principle [51]. It ensures an even illumination of the sample in terms of intensity, whatever the incidence angle. The **source** is a 633 nm laser and its position will be constant all along the campaign. This source produces an intense and coherent light. We have to face a laser speckle, that has to be minimized. To this aim, we use a **diffuser** that consists in a semi-transparent plate located after the source and rapidly rotating (5 tours/sec). In order to select the width of the incident beam and to consider a specific incidence angle, we use then what is called a **pinhole**. It is a metallic plate with a hole in the middle that allows a small part of the incident beam to pass. The incidence angle

depends on the position of the pinhole. (See Fig. 4.10 for the schematic side view of the configuration). The smaller is the hole, the more accurate is the incidence angle. The possible pinhole sizes in this experiment are $20\mu m$ and $200\mu m$. The latter implies a wider angular area of incidence, but it is required for highly absorbing dense samples, to get enough reflected light.

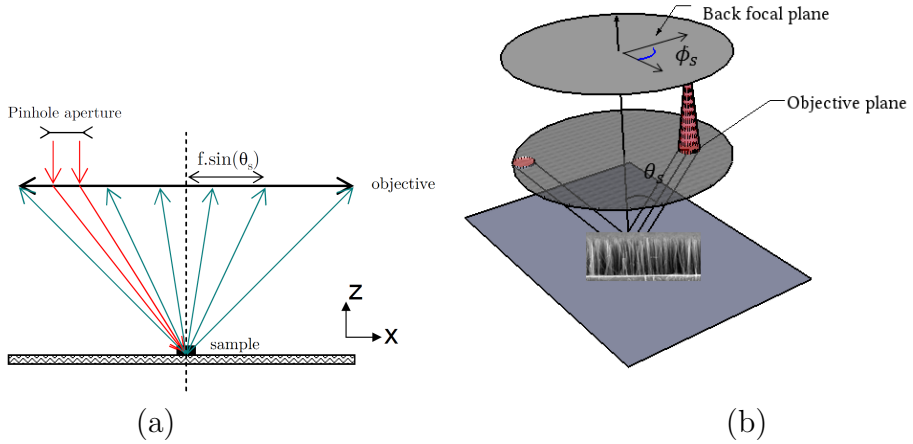

FIGURE 4.10: *(a): Schematic side view of the configuration with the pinhole and the scattering angle position depending on θ_s. The working distance of the objective is $2mm$ and the footprint width that corresponds to the illuminated area is $50\mu m$. The incident beam is colored in red and the received beam is colored in green. (b): Representation of the configuration including the reception azimuth φ_s in Fourier space.*

The polarization state of the incident beam is achieved using a **Polarization State Generator** (PSG), constituted by ferromagnetic liquid crystals and calibrated using the eigenvalue calibration method [49]. Using a **beamsplitter**, the beam arrives finally on a **microscope objective** (Nikon plan Fluor objective of 0.90 for the numerical aperture and with a 100 times magnification) before reaching a part of **the sample**. The working distance of the objective is $2mm$ and the footprint width that corresponds to the illuminated area is $50\mu m$.

The **reflected** light from the sample is focused in the Fourier space of the microscope objective to obtain the angle resolved image [51]. The Fourier space deals with the Fourier transform that a lens performs on a light beam.

It must be noted that all the scattered intensity by the sample is measured, whatever the scattering angle allowed by the numerical aperture of the microscope objective. All contributions pass through the beam splitter towards **the reception part**.

This reception part is composed, first, of a **Polarization State Analyzer** (PSA). As the PSG, the PSA allows to select the polarization state of the scattered beam. A

lens may be placed to produce an image in the real space (x, y). If it is taken off, the image is produced in the Fourier space (θ_r, φ_r) so that:

$$\begin{aligned} x &= \sin\theta_r \cos\varphi_r \\ y &= \sin\theta_r \sin\varphi_r \end{aligned} \tag{4.6}$$

We will use the last mode all along the paper, as it directly corresponds to the radar imaging mode.

The **detector** is a CCD camera that saves the Fourier plane intensity image of the sample corresponding to the specific couple PSG - PSA. If the specular intensity is too strong, it may induce a saturation and therefore no observation could be made. In that case, a mask is set in front of the camera, in order to suppress specifically this strong specular contribution.

In Fig. 4.11, we have represented an example of the image we can measure. This image corresponds to the intensity reflected by the illuminated sample for a specific incident polarization and a selected scattered polarization. The incidence angle is constant, and the image represents the intensity in a polar format, for all the scattered directions, indicated by (θ_r, φ_r). This intensity image results actually from a temporal average applied to reduce the noise induced by the device. Two spatial coordinate systems can be used: on the first hand we can project the received signal in a classical $(\mathbf{x}, \mathbf{y})$ coordinate system, independently of the scattering direction. On the other hand, we can also use the basis $(\mathbf{h}, \mathbf{v})$, that is determined with respect to the scattering direction.

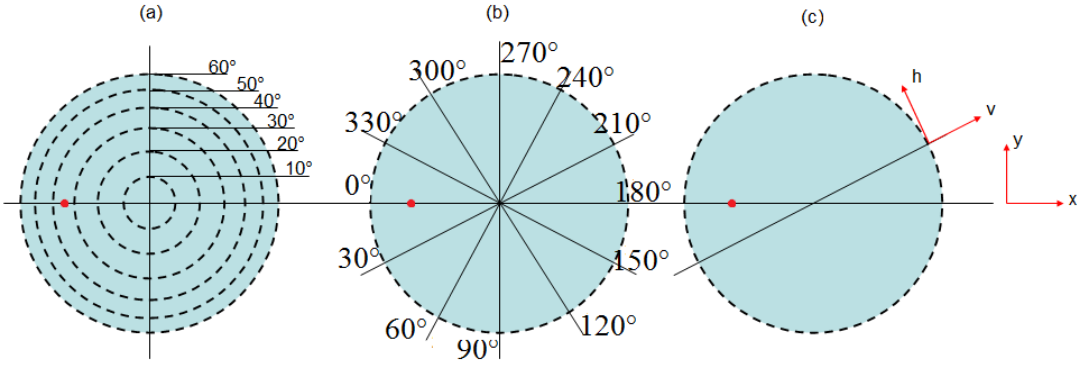

FIGURE 4.11: *The scattered signal is projected in a polar basis, so that the zenith receiving angle θ_r is defined as represented in the left part of the figure (a). The representation of the azimuthal receiving angle φ_r is illustrated in the middle (b). Finally, two spatial coordinate systems are used in this paper to define the polarimetric basis (c): either $(\mathbf{x}, \mathbf{y})$ or $(\mathbf{h}, \mathbf{v})$. The red point corresponds to the backscattering position for our measurements where $\theta_e = 35°$ and $\varphi_e = 0°$.*

Chapter 5

Retained measurement for the analysis

5.1 Major adaptations for the ARMP

5.1.1 Implementation of the laser source

The original setup was developed and described in [49]. The concept of the reflection microscope with the Mueller polarimeter was developed and used in the context of highly reflective samples such as superimposed grating on silica substrate. The original purpose was the overlay characterization in microelectronics but the reflection Mueller microscope can be used in many different area. The study of the beetle skeleton was a good principle example with the circular dichroism of the structure revealed.

For these first works, a white light source was sufficient and it enabled to select any desired wavelength, as depicted in figure 5.1. In the case of the carbon nanotubes, a very intense source is needed in order to counterpart the high absorption of the scene.

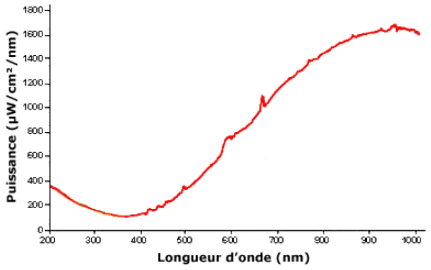

FIGURE 5.1: *Emission spectra of the original white source*

It leads to the adaptation of a laser source. The choice of the source focused to the Helium Neon laser source for several reasons:

- The wavelength which is $633nm$ leads to a good ratio between the elements size and the wavelength.
- This type of laser is common and the cost is reasonable.

The implementation implies a new organization of the setup, with two additional mirrors to be able to reorient the laser beam into the original path.

5.1.2 Ferroelectric liquid crystals for the PSG and the PSA

An other key element of the device is the PSG-PSA couple to create the polarization synthesis. To assure a stable calibration we choose to replace the nematics by the ferroelectrics liquid crystal. The corresponding optical principle are depicted in figure 5.2. In the following, the functioning principles are explained beginning by the nematics.

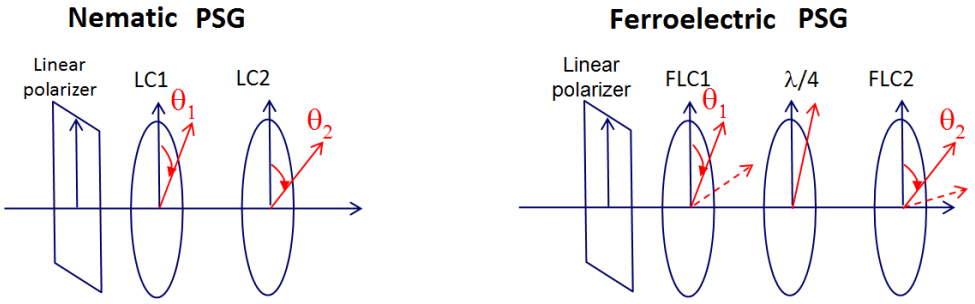

FIGURE 5.2: *Schematic of the nematic and the ferroelectric liquid crystal polarisation state generator.*

The PSG and the PSA are elaborated in a symmetrical way to generate four linearly independent Stokes vectors. These devices are equivalent to a zero-order retarder with electrically controlled variable phase shift. Therefore, they exhibit good angular and spectral acceptance, which constitutes an important advantage for imaging applications. Finally, the PSG and the PSA using nematic modulators allow in principle to reach the optimal conditioning for any wavelength in their range of functioning simply by properly adjusting their voltage command.

In figure 5.2 light propagates along the z axis. The PSG is made of a linear polarizer oriented in the x-axis, followed by two nematic liquid crystals considered as perfect

retarders. s. In this configuration, the Stokes vector of the PSG output light can be written as in equation 5.1:

$$\mathbf{S} = \mathbf{D}(\delta_{\mathbf{2}}, \theta_{\mathbf{2}})\mathbf{D}(\delta_{\mathbf{1}}, \theta_{\mathbf{1}}) \begin{pmatrix} 1 \\ 1 \\ 0 \\ 0 \end{pmatrix} \tag{5.1}$$

wherein δ_1 and δ_2 is the phase shift introduced by the liquid crystal cells 1 and 2 between the ordinary and the extraordinary axes. θ_1 and θ_2 are the angles between the x axis and the extraordinary axis of the cell 1 and 2 and $\mathbf{D}$ is the Mueller matrix of a liquid crystal.

The modulation of the polarization by the PSG is made by varying sequentially the phase shifts δ_1 and δ_2 introduced by the liquid crystals whose orientations θ_1 and θ_2 remain constant. The columns of the expected modulation matrix $\mathbf{W}$ are the four Stokes vectors $\mathbf{g_{1:4}}$ obtained by varying the phase shift of the couple (δ_1, δ_2) such as

$$\mathbf{W} = [g_1 \; g_2 \; g_3 \; g_4] \tag{5.2}$$

In principle only four orientations values θ_1 and θ_2 and four values of phase shift couples are needed to the PSG being complete such that the matrix $\mathbf{W}$ is not singular. The PSA is composed of the same optical elements that the PSG but in reverse order. This choice is not mandatory but facilitates the practical implementation of the instrument. As well as four columns of the matrix $\mathbf{W}$ is obtained by varying phase shift (δ_1, δ_2), the lines of the analysis matrix A are obtained by varying the nematic PSA phase shifts (δ'_1, δ'_2) . For a given Stokes vector $\mathbf{g}$ at the input of the PSA, the detected intensity as a function of phase shifts (δ'_1, δ'_2) is written:

$$I_{\delta'_1, \delta'_2} = \frac{1}{2} [1 \; 1 \; 0 \; 0] \, \mathbf{D}(\delta'_1, \theta'_1)\mathbf{D}(\delta'_2, \theta'_2) \tag{5.3}$$

.

As $(\mathbf{D}(\delta, 0))^t = \mathbf{D}(-\delta, 0)$, if $\theta'_1 = \theta_1$, $\theta'_2 = \theta_2$, $\delta'_1 = \delta'_2$, the analysis matrix is simply $\mathbf{A} = \mathbf{W}^t$ and the conditioning is the same as that of W, which obviously leads to the same direction and optimum values of the phase shifts. In practice, δ_1 and δ_2 are switched to generate the 4-states that optimize the conditioning.

Now let us consider the case of PSG ferroelectric liquid crystal system. PSG is composed of a linear polarizer oriented in the x-axis, followed by two ferroelectric liquid crystal. The ferroelectric crystal are linear constant phase shift retarders. The orientation of their fast optical axis is controlled electrically. This type of cell has two possible orientations that are 45 degrees from each other. Indeed, their switching is fast

and it allows time savings with respect to the nematic cell types. However, the use of these cells has drawbacks. The PSG orientations are constant and a fine optimization of the conditioning as in the case of nematic liquid crystals is not possible. Liquid crystals are switched alternately to generate four polarization states with the following relation:

$$\{(\theta_1, \theta_2), (\theta_1 + 45°, \theta_2), (\theta_1, \theta_2 + 45°), (\theta_1 + 45°, \theta_2 + 45°)\} \tag{5.4}$$

Where θ_1 and θ_2 are respectively the azimuths of the liquid crystal 1 and 2. These orientations have been optimized for a matrix conditioning $1/\kappa \geq 0.25$. The following values are $\delta_1 = 90°$, $\delta_2 = 180°$, $\theta_1 = 70°$, $\theta_2 = 165.5°$. The wavelength range for which the liquid crystal is stable and proper conditioning κ is between 450 and 700 nanometers.

In practice, δ_1 and δ_2 are switched corresponding to the directions θ_1 and θ_2 to generate the 4-states that optimize the conditioning. Then the same process is realized on the second liquid crystal cell.

5.1.3 Setup of the pinhole for the selection of the incidence position

In figure 4.9 the illumination part is highlighted by blue dots line. The selection of the incident angular position is done in this part, after the Polarization state Generator and the pinhole is positioned at the conjugate plane of the back focal plane.

5.1.4 Setup of a new mechanics for the microscope objective

In exposed in [51] the original mount for the objective induces mechanical constraints that influence the polarimetry. A new mount has been elaborated and is represented in Fig. 5.3.

The self supported structure enables the elimination of mechanical clamping. These constraints have been shown to be the source of non negligible polarization artifacts that we have to limit.

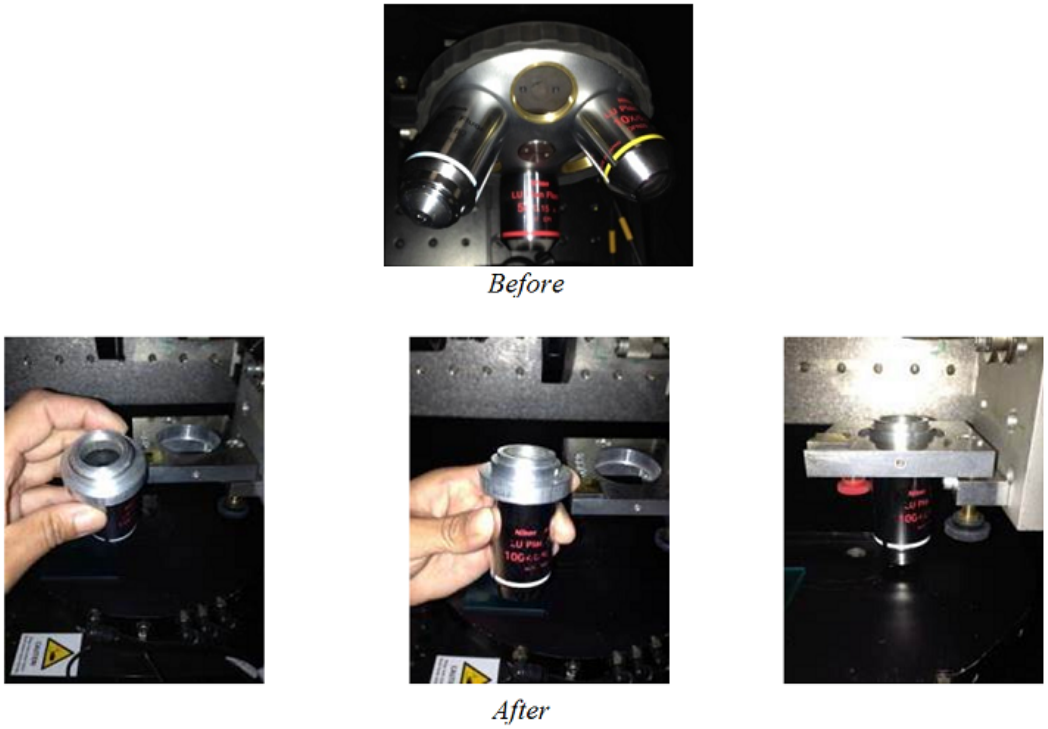

FIGURE 5.3: *Realization of a new mount for the microscope objective reducing the mechanical constraints.*

5.1.5 Polarimetric coordinate system

The coordinate system in polarimetry is of prime interest because measured parameters depend directly on it. In [8] the study focused on the bistatic angle influence in the case of metallic sphere in resonance region. In the classical polarimetric radar the basis is $\mathbf{h}, \mathbf{v}$ but it is not straightforward to apply it in the case of bistatic radar the basis of the transmitter will be different from the receiver one.

A Stokes vector can be described as in equation 5.5, see chapter 2.

$$\mathbf{S} = \begin{pmatrix} I_x + I_y \\ I_x - I_y \\ I_{\pi/4} - I_{-\pi/4} \\ I_{LC} - I_{RC} \end{pmatrix} \tag{5.5}$$

As part of the angular resolved measurements, optical components act simultaneously for all reception and incidence angles. It is thus not possible to have a basis for each polarization plane of incidence, so the image of the sample in the back focal plane of the microscope objective is computed to a fixed polarization basis for the entire image. This is the so-called $(\mathbf{x}, \mathbf{y})$ basis, see chapter 2.

The fixed base chosen for the incident wave is $(\mathbf{x}, \mathbf{y}, \mathbf{z})$, and the reflected wave is $(\mathbf{x}, \mathbf{y}, -\mathbf{z})$, which leads to a Mueller matrix of the mirror whose Mueller matrix is given in equation 5.6. This means that the formalism used for the ARMP is BSA.

$$M_{mir} = \begin{pmatrix} 1 & 0 & 0 & 0 \\ 0 & 1 & 0 & 0 \\ 0 & 0 & 1 & 0 \\ 0 & 0 & 0 & 1 \end{pmatrix} \tag{5.6}$$

5.1.6 Rotation of the Polarimetric basis

To change the orientation α of the Stokes vector basis by an angle ϑ the rotation matrix R is used,

$$\mathbf{g}' = \mathbf{R}.\mathbf{g}, \quad \mathbf{R} = \begin{pmatrix} 1 & 0 & 0 & 0 \\ 0 & \cos 2\vartheta & -\sin 2\vartheta & 0 \\ 0 & \sin 2\vartheta & \cos 2\vartheta & 0 \\ 0 & 0 & 0 & 1 \end{pmatrix} \tag{5.7}$$

It comes $\alpha' = \alpha + \vartheta$. Considering a Mueller matrix $\mathbf{M}$ for our sample and the Stokes vectors $\mathbf{g}_{in}$ and $\mathbf{g}_{out}$ for the transmitted and received light, one has $\mathbf{g}_{out} = \mathbf{M}.\mathbf{g}_{in}$. For

the rotation by an angle α_r of the basis at the reception and by an angle α_i at the transmission it comes:

$$\begin{aligned} \mathbf{R}(\alpha_r)\mathbf{g}_{out} &= \mathbf{R}(\alpha_r).\mathbf{M}.\mathbf{g}_{in} \\ \mathbf{R}(\alpha_i).\mathbf{M}^{-1}.\mathbf{R}(\alpha_r)^{-1}.\mathbf{R}(\alpha_r)\mathbf{g}_{out} &= \mathbf{R}(\alpha_i).\mathbf{g}_{in} \\ \mathbf{R}(\alpha_i).\mathbf{M}^{-1}.\mathbf{R}(\alpha_r)^{-1}.\mathbf{g}'_{out} &= \mathbf{g}'_{in} \\ \mathbf{g}'_{out} &= \mathbf{R}(\alpha_r).\mathbf{M}.\mathbf{R}(\alpha_i)^{-1}.\mathbf{g}'_{in} \end{aligned} \tag{5.8}$$

The Mueller matrix in this new basis can be written as:

$$\mathbf{M}' = \mathbf{R}(\alpha_r).\mathbf{M}.\mathbf{R}^{-1}(\alpha_i) = \mathbf{R}(\alpha_r).\mathbf{M}.\mathbf{R}(-\alpha_i) \tag{5.9}$$

5.1.7 Measurement of the substrate

We illustrate here the operation of ARMP on typical samples. The substrate is measured **without using the pinhole** that selects a specific incidence. It gives an image that contains all positions of specular measurement for incidence θ_i from 0° to 60°. In the ARMP measurements, data for the reception directions $\theta_r < 5°$ are not processed. It correspond to the white area in the center of each image.

As all directions are imaged, if the sample shows no particular structure in a preferred direction, the same behavior should be observed regardless of the azimuth. We see in Figure 5.4 images of the Mueller matrix in the fixed coordinate $(\mathbf{x}, \mathbf{y})$ and recalculating the matrix in the coordinate system as $\alpha_i = \pi + \varphi, \quad \alpha_r = \varphi$, see figure 4.11 for the angle definitions.

The choice of the basis is very important for the interpretation of the Mueller matrix. In $(\mathbf{h}, \mathbf{v})$ basis the azimuthal symmetry is retrieved. In the following, if the incidence angular position remains constant using the pinhole, the substrate alone would induce signal at the specular reception position. But, with the CNT the scattering occurs in all received directions. The next section is focused on the influence of the polarimetry coordinates on these measurements.

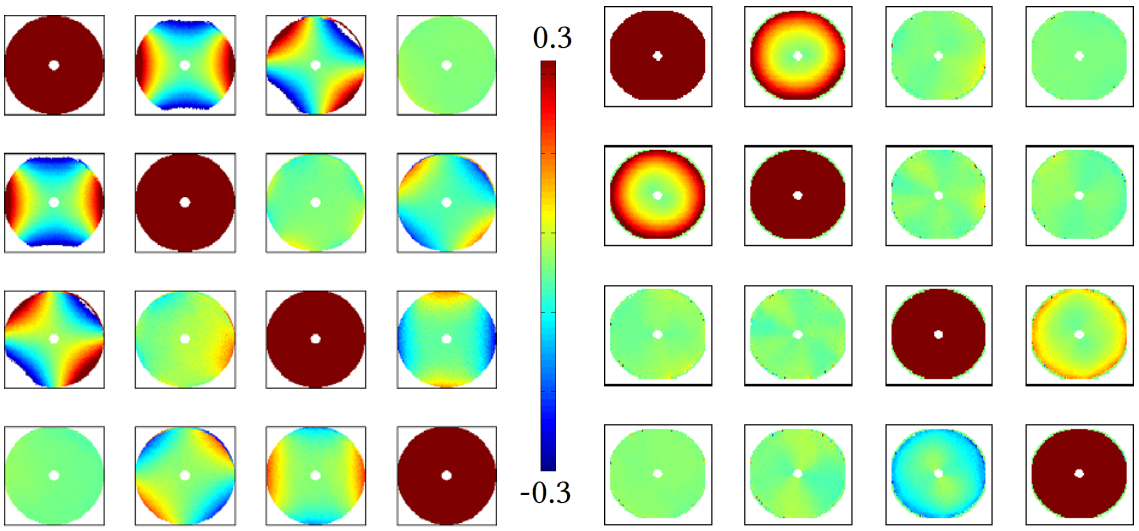

FIGURE 5.4: *Normalized Mueller matrix issued from the measurement of the substrate.* $(\mathbf{x}, \mathbf{y})$ *basis on the left,* $(\mathbf{h}, \mathbf{v})$ *basis on the right.*

5.1.8 Carbon Nanotubes

In the case of measurements on carbon nanotubes, what is for us the most interesting is the behavior of the diffusion out of the mirror direction and thus selecting only one angular incidence area. This is done **using a pinhole that is placed on the illumination path** contrary to the last example. The observed symmetry in the case of the specular scattering is therefore no more expected and the $(\mathbf{h}, \mathbf{v})$ basis is not necessarily the best for easily interpret the polarimetric behavior. A comparison for the choice of this basis is needed.

From the perspective of the rotation of the basis, there will be two different angles to the incidence and reception: $\alpha_e = \varphi_e$, $\alpha_r = \varphi_r$, see equation 5.8.

Sparse forest of random positioned CNTs

Here the angular incidence position is set at $(\theta_e, \varphi_e) = (35°, 0°)$ and figure 5.5 shows the plane projection hemispherical measurement of the sparse forest of CNT with two different polarization coordinate systems. One can see that in the $(\mathbf{h}, \mathbf{v})$ basis the Mueller matrix is symmetric but the fast axis (4 center parameters) turns with φ_s, contrary to the results with $(\mathbf{x}, \mathbf{y})$ coordinate which exhibits constant direction in the horizontal plane for any φ_r.

Dense forest of random positioned CNTs

In figure 5.6 more symmetry can be observed for the two different representations in terms of diattenuation (1^{st} line) and polarisance (1^{st} column). In addition, retardance elements are more difficult to interpret in the $(\mathbf{s}, \mathbf{p})$ basis than in $(\mathbf{x}, \mathbf{y})$ (4 center coefficients).

Consequently, while measurement without pinhole keeps the symmetry in the $(\mathbf{h}, \mathbf{v})$ basis, here with the presence of the pinhole that selects the incidence position it is no more valid. The $(\mathbf{x}, \mathbf{y})$ basis is more appropriate to compare Mueller matrices for different bistatic configurations.

5.1.9 Comparison of the intensity distributions

In figure 5.5 and 5.6 the intensity for respectively the sparse forest and the dense forest is exhibited in place of element $\mathbf{M}_{1,1}$. The ring defined by $\theta_r = \theta_e$ of high intensity can be observed for the sparse forest. The specular direction is hidden because of saturation on the camera caused by the direct contribution of the ground. The elements $\mathbf{M}_{3,3}$ and $\mathbf{M}_{4,4}$ contain saturation and artifact areas. Around $\theta_r = 20°$, $\varphi_r = 0°$ in these elements there is a saturation, the elements are over 1. Consequently this position is not analyzed. Otherwise there is an artifact around $\varphi_r = 330°$. It is a discontinuity with a circular shape and there is not the symmetry at the opposite side $\varphi_r = 30°$.

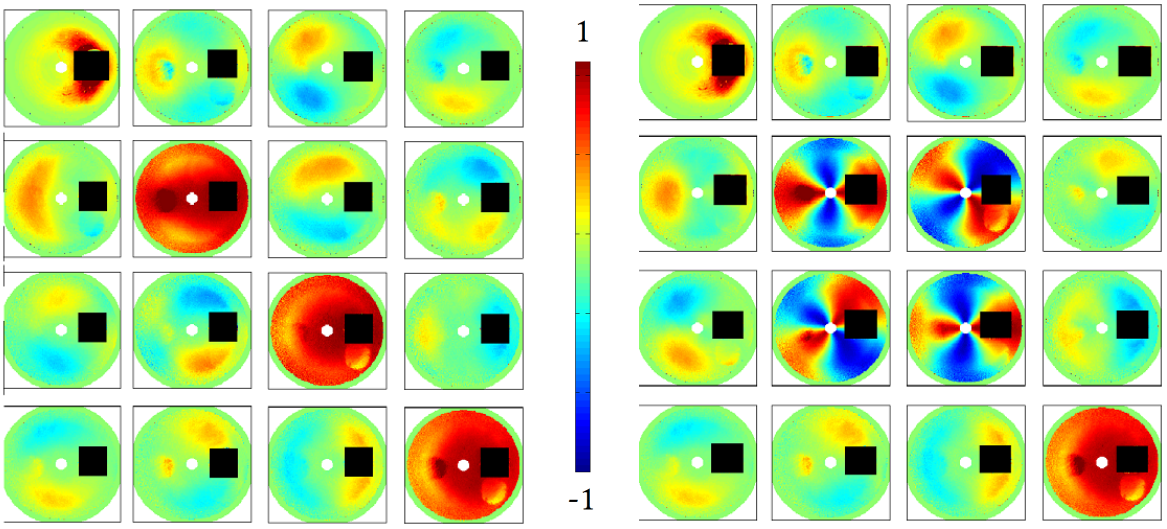

FIGURE 5.5: *Normalized Mueller matrix of the sparse forest in* $(\mathbf{x}, \mathbf{y})$ *basis on the left and* $(\mathbf{s}, \mathbf{p})$ *basis on the right. Here the first element* $\mathbf{M}_{1,1}$ *which is equal to 1 for the normalized matrix is replaced by the total intensity.*

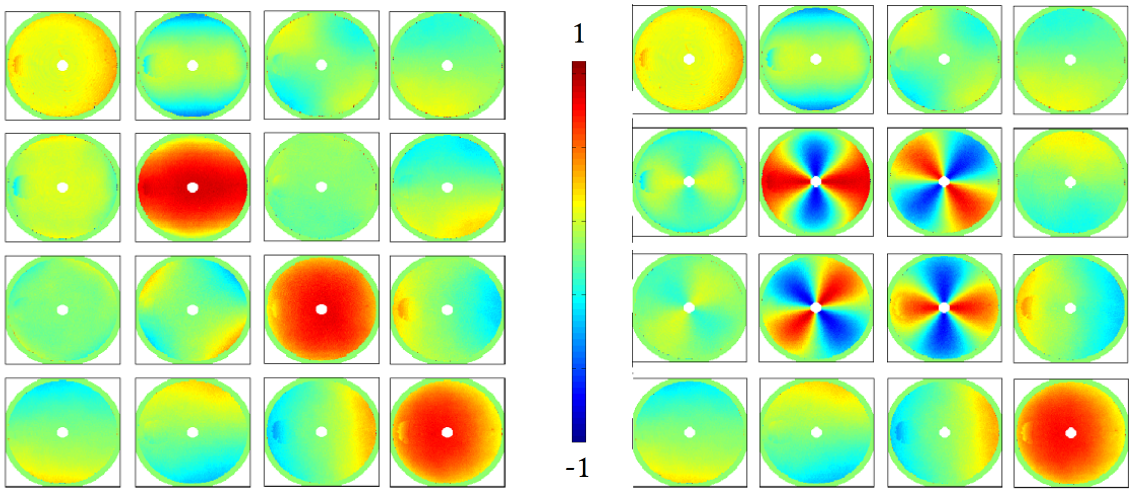

FIGURE 5.6: *Normalized Mueller matrix of the dense forest in* $(\mathbf{x}, \mathbf{y})$ *basis on the left and* $(\mathbf{h}, \mathbf{v})$ *basis on the right.* $\mathbf{M}_{1,1}$ *which is equal to 1 for the normalized matrix is replaced by the total intensity.*

These two areas of saturation and artifact in the sparse forest measurement will be masked in the following.

For the case of the dense forest the intensity of more homogeneous, as represented in on element $\mathbf{M}_{1,1}$ in the figure 5.6. The response for high density of nanotubes is more diffusive. The intensity level is higher around a crescent in the specular direction but the contrast in lower in comparison to the sparse distribution of CNTs. There is also a intensity enhancement at the backscattering position $\theta_r = 40°$, $\varphi_r = 0°$. This effect is not observed for the sparse nanotube forest.

5.2 Analysis of the measured Data

5.2.1 Application of the Cloude-Pottier decomposition

The Cloude Pottier decomposition has already been extended to the bistatic case in previous works. Nevertheless the physical interpretation of the parameters in the case depending on the bistatic angle has not been tested on real measurement of forested environment. Some of these parameters have been tested for canonical objects or set of canonical objects observed in bistatic configurations in an anechoic chamber [11]. In this case, the entropy has been shown to be quite similar to the polarization index of Gil (PI) [52]. In [12], the different decompositions have been compared in the backscattering case. A close relation between H and PI has also been observed, as well as for $\bar{\alpha}$ and D but with different dynamics. We tested these parameters for our two samples and for all the receiver positions. In the presented measurements the incidence position is set with $\theta_e = 35°$, $\varphi_r = 0°$. In that way the backscattering position is located on the middle left of each hemispherical representation of the parameters. For the purity parameters $A_{i,j}$ introduced by Gil in [50] we restrict the study to $A_{1,2}$ which corresponds to the anisotropy parameter considered in the Cloude-Pottier decomposition. On Fig 5.7 and 5.8 it can be seen that for the position of reception around the specular there is a black square mask to avoid saturation on the camera, and to keep a good contrast for all other reception positions.

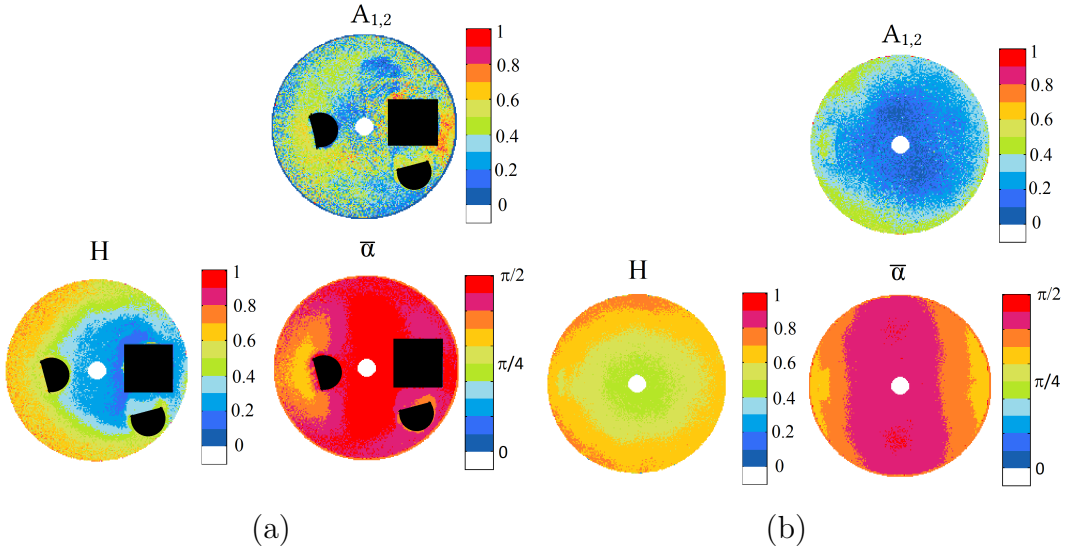

FIGURE 5.7: *Decomposition parameters of Cloude-Pottier issued from the Mueller matrices of the sparse (a) and the dense (b) forest measurements.*

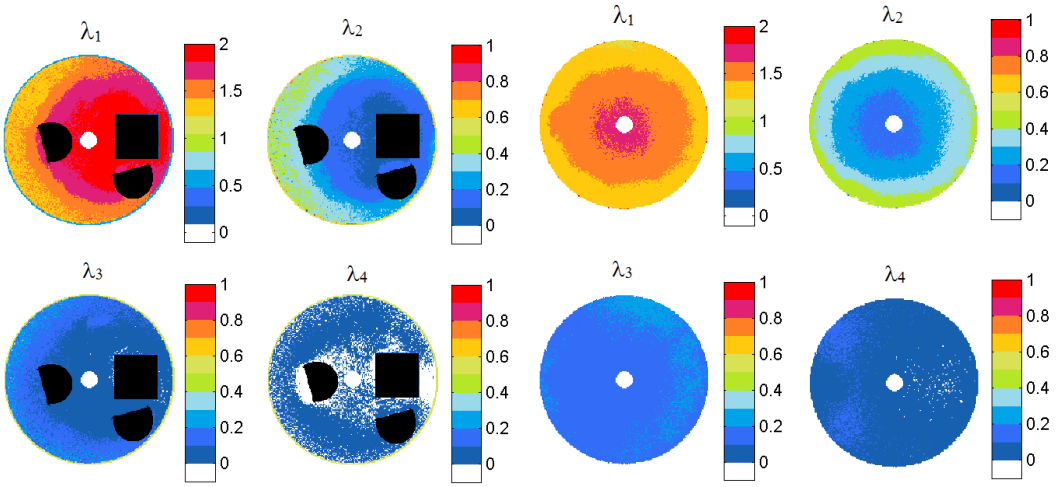

FIGURE 5.8: *Eigenvalues of the coherency matrices issued from the Mueller matrices of the sparse (a) and the dense (b) forest measurements.*

As a first analysis, we propose to compare the variation of the Cloude Pottier parameters with respect to the well-known backscattering case and to study the impact of the density.

1. For the backscattering case, the entropy H is around 0.5 for the both densities of forest. It seems to be linked to the high value of λ_1 in the both cases. If we look at the receiving positions close to the specular, H becomes lower for the sparse forest while it keeps a high value for the dense forest.

2. For the parameter $\bar{\alpha}$ in both cases it has lower value for the position of reception with $\varphi_r = \varphi_i$ and $\theta_r \geq \theta_i$. For other bistatic positions α is higher for the sparse forest than for the dense forest. This parameter informs us on the type of mechanisms that are weighted by the eigenvalue of the coherency matrix. When $\bar{\alpha}$ is high there would be a mix of different scattering mechanisms.

3. The anisotropy provides information about the variation of depolarization with change in polarization. If it approach 1 it exist subspaces in the polarization domain where the depolarization can be small. The anisotropy parameter $A_{1,2}$ is about 0.6 for the backscattering in the case of the sparse forest, and around 0.4 for the backscattering in the dense forest. For the other positions of reception it is very fluctuating. Nevertheless it seems to have similarities with the fourth eigenvalue of the coherency matrix λ_4 especially in the case of the dense forest. In this case it is close to 1 in the specular and close to 0 if the receiver is alongside the transmitter (blue regions). In any case the anisotropic signature is more readable in the dense case.

4. The fourth eigenvalue reach zero for the backscattering case and for the sparse forest. It is characteristic of the rank of the coherency matrix. However even if, in the dense case, λ_4 is close to zero, it does not reach the very value of zero. This remarks is important and it is maybe linked to the multiple interaction that occurs.

Now we will investigate the decomposition that is often used in optics for common bistatic configurations, and the relations that we can do with the parallel decomposition of Cloude-Pottier.

5.2.2 Application of the Lu and Chipman decomposition

1. $M_{1,1}$ gives the information of the total transmitted intensity depending on the position of reception. We confirm some previous results [11] and first, that the higher intensity is obtained around the specular reception angular position. Fig 5.9 and 5.10 show that the range of intensity is larger in the sparse forest case.

2. For PI, it shows that the depolarization increases with the density and with the reception inclination θ_r, as it was investigated in [12].

3. The diattenuation parameter is more homogeneous for the dense case, and is restricted in the backscattering reception cone with $\theta_r = \theta_e$ for the sparse one. It means that the dominant bounce process is different in the two cases. The parameters of the diattenuation stokes vector underline that for $\varphi_r = 90°$ the circular polarization state is less attenuated and it would be an interesting configuration for detection.

4. The retardance parameters exhibit similar conclusions, except for the phase shift process. In any case it is low.

5. The parameter $\varepsilon(\mathbf{D})$ informs us on the good transmission of the circular polarization state for 90° bistatic angle. The information is given in figure 5.9 for the sparse forest and in figure 5.10 for the dense forest. It means that the circular polarization is less impacted and is better transmitted through the forest. The effect is even more underlined by the ellipticity of the diattenuation $\varepsilon(\mathbf{D})$ in the case of the dense forest.

Now if we compare these comments with the ones obtained by the parallel decomposition, the entropy H and the PI parameter shows the same behavior whatever the bistatic angle for the both densities. Now it is quite difficult to deduce direct links with the other parameters. The reason is that the other parameters of Cloude-Pottier are linked to the purity indexes [23] and are somewhere of more detailed information of H. In the case of the serial decomposition, $\mathbf{D}$ and $\mathbf{R}$ gives the information of other physical behavior. It is a great advantage of the Lu and Chipman decomposition.

In Chapter 2 we explained that the order of the decomposition matrices in the Lu and Chipman decomposition can influence the result.

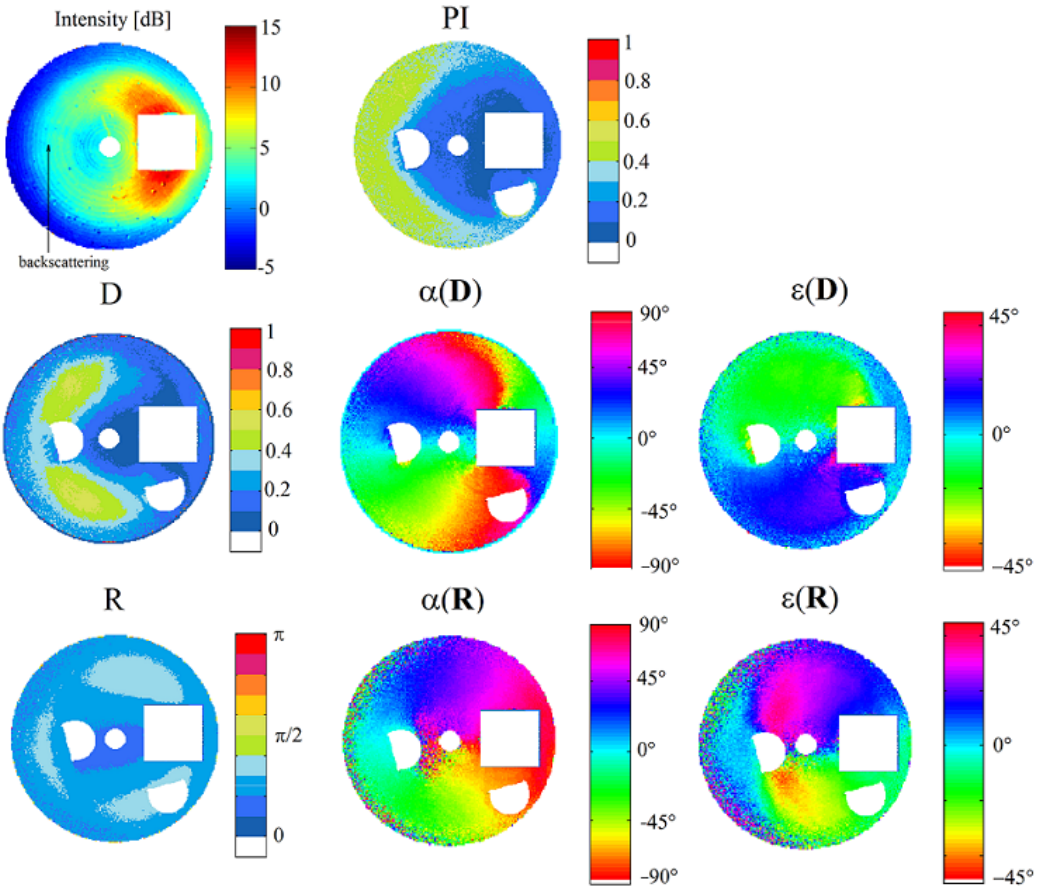

FIGURE 5.9: *Intensities and Lu and Chipman decompositions parameters issued from the Mueller matrices of the sparse forest measurement.*

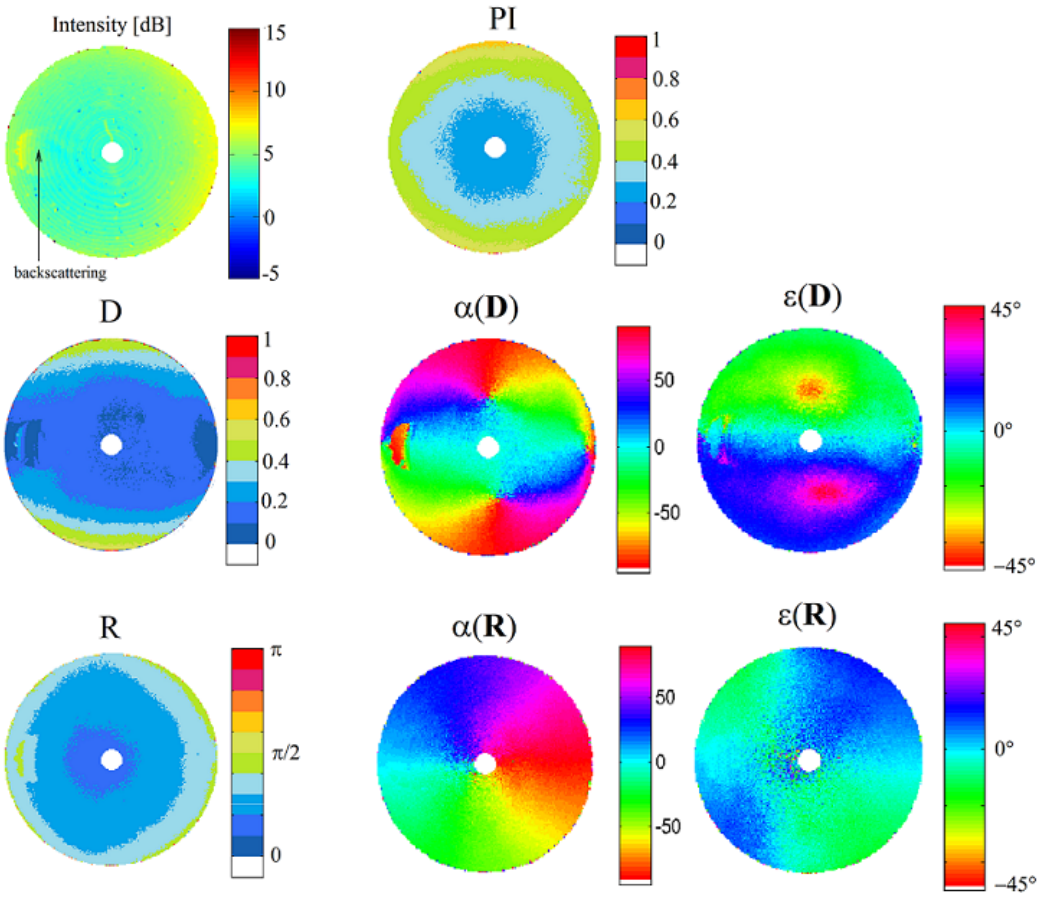

FIGURE 5.10: *Intensities and Lu and Chipman decompositions parameters issued from the Mueller matrices of the dense forest measurement.* $(\mathbf{h}, \mathbf{v})$ *basis.*

5.2.3 Alternative decompositions in the case of the measurement for the density comparison

Reverse decomposition

In order to check influence of the position of the decomposition matrices in the Lu and Chipman decomposition, we test the reverse decomposition [53], that decomposes $\mathbf{M}$ such as $\mathbf{M} = \mathbf{M_D M_R M_\Delta}$.

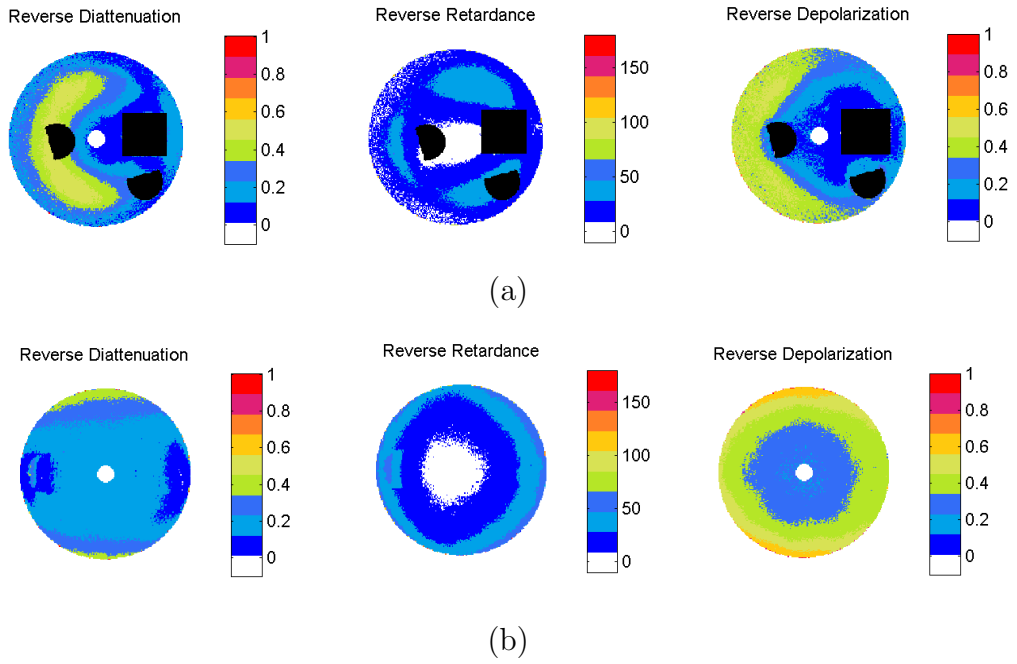

FIGURE 5.11: *Reverse Lu Chipman decomposition for two densities of measured forests. (a) the sparse forest, and (b) the dense forest.*

In figure 5.11 one can observe that for most of the bistatic configurations, no large difference can be observed. However, the reverse diattenuation at position close to monostatic in the sparse forest does not exhibits the fall down to 0 as in the forward decomposition case, see figure 5.9. It shows the discontinuities that the monostatic induces. However the reverse depolarization is close the the forward one and we cannot predict here which one of the decomposition order is better in our case, especially because the depolarization is inside the global scattering events in the CNT forest and it is difficult to declare that the depolarization appends at the beginning or at the end of the scattering process.

In order to determine which is the more accurate diattenuation value in monostatic, the symmetric decomposition of Ossikovski is applied, see chapter 2. Its advantage is to be independent of decomposition element position choice.

Ossikovski decomposition

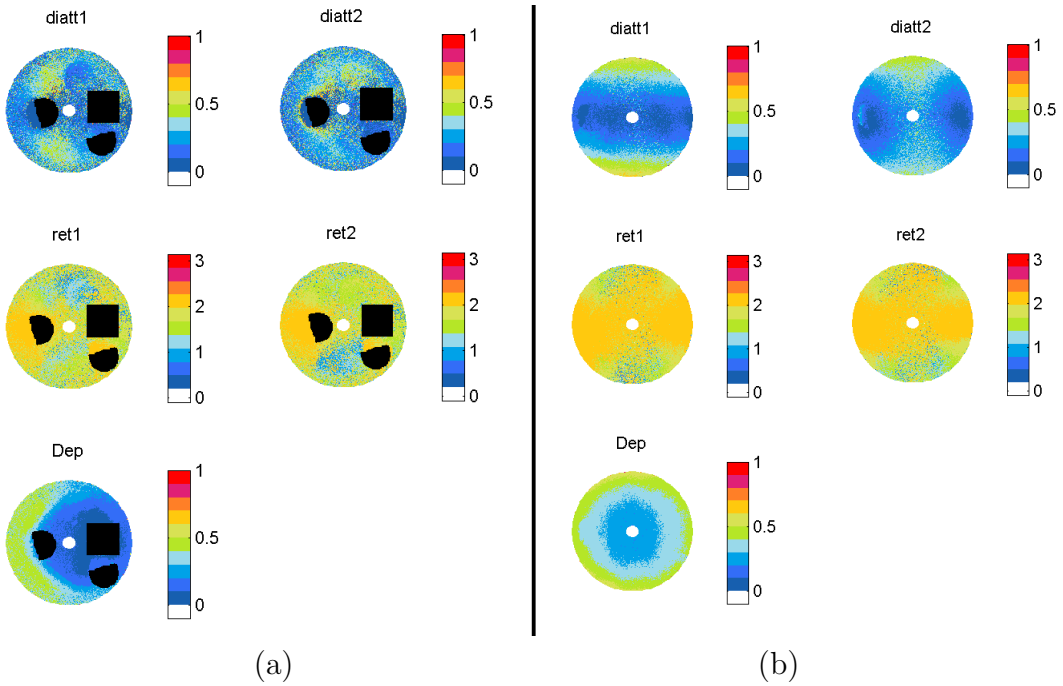

FIGURE 5.12: *Ossikovski decomposition for the case of two densities of measured forest, (a) the sparse forest, (b) the dense forest.*

In figure 5.12 on can see the the two diattenuation exhibit the discontinuity near the monostatic. It would mean that the forward Lu and Chipman decomposition is better in the case of the CNT forest because the forward diattenuation relates the same behavior. It would also mean that the depolarization process occurs.

The monostatic discontinuity that we have noticed is also observed for the depolarization and it can be related to the coherent backscattering effect. In any case, these observations should be done with a more robust version of our ARMP to ensure that their is no measurement artifact, for example it would be interesting to have a accurate mechanical positioning of the pinhole that select the incidence angular position.

The pinhole at the incidence leads to a variability of incidences that are averaged. It adds a variability for the paths that the light encounters in addition to the temporal integration. Theoretically, the solid angle of the CCD pixel at the reception does not

induce a sufficient angular variation to increase the depolarization. Consequently the large diameter of the pinhole can overestimate the depolarization level. It would be interesting to study the influence of the pinhole diameter on the PI in future works.

RGB Color visualization using the Kennaugh matrix

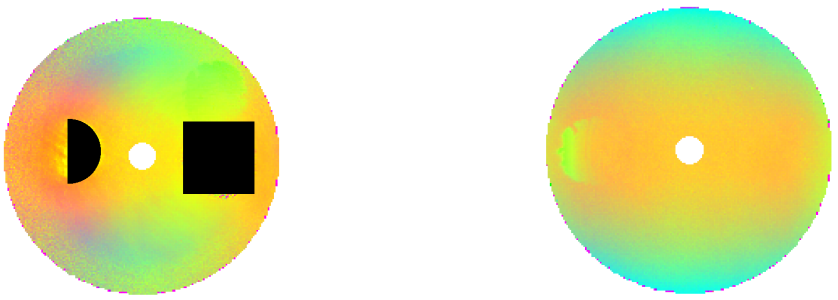

(a) (b)

FIGURE 5.13: *RGB color channel visualization issued from the Kennaugh matrix equivalents to the Mueller measured matrices.*

The color visualization, see figure 5.13, enables a compact representation of the polarimetric behavior. The method is convenient to retrieve the coherent decomposition realized for the scattering matrices. Here each color channel, red, green, blue is associated to a polarization channel absolute value, via $red = |HH|$, $green = |VV|$ and $blue = \frac{1}{2}(|HV| + |VH|)$. Consequently on the figure 5.13 the resulting colors code the relative power of the polarization channels. One can see that on the side the cross polarization have higher relative weight (blue color). The monostatic discontinuity is also highlighted with a yellow color for the sparse forest and more green color in the dense forest. The yellow color means that horizontal co polarization channel has the same weight as the vertical co polarization channel. That is linked to the low diattenuation of the Lu-Chipman decomposition. This kind of representation is more common in radar domain and it is useful to have a compact polarimetric information that is adapted to our human eyes.

* * *

Summary
The imager polarimeter, the spectral Mueller polarimeter, and the angle resolved Mueller polarimeter were investigated in chapter 4. All measurement are not exploitable and results are more promising for the angle resolved device. Nevertheless the setup required adaptations for our case of study. They consist in using a laser source, an element to control the incidence angular position and a mask to avoid saturation. A new component to sustain the microscope objective was also realized. CNT random positioned with two different densities are kept for further investigation. Two polarimetry coordinate systems were tested on the angle resolved Mueller matrices. The $(\mathbf{x}, \mathbf{y})$ polarimetric coordinate system seems to be more relevant in our case of constant angular incidence position and bistatic configurations.

Part III

Analysis of the measurements using simulations and applications in radar domain

Chapter 6

Methodology and tools to assess the contribution of the optical measurement to bistatic radar

We saw in the previous part that the developed angle resolved polarimeter can produce an entire domain of bistatic configurations at once and the laser source is very efficient to illuminate the CNT samples with enough light in every collected scattering angles. What is more, the polarimetry is fully mastered with this device. These advantages make the measurement useful to:

- Make a parametric analysis on the CNT density comparing the two selected CNT samples.
- Collect validation data to further validate the simulation model.
- Understand the polarization mechanisms that occur in such structure. For that purpose, we will use additional information from the scattering theory and from the data simulated by our model.

Indeed, we propose to use a simulation tool to evaluate the capability of the measurements with optical scale to reproduce the polarimetric behavior in radar observable over forest. In parallel, as the lack of bistatic radar measurements prevents from a deep and advanced validation of our bistatic model, we will use the optical measurements instead. Consequently, we present in this chapter a comparison between the measurements at optical scale and the simulation knowing that the monostatic configuration has already been validated [54] as well as some very simple cases for few bistatic configurations in anechoic chamber [11].

The simulation code that we use is called COBISMO. It has originally been developed in Fortran, as an extended version of COSMO, its monostatic version. In order to speed up the calculations, to make it more user friendly, and to ease its compatibility with ONERA post processing tools, mainly developed in Matlab, we decided to rewrite it with this language. The transition from COSMO to COBISMO, then from its original version to its Matlab version will be presented further in this chapter.

In addition, COBISMO has been modified to reproduce the CNT ARMP measurements. The adaptations will be also reported.

6.1 Specification for the simulation

There are several ideal requirements for the simulation code which are listed below:

1. Scattering of long cylinder dielectric element above ground. Indeed, the forest and trees can be modeled by dielectric cylinders in an electromagnetic point of view. Exact diffraction solution exist for this kind of canonical elements.
2. Entire bistatic configuration domain because we want to investigate every possible bistatic angle configurations that a radar system could use.
3. In our case we want to reproduce with the same simulation tool for the EM propagation in forest at UHF frequency radar and also for the light propagation inside the CNT samples. Consequently, our code have to be suitable for radar and optical wavelength.
4. Being full polarimetric.
5. Giving the Mueller matrix of the scene in order to take into account the depolarization process.

6.2 State of the art

The simulation of the propagation in forested environments has been a long time effort to be able to understand and anticipate the radar measurement. Several types of approximations exist:

- Approximations of the scene description,
- Approximations on scattering by single elements,

- Approximation of the interactions between the elements.

The description of the scene is arbitrary because the forest environment design a very diversified environment and to be able to reproduce a diversity of forest stand the simulation codes at UHF band always use elementary scattering part. For example a branch can be approximated by an ensemble of parallelepiped, or by one smooth cylinder. In any case, the models fall into several categories, according to their scattering approximation [1]:

- "Exact" codes using numerical solution of Maxwell's equations as a result of the target mesh and integral methods. They are very accurate but computationally expensive. Most of this type of code use the MoM or the Discrete Dipole Approximation [55] [56].
- "Descriptive" codes in which the resolution of Maxwell's equations is performed for canonical element as cylinders via the Born approximation which enable to consider the scattering of the trunks and large branches independently, for example the model presented in [57]These two first kind of model are coherent, they have the capability to preserve the absolute phase information
- Incoherent model that do not consider the absolute phase of the EM wave and that only consider the forest as a random media. They often us e the radiative transfer theory, for example [58].
- Empirical codes that are based on actual observations by regressing. It is statistical model that evaluate the statistical properties of the forest clutter in the radar images. In [59] a statistical analysis is realized to judge the accuracy of distributions for the forest clutter. This paper analyzes the statistical properties of the very high frequency VHF-band radar backscattering from coniferous trees by incorporating forest ground truth data into a physical-optics (PO) model that assumes horizontally transited and received polarizations and dominant double-bounce scattering from vertical stems standing on an rough ground surface. The analysis shows that a statistically adequate model for the tree backscattering amplitude can be presented as a mixture of generalized gamma or lognormal distribution, and the mixture model can be reduced to a single density model if the trees with trunk volumes exceeding an appropriate threshold are to be taken into account. The results can be used to design statistically adequate models of forest clutter for VHF synthetic aperture radar systems. It is limited in the fact that here only the horizontal transmitted and received polarization are taken into account and moreover it is only in the monostatic configuration. But if the matching with experimental data is confirmed it may have significant advantages

for detection purposes, and this kind of approach have to be investigated in the bistatic modes.

The coherent information is necessary to be able to take the interference between the elements into account. In the literature few models exist that have been developed in the bistatic configuration. To our knowledge, this is essentially descriptive models, since empirical models require observations of the forest by bistatic radar. We have identified the following for the UHF band:

- Tor Vergata Model [60]. It is a descriptive model based on the radiative transfer theory. Therefore, the absolute phase signal required for imaging or interferometry applications, cannot be considered .
- An extension of Mimics, a descriptive code which is also an incoherent code, was proposed by Liang, Pierce and Moghaddam [58].
- Exact code deals more easily with bistatic configurations [61], [55] [62]. It is a coherent end exact code. Its main disadvantage comes from its intensive calculation needs. It have been confronted to anechoic chamber measurement and exhibits good results for several independent scatterers.
- The code of ONERA-Toulouse [63]. It is a code descriptive. It is coherent. His bistatic version has not yet been validated on real bistatic forest data.
- COBISMO is a bistatic coherent code using cylinders and ellipsoids as building blocks [10] [64]. The monostatic version has been tested in many cases and for applications (polarimetry, interferometry). His Fortran bistatic version was confronted to indoor measurement of three vertical dielectric cylinders in [65].

We choose to use the code COBISMO for our application. It presents it is bistatic, coherent and it as been confronted to different monostatic and bistatic measurements, and it is accessible at ONERA.

6.3 Scientific Approach

In figure 6.1 we propose an approach for the use of COBISMO to understand the ARMP measurements and the use of the ARMP bistatic measurement to further validate COBISMO. The main step is the comparison of the measurement and the simulation when parameter are kindly adjusted. The comparison possibly leads to a loop in our approach if some polarimetric parameters are not correctly reproduced. In this loop,

that corresponds to the "no" answer in the diagram, the simulation hypotheses are in question, either the hypotheses made in the code, including the simulated mechanisms of interactions or the cylinder shape of the elements, or the post processing that denotes the way that the Mueller matrix is computed. The comparison is realized in section 7.2 on polarimetric decomposition parameters. The analysis of the well reproduced parameters will also takes place in section 7.2. The code hypothesis are questioned in section 7.3 where we try to bring some answers.

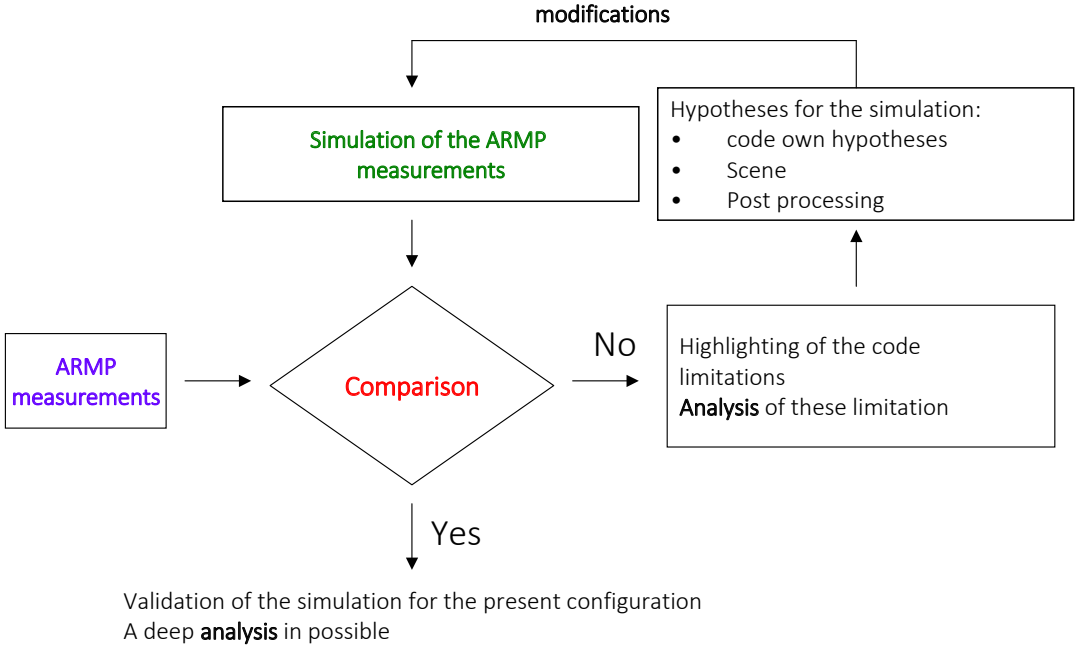

FIGURE 6.1: *Diagram of our approach to use the simulation in order to understand the scattering mechanism contributions and for validations.*

In the next section we present the adaptation of COBISMO to reproduce the ARMP measurement and we present the Mueller matrices that are produced in the entire bistatic domain for the two case of trunk density.

6.4 Adaptations of the simulation code to accommodate many scatterers in the bistatic configuration

6.4.1 Presentation of COBISMO

COBISMO is a coherent model, that is to say it keeps the relative phase information due to the element positioning (it is a sum of the complex amplitudes and not directly the intensities). For that reason, it can be used to simulate interferometric coherence for instance.

Then, it is a descriptive model, in opposition to analytic models as the Random Volume over Ground for example [66], that provides a literal expression of an observable in terms of various input parameters. COBISMO is based on a number of restrictive physical assumptions (eg approximation of the infinite cylinder, Rayleigh Gans approximation, etc.). The code is also full polarimetric because it calculates the Jones matrix, that is the four couples of emitted and transmitted polarizations in the $(\mathbf{h}, \mathbf{v})$ basis.

For each scatterer in the scene, four main mechanisms are calculated (see figure 6.3).

- Direct scattering
- Ground-element and element-ground scattering (double-bounces)
- Ground-element-ground scattering (triple-bounces)

Types of targets that can be described

The scene is modeled using three different types of elements that are the ground, cylinders (for trunks and branches) and ellipsoids (for the leaves).

- The ground contribution is considered via the multi bounce mechanisms and its direct diffusion is neglected [1]. The ground contribution is of prime significance in the total transmitted signal. It steps in the double bounce mechanism and also in the direct view of the ground especially near the specular configuration. Her the ground contribution is computed via the Fresnel coefficient. The main parameters of the ground are its roughness, its dielectric property and the incidence and reception angle. The roughness of the ground is taken into account

[1] This approximation is relevant for general bistatic case but it can be questioned when the receiver is near the specular configuration.

using the multiplicative term $exp(-2(k_0 h_{rms} \cos\theta_e)^2)$ applied to the usual reflection coefficients of a dielectric plane, with h_{rms} the root mean squared value of the height variations of the ground roughness.

- The branches and trunks are considered as long cylinders and parametrized by their length, their radius, their orientation, their dielectric property, their density and spatial distribution.
- The ellipsoids are taken into account to play the role of the leafs and needles. They are supposed small and as for the cylinders their parameters are their orientation, their dielectric property, their density and spatial distribution. The leaf contribution is not studied in this work as their contribution is small at large wavelengths.

Validity domain

For branch cylinders with small radius a in comparison to $1/k$, with $k = 2\pi f/c$, the infinite cylinder approximation is used: their height are larges in comparison to their radii, their heights are large in comparison to the wavelength and their radius is large in comparison to the wavelength. The dielectric property of each scatterers are supposed as constant inside each element.

In the UHF band, the minimum wavelength used is around 70 cm. In average it will be around one meter. With this value, constraints are given on the size of elements that have large lengths in comparison to, the wavelength and also small radii in comparison to the wavelength.

For large cylinder type (large radius in comparison to the wavelength) Physical Optics model is used [1].

In the case of the ellipsoids they are inside the validity domain defined by $kd|n-1| << 1$, n the refractive index and d is the smallest axis dimension of the ellipsoid. As for the case of the cylinder, the permittivity is considered as homogeneous inside each ellipsoid.

Symmetry breakdown on general bistatic configuration

Under monostatic configuration, there is the reciprocity by the inclusion of the two double bounces which are symmetrical between the path "element-ground" bounce and the path "ground-bounce element". In bistatic configuration, there is no more symmetry between the two double bounces, see figure 6.2 and the reciprocity when the emitter and the receiver are inverted can be lost which it induces $J_{hv} \neq J_{vh}$.

The four mechanisms considered in the bistatic situations are summarized in the figure 6.3.

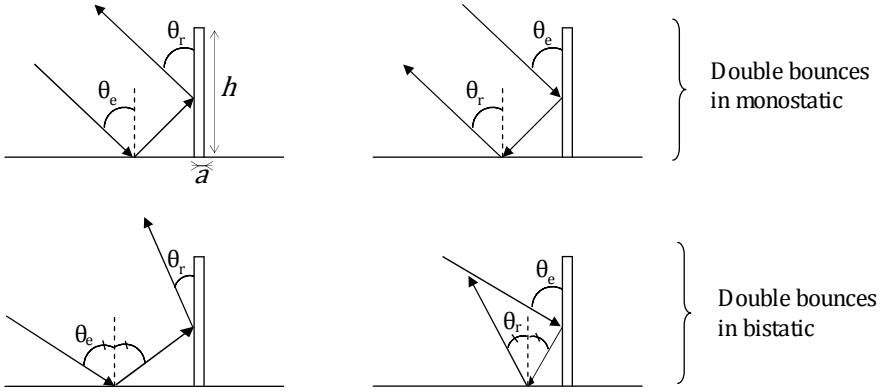

FIGURE 6.2: *Double bounce mechanism for monostatic and one bistatic configuration. See chapter 1 for the definition of the angles.*

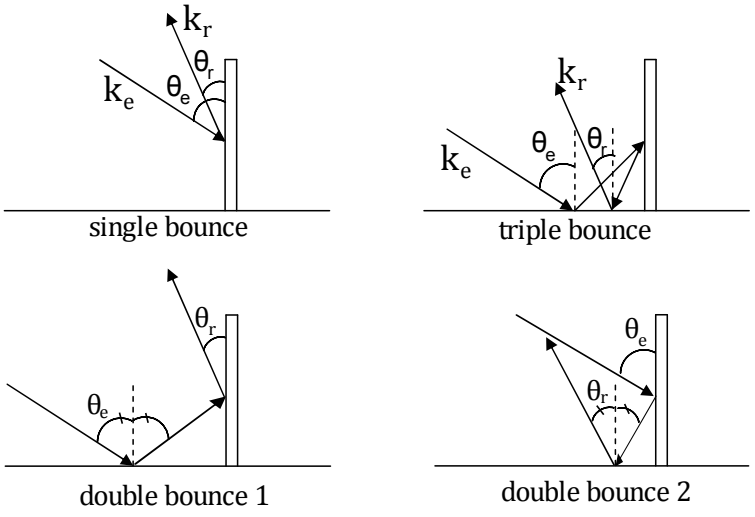

FIGURE 6.3: *The four bounce mechanisms in bistatic. See chapter 1 for the definition of the angles θ_e and θ_r and the vectors $\mathbf{k_e}$ and $\mathbf{k_r}$.*

6.4.2 Modifications in the structure of the code

To compute the scattering from an entire forest the computation needs to be as fast as possible. Parallelization of the computing has been realized to have gain in time and we have done other modifications of the code in order to have a scene description independent on the bistatic configuration.

6.4.2.1 Prediction of the attenuation

Each cutting cell is related to one attenuation matrix calculation. The main parameters are the element density, the traveled distance and the mean scattering matrix of constitutive elements.

In practice the evaluation of the global attenuation of the scene is realized in comparing the transmitted signal by a target with and without the surrounding media, in this case the forest. The magnitudes are measured on each channel and the attenuation is deduced from the ratio between the paths over and under the canopy. Here the evaluation of the attenuation in the context of the simulation follows the same principle.

The attenuation matrix that reports the forward multiple scattering between small elements such a small branches and leaves can be computed through the Foldy-Lax approximation [67], [68]. Each scattering matrix for each scattered and for each mechanism is weighted by the attenuation matrix that corresponds to the traveling of the wave in the surrounding media (shadowing effect). It is three attenuation matrices for the incidence part and three for the reception part. The matrices for each cell indexed by i are expressed as follows:

$$\mathbf{A}_i = exp(d_i \cdot \left[-ik_0\mathbf{Id} - i\frac{2\pi}{k_0}N_0\langle\mathbf{J}_i\rangle\right]) \tag{6.1}$$

d_i accounts for the distance traveled in the layer. $\langle\mathbf{J}_i\rangle$ is for the averaged Jones matrix of the elements inside the cell. N_0 the element density per volume, k_0 the wave number and $\mathbf{Id}$ is the 2×2 identity matrix.

6.4.2.2 Modification of the resolution cell for the attenuation matrices

The computed attenuation was previously dependent on the bistatic configuration. Although the simulation with COSMO was not conceived to simulate the SAR process, the cell cutting idea was originally designed to follow the resolution cell of the SAR image [69] (see figure 6.4). Indeed, the simulated forest density can be inhomogeneous.

It is then important to take into account the impact of this possible inhomogeneity of element densities on the total scattering. With a good resolution, the evolution of the density of the forest depending on the position in the forest is taken into account. In the first version the cell orientation was collinear to the wavevector. Since $\mathbf{k_e}$ and $\mathbf{k_r}$ are collinear in monostatic, this cutting choice corresponds to the volume that is projected in the resolution cell of the SAR image. However, in bistatic such approach is not possible and the resolution is not as simple, see chapter 1.

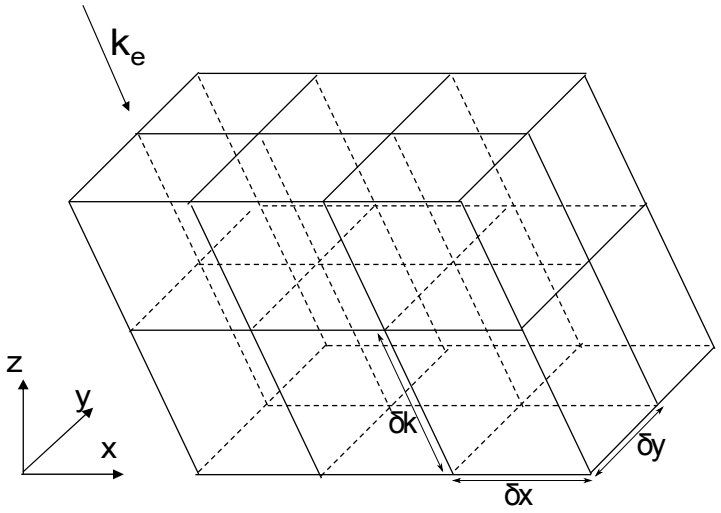

FIGURE 6.4: *Original cells with monostatic COSMO simulation.* $\mathbf{k}_i$ *is the incidence wavevector, which is aligned with the cell orientations in this case.* δx*,* δy *and* δk *are the resolutions in the* $(\mathbf{x}, \mathbf{y}, \mathbf{k}_i)$ *basis.*

Consequently, we choose to introduce a cubic resolution cell independent on $\mathbf{k_e}$ and $\mathbf{k_r}$, see figure 6.5, and that enables to take into account the density inhomogeneities as well.

6.4.2.3 Accelerations of the code

To benefit as far as possible from the Matlab language, vector calculation was developed, i.e. each element parameters is set in a line of a matrix. The time efficiency of the new architecture was evaluated to be around 15 time faster for the test forest constituted of 5.10^6 elements (cylinders and leaves). In order to express properly the acceleration of the calculation the benchmark in table 6.1 was made for that forest example. $\mathbf{J}_{forest}$ denotes the Jones matrix of the entire forest.

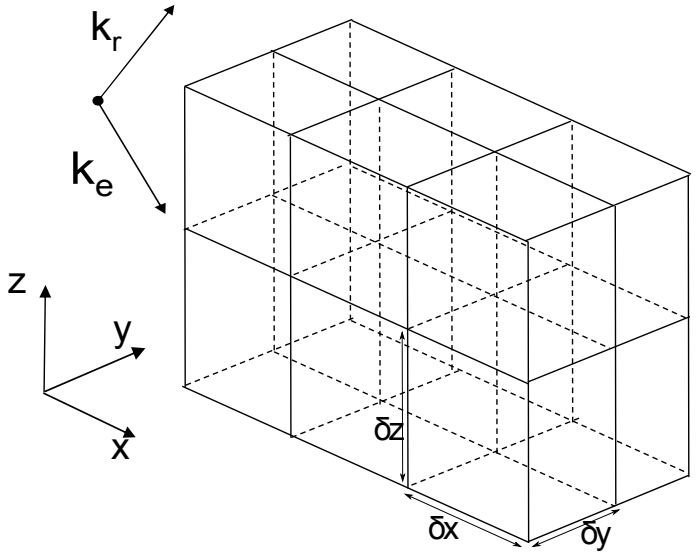

FIGURE 6.5: *New cells with bistatic COBISMO simulation. δx, δy and δz are the resolutions in the $(\mathbf{x}, \mathbf{y}, \mathbf{z})$ basis. δz is independent of $\mathbf{k}_i$ and $\mathbf{k}_r$.*

TABLE 6.1: *Benchmark test on a forest stand that counts 5.10^6 elements. V_F is for the primary fortran version, V_M denotes the vectorized Matlab version.*

Processor:	Intel(R) Xeon(R) CPU	W3530	@2.80GHz
RAM	6Go		
Type	64 bits		
	t	$\mathbf{J}_{forest}$	
V_F	$507s$	$\mathbf{J}_{forest} = \begin{pmatrix} -5.16+0.67i & -0.25+0.12i \\ -0.00-0.04i & 57.43-50.42i \end{pmatrix}$	
V_M	$33s$	$\mathbf{J}_{forest} = \begin{pmatrix} -5.16+0.67i & -0.25+0.12i \\ -0.00-0.04i & 57.43-50.42i \end{pmatrix}$	
time gain factor for 5×10^6 elements	**15**		

6.4.3 Interfacing with polarimetric processing

The diagram 6.6 summarizes the different steps of the code. From the output scattering matrix $\mathbf{J}_{forest} = \sum_i \mathbf{J}_i$, with i is the cell index, numerous processing can be realized. For the polarimetry the main outcome is the evaluation of the Mueller matrix $\mathbf{M}$. We use the table 2.1 for the correspondence between the polarimetric formalisms. The Mueller matrix is calculated from one (no depolarization) or several (possible depolarization) Jones-Sinclair matrices. The averaged Jones-Sinclair matrices come from

different possible realizations. It can be different structures realizations, different angular configurations or different forest areas or even a mix of these realizations. The main question is to choose the more realistic way of averaging for the simulation of the final Mueller matrix.

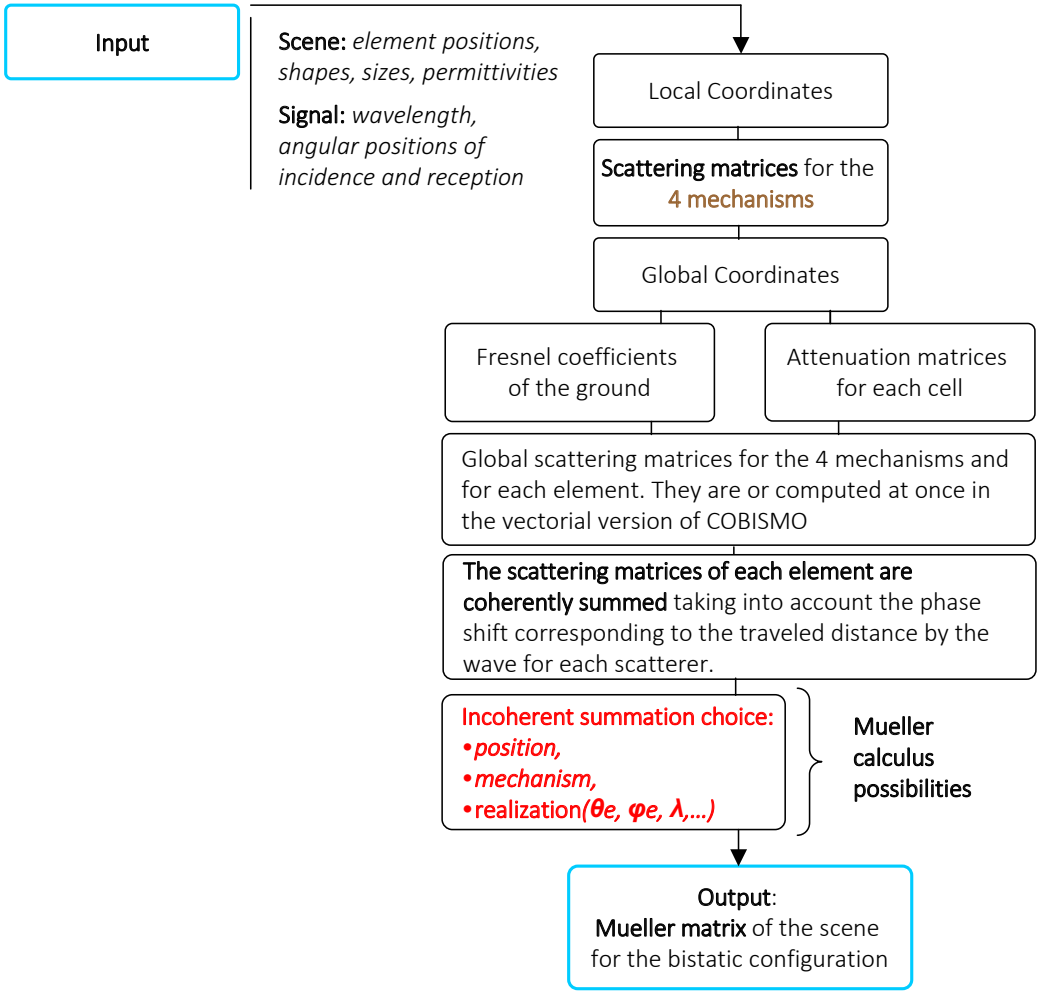

FIGURE 6.6: *Main steps in COBISMO simulation process.*

Verification for a limited number of elements

Important modifications of the code were realized and we want to check the computed Jones matrix before comparing the Mueller matrix simulation with the ARMP CNT measurement. To proceed to the verification a past validation of COBISMO involving indoor measurements on one and three vertical cylinders [11] .

Firstly the norm of the simulated Jones matrix is compared with the measurement for one cylinder. Figure 6.7 corresponds to the evolution the absolute value of the four elements of the Jones matrix depending on the receiver azimuth position φ_r. At $\varphi_r = 0$, we are in the monostatic configuration and $\varphi_r = 180°$ corresponds to the specular configuration. There is a good correspondence between the measured data and the simulated data with the vectorized version of COBISMO. In the case of vertical cylinders the simulated cross polarizations absolute values are equal ($hv = vh$) while differences exist for the measured ones. However their values are far much lower than the co polarizations ($\simeq -20dB$).

Then, three cylinders where measured in the configuration that is described in figure 6.8 where $\lambda = 0.07m$ is the wavelength, $H = 0.3m$ denotes the height of the cylinders and $\varnothing = 0.02m$ is the diameter of the cylinders.

The case of three cylinders is considered to verify the coherent summation of the scattering by each cylinder. The comparison again leads to satisfying results, see figure 6.9. In the case, the cross polarizations exhibit higher values.

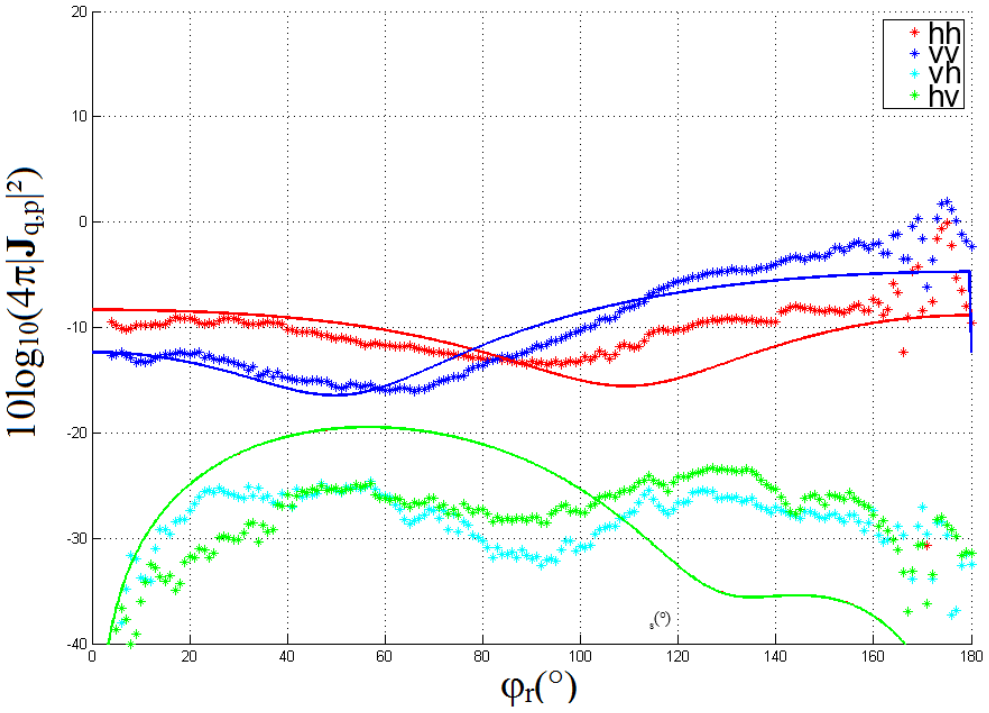

FIGURE 6.7: Validation for the four couples of polarization in the case of one cylinder

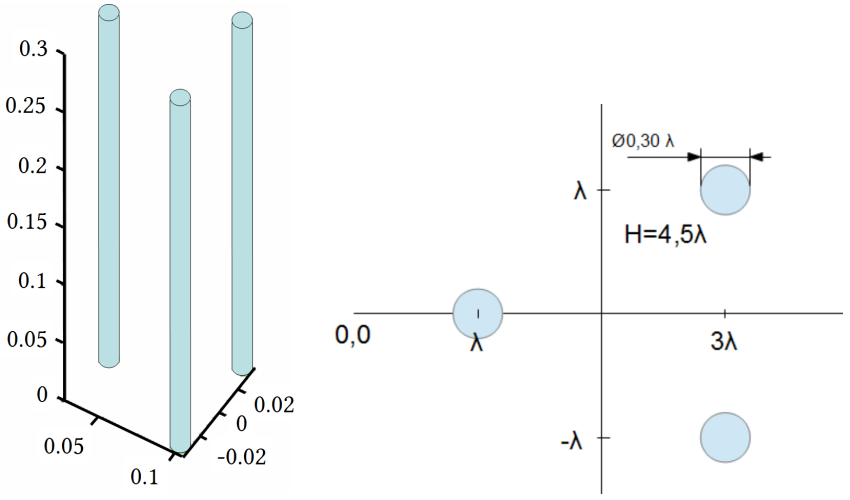

FIGURE 6.8: Configuration of the cylinders for the validation of the simulation code

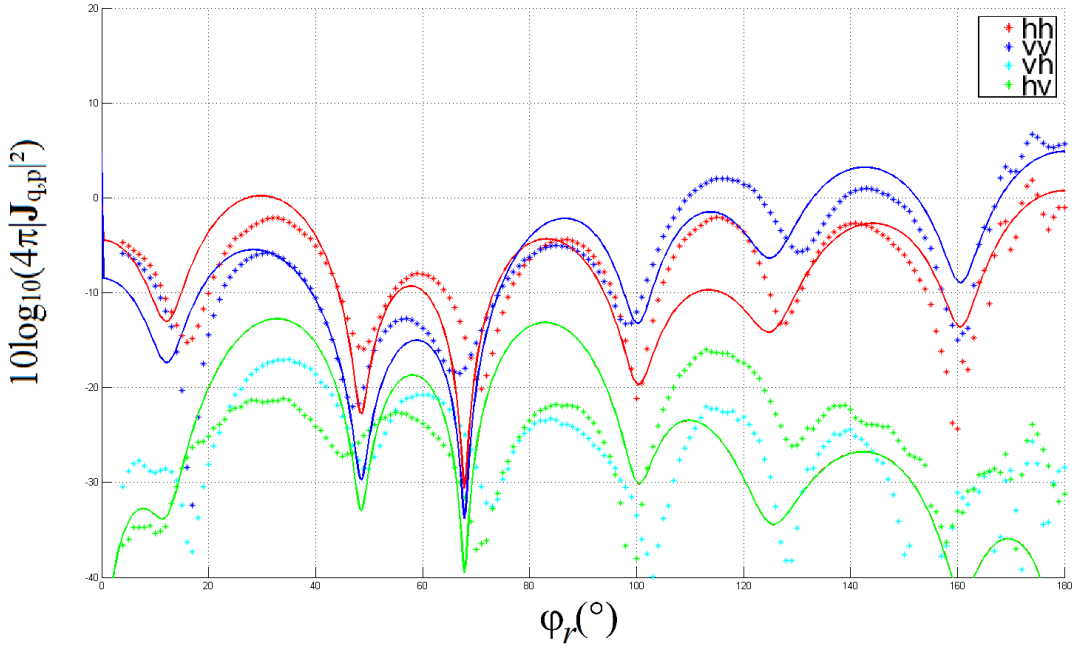

FIGURE 6.9: Validation for the four couples of polarization in the case of three cylinders

6.5 Simulation of the measured Mueller matrices with first hypothesis

We propose here to use COBISMO to reproduce the CNT measurements realized with the ARMP. We are still in the same domain of validity because the ratio between the sizes of the element and the wavelength a/λ remains almost the same, but effective permittivities for the ground and for the CNTs are needed.

As introduced in chapter 4, the CNTs are constituted by graphite shits unrolled to form long cylinders. The problem for us is the evaluation of the CNT permittivity ε_{CNT}. This value constitutes a main input argument for the code and its evaluation is of prime importance. The permittivity for a single CNT is not directly measurable but effort has been conducted to retrieve a credible values at visible wavelength. In 6.10 the methods is based on graphite shit permittivity and Drude-Lorentz model [70], [71].

6.5.1 Determination of the input parameters

6.5.1.1 Relative permittivity values for the CNT sample

In [70] and [71] it is shown that one can reasonably use the graphite permittivity in the case of the CNT. In [72] the permittivity is calculated via a Drude-Lorentz model with a Drude free electron contribution expressed as:

$$\varepsilon_{Drude}(\omega) = 1 - \frac{\omega_p^2}{\omega^2 + i\frac{\omega}{\tau}} \tag{6.2}$$

with ω_p and τ the free electron plasma frequency and the relaxation time. The Drude free electron contribution is added to a Lorentz oscillations contribution corresponding to interband transition and expressed as:

$$\varepsilon_{Lorentz}(\omega) = \sum_{m=1}^{7} \frac{\sigma_m^2}{(\omega_m^2 - \omega^2)} \tag{6.3}$$

The parameters ω_m are given in [72] and finally:

$$\varepsilon_{CNT}(\omega) = \varepsilon_{Drude} + \varepsilon_{Lorentz} \tag{6.4}$$

In our case, at $\lambda = 633nm$, $\varepsilon_{CNT} = 4.9 - 9.5j$. The variation of $\varepsilon_{CNT}(\omega)$ in the optical domain is depicted in figure 6.10.

Concerning the substrate layer, the value can be found in the literature for our sample it is Silicon. The Silicon refractive index is $n = 3.88$ at $\lambda = 633nm$ [73], the real permittivity is $\varepsilon_r = 15.05$.

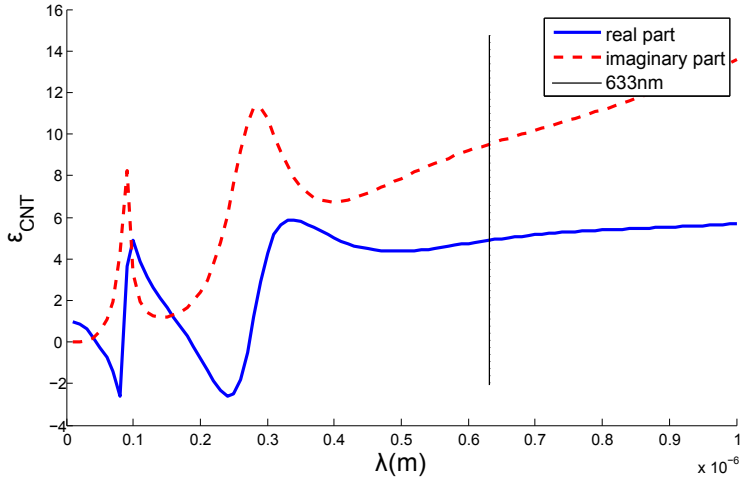

FIGURE 6.10: *Wavelength dependency of the real and imaginary parts of the Drude-Lorentz model for the permittivity of a CNT.*

6.5.1.2 Simulation of the ARMP Mueller matrix

In the precedent paragraph the permittivity values to obtain the CNT Jones matrix for one realization of the scene was presented. Now we describe the way to simulate the Mueller matrices.

The Mueller matrix elements are obtained from a set of realizations of the scattering of polarized light. Experimentally, there is an integration during the time of acquisition. The acquisition time which is about one second in our cases make the Signal to Noise Ratio (SNR) increase. It is limited by the saturation of the camera, but the higher is the capturing time, the more accurate is the measurement, and the more accurate is the depolarization evaluation. For a depolarizing scene, even with an infinite SNR the depolarization index is not zero. Nevertheless, it is worth noticing that a very low SNR would lead to an overestimation of the depolarization and a deterministic target would sign in that case with a non null depolarization. To sum up the precedent paragraph the equation 6.5 describes the calculation of the Mueller matrix from a realization set of Jones matrices:

$$\mathbf{M} = \mathbf{A}^{\dagger} \left\langle \mathbf{J} \otimes \mathbf{J}^{*} \right\rangle \mathbf{A} \tag{6.5}$$

A is the matrix that transforms the complex correlation quantities of the scattering matrix into a real set of quantities thanks to the Pauli basis:

$$\mathbf{A} = \frac{1}{\sqrt{2}} \begin{pmatrix} 1 & 1 & 0 & 0 \\ 0 & 0 & 1 & -j \\ 0 & 0 & 1 & j \\ 1 & -1 & 0 & 0 \end{pmatrix} \tag{6.6}$$

The pinhole selection

Experimentally, the selection of an angular incidence position θ_e, φ_e is not specific due to the width of the pinhole. For this reason, realizations that lead to the Mueller matrix follows the scope of incidence positions. In our case, a $200\mu m$ **diameter pinhole** induces a circular spot in the polar basis, as dipicted in figure 4.10. This domain Ω is defined as:

$$\Omega : \sqrt{sin^2\theta + \sin^2\theta_e - 2\sin\theta\sin\theta_e\cos(\varphi - \varphi_e)} \leq t_e \tag{6.7}$$

θ_e and φ_e are the central angular incidence coordinates and t_e is the angular radius of the spot. For the presented measurement the value are: $\theta_e = 35°$, $\varphi_e = 180°$ and $t_e = 5°$.

And the final Mueller matrix for this integration domain Ω can be expressed as:

$$\mathbf{M}(\theta_r, \varphi_r) = \mathbf{A}^\dagger \cdot \frac{1}{\Omega} \int_\Omega (\mathbf{J}(\theta, \varphi, \theta_r, \varphi_r) \otimes \mathbf{J}^*(\theta, \varphi, \theta_r, \varphi_r)) d\theta \cdot d\varphi \cdot \mathbf{A} \tag{6.8}$$

This incidence position scope would lead to another depolarization source that is related to the fluctuations of the polarization of the scattered light according to little variation of the incidence angular position as discussed in chapter 7. In practice, we simplify the integration over the whole Ω domain by only calculating the Mueller matrix for 4 perimeter angular positions in addition to the barycentric one, as represented in figure 6.11.

Scene

The distributions of the positions, the sizes and the inclinations of elements are evaluated using electronic microscope images.

The samples of the two densities that are selected in Chapter 5 are reproduced. The corresponding values that we use in our simulations are listed in the table 6.2. The radius of the cylinders is set to $0.1\mu m$ as a constant. The heights are set with uniform

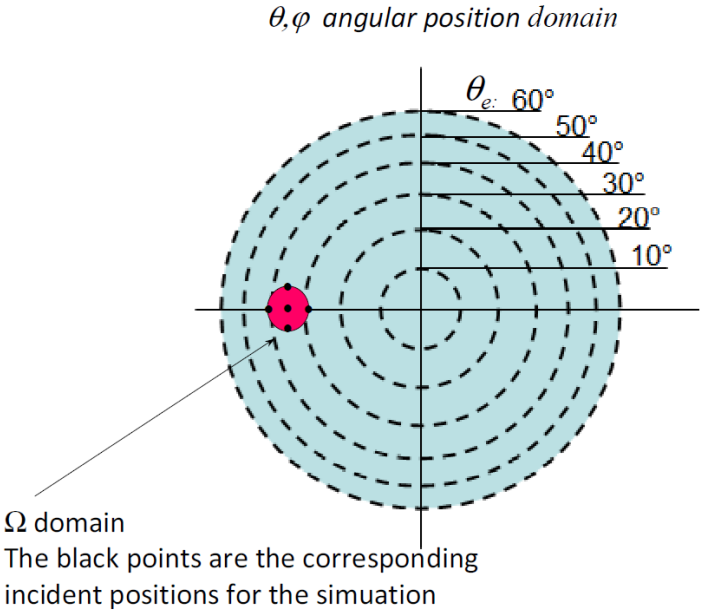

FIGURE 6.11: *Representation of the incidence position of the pinhole for the simulation.*

distributions with mean values of $6\mu m$ and $7.5\mu m$ and the distribution half widths are $2\mu m$ and $5\mu m$ receptively for the sparse and the dense sample. The nanotubes inclination are uniformly distributed around the vertical inclination with a variability of 2°. Using the specified parameters, the Mueller matrices were simulated.

TABLE 6.2: *Shape values for nanotube samples at optical scale and an example of forest at radar scale (Nezer pine forest [54]) H: height, r: radius, λ: wavelength, v.f: volume fraction, d: mean distance between elements*

	H/r	λ/r	$v.f$	d/λ
optical scale:				
$\lambda = 633nm$ Sparse CNT	60	6.3	$5 \cdot 10^{-3}$	5.04
$\lambda = 633nm$ Dense CNT	75	6.3	$75 \cdot 10^{-3}$	0.53
radar scale:				
$\lambda = 0.68m$, Nezer trunks	76	4.69	$6 \cdot 10^{-3}$	6.47
$\lambda = 0.24m$, Nezer trunks	76	1.65	$6 \cdot 10^{-3}$	18.3

Simulation

The simulation is done in a polarimetric basis $(\mathbf{h}, \mathbf{v})$, but to match the measurement convention, an azimuth rotation of the basis should be applied (equation 6.9) as for the measurement in Chapter 5.

$$\mathbf{M}_{x,y} = \mathbf{R}(-\varphi_r)\mathbf{M}_{h,v}.\mathbf{R}(\varphi_i) \tag{6.9}$$

with $\mathbf{R}$ the rotation matrix presented in equation 5.7. φ_r is defined in figure 4.11.

We are interested in the normalized Mueller matrix for the simulated CNT forest and for this reason, the color range for each parameter is $[-1 : 1]$. We first show in figure 6.12 the Mueller matrix image for the simulated sparse forest.

Firstly we can compare visually the simulated matrix with the measured one that are depicted in figures 5.5 and 5.6 and that are represented here again in front of the simulated ones in figure 6.12 and 6.13.

Before the complete analysis of chapter 7 some observations can be noticed:

1. There is a higher level of contrast in the simulated matrix elements which must be the effect of the under estimation of the depolarization. Indeed an isotropic depolarizer has the following Mueller matrix:

$$\mathbf{M} = \begin{pmatrix} 1 & 0 & 0 & 0 \\ 0 & p & 0 & 0 \\ 0 & 0 & p & 0 \\ 0 & 0 & 0 & p \end{pmatrix} \tag{6.10}$$

   with $0 < p < 1$ and $p = 0$ for the ideal depolarizer. Consequently, a depolarizing matrix presents the characteristic to have lower off diagonal elements than a non depolarizing Mueller matrix. In the case of the measured dense forest, the off diagonal elements are lower than in the case of the sparse forest (figure 6.13) but the general form of the matrix remains quite close to the sparse one. Moreover the lower is the p value the more the scene depolarizes. The diagonal element of the simulation seems to be higher than for the measurements, especially for high θ_r.

2. The intensity for the sparse forest – at the place of $\mathbf{M}_{1,1}$ – is well reproduced with the particular ring of high intensity. In contrary, for the dense forest the measurement exhibits more diffuse intensity while the simulation keeps the ring of high intensity.

3. The second main remark is if the depolarization and level contrast of the element is set aside, there is the very close distribution of each parameters for every

bistatic position. It make us confident about our simulation model for the bistatic configuration and its use in the case of the CNT. From these prime results, a more detailed analysis is well justified and will be developed in the next chapter.

Consequently, the dense forest behavior similarity between the measurement and the simulation is lower than in the sparse case. As the multiple interaction increase with the density of a media, it would be due to multiple interactions between the elements but further investigation, using decomposition parameter have to be done. This is the purpose of the next chapter. The simulated matrices will be analyzed thanks to a parametric analysis and an analysis using decomposition parameters. The hypothesis that have been made are in question after comparing the decomposition results with the measurement.

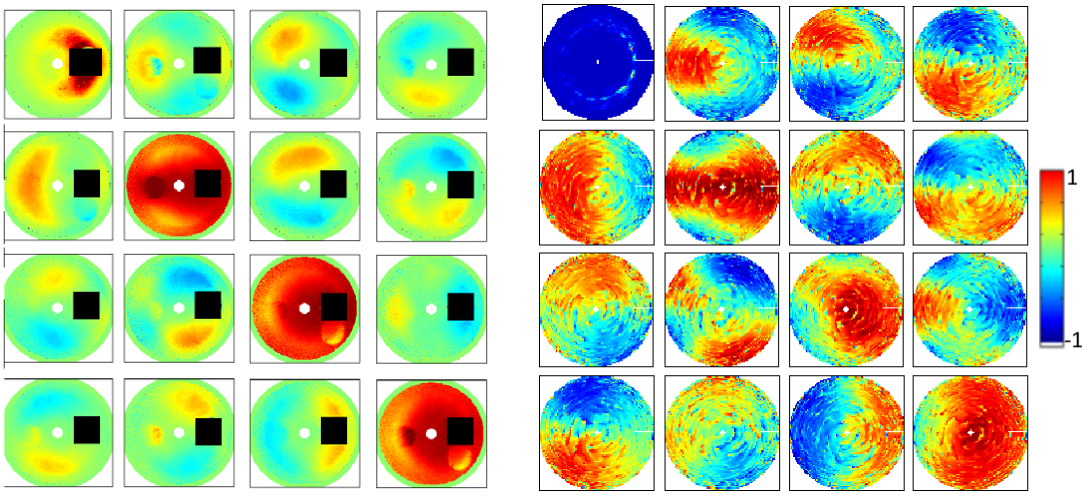

FIGURE 6.12: *(a) Sparse forest measurement, (b) Conoscopic normalized Mueller matrix for the simulated Carbon Nanotube Forest for sparse distribution.* $\mathbf{M}_{1,1} = 1$ *is replaced by the total intensity*

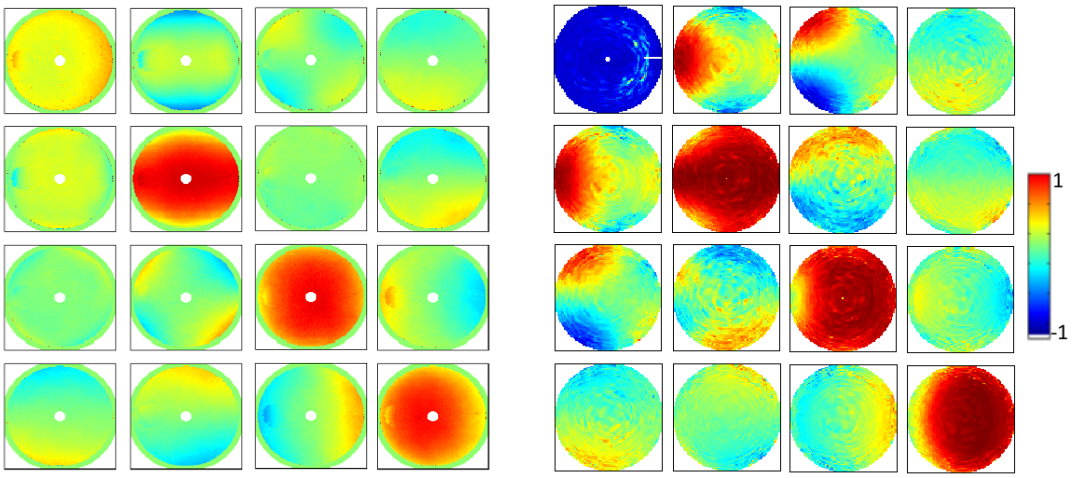

(a) (b)

FIGURE 6.13: *(a) Dense forest measurement, (b) Conoscopic normalized Mueller matrix for the simulated Carbon Nanotube Forest for dense distribution.* $\mathbf{M}_{1,1} = 1$ *is replaced by the total intensity.*

* * *

Summary
To control the relevance of the CNT polarimetric measurements we chose to compare the results with our simulation tool COBISMO that has been developed to model the radar measurement on forests. The use of the code necessitates adaptations and validation to the bistatic configuration. After validation with canonical target measurement. Thus we have simulated the case of the distributed CNTs. It led to close behavior that encourages us for a cross validation between the measurement on CNT samples and the simulation in bistatic configuration for forest scene.
The next step is to analyze the simulated Mueller matrices with firstly a parametric analysis to see what characteristics of the scene mostly influence the results, and with a decomposition analysis. From the polarimetric decomposition analysis a deep comparison is possible with the measurements. In case of badly reproduced parameters, solution for the simulation will be proposed.

Chapter 7

Analysis for the ARMP measurement using simulated data

We presented in the previous chapters the retained measurements and our approach in order to use the measurement on dense CNT trunk forest for comparing and understanding the limits of the simulated trunk forest at P-band. This must enable us to trust the simulation tool in order to further analyze radar bistatic configuration. Firstly, we try to understand the scattering interactions that occur in such forests and how they impact the polarimetric measurement. It consists in a parametric analysis beginning from the scattering regime for one cylinder and its interactions with the ground, to the effects of multiple interactions of densely positioned cylinders when observed via the Jones and the Stokes formalism. The evolution of the scattering matrix is studied depending on the incident and reception position parameter and also the cylinder radii and permittivities. Then, we study the impact of the characteristic of the scene and of the configuration on the radar and optical polarimetric decomposition parameters. In that way, the ability of COBISMO to reproduce the scattering event observed in the more or less dense forest is studied. It leads to an analysis of the well reproduced parameter with the simulation and we also underline the parameters that are more likely to give information about the structure of the forest. Then with the information of the limitations of our simulation we can study the origin of the depolarization in the measurement and we propose modifications of the simulation in order to reproduce it.

7.1 Parametric study of the simulated trunk forests

Following our scientific approach, the question here is what descriptive parameters are critical in order to reproduce the measurement with COBISMO. The input parameters

of the code are given by electronic microscope pictures for the case of the geometric parameters and by Drude-Lorentz model for the case of the cylinders. Consequently they are not certain. The main objective of this section is to study the sensitivity of the simulation and of the decomposition parameters to the inputs.

The forest is not a homogeneous medium. It presents a strong structure in which the relative size of the branches compared to the wavelength plays a very important role in the scattering process. Our simulation code COBISMO handle the radar wave propagation through the forest considering that trees are composed of skeletons of wood cylinders. What is more, the internal structure of the wood is considered as homogeneous with an equivalent permittivity ε_{wood}. Each species has his own structure that can be described by a very large cylinder for the trunk and several cylinders with given orientation distribution for the branches, as depicted in figure 7.1. Considering the length l_e of a branch and its radius r_e, the ratios between the wavelength and the size of the elements are various and conduct to different types of scattering regime. Depending on the season, rods, buds or leaves can surround the branches. The wavelengths that are considered in this work lie between 0.3 meter and 0.6 meter. At P-band, the contribution of isolated leaves is very small and for this present study the leaves are neglected, even if a high density of leaves would influence the attenuation process and the radar cross section of an entire tree. This effect is enhanced with a high water content which is of prime importance for the value of the permittivity of the elements [1]. To begin the parametric study, polarimetric response of isolated elements is realized.

FIGURE 7.1: *Typical structure of a tree for two different species*

7.1.1 Interpretation of the simple scattering mechanisms of the single dielectric cylinder

a) Scattering regimes

The Mie theory describes the plane wave interaction with spherical particles. It underlines an elastic scattering regime for which the forward scattering by the particle overcomes.

Trunks and branches form electrically large scatterers if we consider trees with heights around several meters and a wavelength around 0.7m such as

$$l_e >> r_e \tag{7.1}$$

where l_e corresponds to the length of the cylinder and r_e corresponds to the radius. The various regimes of the scattering depend on the following equations:

- Type 1. $l_e >> r_e, \quad l_e >> \lambda, \quad \lambda >> r_e$

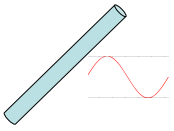

- Type 2. $l_e >> r_e, \quad l_e >> \lambda, \quad \lambda \approx r_e$

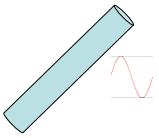

- Type 3. $l_e >> r_e, \quad \lambda > l_e, \quad \lambda >> r_e$

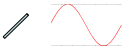

- Type 4. $l_e >> r_e, \quad r_e > \lambda,$

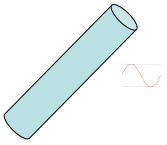

Considering the circular section of a cylinder, type 1 would correspond to Rayleigh scattering, type 2 would correspond to Mie scattering. Mie scattering regime denotes interaction with metallic sphere but here similar effect occurs in 2D, in the plane perpendicular to the one containing the wavevector of the incident wave and the cylinder axis, as shown in figure 7.2. Otherwise type 3 corresponds to small elements and type 4 corresponds to the physical optic interaction model. It is not considered here for the P-band study of tree elements where the wavelength is around $70cm$, but it can be encountered for the case of large targets. This present work focuses essentially on type 1.

b) Analysis of the scattering matrix of a single cylinder in free space at P-band radar

i) Case of normal incidence

In figure 7.2 the absolute values of the scattering from a vertical cylinder of type 1 for the four couples of coherent polarizations at perpendicular incidence, $\mathbf{k}_e$ perpendicular to the cylinder axis, is depicted. The scattered signal is calculated using COBISMO for every $\mathbf{k_r}$ perpendicular to the cylinder axis. The parameter of the cylinder are $\varepsilon_e = 12 - 3j$ for the permittivity, a length $l_b = 10m$, a radius $r_b = 0.1m$ and the considered wavelength is $\lambda = 1m$ and the cylinder axis is collinear to the vertical polarization V.

The cross polarizations responses hv and hh are null. One can see a distinction between the forward and the backward scattering. The vv forward signal is higher than the hh forward signal but it is no more the case in the backward direction. Around the reception angles $\theta_r = 90°$ and $\theta_r = 270°$ the values are lower. These remarks are important to understand the choice of the bistatic configuration because backscattering is favored in the monostatic configuration whereas forward scattering is accounted for a larger part to the bistatic scattering contributions.

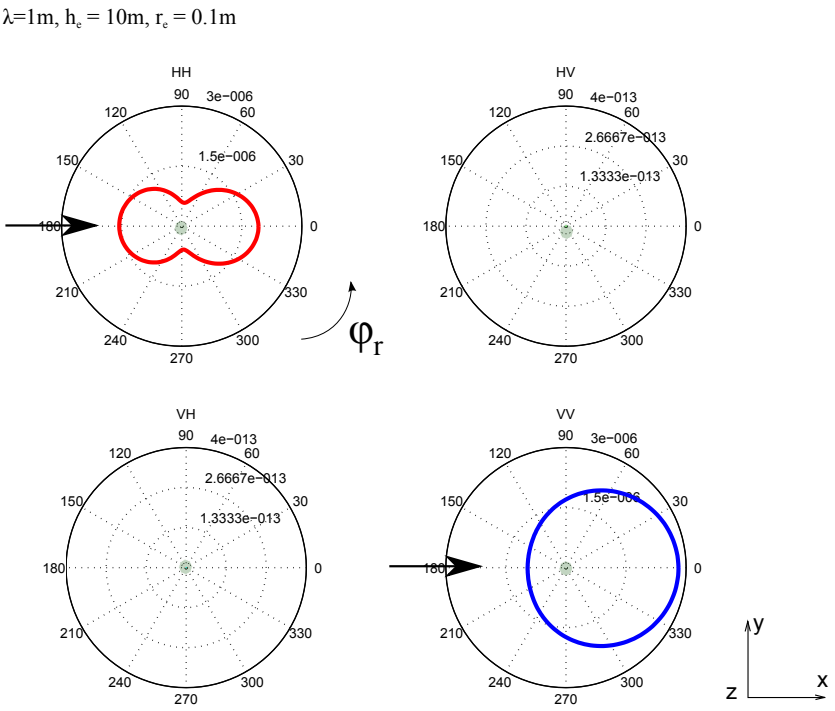

FIGURE 7.2: *Scattering coefficients varying with φ_r for the cylinder alone with incidence perpendicular to the cylinder axis. The direction of incidence is showed by the black arrow.*

ii) Oblique incidence

At oblique incidence the same behavior in the ratio between $|J_{vv}|$ and $|J_{hh}|$ can be observed. Figure 7.3 exhibits this ratio for every angular positions of reception without being restricted to the ring of maximum intensity defined by $\theta_r = \theta_e$. The co polarization channel $|J_{vv}|$ is six time larger in the forward directions ($\theta_r = [0°, 180°], \varphi_r = 180°$) than the $|J_{hh}|$ channel. It decreases in the backward hemisphere, and $|J_{hh}| > |J_{vv}|$ for reception position near the vertical ($\theta_s \to 0°$), see figure 7.3.

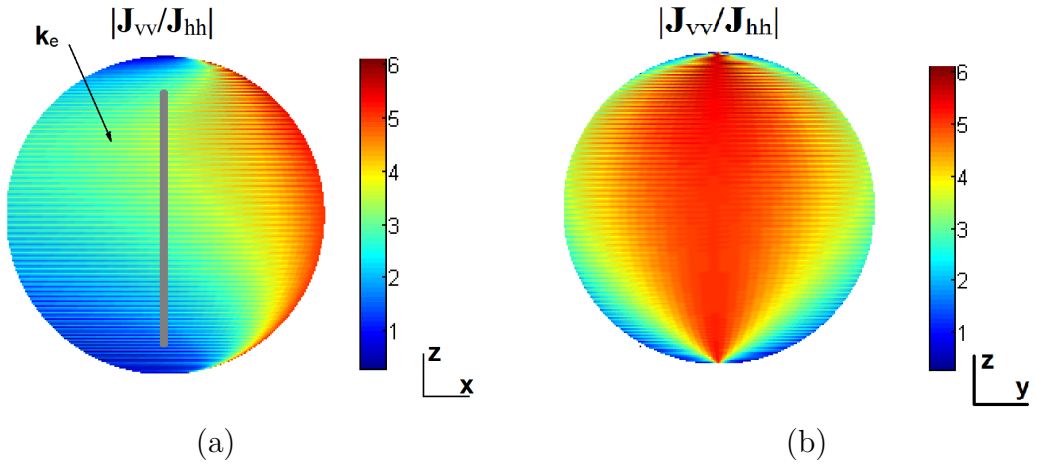

(a) (b)

FIGURE 7.3: *Amplitude ratio $|J_{vv}/J_{hh}|$ of the cylinder on a reception sphere at oblique incidence. $\theta_e, \varphi_e = 35°, 0°$, $\theta_r = [0° : 180°], \varphi_r = [0° : 360°]$. (a) Side view, (b) forward view.*

iii) Polarimetric signature of the dielectric cylinder at oblique incidence

At the oblique incidence ($\theta_e < 90°$) the cross polarization are non zero, and here the scattering signature is used to study the relative amplitude of the different polarization channels at the forward position for reception: $\theta_s = \pi - \theta_e, \varphi_s = \varphi_e + \pi$.

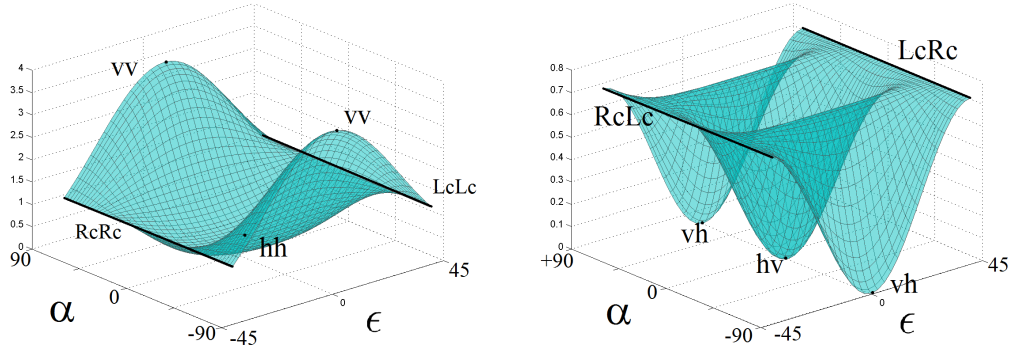

(a) (b)

FIGURE 7.4: *Forward polarimetric signature vertical dielectric cylinder illuminated at oblique incidence ($\theta_e = 60°$). (a) co polarizations, (b) cross polarizations.*

The polarimetric signature is a way to explore the polarimetric property of a material. It enables to consider the linear polarization but also some or other elliptical polarization state from linear to circular and any orientation. The parameters that describe these properties of the wave are receptively ϵ and α. The polarimetric signature is distinguished between the co polarization response of the target and the cross polarizations. As a reminder the cross polarization of any elliptical polarization state defined by ϵ, α has as parameters $-\epsilon$ and $\alpha + \pi/2$, see chapter 2.

On figure 7.4 (a), one can observe that vv corresponds to much more intensity that hh at the forward position and that the circular polarization is higher than hh. For the case of cross polarization, figure 7.4 (b) exhibits an higher level for circular polarizations ($\epsilon = \pm\pi/4$) and for orientation $\alpha = (45°, 135°)$. It means that commonly used horizontal and vertical polarization are not always the better states to observe this type of canonical object.

The described effects depend on incidence and reception position and the permittivity plays an important role in these variation. But before going further, we introduce the ground interaction that is always present on our measurements.

The influence of the permittivity on the scattering variations with the incidence is partially explained by the Brewster effect. This effect occurs also during the interactions with the ground.

c) Ground interactions

The interactions with the ground contribute to the second order interactions. They are represented in figure 7.5. Taking into account these interactions the result depends in the same time on the Fresnel interactions with the ground and on the scattering with the trunk or branch cylinders. Consequently the precedent effects follow each other. Figure 7.5 (b) represents the ring of maximum intensity caused by the cylinder scattering. For the case of a vertical cylinder, the ring occurs at $\theta_r = \theta_e$ in a plane parallel to the ground.

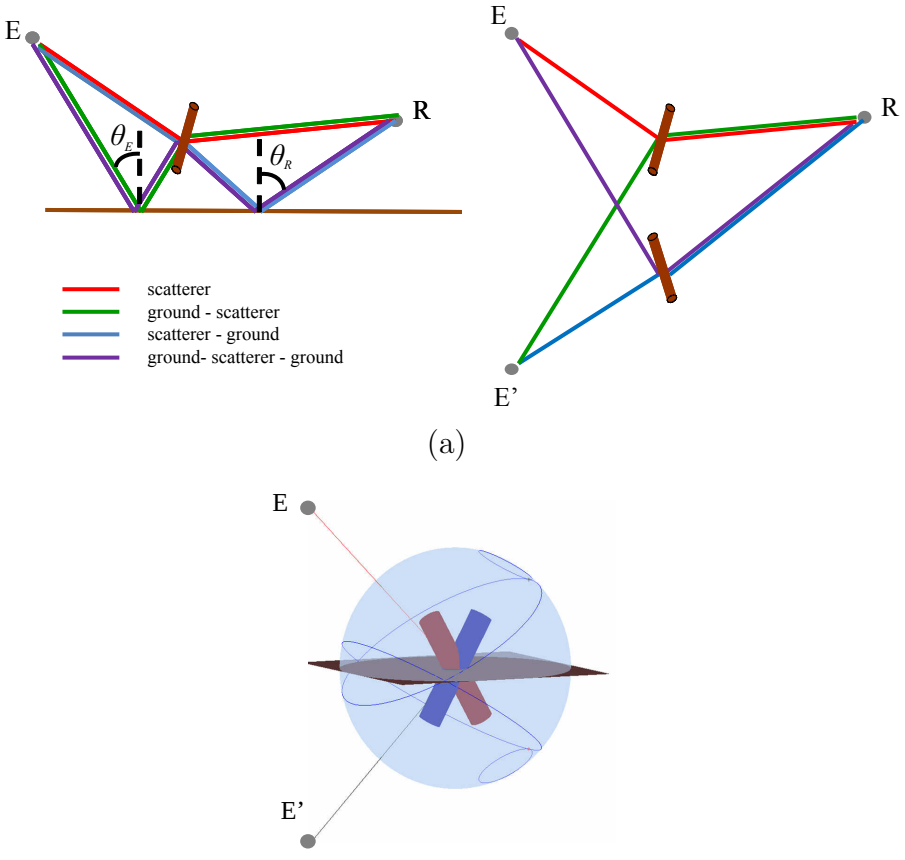

FIGURE 7.5: *Representation of cylinder interactions with the ground. (a) double bounces and mirror principle. (b) line of maximum intensity.*

i) Brewster effect

The Brewster angle is linked with the refraction phenomenon. It is defined in the framework of a study about the reflection and transmission of a polarized field on a surface and was firstly observed by Etienne-Louis Malus [74]. Above a certain angle of incidence θ_B the vertical component of the polarization is not reflected and only refracted. It occurs when the transmission direction is perpendicular to the reflection direction, as depicted in figure 7.6.

This Brewster angle θ_B depends on the refractive indexes of the two media at the considered wavelength, and can be retrieved from the Malus laws [75]. For example in the case of optical wavelength at the air-water interface, this angle is approximately 53°.

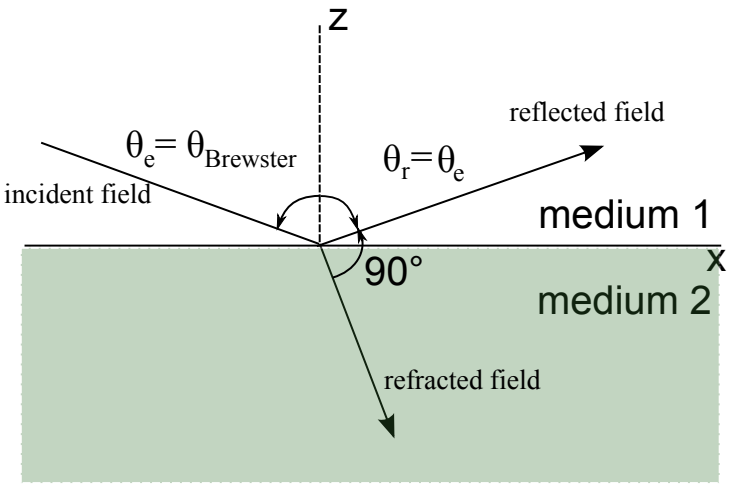

FIGURE 7.6: *Definition of the Brewster angle between two media. At the Brewster angle the vertical polarization is not reflected.*

Although is not precisely the Brewster effect, for the case of the scattering by the forest element, a similar effect can be observed that occurs on the cylinders, as represented in figure 7.7. In this case, for an incidence angle just below 20°, the vertical polarization drops.

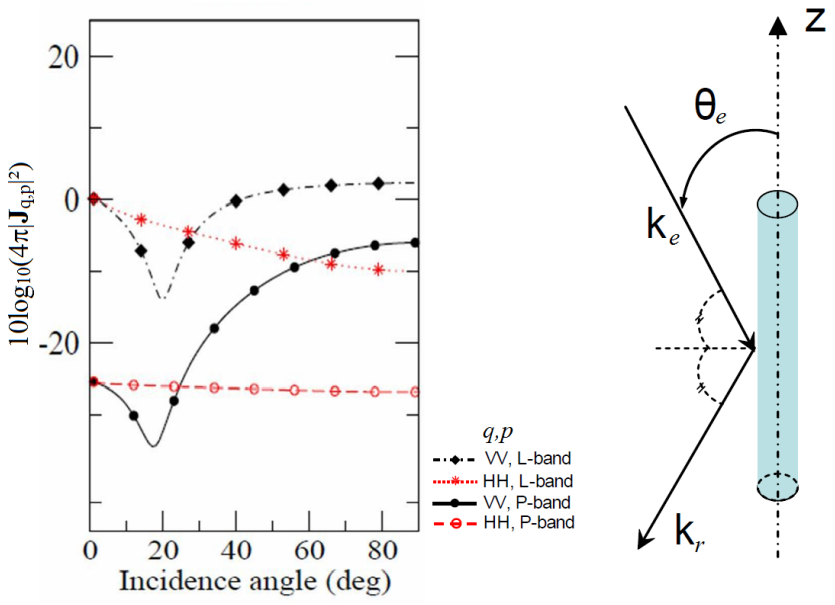

FIGURE 7.7: *Variation of the intensity with the incidence angle* $\theta_r = \pi - \theta_e$ *for vv and hh polarizations. Extracted from [1]. P-band:* $\lambda = 0.68m$*, L-band:* $\lambda = 0.23m$*,* $r_e = 0.015m$*,* $h_e = 1.5m$*,* $\varepsilon_e = 15 - 7j$

ii) Specular variations

Here we look at the the variation in the co-polarization responses when $\theta_r = \theta_e$ and $\varphi_r = \varphi_e + \pi$, with θ_e varies from 0° to 90° at P-band: $\lambda = 0.68m$. Figure 7.8 shows the corresponding response with a vertical cylinder and a dielectric ground. The vertical cylinder height is $h_e = 10m$, the radius is $r_e = 0.015m$ and its permittivity is $\varepsilon_e = 12 - 3j$. In contrary to the precedent example, the ground is dielectric with a permittivity equal to the permittivity of the cylinder. $\varepsilon_{ground} = \varepsilon_e$. The hh polarization is relatively constant with the variation of $\theta_{e,r}$. The vv polarization, which is parallel to the cylinder axis, dominates the hh polarization channel for $\theta_{e,r} \in [35° : 75°]$. The effect increases as the incidence angle θ_e grows. The decreasing of vv is explained by the Brewster effect on the cylinder for θ_e around 20° and by the Brewster effect on the ground for θ_r around 75°. Consequently for low and high incidence angle the effect can have an impact on the results.

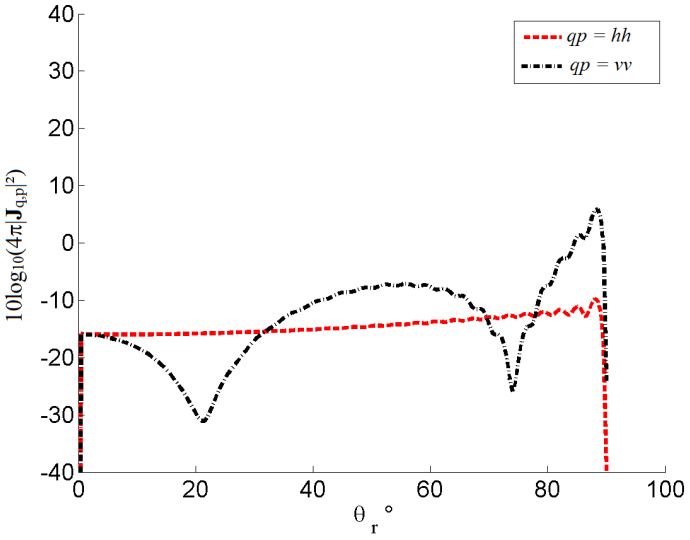

FIGURE 7.8: *Specular variation of the scattering coefficients of the vertical cylinder on the ground.* $\theta_r = \theta_e$, $\varphi_r = \varphi_e + 180°$. *P-band:* $\lambda = 0.68m$.

This specular variation showed that the diattenuation of the co-polarization rises as θ_e increases, however if θ_e is constant it is interesting to study the evolution of the scattering matrix on the bistatic ring that is defined by $\theta_r = \theta_e$ and $\varphi_r \in [0°, 180°]$.

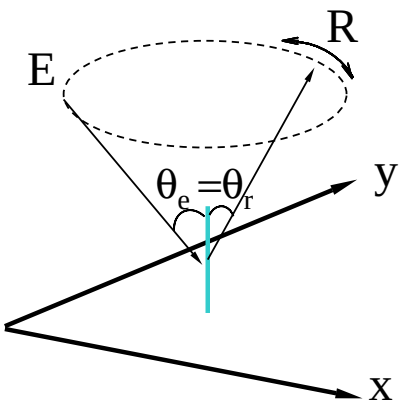

FIGURE 7.9: *Configuration for the azimuth ring study*

d) Azimuth variation with constant incidence

Here we want to keep the same configuration that was used for the bistatic chamber measurement campaign on dielectric cylinders [64], which has been used as first validation data for COBISMO, figure 7.9 represents the studied configuration. For theses simulations, only one cylinder above ground is considered of radius $r_e = 0.15m$, height $h_e = 10m$ and the wavelength is $\lambda = 1m$, that corresponds to P-band.

The measurement of the single cylinder is reproduced in figure 7.10 (a). In (b) and (c) respectively the ground permittivity and the incidence angles are changed from the configuration (a). In figure 7.10 (b) the ground is moved from the perfectly reflecting metallic case, to the dielectric case with a permittivity $\varepsilon_{ground} = 12 - 3j$. It has a dramatic influence on the level of the vv intensity which is reduced of about 20dB for the entire domain of reception position. The other polarization couples are less reduced and consequently the relative intensities of the polarization couples are totally different that for the case of the metallic ground. In figure 7.10 (c) the metallic ground is retrieved as in (a) but the incidence angle θ_e is modified from $\theta_e = 70°$ to $\theta_e = 35°$. It results in an high increasing of the cross polarization relatively to the co polarization channels hh and vv. One can also notice the higher relative value of the vv polarization to the hh polarization in the specular direction ($\varphi_r = 180°$).

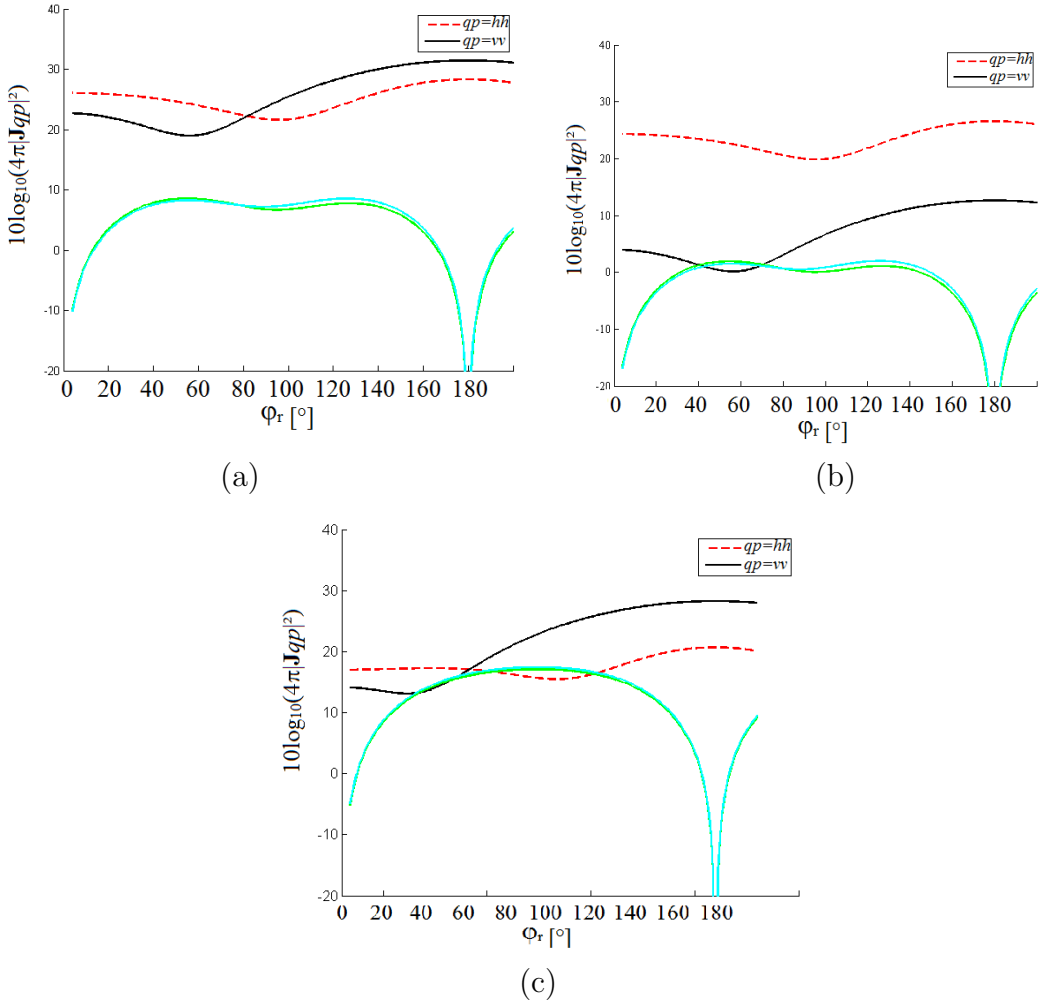

FIGURE 7.10: *Scattering coefficients of a single dielectric cylinder taking into account the ground interactions. (a) $\theta_e = 70°$ and metallic ground, (b) $\theta_e = 70°$ and $\varepsilon_e = \varepsilon_{ground}$, (c) $\theta_e = 35°$ and metallic ground.*
Legend: black line: *vv* polarization, dashed red: *hh* polarization, cyan line: *hv* polarization, green line: *vh* polarization.

i) Dependence with the cylinder permittivity

The impact of the cylinder permittivity in now studied. For this study we retrain us on the imaginary part variation which is related to the conductivity of the material, see chapter 4. Three values are investigated in figures 7.11 and 7.12 which correspond to the intensity the the four couples of polarization and the polarimetric decomposition parameters.

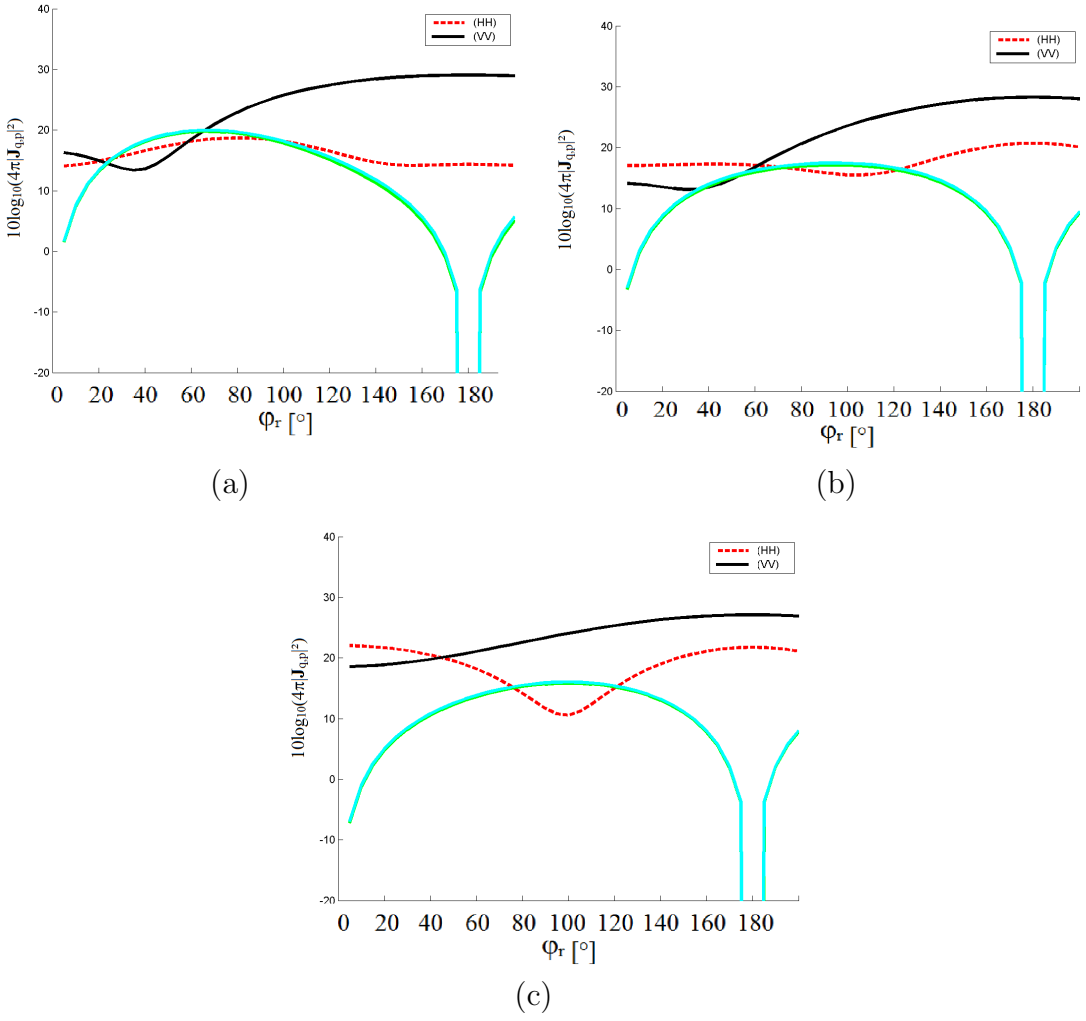

FIGURE 7.11: *Study of the influence of ε_e on the scattering coefficients of the single cylinder varying with φ_r. (a) $\varepsilon_e = 12 - 0.3j$, (b) $\varepsilon_e = 12 - 3j$, (c) $\varepsilon_e = 12 - 30j$.* Legend: black line: *vv* polarization, dashed red *hh* polarization, cyan line *hv* polarization, green line *vh* polarization.

One of the main behavior in figure 7.11 is the change in the variation in the horizontal co-polarization depending on φ_r. This polarization channel decreases around a bistatic angle β of 90° ($\varphi_r = 90°$) as the conductivity of the cylinder increases.

The decomposition principle on the Mueller matrix calculated from the Jones matrix of this deterministic target is applied, and emphasis is placed on the retardance vector $\mathbf{R}$ and diattenuation $\mathbf{D}$. As for the study of the measurement in chapter 5, $\mathbf{R}$ and $\mathbf{D}$ are decomposed into R, $\alpha(R)$ and $\varepsilon(R)$,and D, $\alpha(D)$ and $\varepsilon(D)$. Here the case (a) of figure 7.11 corresponds to the red line in figure 7.12, the case (b) of figure 7.11 is the dashed blue line and the case (c) of figure 7.11 is the doted gray line.

- The relative positions of the curves in figure 7.11 can be retrieved in the parameter D but it contains also the relative intensity of the circular polarization. This one is high when D and $\varepsilon(D)$ are high. Here it seems that the circular co and cross polarizations are equally reflected because $\varepsilon(D)$ remains zero.

- The retardance parameter is related to the induced phase shifts of the polarizations. Here it decreases from the monostatic to the specular when it covers the ring of $\theta_r = \theta_e$. The retardance is higher for the circular polarization in the reception position of high bistatic angle, $\varepsilon(R) \simeq 40°$. It is characteristic of the measurement. In the monostatic it is the vertical polarization that is more shifted whereas in the specular position, the horizontal polarization is more shifted (see $\alpha(\mathbf{R})$).

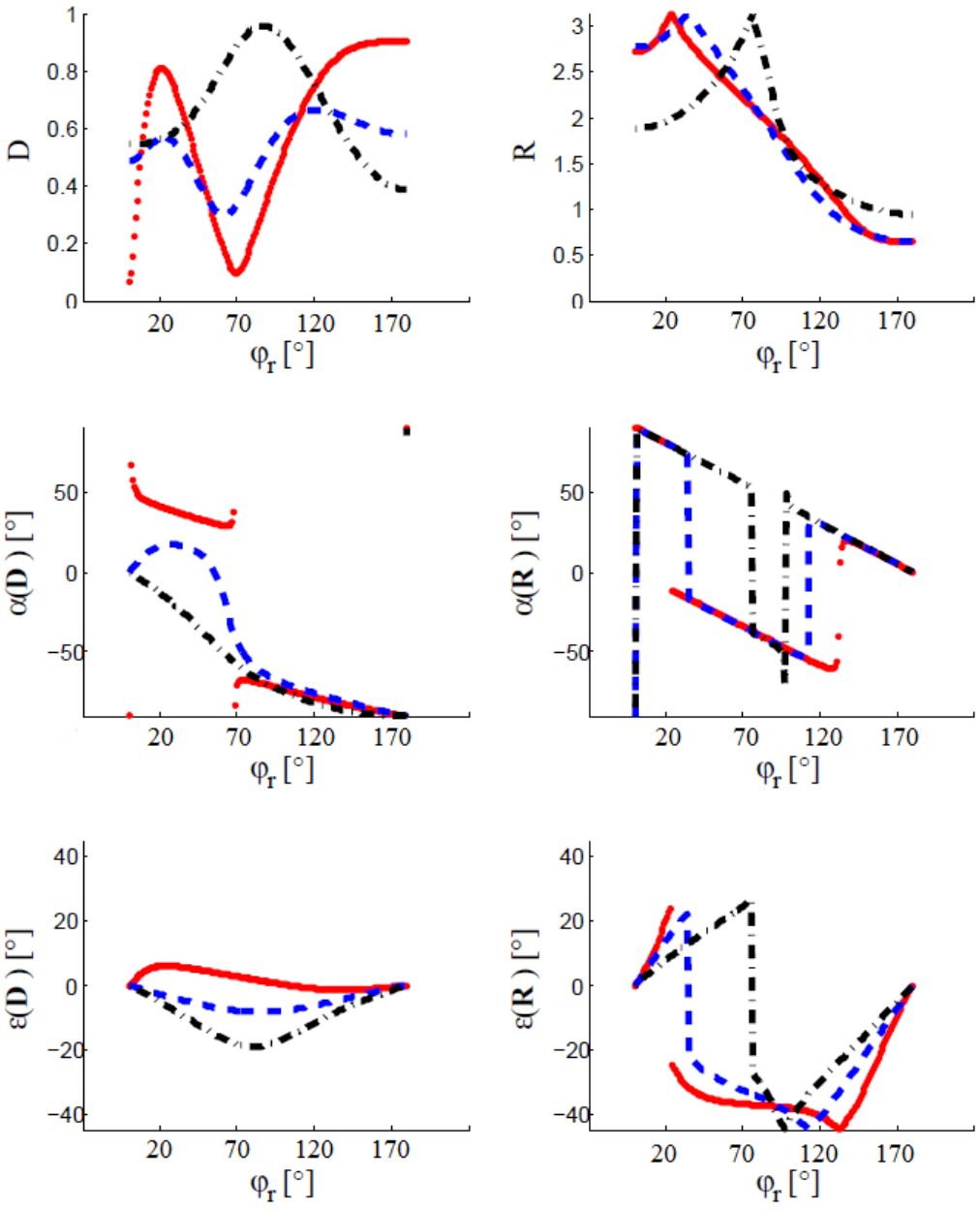

FIGURE 7.12: *Study of the influence of* ε_e *on decomposition parameters* **R** *and* **D** *varying with* φ_r Legend: red $\varepsilon_e = 12 - 0.3j$, in dashed blue $\varepsilon_e = 12 - 3j$, in doted black $\varepsilon_e = 12 - 30j$.

ii) Dependence with the cylinder radius

The parametric analysis of the influence of the cylinder radius is investigated using figures 7.13 and 7.14.

- As for the case of the permittivity, the cylinder radius value can change mostly the horizontal co-polarization.
- For φ_r around 60° the differences depending on the cylinder radius is higher for parameters D and R.
- It can be remark that when the hh polarization channel falls down, the retardance ellipticity is close to zero. On the contrary, when the four polarization channel are high, the retardance ellipticity is high. The retardance parameter issued from the Mueller matrix is useful to summarize it. It inform us on the way that the incident polarization is changed. Namely, how the orientation and ellipticity of the incidence are changed. In our study it exhibits discontinuities or sign inversion when the bistatic angle varies and because of its nature, it is sensitive to the polarization basis. Consequently, the sign inversions in its ellipticity and orientation are not necessary related to to physical change but it would be mostly related to the relative values in the used polarization basis.

As a conclusion, this parametric comparison informs us on the fact that the results are very sensitive to the geometrical and dielectric parameters of the scene. Consequently for the simulation, if the tendencies are well reproduced it would means that the parameters are set correctly.

In the next paragraph we study the case of CNT forest simulation. A sensitivity study for the density is realized. The non deterministic effect simulation in the Mueller formalism is also investigated.

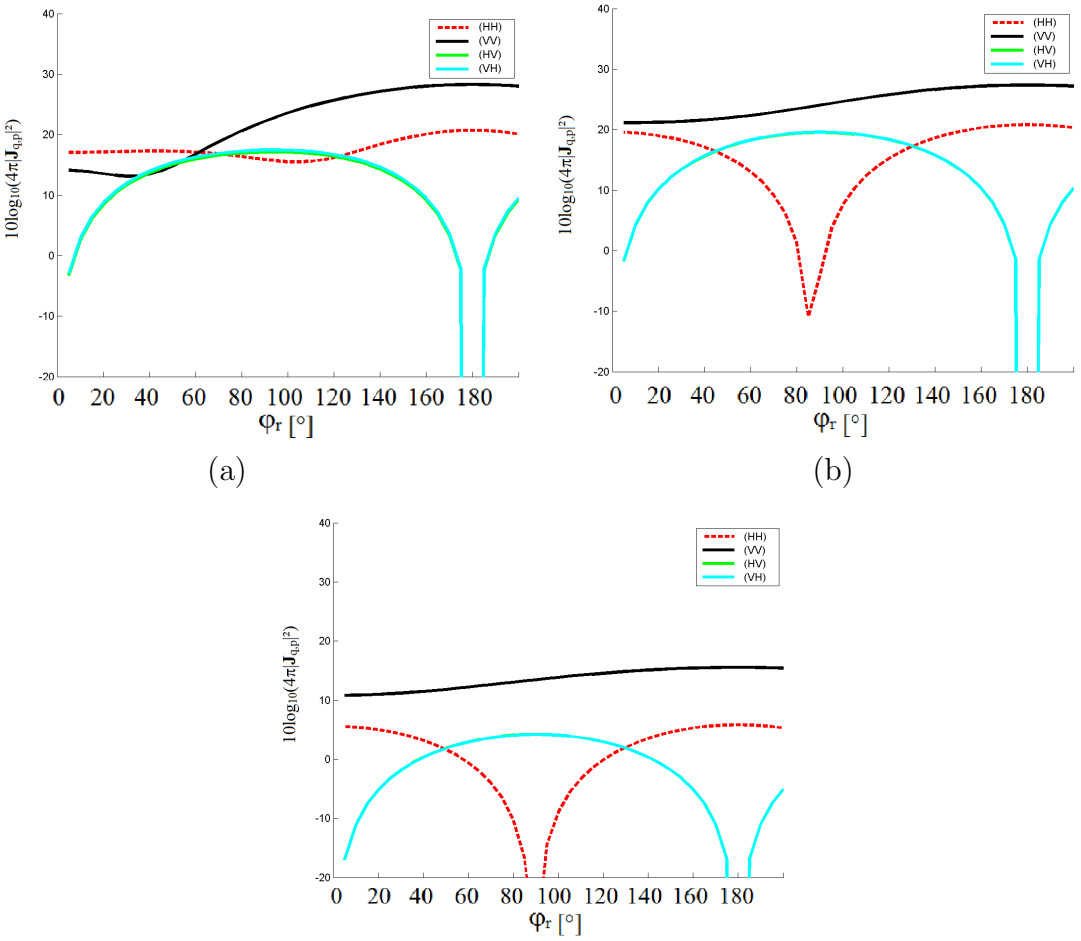

FIGURE 7.13: *Study of the influence of ε_e on the absolute values of the scattering matrix varying with φ_r. (a) $r_e = 0.15m$, (b) $r_e = 0.15/2m$, (c) $r_e = 0.15/4m$.* Legend: black line: *vv* polarization, dashed red *hh* polarization, cyan line *hv* polarization, green line *vh* polarization.

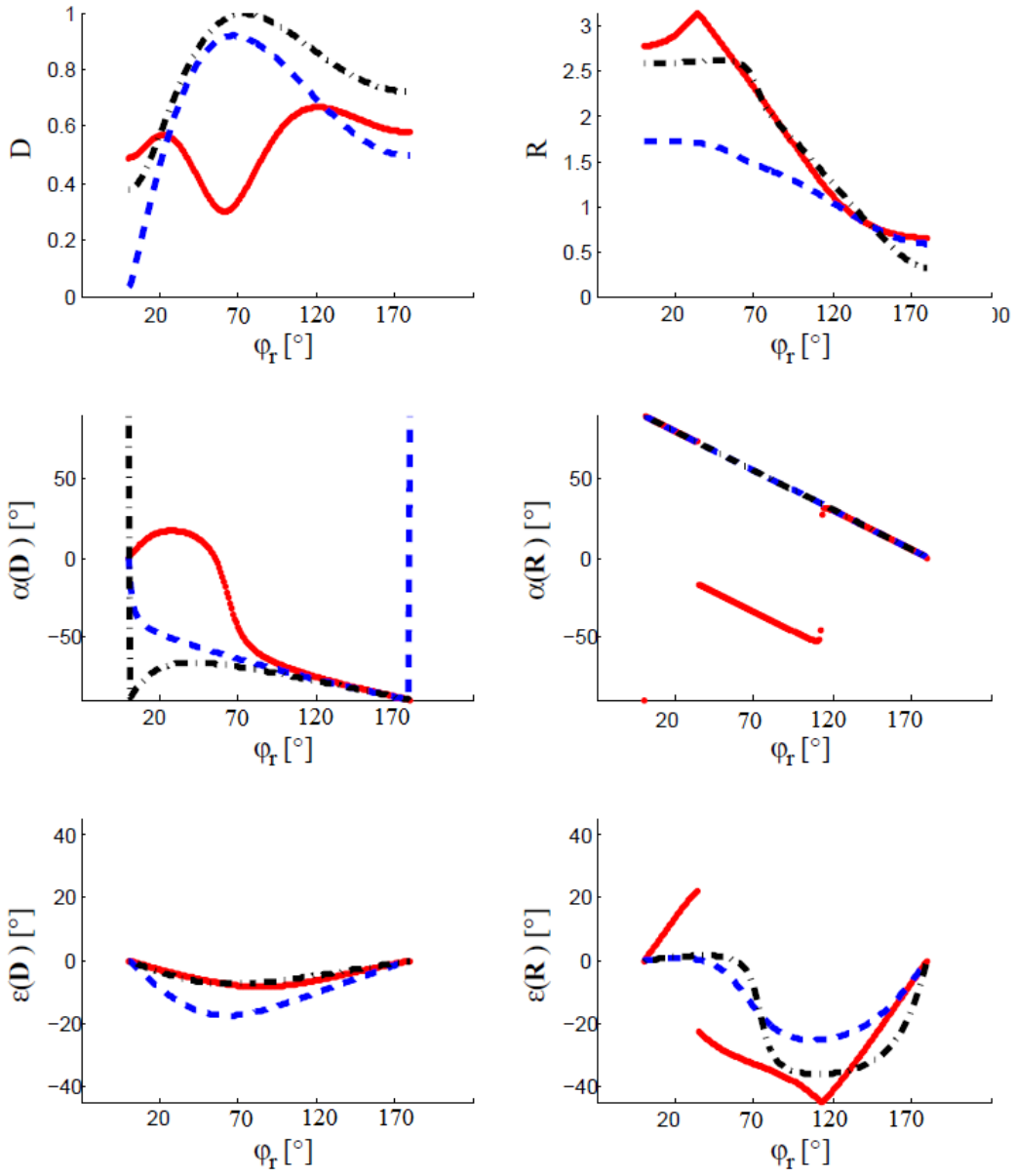

FIGURE 7.14: *Study of the influence of the radius on decomposition parameters* **R** *and* **D** *varying with* φ_r
Legend: red $r_e = 0.15m$, in dashed blue $r_e = 0.15/2m$, in doted black $r_e = 0.15/4m$

7.1.2 Complex mechanisms of interaction

In contrary to the previous study on simple scattering of the single dielectric cylinder at P band radar, now only optical scale simulation at 633nm of groups of CNT are considered. Consequently comparisons with the ARMP measurements are possible.

In addition to the single, double and triple bounces with the trunks, multiple interactions occur between the tree elements. Past effort had been conducted, as in [76] where the expression of the double interaction between branches is studied. This kind of model for the second order is time consuming and no clear proof enables to conclude that the second order interactions are sufficient to model all the multiple interaction impacts. In any case the contribution of the multiple interactions in the final signal has been proven in monostatic study as in [54].

The entropy parameter of Cloude Pottier H has been studied, for example in [12], and H it is correlated with the density of the forest environment. However the analytic formulation of the relation between the depolarization, or entropy is not formulated in the case of the forest. Consequently it is important to examine the relation of the forest density and the depolarization level and to work on the formulation on the link between multiple scattering, attenuation and depolarization.

In [77] the transport properties of multiples scattered light is studied. Here the context in which such scattering occurs is called "optically" dense medium which means that the medium is dense comparatively to the optical wavelength $(400nm - 900nm)$ and the particles that compose the medium are in the near field from each other. The multiple interaction leads to weak localization effects [67]. This effect is linked to the fact that in the case of monostatic the coherence is higher in the backward direction because of the reciprocal wave paths (fig. 7.15). These works highlight the relation between the coherence of the wave and the multiple scattering. For the study of multiple interactions in the forest, one can consider the environment as a random media characterized by its volume fraction.

In the state of the are the behavior of light in such media is performed through the radiative transfer method which enables to predict the scattered light by a dense media. The method is presented for example in [78]. It can also be expressed by the equivalent bistatic scattering matrix with the S-matrix approach [79]. Our code COBISMO uses the Foldy-Lax approximation for this purpose. In addition, Monte Carlo methods [80], [81] enables to consider the depolarization effect because it introduces a variability of realizations.

Measurements and studies in the context of hydro meteor particles show the Muller matrix behavior in bistatic configuration and we raise the works in [82] where hemispherical Mueller matrix of different particles shape dense media are presented and the study is realized on the symmetry relations in the Mueller matrix, with no reflecting

sub-surface boundary contrary to our case because of the ground. It is interesting for us because these symmetries are also observed in our case when the Mueller matrix is observed in the $(\mathbf{h}, \mathbf{v})$ polarization basis.

Finally, these methods are well suited for random distribution, but it is limited for our case. Indeed these cited works do not study the case of the radio wave in the forest, and even if the forest environment exhibits similarities with random dense environment, the structure of the trees, i.e. the large trunk and the relative position of the large branches and corresponding coherent effects have to be kept in mind.

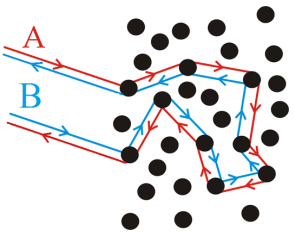

FIGURE 7.15: *Illustration of the coherent backscattering. The two paths interfere coherently.*

Otherwise, a time efficient method to model the attenuation caused by multiple scattering, also called the forward path-loss, is the Foldy's approximation [83], [84] which was presented in section 6.4.2.1. Here we want to study the polarimetric response of a group of vertical cylinders taking into account the effect of the attenuation in the simulation. Here we do not consider the previous parameter for the single cylinder that was measured in anechoic chamber for validation purposes, but we directly move to the case of the CNT simulation, see chapter 6 in order to initiate a comparison with the ARMP measurements.

a) Comparison on the Jones matrices for the bistatic variation with φ_r for two CNT densities

The simulated scene is composed of vertical distribution of cylinders with a variability of 10° in their inclinations. The lengths of the cylinders are around $10\mu m$ with a variability of $5\mu m$ and the radii are $r_e = 0.1\mu m$. The figure 7.16 shows the two density of simulated forests with volume fractions $v.f = 1.5.10^{-3}$ for the sparse forest and $v.f = 75.10^{-3}$ for the dense forest. The cylinder are positioned into a square surface with a side length of $20\mu m$. In order to compute the attenuation matrices, a squared resolution cell is used of $2\mu m$ side length in the x and y direction and a $5\mu m$ side length in the z direction. The wavelength is 633nm.

One can see on figure 7.17 (a) and (b) that the attenuation matrices modeling multiple bounces reduces the signal by an amount of about 5dB for the sparse forest.

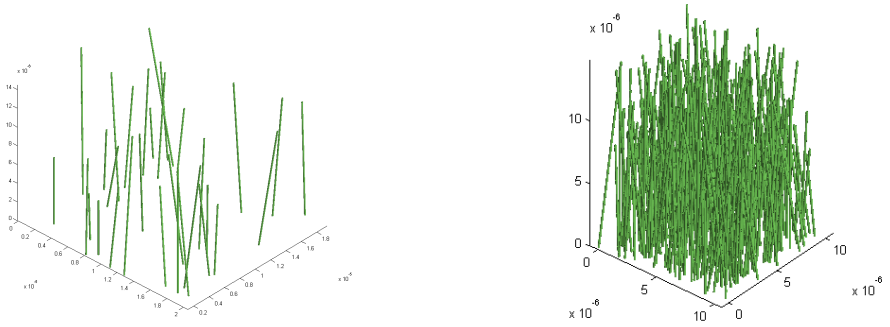

FIGURE 7.16: *Realization of the simulated distribution with (a) sparse distribution,* $v.f_1 = 1.5.10^{-3}$*, and (b) dense distribution (*$v.f_2 = 75.10^{-3}$*). At radar scale* $v.f$ *is around* 6.10^{-3} *for the trunks and* 20.10^{-3} *for the branches.*

For the dense forest, see figure 7.18, the reduction level is about 15dB to 25dB and the backscattering and forward directions are more impacted than the others. On the figures 7.17 and 7.18 (c) (d) (e), one can see how the bounce mechanisms are affected. As expected, the double bounce mechanisms are higher because of the vertical orientation of the cylinders. On can notice that the cross polarization are more distinct from each other for the single and triple mechanisms.

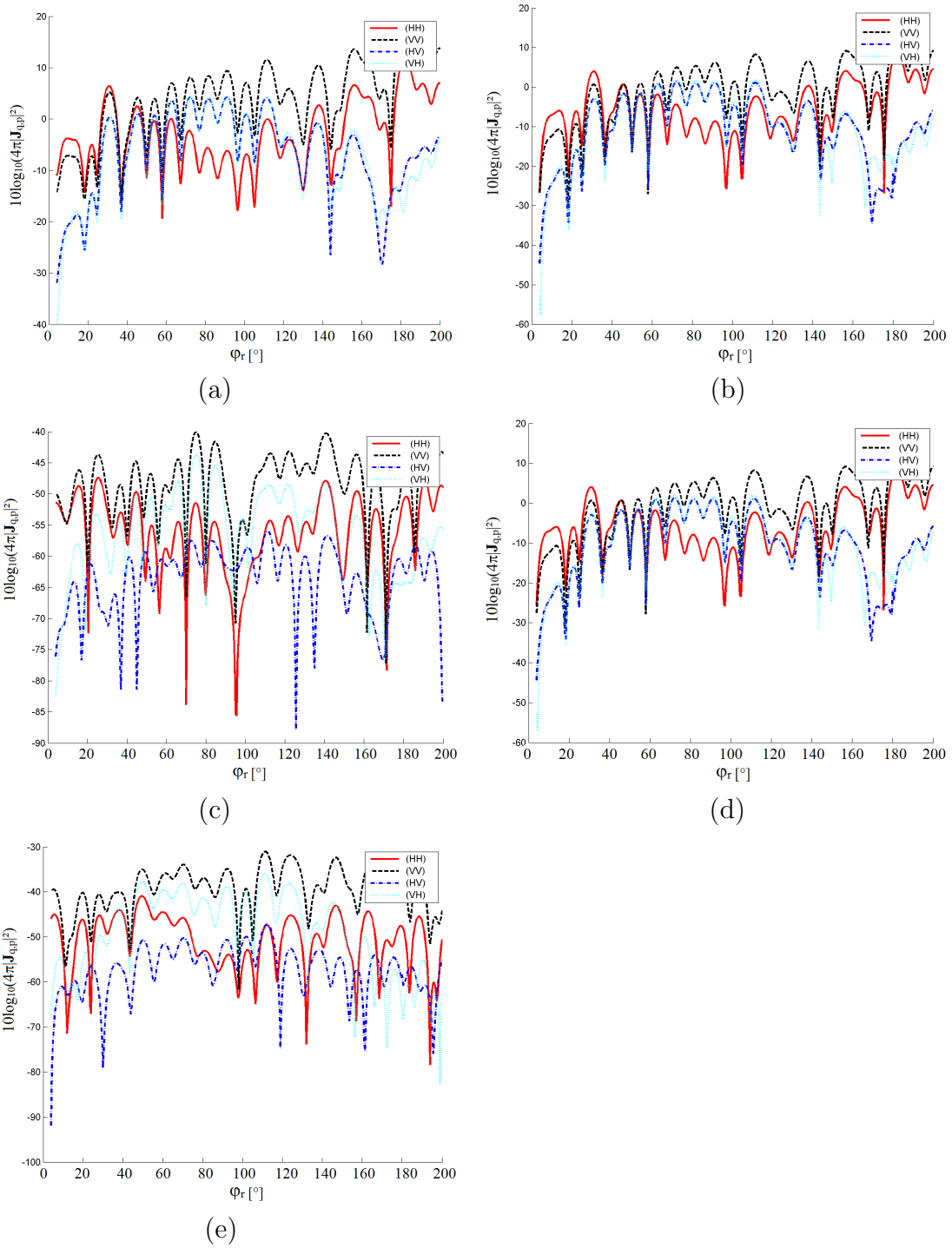

FIGURE 7.17: *Scattering coefficients for the group of trunks above ground. (a) without taking the attenuation into account (b) taking into account the attenuation, (c) only the single bounce (d) only the double bounces, (e) only the triple bounces.*

As a conclusion, one can see that the double bounce mechanism dominates for these configuration. The attenuation also plays an important role for the case of the dense forest where the cross-polarization are more distinguished and the relative value of hv is enhanced. We now study the simulation of the non deterministic effect with Mueller matrix and the incoherent averaging process.

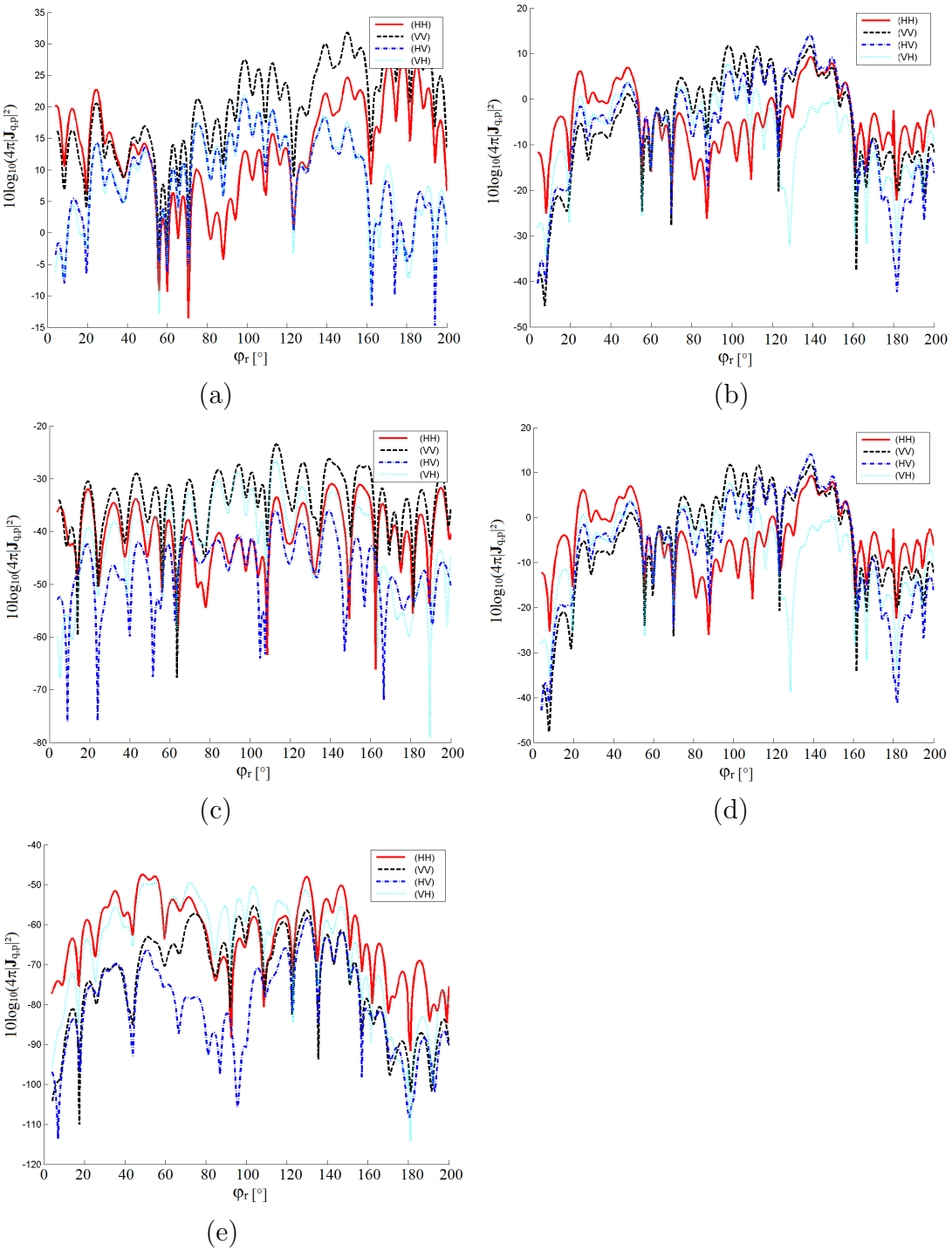

FIGURE 7.18: *Scattering coefficients for the group of trunks above ground. (a) without taking the attenuation into account (b) taking into account the attenuation, (c) only the single bounce, (d) only the double bounces, (e) only the triple bounces.*

b) Comparison of the methods to obtain the Mueller matrices for two CNT densities

Then the simulation of the Mueller matrix to reproduce the non deterministic effects is now in question. We want to compare three choices for the averaging process:

1. Incidence angle averaging
2. Position averaging
3. Interaction mechanisms

During the ARMP measurements we have seen that several incidence angles lead to an incoherent intensity summation at the reception. This incoherent averaging process seems to be the more evident among the possible incoherent averaging. Nevertheless, among other possibilities we try to test the position averaging which could be explained by a spatial incoherence of the scattering field due to multiple interaction. We have tested also the possibility that different mechanisms of interaction would constitute independent mode, analogously to the different modes that can be exhibited in the light propagation in optical fiber [85]. Here there is no variability in the frequency, but in radar the frequency averaging is a possibility to take into account averaging process.

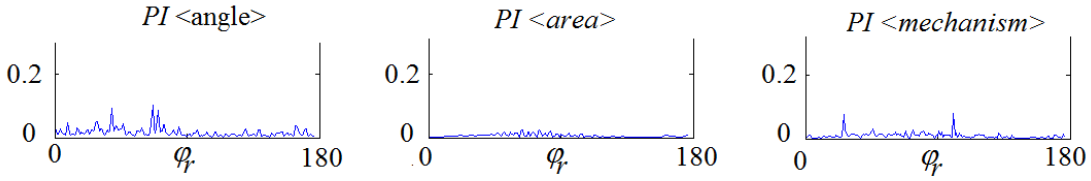

FIGURE 7.19: *Comparison of the depolarization index PI for three averaging methods.* $\theta_r = \theta_e = 40°$, $\varphi_r = 0°, 180°$, $\varphi_e = 0°$.

In figure 7.19 the simulated depolarization PI is plotted for the three types of averaging process. In the three cases the depolarization is low for the variation of φ_r in the ring defined by $\theta_r = \theta_e$, it do not exceed 1%. Nevertheless it seems to be higher for the case of the averaging on incidence angles. It can be explained by the fact that for the vertical distribution of the cylinder there no much variability between the observed areas, whereas the variability of incidence angles induces more variability in the response. When the interaction mechanisms are incoherently averaged the depolarization is also weak, the argument of low variability in cylinder inclination can explain it as for the case of area averaging

In figure 7.20 the incidence averaging is retained because it seem closer to the measurements. The Lu and Chipman diattenuation and retardance of the simulated dense

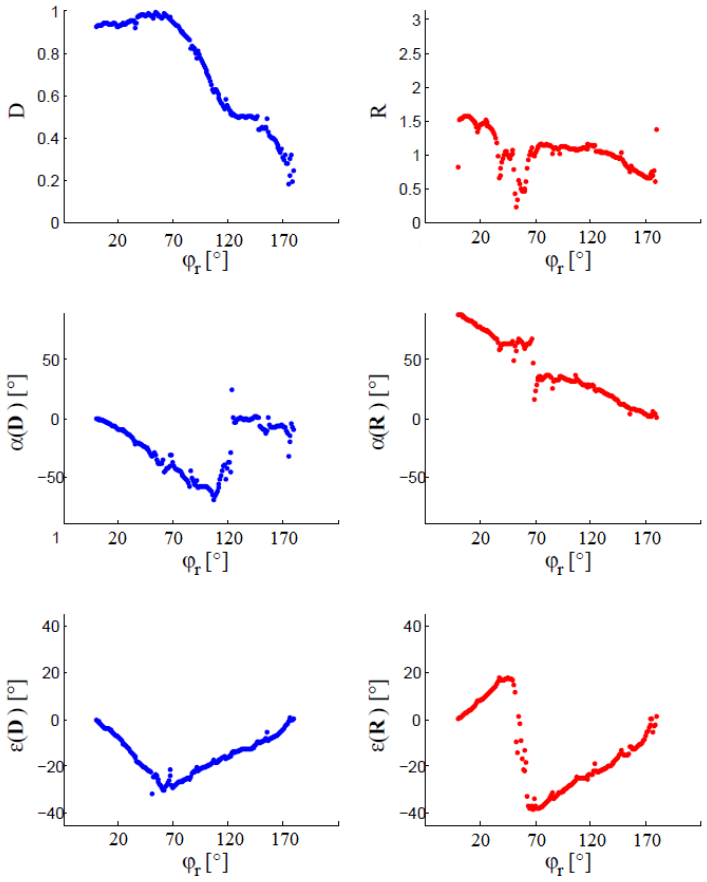

FIGURE 7.20: *Bistatic decomposition of Lu and Chipman for the simulated group of CNT with sparse distribution (v.f* $= 1.5.10^{-3}$*) applying the incidence angle averaging process.* $\theta_r = \theta_e = 40°$, $\varphi_r = [0°, 180°]$

forest of CNT are plotted. As a remainder, the wavelength is $\lambda = 633nm$ the relative size of the radius is $\lambda / r_{CNT} = 6.3$ and the complex relative permittivity is $\varepsilon_{CNT} = 4.9 - 9.5j$. Even if it is not the exactly the same relative sizes and permittivity as for the vertical cylinder at P-band radar similarities can be retrieved with the case $\varepsilon_e = 12 - 30j$ in figure 7.12 and with the case $r_e = 0.075m$ in figure 7.14.

c) Study of the evolution of the simulated Mueller matrix according to the density

The measurements lead to a strong increasing of the depolarization level with the density. Figure 7.21 shows that this effect is not well reproduced, the measurements are depicted in chapter 5. Moreover the other decompositions parameters remain relatively constant whatever the density. One can see that the normalized intensity increased with the forest density, and that there is a variability in the parameters because the realization of the forest is different at each step. Here the averaging process is executed via incidence angles. We will try to explain this limitation in the next section but one can already note that the realized trunks forests are composed of nearly vertical cylinders. Consequently the variability is low in the simulated scattering matrices for each element.

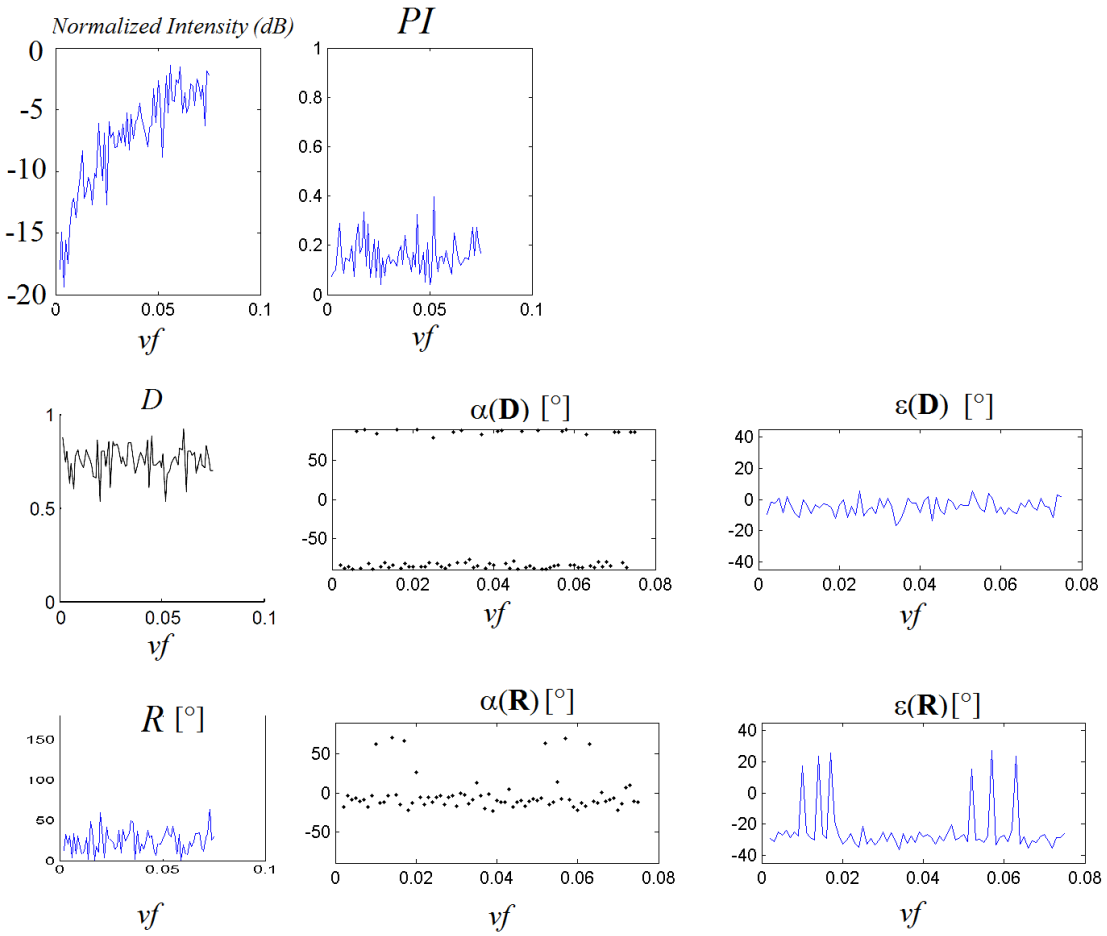

FIGURE 7.21: *Density influence on the Mueller matrix parameters.* $(\theta_e, \varphi_e) = (40°, 0°)$, $(\theta_r, \varphi_r) = (70°, 90°)$.

To conclude, the growth of the density in the simulation leads to an increasing of the intensity but the mean value of the other parameters do not exhibit strong modifications even if there is an important variance. It means that the multiple interactions in the simulation of the vertical cylinder do not impact the evolution of **D** and **R**. A more complete comparison with the measurement is realized in the next section. It will lead to proposition in order to modify the simulation of the Mueller matrix.

7.1.3 Summary

Numerous parameters can change the results and have to be taken into account. The result is very sensitive to the geometrical parameters in the simulation especially the diattenuation and the retardance vectors. Consequently, if the diattenuation and retardance vectors are well reproduced in the CNT simulation we can conclude that the geometrical and permittivity parameters on the scene are correctly set. The evolution with the bistatic angle of the Jones matrix and Lu and Chipman decomposition parameters of the Mueller matrix enabled to give links between them. Here we summarize the polarimetric and bistatic behavior of one single vertical cylinder or a group of vertical cylinders:

- Single element - vertical cylinder at P-band radar
  - Amplitude: Large incidence angle θ_e induces stronger vv polarization amplitude and consequently higher linear diattenuation, however a dielectric ground or the radius change significantly the relative amplitude of the polarizations.
  - Phase: As the phase shifts in the Jones matrices is not easy to investigate and only the horizontal h and vertical v polarization can be studied, the retardance parameter issued from the Mueller matrix is useful to summarize it. It inform us on the way that the incident polarization is changed. For the moment we can conclude that there is strong variation with the bistatic angle and it is also dependent on the radius and the permittivity. Physical interpretations are realized in the next sections.
- Group interaction - CNT forest at 633nm
  - Amplitude: The attenuation is of the order of 10 dB for the investigated bistatic configurations and for every emission-reception polarization couples in the case of the dense forest.
  - Phase: The phase shift is investigated via the retardance parameter that the Lu and Chipman decomposition enables to retrieve. For the group of simulated CNT a strong effect is observed around 55° and further investigations are done in the next section.

– A depolarization effect can be simulated via an averaging process. Four our simulation it remain low whatever the averaging process and the three investigated averaging processes give similar results. The depolarization PI is relatively constant in the simulation when the density of the vertical cylinder varies.

As a conclusion we can see that for the simulation, the depolarization is more sensitive to the variability of the configuration and to the cylinder characteristics than to the density. The attenuation matrices evaluated via the Foldy Lax expression cannot directly reproduce the behavior of the depolarization that is observed in the measurement. In the next section we study and analyze the simulated Mueller matrix for the entire measurement domain of the ARMP, in order to compare both measurement and simulation data.

7.2 Analysis of the simulated Data for the CNT samples using incidence angle averaging

Here we use the hemispherical display Lu and Chipman decomposition issued parameter that enables a better comparison with the measurement. The measurement data are depicted in chapter 5. First, let us consider the simulation of the sparse forest. The decomposition parameters are displayed on figure 7.22. The distribution of the intensity on the ring $\theta_r = \theta_e$ is in good agreement with the sparse forest measurement and it takes into account the cylinder shape scattering. That is a proof of the non dependency between the elements when there is such a low density.

The depolarization PI does not have the same distribution between measurement and simulation. We retrieve the same levels (maximum value of 25%) but without privileged scattering direction. In the measurement, it is the backscattering space that presents more depolarization. The averaging in incident position is not the time averaging that occurs during the measurement. One can find here a reason for the differences.

- The simulated diattenuation parameter has a very close distribution to the measured one, with a minimum in the specular direction and maximum on the ring when $|\varphi_r - \varphi_e| < 90°$, in particular at $|\varphi_e - \varphi_r| = 30°$.
- The retardance parameter is overestimated in the simulation for reception direction around those of maximum retardance ie $|\varphi_e - \varphi_r| = 30°$, $\theta_r \geq \theta_e$. We can notice that it corresponds to a discontinuity in the ellipticity of the retardance $\varepsilon(\mathbf{R})$. If we compare the ellipticity parameters we see very close values and distributions between the measurement and the simulation (figures 5.9 and 7.22). Since the retardance summarize the change of the orientation and ellipticity of the incidence polarization state, it means that bistatic geometrical configuration has a crucial role in this phenomenon that is not obvious and not easily predictable.

The figure 7.23 displays the impact of the high density. It leads to a non negligible attenuation contribution. The intensity is more equally distributed on the ring but does not reach the homogeneity shape that shows the measurement of the dense CNT forest.

Otherwise the ellipticities are still very close to the reality, in particular the maximum value for $\varepsilon(\mathbf{D})$ at $\varphi_r = \pm 45°$, $\theta_r = \theta_e$ is retrieved and was not observed in the low density case. It underlines the relevance of circular polarization because of the high ellipticity of the decomposition parameters, when the bistatic angle is high.

The retardance in the simulated dense case is similar to the sparse simulated forest. In contrary in the simulation the ellipticity of the retardance is lower in the measured

dense case for large bistatic angles. It means that the circular and the linear polarizations are more equally changed in this case. These effect are investigated in the next section via the polarimetric signatures at some positions.

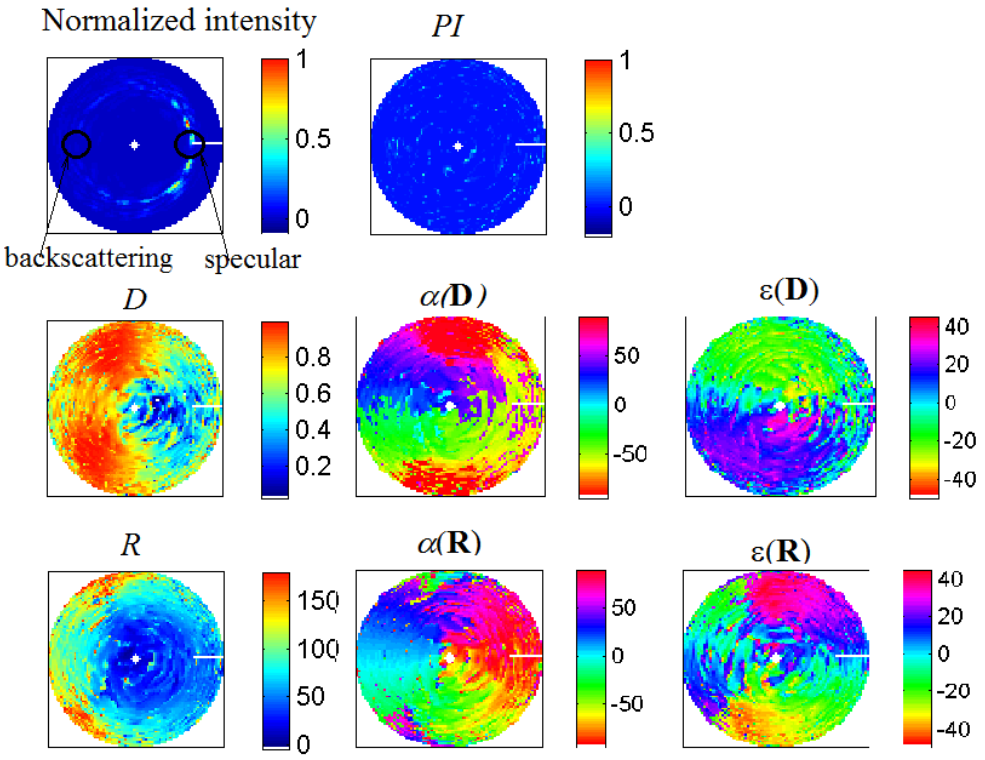

FIGURE 7.22: *Lu and Chipman decomposition parameters in the* $(\mathbf{x}, \mathbf{y})$ *basis for the simulated sparse forest.*

This comparison enables us to go ahead in the validation of the simulation tool, for the case of low density, i.e. when trunks are in the far field of each others. It demonstrates the usefulness of the ARMP measurement tool to produce bistatic data for very dense trunk forest and it shows the high potential of the depolarization process in such environment, even if this process is difficult to reproduce in the simulation. The next section deals with this depolarization phenomenon that is observed in the measurement and aims at linking this parameter with the multiple scattering of the wave and also with the coherency of the wave. Some solutions are tried to take this effect into account in the simulations.

It is important to study the impact of the depolarization and the relation between the depolarization and the other polarimetric behaviors in the ARMP measurement

data on the CNTs, to see how such physical phenomenon would impact polarimetric radar measurements.

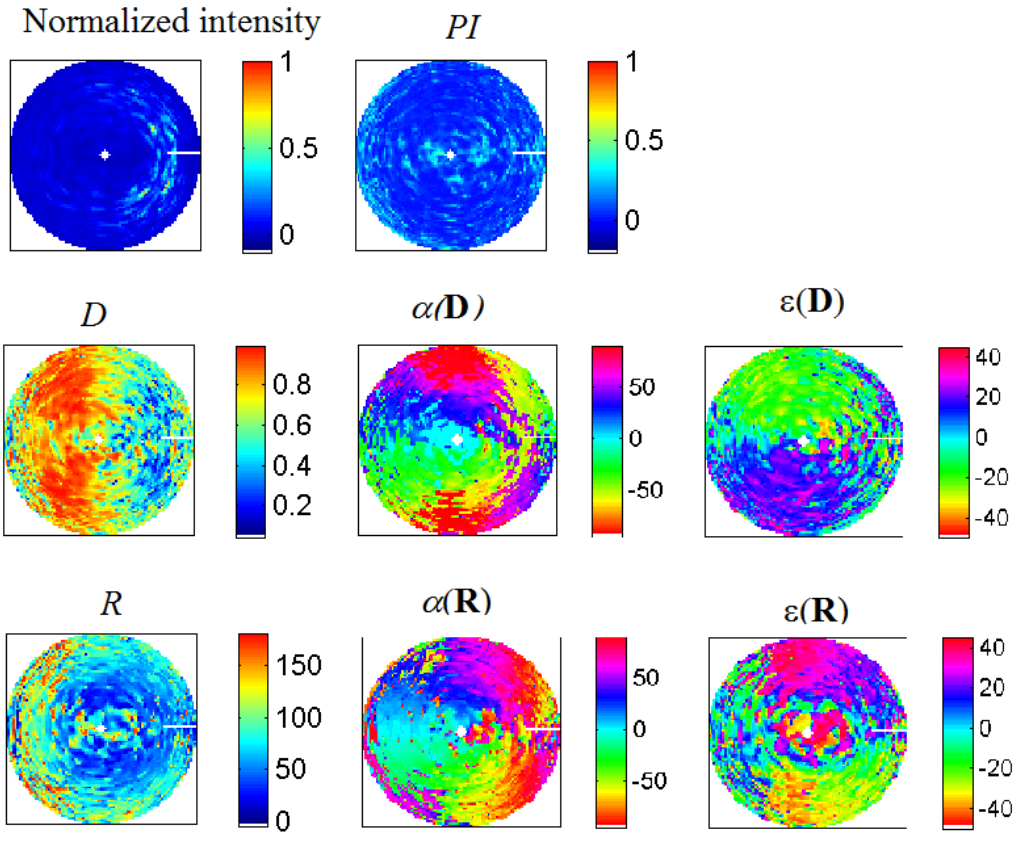

FIGURE 7.23: *Lu and Chipman decomposition parameters in the* $(\mathbf{x}, \mathbf{y})$ *basis for the simulated dense forest.*

7.3 Study of the depolarization in the measurement

7.3.1 Inversion of the depolarization

The Lu and Chipman decomposition has been applied on the measured and simulated matrices. We have seen that the main difference between the measurement and the simulation resides in the depolarization parameter.

The first objective here is to remove the depolarization in the measured Mueller matrices to see the impact on output polarization states. When the depolarization matrix is removed, the Mueller matrix can be expressed as:

$$\mathbf{M}_{pure} = \mathbf{M}_{\rho}^{-1}\mathbf{M} = \mathbf{M}_R\mathbf{M}_D \tag{7.2}$$

For comparison purpose, a superposition of the polarization ellipses at reception is realized in figure 7.25. The angular positions of investigation are explained in figure 7.24.

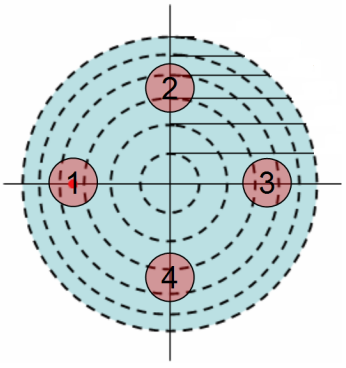

FIGURE 7.24: *Definition of the area of investigation. Four angular positions of reception are observed here: ① the backscattering, ② the left view $\beta = -90°$, ③ the specular, ④ the right view $\beta = 90°$. For the four positions, the reception angle θ_r is equal to the incidence angle θ_e.*

It can be seen in Table 7.1 that the intensities of the Stokes vectors are not affected by the removal of the depolarization matrix $\mathbf{M}_{\rho}$ from the direct Lu and Chipman decomposition. This implies that the depolarization does not change the overall attenuation amplitude of the signal. Then, as it is expected, the *DoP* are all at 100% when this matrix is removed.

Nevertheless small impact is noticed in the reception polarizations and figure 7.25 enables to distinguish this impact depending on the incident polarization state. For the purified Mueller matrices $\mathbf{M}_{pure}$, the *DoP* is always 1 and the intensity remains the

TABLE 7.1: *Dop and norm of the reflected Stokes vector $|g_{out}|$ for normalized Mueller matrices* $\mathbf{M}$ *of the ARMP measurements. The incident polarization states are horizontal H, vertical V, 45°, −45°, right circular RC and left circular LC.*

$\mathbf{g}_{in}$		H	V	45°	−45°	RC	LC
Area 1	DoP sparse	0.76	0.77	0.55	0.59	0.62	0.64
back-	DoP dense	0.94	0.71	0.57	0.63	0.61	0.55
scattering	$\lvert\mathbf{g}_{out}\rvert$ sparse	1.07	0.93	0.98	1.02	1.02	0.98
	$\lvert\mathbf{g}_{out}\rvert$ dense	1.32	0.67	1.04	0.96	0.94	1.06
Area 2	DoP sparse	0.80	0.47	0.68	0.62	0.40	0.71
Left view	DoP dense	0.73	0.70	0.84	0.65	0.68	0.88
	$\lvert\mathbf{g}_{out}\rvert$ sparse	0.82	1.17	0.99	1	0.82	1.17
	$\lvert\mathbf{g}_{out}\rvert$ dense	0.83	1.16	1.22	0.77	0.81	1.18
Area 3	DoP sparse						
Specular	DoP dense	0.58	0.60	0.44	0.47	0.61	0.59
	$\lvert\mathbf{g}_{out}\rvert$ sparse						
	$\lvert\mathbf{g}_{out}\rvert$ dense	1.17	0.82	0.99	1	1.01	0.98
Area 4	DoP sparse	0.79	0.47	0.65	0.68	0.66	0.47
Right view	DoP dense	0.73	0.71	0.59	0.85	0.84	0.66
	$\lvert\mathbf{g}_{out}\rvert$ sparse	0.80	1.20	0.96	1.04	1.18	0.82
	$\lvert\mathbf{g}_{out}\rvert$ dense	0.77	1.23	0.71	1.29	1.27	0.73

same. The difference is low, especially for specular positions and the backscattering. For specular, the effect is more important for the sparse sample observed with a ±45° or circularly polarized field.

From the representation 7.25 and table 7.1 we do the following observations:

- The polarization H is almost not turned or retarded, whatever the region.
- In the specular direction, there is no asymmetry between left and right reception positions.
- At position ① the vertical polarization is more attenuated, but in position ② this effect is not observed.
- The effects of asymmetry between the left and right position ② on the retardance are not found in specular scattering direction. Otherwise, the horizontal polarization is favored for the backscattering direction (area ①).
- In bistatic position ② and ④ the polarization state are more changed, especially the vertical polarization for both densities of forest.

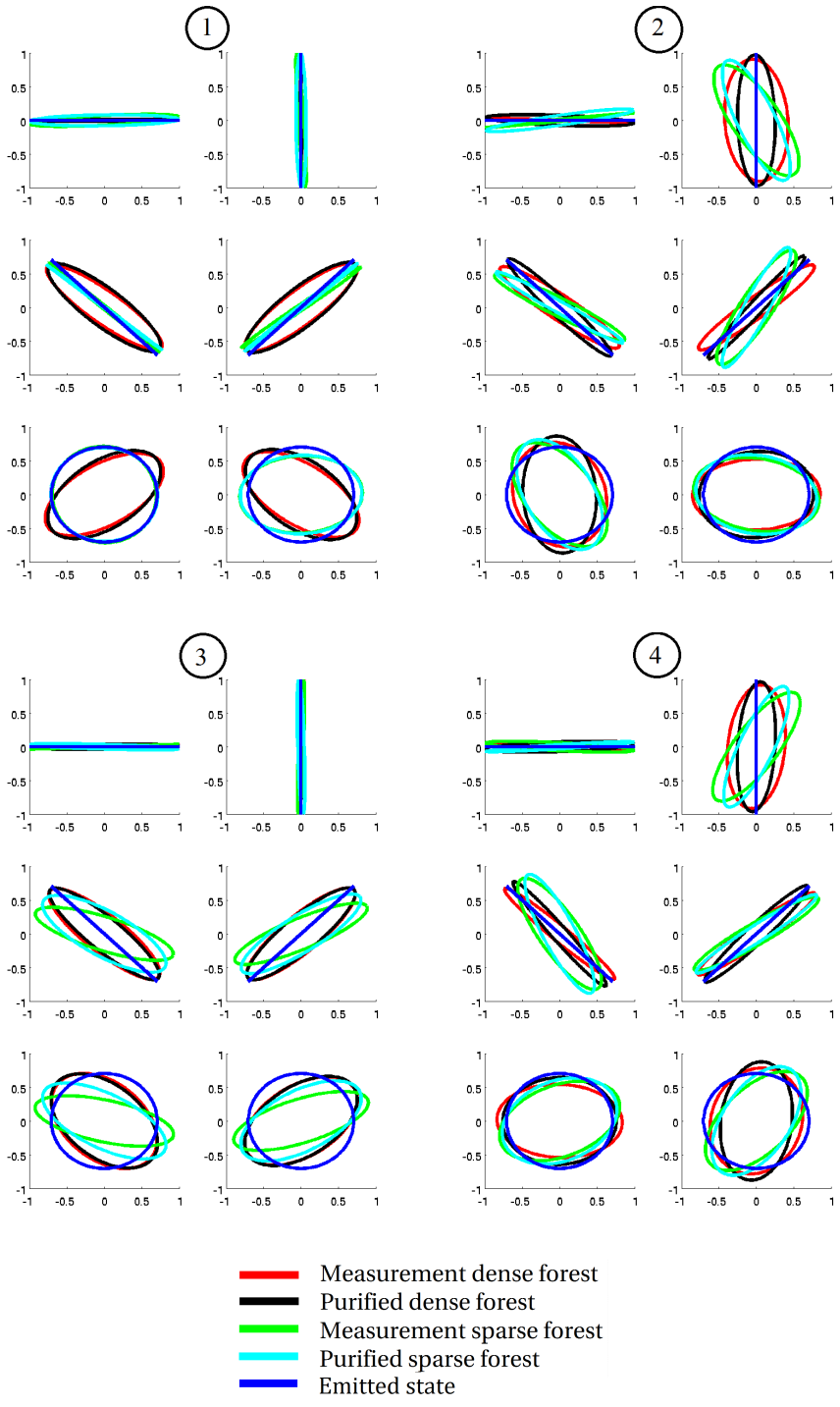

FIGURE 7.25: *Overlays of output ellipses in both samples (densely distributed and sparsely distributed) purified or not for the four areas of investigation. For each area, the input states are: top left: H, top right: V, middle left: −45°, middle right: +45°, bottom left: left circular, bottom right: right circular.*

7.3.2 Polarimetric signature representation and interpretation for the carbon nanotube forests

To complete the comparative analysis of between the purified Mueller matrices and the depolarizing Mueller matrices we use here the polarization signature method as in figure 7.4. It is a well established representation for the polarimetric response of radar targets. One can find the use of this representation for example in [34]. These observations can be seen as redundant because they have already been made via the Lu and Chipman decomposition. However, as this decomposition in not common in the radar domain, the polarimetric signature enables to explain clearly the polarization transformation generated by the CNT forests.

a) Polarization signature without the information of depolarization

The polarization signatures are distinguished between the co-polarization intensities and the cross-polarization intensities. Co-polarization means that the same polarization are considered for the transmitter and the receiver, and the cross polarization means that the received polarization is orthogonal to the transmitted polarization. The polarization signatures enables to plot every orientation and ellipticity polarization states at once. We want to check if this representation can bring additional information to our analysis. For our case, four receiver configuration positions are selected among the whole bistatic positions: backscattering, right view, specular and left view. The results are presented in figure 7.26 and 7.27, for the sparse forest and the dense forest. For the sparse forest at specular position, it is a more grazing position outside of the saturation area.

The vv polarization is higher in backscattering for the two different densities. It is also the case for the specular position for the dense forest but in the case of the sparse forest the incident vertical polarization ($\alpha = \pm 90°$) [1] conducts also to high reception level. If the two side views, there is a symmetry. This symmetry is strong between the right and left circular polarization in the case of the dense forest. In the case of the sparse forest, in addition there is also an influence of the orientation α. For example the $+90°$ polarization state is better transmitted in the left view than the $-90°$ polarization, and it is the opposite for the right view.

[1] the polarization state parameters are desribed in chapter 2

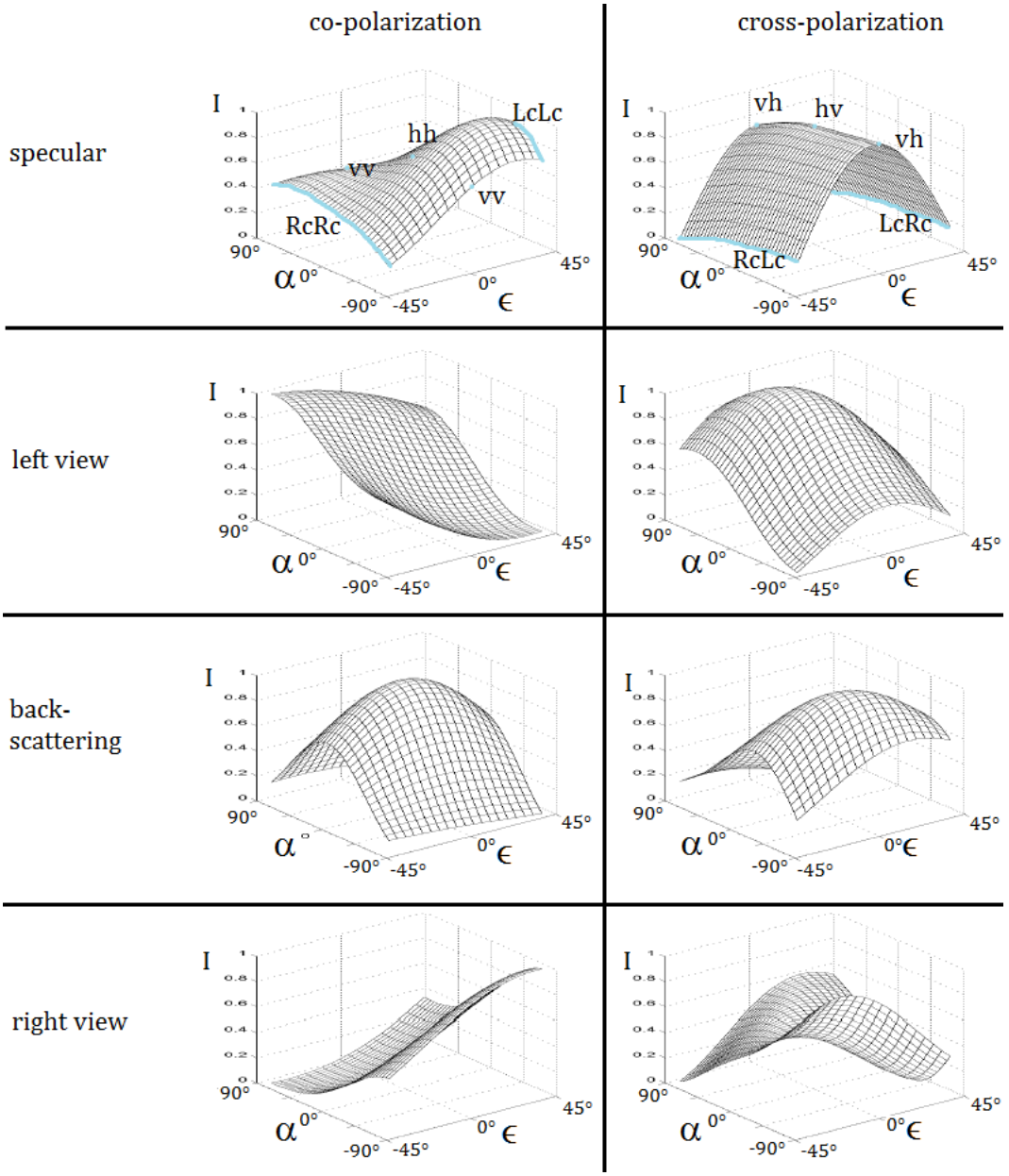

FIGURE 7.26: *Polarimetric signature for the four antenna configurations of the* ***sparse*** *forest. Line 1: specular, line 2: left view, line 3: backscattering, line 4: right view. 1st column: co polarizations, 2nd column: cross polarizations. The coordinates are the ellipticity ϵ of the incident wave from $-45°$ to $+45°$, and the orientation α of the incident wave $-90°$ to $90°$. The level between 0 and 1 corresponds to normalized intensity.*

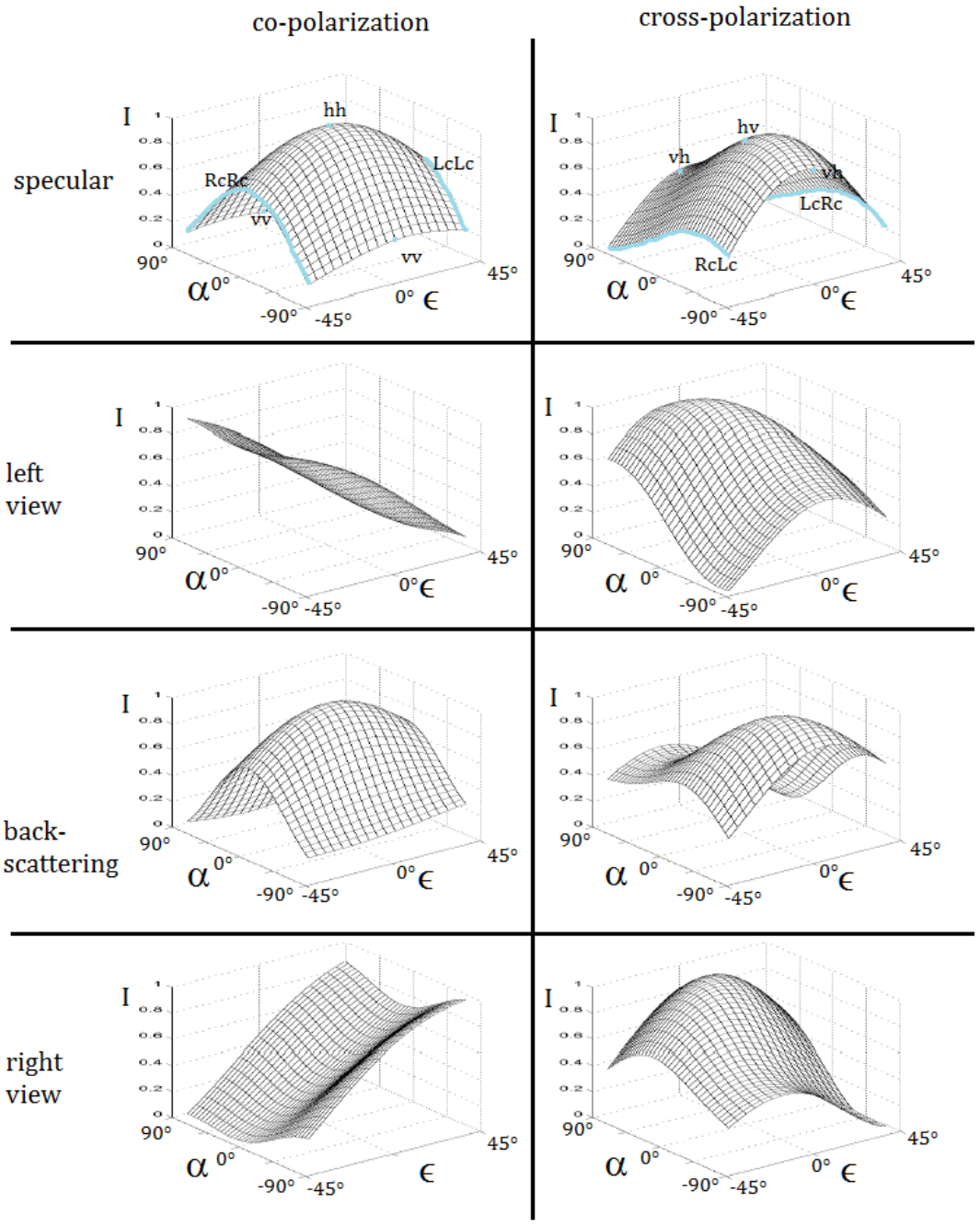

FIGURE 7.27: *Polarimetric signature for the four antenna configurations of the* ***dense*** *forest. Line 1: specular, line 2: left view, line 3: backscattering, line 4: right view. 1st column: co polarizations, 2nd column: cross polarizations. The coordinates are the ellipticity ϵ of the incident wave from $-45°$ to $+45°$, and the orientation α of the incident wave $-90°$ to $90°$. The level between 0 and 1 corresponds to normalized intensity.*

b) Polarimetric signatures colored by the *DoP*

We try now to add the information of the DoP in the precedent signature, because we know that it is an important parameter in our the case of non deterministic target. The corresponding figures for the sparse CNT forest and the dense CNT forest are figures 7.28 and 7.29.

The polarization of higher intensity are no necessarily the position of higher *DoP*, especially for the case of the dense forest, figure 7.29. Figure 7.29 shows the strong difference between right circular and left circular co polarizations when the bistatic angle is $\beta = 90°$ (left view and right view). For the case of the sparse forest, this effect on the circular polarization depends also on the orientation α. Indeed, there is an higher intensity for the polarizations having an orientation moving toward $+90°$ on the left view (2nd line of figure 7.28) and there is a higher intensity for the polarizations having an orientation moving toward $-90°$ on the right view (4th line of figure 7.28). Nevertheless the orientation means nothing for a perfectly circular polarization state ($\epsilon = \pm 45°$).

The polarization signature colored by the *DoP* has the advantage to be compact and to bring many information about the transformation of the polarization state. Nevertheless, it is only possible to represent one bistatic configuration at once in contrary to the hemispherical image representation. Consequently, it can be concluded that even if the polarization signature, and also the polarization ellipse representation, can enable to have clear ideas about the polarization transformations induced by the scene, the hemispherical Lu and Chipman parameters would be preferred for our case of the study of the entire bistatic domain.

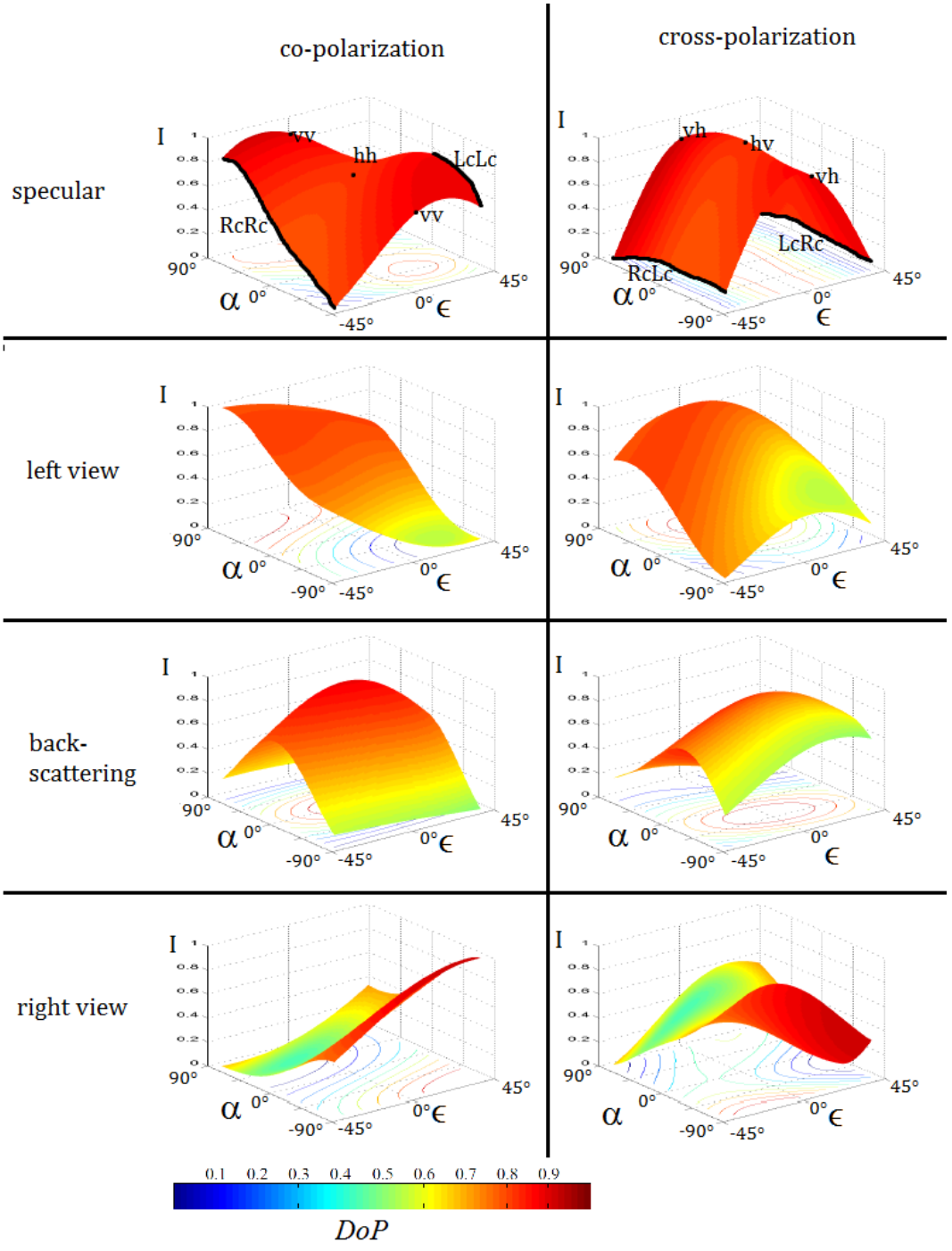

FIGURE 7.28: *Polarimetric signature for the four antenna configurations of the* ***sparse*** *forest. From top to bottom: specular, bistatic left, monostatic, bistatic right. Left column: Co-polarization, right column: cross-polarization. The surface of the signature is colored here by the degree of polarization DoP of the scattered wave. The coordinates are the ellipticity of the incident wave from* $-45°$ *to* $+45°$*, and the orientation of the incident wave* $-90°$ *to* $90°$*. The level between 0 and 1 corresponds to normalized intensity.*

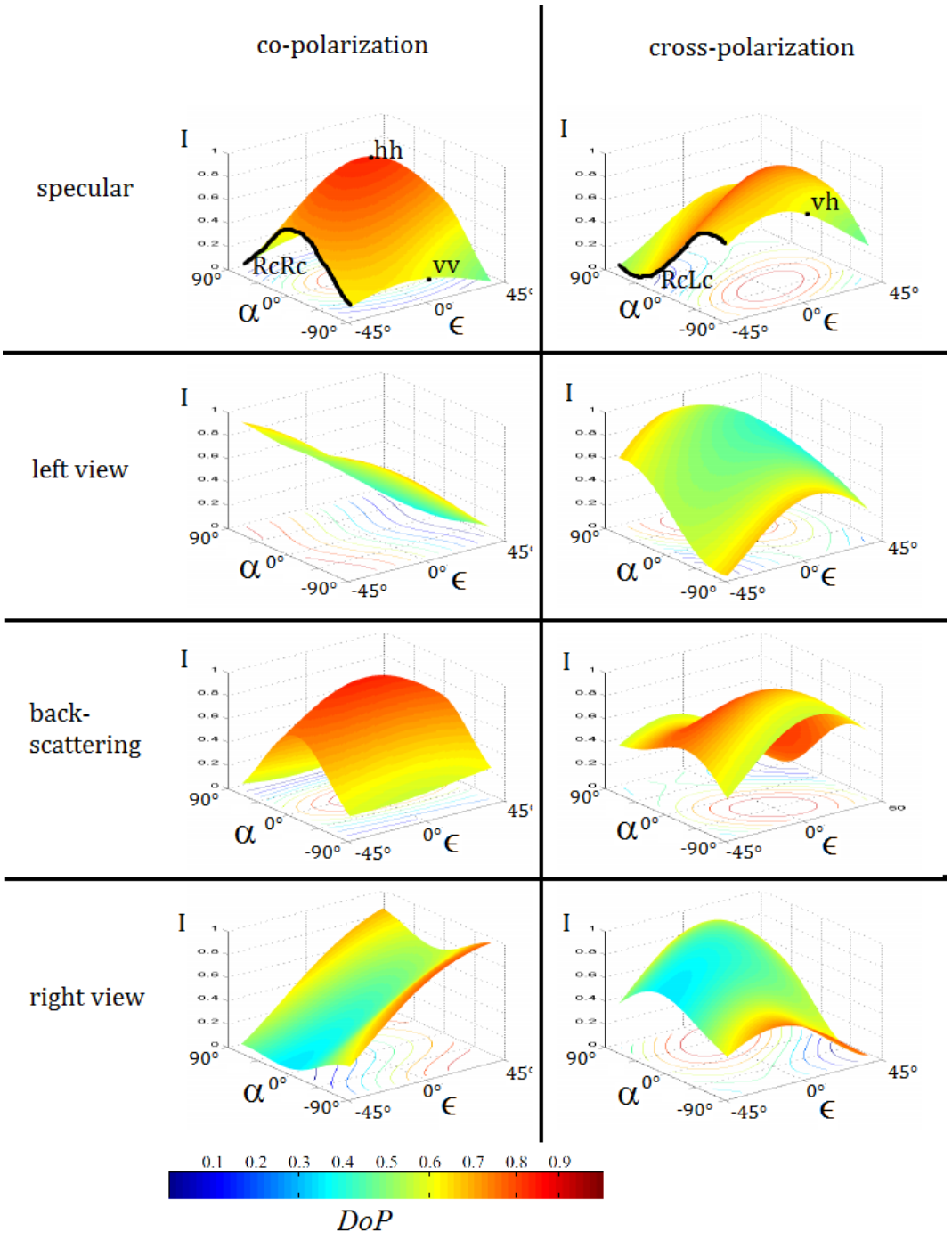

FIGURE 7.29: *Polarimetric signature for the four antenna configurations of the* ***dense*** *forest. From top to bottom: specular, bistatic left, monostatic, bistatic right. Left column: Co-polarization, right column: cross-polarization. The surface of the signature is colored here by the Degree of Polarization of the received Stokes vector. The coordinates are the ellipticity of the incident wave from* $-45°$ *to* $+45°$*, and the orientation of the incident wave* $-90°$ *to* $90°$*. The level between 0 and 1 corresponds to normalized intensity.*

7.4 Interpretation of the depolarization and adaptation of the simulation

The precedent observations tend to clarify our understanding of the depolarization process. We have seen that the degree of polarization DoP in not the same depending on the incident polarization state. This effect is linked to the structure of the forest but it depends also on the bistatic angle. Now we can discuss about the origin of the depolarization and about the way that is observed. We will see that this effect that randomize the polarization state of the EM wave is linked to multiple interactions and also to the incoherence of the wave. We have seen that the simulation fails to reproduce all the evolutions of the depolarization. This reasoning will help us to propose solution in order to reproduce it more precisely in the simulation.

Firstly, for the dense forest, the cylinder can be in near field of each others. The near field denotes the distance d from a cylinder when $d < (2r_e)^2/\lambda$, with r_e is the radius of the cylinder and λ the wavelength. For the case of the measured dense forest of vertical CNT, $r_e = 100nm$ and $\lambda = 633nm$. Consequently, the near field is defined here by:

$$d < 63nm \tag{7.3}$$

For the dense forest, the mean distance between elements is $d = 139nm$. The CNT are randomly positioned and considering this mean distance, the near field sometimes occurs for the dense forest. It is hardly ever the case in the sparse forest. The near field is characterized by complicated amplitude and phase variations of the wave [86]. This complicated variations can explain the observed depolarization. Since the Foldy-Lax multiple scattering approximation that is used in our simulation does not account for the near field interaction this effect cannot be reproduced in our simulations.

In practice, the depolarization effect is commonly produced by the integrating sphere device [87], which is illustrated in figure 7.30. The polarized light enter via a little hole on the sphere an is reflected numerously on isotropic highly reflective surface that covers the sphere surface. The light exits the sphere by another hole and is perfectly depolarized. The multiple bounces that undergo the light is essential in the depolarizing process.

As stated in section 7.1.2 the multiple scattering in random media has been studied in the literature. The entropy production of a random media has been proven for the case of Rayleigh scatterers in [88]. In this article, a link is done between the spatial coherence and the depolarization (increasing of the entropy H) using the principle of maximum entropy. There is a distinction between the time variant media and the time invariant media. Here we can consider that the forest is time invariant. In [88] analytic study shows that the DoP of the Stokes vector is monotonically decreasing with the number of scattering events inside a time invariant media. For our case the number of

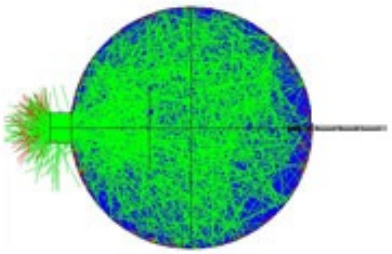

FIGURE 7.30: *Illustration of the principle of the integrating sphere. The polarized light enters the sphere by a little aperture and accouters many scattering on the rough surface in the sphere. The output light is totally depolarized.*

scattering event would depends on the distance traveled by the wave into the forest. The distance increases as the reception position is more grazing. Consequently, the observation of increasing of depolarization with increasing reception angle is explained by the theory of multiple scattering in random media.

In the measurement of the dense forest the depolarization is clearly identified, and the characteristic coherent backscattering phenomenon [67] is observed in figure 5.10. Indeed, in $\mathbf{M}_{1,1}$ there is a sudden increasing of the intensity at the backscattering position. It is explained by coherent summation of waves traveling the same paths of multiple scattering in different directions. Consequently in backscattering it resists more to the time averaging on the sensor.

7.4.1 What is the coherent and incoherent intensity in our simulation?

In our case of simulation, the multiple scattering is translated into an attenuation matrix via the Foldy approximation in the forward direction. Several Jones matrices of the scene are obtained for each event. It can be

- interaction mechanisms with the ground,
- incidence angle
- resolution cell

They are referenced by index i:

$$\mathbf{J}_i, \qquad i \in [1:N] \tag{7.4}$$

with N the total number of of Jones matrices considered here.

To produce the Mueller matrix from this ensemble of Jones matrices several way are possible.

If one consider totally incoherent summation of the different events indexed by $i, j \in [1, N]$, the total Mueller matrix $\mathbf{M}_t$ of the scene at the reception position is:

$$\begin{aligned} \mathbf{M}_t &= \mathbf{M}_1 + \mathbf{M}_2 + ... + \mathbf{M}_N && (7.5)\\ &= \mathbf{A} \cdot (\mathbf{J}_1 \otimes \mathbf{J}_1 + \mathbf{J}_2 \otimes \mathbf{J}_2 + ... + \mathbf{J}_N \otimes \mathbf{J}_N) \cdot \mathbf{A}^\dagger && (7.6)\\ &= \mathbf{A} \cdot \textstyle\sum_{i=1}^{N} (\mathbf{J}_i \otimes \mathbf{J}_i) \cdot \mathbf{A}^\dagger && (7.7) \end{aligned}$$

Then, an incoherent averaging of scattering realization is done, see section 7.1.2. The resulting coherency matrix is expressed as in 7.8 and the Mueller matrix is obtained from this coherency matrix, as explained in Chapter 2.

$$\mathbf{C} = \sum_{i=1}^{N} (\mathbf{J}_i \otimes \mathbf{J}_i) = \sum_{i}^{N} \mathbf{J}_i \otimes \mathbf{J}_i + \sum_{i,j,i\neq j}^{N} \mathbf{J}_i \otimes \mathbf{J}_j \tag{7.8}$$

The first term of equation 7.8 corresponds to the incoherent intensity, and the whole terms of equation 7.8 correspond to the coherent intensity. Consequently both terms coherent and incoherent are taken into account in our processing. Nevertheless depolarization dependence with the reception angle is not well reproduced. The ensemble averaged covariances that we have tested would correspond to physical process, as stated in section 7.1.2. However, the Foldy attenuation matrix does not increase the depolarization depending on θ_r. It would be explained by the fact that the averaged Jones matrix computed in equation 6.1 is not the one that effectively "sees" the wave when the path through the media increases. In the reality the averaged Jones matrices would come from other variabilities as for example near field interactions, but they cannot be simulated. We propose to test empirical methods that aim at taking these effect into account. Empirical methods that reproduce the depolarization effect are tested in the next paragraph. We try firstly a weight on the incoherent term in the matrix $\mathbf{C}$. Then we try an empirical method with a weighted summation of a perfect depolarizer Mueller matrix.

7.4.2 Mitigation of incoherent and coherent terms of the mechanism contributions

Figure 7.31 shows the simulation including a partial incoherence between the scattering bounces mechanisms. Indeed, the set of averaging terms considered here is the bounce mechanisms. The coherent term in the total Mueller matrix is decreased depending on θ_r by a coefficient $\alpha_c = \cos\theta_r$. This coefficient is chosen because it fit with the linear increasing of the depolarization with $\cos\theta_r$ in the measurement of the dense forest.

$$\mathbf{C} = \alpha_c \sum_{i}^{N} \mathbf{J}_i \otimes \mathbf{J}_i + \sum_{i,j,i\neq j}^{N} \mathbf{J}_i \otimes \mathbf{J}_j \tag{7.9}$$

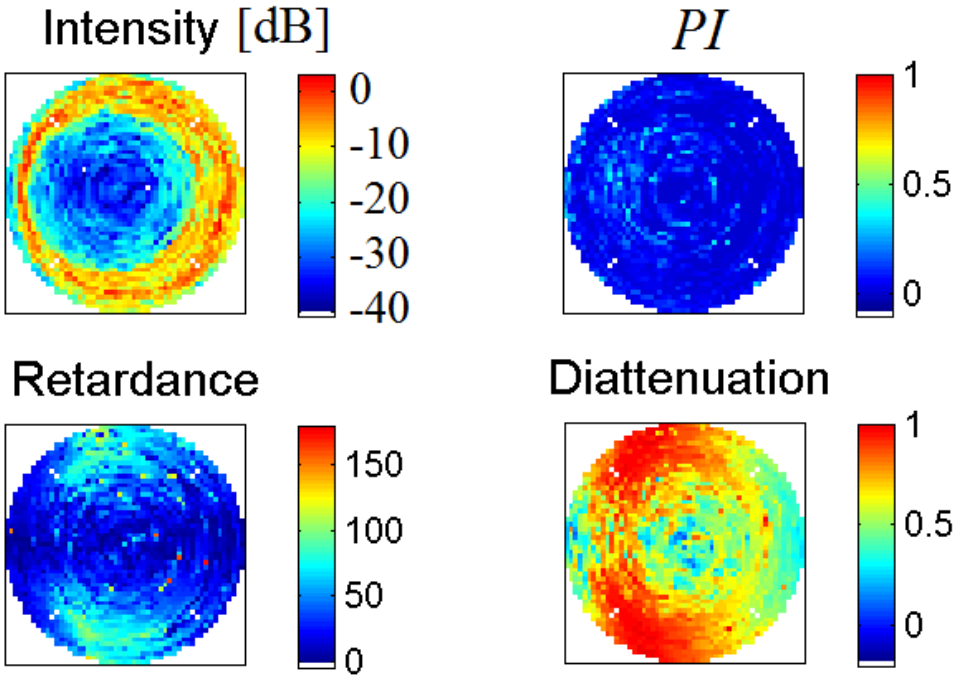

FIGURE 7.31: *Scalar parameters from the Lu and Chipman decomposition for the simulation of the* ***dense*** *forest with coefficient α_c on the coherent part, $\theta_e = 35°, \varphi_e = 0°$, $\theta_r = [0° : 60°]$ $\varphi_r = [0° : 360°]$ in $(\mathbf{x}, \mathbf{y})$ polarization basis.*

The result does not correspond to the expected behavior that would be explained that averaging considered here is not the good solution.

7.4.3 Empirical model to take the depolarization into account with additional Mueller matrix

In [89] a study is realized on the incidence plane Mueller matrix of the typical depolarizing target in optics. The most depolarizing target at this scale is called "spectralon". It is often used for calibration purposes. Nevertheless, the model of its depolarizing behavior remains an important issue. In is worth noting that the Mueller matrix of this material does not follow the form of the expected Lambertian surface response when the incidence is moved away from the normal position. In [89] a method is proposed to simulate the Mueller matrix of the spectralon. It relies on an empirical Mueller matrix model for the surface $\mathbf{M}_{Lambertian}$ that is added to the pure theoretical Mueller matrix weighted by a ratio depending on the reception elevation angle θ_r. All the parameters of the model are optimized to match measured data. It is depicted in the following equation:

$$\mathbf{M}_{Spectralon} = \mathbf{M}_{11} \left(PI \cdot \begin{pmatrix} 1 & 0 & 0 & 0 \\ 0 & 0 & 0 & 0 \\ 0 & 0 & 0 & 0 \\ 0 & 0 & 0 & 0 \end{pmatrix} + \mathbf{M}_{Lambertian} \right) \tag{7.10}$$

with PI the depolarization index defined in 2.14. This method could be relevant for our problem because the chaotic behavior from which the depolarization is derived cannot be simulated directly from the Maxwell equations and from the tested averaging. The same principle is thus applied to our simulated dense nanotube sample hemispherical measurement. The results are plotted in figure 7.32 In [89] $PI = |\frac{\theta_r - \theta_e}{22}|$. For our measurement of dense forest PI seems to be independent of the relative value of θ_r and θ_e, and $PI = cos\theta_r$ is a good approximation.

With this solution, we added artificially an isotropic depolarizer to match the measurement. It is interesting to notice that the impact of the diattenuation is reduced as in the case of the dense forest measurement.

Here the empirical model is set to match the optical measurement but in radar the values can be different. As the radar measurements are coherent, the depolarization is not directly sensed by the antenna and there is no time averaging. However, each pixel is computed from a set of measurement coefficients. The depolarization is retrieved in radar via the averaging between neighbor pixels, or also in multi-look. Multi-look consists in summing incoherently different frequency domains, or Doppler domains, that the radar measures. We have not studied this multi-look incoherence because we have only considered constant frequency but it seems obvious that the evaluation of the depolarization can also be realized in that way. Finally, in radar measurements and in ARMP measurements of CNT the origin of the depolarization are the same,

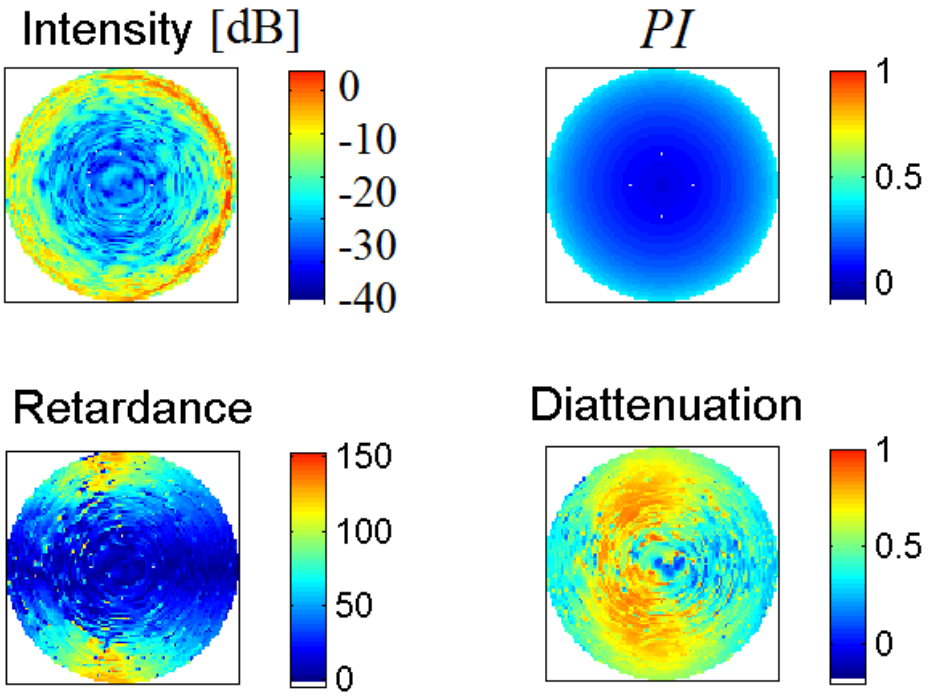

FIGURE 7.32: *Scalar parameters from the Lu and Chipman decomposition for the simulation of the* ***dense*** *forest with additional ideal depolarizer Mueller matrix in the basis* $(\mathbf{x}, \mathbf{y})$.

namely multiple interactions and near field interactions. However, the evaluation of the depolarization value are different in both domains. Consequently the same variation with the bistatic angle would be observed in both domains but the absolute values of the polarization index PI or the entropy H can be different.

* * *

Summary
Analysis of the measurements is difficult because the hemispherical measurement induces many bistatic configuration at once. The simulation is useful to relate mechanisms and permittivity influence to the measured parameters. The bistatic ring shape is observed for relatively low density case. But it is no more the case for high density forest which must be related to the multi scattering. The good transmission of the circular polarization at 90° bistatic angle is also one of the most striking observation. It was shown that the simulation well reproduce the diattenuation and retardance behavior of the measurements. However the depolarization is more difficult to reproduce.
The study of the depolarization behavior using DoP showed that all states are not depolarized in the same way. We also highlighted that polarization states can be slightly attenuated but highly depolarized, for example it is the case of the horizontal polarization in the dense forest when the bistatic angle is $\beta = 90°$.
Depolarization can be explained by multiple interactions and near field interactions between forest elements when the density is high, and the depolarization increases when the path inside the forest increases. In order to reproduce it in the simulation we proposed an empirical method in the case of the dense CNT forest measurement. So, we followed the process described in chapter 6 to improve the simulation.
As the averaging method in ARMP measurement is not the same as in radar, the depolarization absolute values in radar measurement would be different. However, these bistatic ARMP measurements shall give the same variation of the depolarization and the relative values depending on the bistatic angle as in P-band bistatic radar measurement.

Chapter 8

Application of the simulation for structure parameters inversion and FoPen target detection

Within the limits of its validity, the code of simulation can now be applied and analyzed through the use of the decompositions studied previously. Two application perspectives are proposed. First, the inversion of parameters of forest is investigated. It is possible to underline the capacity of the polarimetric bistatic configuration to be sensitive to the density and to the orientation of branches. The second perspective of study is the detection of target in the forest. A statistical test will be applied on simulations which take into account the attenuation due to the branches on several cases of canonical targets.

8.1 Simulation for the evaluation of the forest structure influence

8.1.1 Configuration and parameters

The forest structure

To our knowledge, several studies have examined the impact of the structure of the forest as for instance in [90], but not in a bistatic mode. In this section we are not interested in a detailed analysis of structure influence but more in understanding consequences of different positions and orientations. More precisely, we propose to limit our study to the branch spatial organization in the forest. We will thus have a look on

potential effects of structural variations of forests by simulating different scenes using same descriptive cylinders in all cases and changing only their orientations and places. For the simulations we defined a $10m \times 10m$ forest area containing tens trees with vertical trunks. Trees have a mean spacing equal to 6 meters with variations up to 4 meters. In a first step we want to see the impact of the relative position in a case of fractal positioned branches relatively to a forest where the branches are randomly positioned. In a second time three types of forests are tested depending on the branch orientations. One with horizontal branch orientations, another with 45° inclination branches, and a last with random orientations as shown in figure 8.1.

For the fractal generation we chose to create three main branches per trunk with two other levels.Their inclination angles β as well as their sizes are selected as shown in table 8.1 and 8.2. The branches in the fractal generation are endwise which is not the case for the other generations. For the random generation the same canonical cylinders are used but their positions are determined randomly within the forest expansion. Oriented forest is derived from the fractal one and branches orientations β are set to respectively 0° and 45°.

TABLE 8.1: *Table of the fractal forest structure*

-	**trunk**	**branch** 1^{st} **layer**	**branch** 2^{nd} **layer**
diameter	0.2m	0.17m	0.13m
heigth	10m	7m	5m
number	25	3 per trunk	9 per trunk

TABLE 8.2: *Table of forest branch inclinations.*

-	**structure**	β 1^{st} **layer**	β 2^{nd} **layer**
Forest 1	fractal	30°	$[0, 60°]$
Forest 2	horizontal	0	-
Forest 3	45°	45°	-
Forest 4	random	0° : 90°	-

The radar parameters

For each structure, the emitter is fixed at $\theta_r = 35°$, $\varphi_e = 0°$. It is located at a far field distance from the scene, $d_e = 10000$m). Frequency is set to 500MHz. The electric field is simulated for all positions of the receivers on the hemisphere described by $\theta_r \in [0°, 60°]$, $\varphi_r \in [0°, 360°]$ and $d_r = 10000$ m. The angle step for θ_r and φ_r is two degrees.

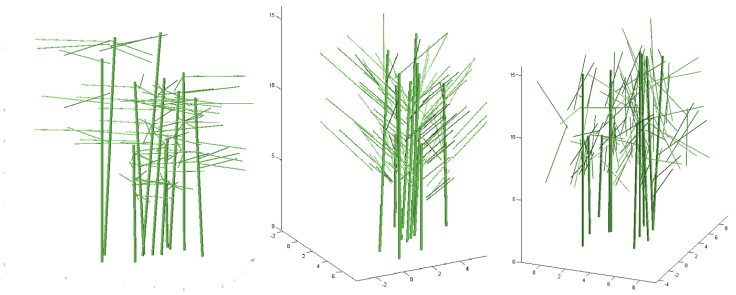

FIGURE 8.1: *The three different forests in order to study the branch orientations influence.*

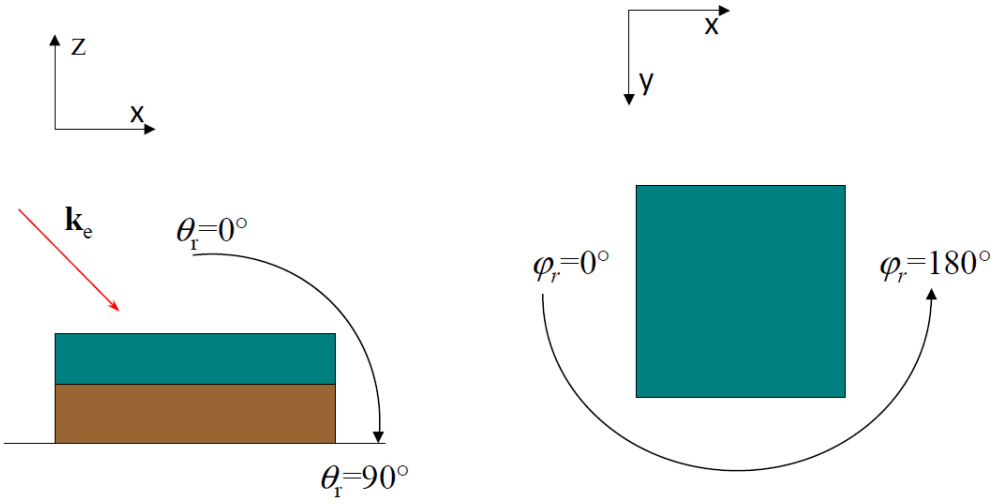

FIGURE 8.2: *Geometrical configuration and conventions for the simulations.*

For each angular position of the receiver, the complex scattered field is obtained for the four polarization pairs in the $(\mathbf{h}, \mathbf{v})$ basis. Then the coherence matrices are computed and added inside a solid angle of 5° radius. The choice of this kind of estimation can be related to the position uncertainty of the receiver and to the angular variation during the receiving time.

8.1.2 Results

8.1.2.1 Intensity for fractal forest structures

We have first analyzed the scattering levels for the different types of forest. Figure 3 and 4 correspond to the scattering level of the fractal forest and the vertical forest respectively. These figures show the amplitude information as well as information on the preferred mechanism according to the angle of reception. They are represented in polar coordinates where $\sin\theta_r$ stands for the radius and φ_r is the polar angle. Green and red colors are used to code the polarimetric information in the Pauli basis for the copolarization only: red color stands for $|E_{hh} + E_{vv}|$ and green color stands for $|E_{hh} - E_{vv}|$, where E denotes the complex electric scattered field.

In Figure 8.3 different crowns can be distinguished. The same kind of representation made on the contributions of branches and trunks separately, enables to interpret the different patterns of the returns and to link them to the different elements and mechanisms:

- A crown at $\theta_e = \theta_r, \forall\varphi_r$ where the scattering level is high should correspond to the double bounce contribution of the vertical trunks.
- A smallest crown is visible for $\varphi_r \in [90°, 180°]$ and corresponds to the double bounce contribution of oriented branches.
- A last more diffuse pattern is visible $\varphi_r \in [0°, 90°]$ and corresponds to the single scattering of branches.

The fractal forest follows exactly the same trend than the forest with same orientations and random positions. That means that exact positions of elements are not critical in this case.

From this observation we can conclude that the relative position of the branches does not impact significantly the result is this case. But the orientation and vertical structure of the tree may be significant in the polarimetric result.

Polarimetry for branch inclinations study

To carry a polarimetric analysis of our simulations, we propose to compute first classical polarimetric parameters $\bar{\alpha}$ derived by Cloude [91] for the bistatic setting, and to compare them to the tools developed around the optical polarimetric domain. This approach is supported by the following reason: the existing polarimetric decompositions of Mueller matrices are multiplicative decompositions, corresponding to a description of

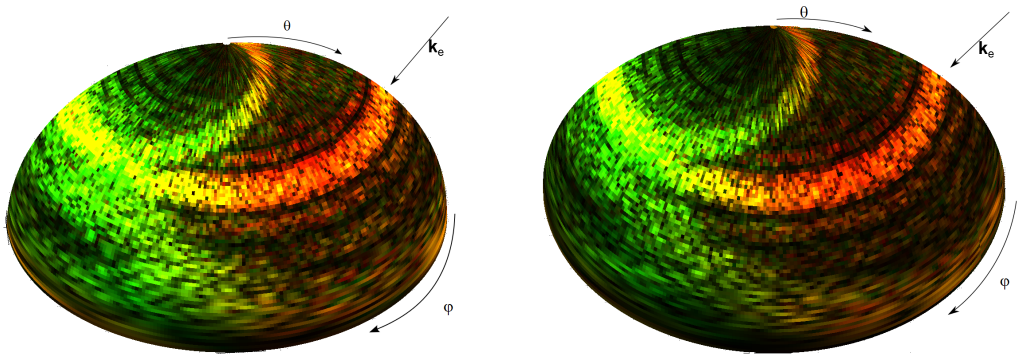

(a) (b)

FIGURE 8.3: Pauli basis co polarization intensity representations. (a) Intensity for fractal forest (b) Intensity for fractal forest with randomly positioned elements. red: $|hh + vv|$, green: $|hh - vv|$

the environment in successive layers. Yet most descriptions of existing forests are precisely layered descriptions. The decomposition process is the one explained in chapter 2.

In figures 8.4 we have represented $\bar{\alpha}$ We can see that classically, the alpha parameter

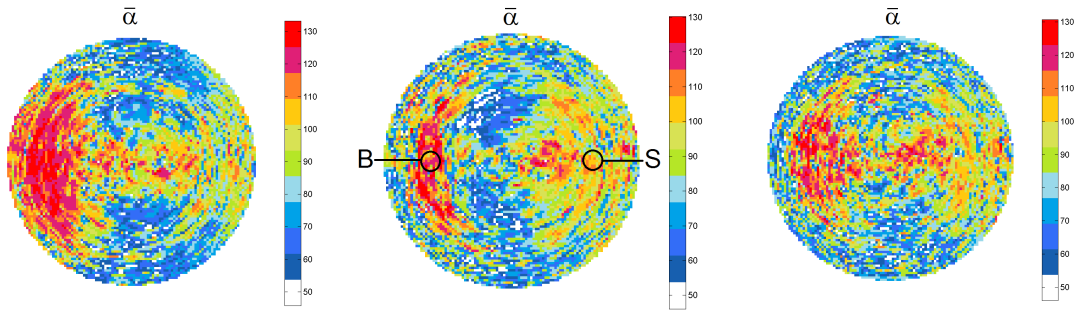

(a) (b) (c)

FIGURE 8.4: *Cloude-Pottier $\bar{\alpha}$ parameter for the three types of branch inclinations. (a) horizontal, (b) 45°, (c) random. The circles B and S correspond respectively to the backscattering position of reception and the specular position of reception.*

for vertical trunks extends from π (red) in a monostatic settings to lower value in a specular setting. Outside the azimuth plane of reception, the interpretation of alpha seems to be a tricky task. We can only say in figure 8.4 that the value of alpha seems to be explained by branches outside this plane. Indeed, for $\theta_r > \theta_e$ and $\varphi_r = \varphi_e$ the $\bar{\alpha}$ parameter is higher in the case of horizontal branches than in the other cases.

In figure 8.5 the complete Lu and Chipman decomposition is applied for the three types of orientation branches. PI significantly depends on intensity: it is high when intensity is low, and viceversa. It is higher for the randomly oriented branches that indicate that the diversity of the scattering matrices of the elements is very significant for the depolarization. The retardance is also more random as the orientation of the branches is randomized and the diattenuation is lower for random orientation of branches.

Using those parameters, we evaluate a distance between the Mueller matrices obtained for each bistatic configuration. This distance is constructed from the more contrasted parameters in the decomposition. Its expression is:

$$|Lu|_{i,j} = \frac{1}{4}\left(|PI_i - PI_j| + \frac{|R_i - R_j|}{180} + \frac{|\epsilon(\mathbf{R})_i - \epsilon(\mathbf{R})_j|}{45} + |D_i - D_j| + \frac{|\alpha(\mathbf{D})_i - \alpha(\mathbf{D})_j|}{90}\right) \tag{8.1}$$

$|Lu|_{1,2}$ is the distance between horizontal branch case and 45° branch case. $|Lu|_{1,3}$ is the distance between horizontal branch case and randomly inclined branch case and $|Lu|_{2,3}$ is the distance between randomly inclined branch case and 45° branch case. In figure 8.6 the parameter $(|Lu|_{1,2}+|Lu|_{1,3}+|Lu|_{2,3})/3$ is imaged in logarithm scale for the entire domain of bistatic possibilities. It is important to note that here the intensities are not taken into account because we consider that is an additional information to the only polarimetric one.

On case see that the yellow zones correspond to the bistatic configuration that enables better distinction between the forest structure in spite of the same trunk contribution in the three cases and without considering the intensity value. The main bistatic domain to retain here are described by

- $\theta_r < \theta_e$ and $\varphi_r < 90°$
- $\varphi_r = 90°$, $\forall \theta_r$

In this section we have represented the response of some forests for all possible receiver positions. The interpretation of the results highlights the importance of the branches inclinations. Exact positions have less consequences on polarimetric analysis. The calculation of various parameters from the optics polarimetry or radar polarimetry gives mostly the same kinds of interpretation, except for some specific cases. However, we must keep in mind that the analysis of the polarimetric response has been restricted here to effects that do not include the possible impact of mutual coupling on depolarization.

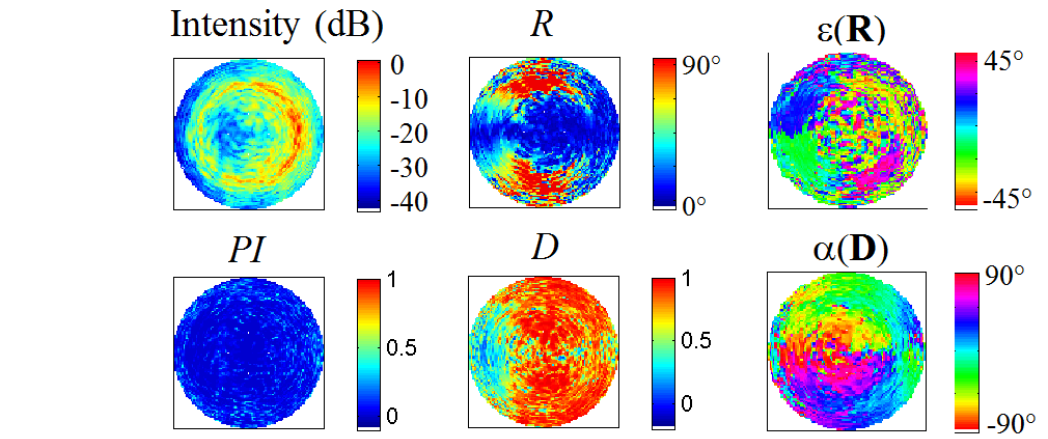

(a)

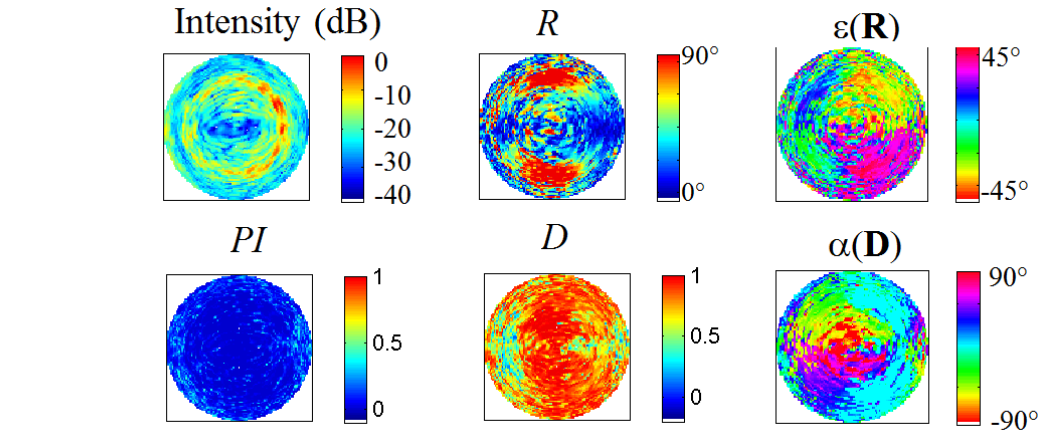

(b)

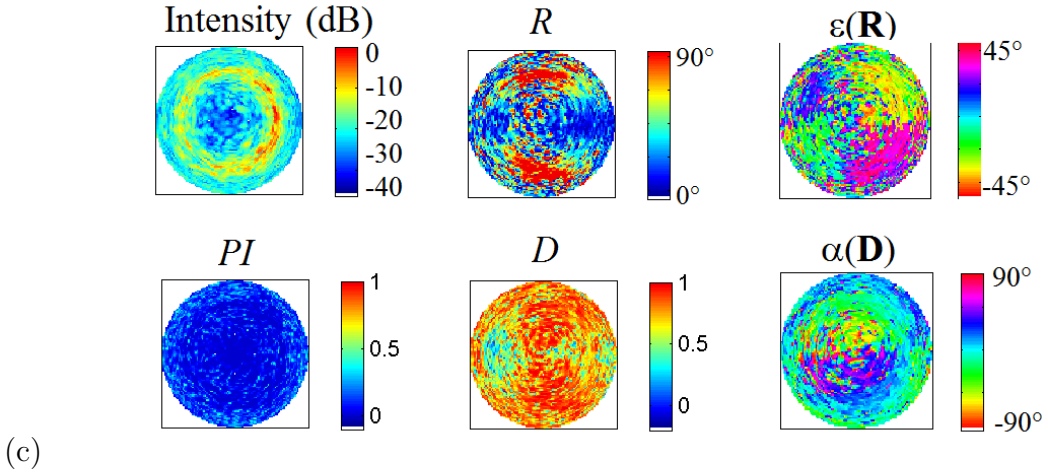

(c)

FIGURE 8.5: *Lu and Chipman decomposition applied on the three types of branch inclinations. (a) horizontal branch orientations (b) 45° horizontal branch orientations, (c) random horizontal branch orientations.*

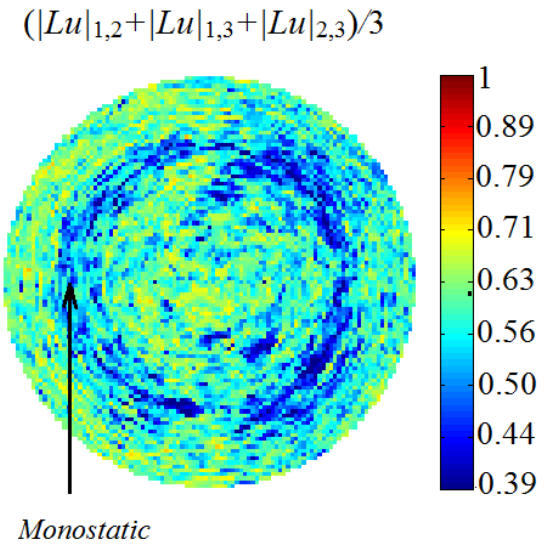

FIGURE 8.6: *Distance between the Mueller matrices of the three cases of forest. It is evaluated using the decomposition parameters* $D, \alpha(\mathbf{D}), R, \epsilon(\mathbf{R})$.

8.2 Performance evaluation in specific cases of detection

In the first part of this manuscript, the context, the tools and the main issues for bistatic SAR applications in the forest were studied. Then we have deal with the development of the measurement device and the simulation that work conjointly to understand the main propagation mechanisms whatever the polarization of the field. It brings key information to foresee results in remote sensing applications. The remote sensing of biophysical parameters is briefly studied in the precedent section and now the anticipation for target detection under the foliage is evaluated using the simulation. Performance comparison depending on the bistatic angle is performed. We consider one resolution cell of a forest scene containing a man-made target. The attenuation from the branches and the trunks is taken into account for every bistatic configurations. Consequently it would evaluate the contrast between a forest clutter and a target on the ground for an entire domain of bistatic configurations.

The prediction of the attenuation in the simulation using scattering for independent cylinders and also the Foldy Lax attenuation formulation. It is straightforwardly of prime importance for the detection possibility and COBISMO takes it into account, that is why the use of the simulation to compare bistatic configuration performances on detection is well justified.

The forest is non deterministic and the forest pixel that contain the target also present a non deterministic response. That is why the second order polarimetry is considered here using the coherency matrix or the Mueller matrix of the scene. The depolarization effect on the detection performances have never been tested. No conclusion about its negative impact on detection can be done for the moment, and it can also have positive impact. As the section 8.1 shows that this parameter enables a better distinction between the forest structure, its knowledge could also have benefit impact on the detection because, for example, target could be related to less depolarizing area in the SAR image. In any case non deterministic scattering and depolarization are modeled here via realization of Gaussian distribution of the Stokes vector of the forest pixel.

This application, called FoPen, has been a long-term effort [92]. The early FoPen measurement were GMTI and stationary. In 1974 a $10m$ long antenna detection of walking people and also the Sotas campaign was a GMTI on a helicopter. In the 90's the Boomsar campaign was an important set up to detect mines. Several other missions were conducted such as P-3 SAR, FOA CARABAS, SRIFOPENII and the Nasa-JPL AIRSAR. The main observed defect was the presence of artifacts up to L band. The need for polarization diversity was shown for statistical characterization due to attenuation. Another important highlighted problem is the presence TV radio

frequency that decreases the discrimination. The problem is not taken into account here but it must be known for the practical applications. The motion compensation for wide area focus is very important. It was exposed that the larger frequency are better for the detection because the attenuation is decreased. Moreover, the polarimetry plays the role of a whited filter in the processing chain. The majority of FoPen devices works in monostatic and for this configuration, the log normal distribution is used for the forest clutter in the detection processing chain.

Classical SAR processing may not use the best reconstruction model for the false alarm generation. In [69] a method is proposed to evaluate the detection performances. The monostatic SAR image is not realized, but a projection into a target subspace replaces it. It is an interesting approach but here we are not interested in the processed signal but only with polarimetric signal received for bistatic angle configuration at fixed frequency for one pixel in order to compare the performances for different bistatic configurations.

In LORAMBIS campaign [2] the bistatic configuration in the target detection possibility was studied. However only several small bistatic angles were studied and the measurement was not polarimetric. In this present study the effect of branches and the attenuation is included and as final result we present probability of detection P_d depending on the bistatic angle for the entire hemisphere of reception and considering a constant emitter position. In [93] and [94] a bistatic SAR system was developed to study the detection performance at VHF band. It proved that the bistatic configuration reduces the forest clutter.

Here we will present and justify the stochastic model that is used and the obtained results with our simulated data for the bistatic detection of a cylindrical and ellipsoidal target. In addition to the present results, the image quality has to be borne in mind with two quantities as a metric, namely the resolution and the integrated sidelobe ratio (ISLR) which change depending of the bistatic configuration among others.

Our objective is to manage a procedure for the evaluation of bistatic configuration influence on the Probability of Detection P_d depending on the Probability of False Alarm P_{fa} in a case of hidden target inside a forest. For that purpose, we use a statistical model for the scattering vector. The statistical models for a polarimetric measurement are described in [12]. They depend on hypothesis about the nature of the signal. The polarimetric information is contained in the measurement Stokes vector $\mathbf{k}$. For a deterministic target with a fixed value for the amplitude, a realization of $\mathbf{k}$ is described by 8.2:

$$\mathbf{k_i} = a_0\mathbf{k} + \mathbf{b_i} \tag{8.2}$$

with a_0 the amplitude and $\mathbf{b}_i$ the realization of the additional noise vector. If only the polarimetric behavior of the target is deterministic it comes 8.3:

$$\mathbf{k_i} = a_i \mathbf{k} + \mathbf{b_i} \tag{8.3}$$

with a_i the realization amplitude and $\mathbf{b}_i$ the realization of the additional noise vector.

If the measurement is non deterministic, as here with the forest where the depolarization is high, the measurement can be expressed using the coherency matrix $\mathbf{C}$ which is presented in section 2 with equation 8.4

$$\mathbf{k_i} = a_i \sqrt{\mathbf{C}} \mathbf{x_i} + \mathbf{b_i}, \qquad \mathbb{E}(\mathbf{x_i} \mathbf{x_i}^\dagger) = \mathbf{I} \tag{8.4}$$

with a_i the realization amplitude, $\mathbf{C}$ the coherency matrix of the forest, $\mathbf{x}_i$ corresponds to the multiplicative noise realization and $\mathbf{b}_i$ the additional noise vector. The vector $\mathbf{k}$ is a 4 dimension vector because here we are in the bistatic cased. As we deal with natural media with large resolution cells and homogeneous forest stands, we assume to be in the classical circular Gaussian distribution.

The evaluation of P_d depending on the P_{fa} uses the following hypothesis test:

$$\begin{aligned} H_0 : \hat{\mathbf{y}} &= \hat{\mathbf{k}}_\mathbf{0} && \text{and } (\hat{\mathbf{k}}_{\mathbf{0,1,\ldots,N}}) \text{ follow the same distribution} \\ H_1 : \hat{\mathbf{y}} &= A\hat{\mathbf{s}} + \hat{\mathbf{k}}_\mathbf{0} && \text{and } (\hat{\mathbf{k}}_{\mathbf{0,1,\ldots,N}}) \text{ follow the same distribution} \end{aligned} \tag{8.5}$$

where $\hat{\mathbf{y}}$ is the simulation result, $\hat{\mathbf{k}}_\mathbf{0}$ corresponds to the forest alone, $\hat{\mathbf{s}}$ is the target alone and A is the attenuation from the forest to the target. In our simulations, the number of realization is set to $N = 1 \cdot 10^6$. The generalized likelihood ratio uses a coherency matrix estimated using the maximum likelihood and for the detection the expression in equation 8.6 follows:

$$\frac{\hat{\mathbf{s}}^\dagger \mathbf{C}^{-1} \hat{\mathbf{y}}}{\hat{\mathbf{s}}^\dagger \mathbf{C}^{-1} \hat{\mathbf{s}}} \underset{H_0}{\overset{H_1}{\gtrless}} \tau_G \tag{8.6}$$

where τ_G is the detection threshold determined by the P_{fa} value.

The simulations have been realized on a forest stand in a $10m \times 10m$ resolution cell. The trees are $12m$ high and the diameter of the trunks are $0.32m$. The density is 3 trunks per scare meters. The transmitter antenna has an incidence of $\theta_e = 50°$ and the azimuth angle is $0°$. The wavelength is $\lambda = 0.6m$. The bistatic positions for the receiver are $\theta_r \in [0°, 70°]$ and $\varphi_r \in [0°, 360°]$. The distances of the antennas from the forest stand is $D = 10km$.

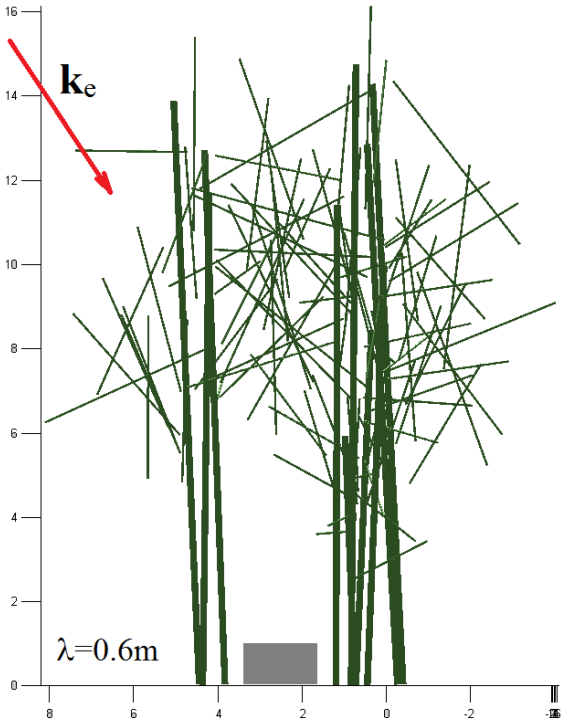

FIGURE 8.7: *Representation of the simulated scene to test the detection capabilities in bistatic configurations at P band.*

The target under consideration is a horizontal cylinder. This choice of the simulated target is based on the following considerations:

- We are able to simulate the target for a set of bistatic situations
- This target has a different geometry of the vegetation, which contains no or few large elements in a horizontal direction.
- It is representative of the guns found on military vehicles, and for which previous studies have shown that the scattering was relatively large.

The target permittivity is set to $\varepsilon_{target} = -100j$ in order to be close to a metallic behavior. The size of the target is $h_{target} = 3\lambda$ and $r_{target} = 0.5\lambda$. It is horizontal and the axis is perpendicular to the incident plane, the scene is represented in figure 8.7.

For target detection it is common to set a low false alarm probability to compute the threshold for the likelihood ratio. The P_{fa} is set to 10^{-3}. For each reception angle in $\theta_r \in [0°, 70°]$, $\varphi_r \in [0°, 360°]$, the likelihood ratio is computed for both hypothesis

and the threshold is computed. It leads to an evaluation of the detection probability which corresponds to the optimal Gaussian detector [95].

The attenuation influence is depicted in figure 8.8. The results for the probability of detection in the case of a horizontal metallic target is shown in figure 8.9.

The evolution of the probability of detection follows a crescent shape from a zero probability of detection in monostatic case, to probability of detection equal to 1 in specular configuration. It shows that the monostatic configuration leads to bad detection probability whereas probability of detection for bistatic configuration with $\theta_r \neq \theta_e$ or around the specular is far better. Moreover, small bistatic angles does not lead to better results as the monostatic configuration.

These first simulations simply intended to illustrate the steps to anticipate the detection probabilities in a forest and to compare the bistatic configurations. Here we present some recommendations to continue this kind of works based on simulations:

- Resolution effects should be considered
- Different polarimetric change detection techniques could be considered.
- As the direct contribution of the ground is not included in the simulation, we should keep in mind that it becomes a problem when real measurement where the direct specular scattering of the ground could hide the target. As a result, if one takes this contribution into account, performances in the specular configuration should be reduced in comparison to a side view configuration.
- Again, the results using second order parameters for detection must be considered with caution in the case of dense crown. In this case, the multipath between branches should be taken into account in the simulation.

In this chapter, we looked at how a simulation tool validated in a number of cases can help us anticipate bistatic radar measurements and for different applications. The first application considered concerns the influence of the structure of the tree on the recorded signal. Our simulations have shown that the most important parameter for the branches is that of the statistics distribution of orientations. On the contrary, the relative positions of branches have little effect in the polarimetric signal. In the second case, we consider the anticipation of the most favorable geometries for the detection of targets under forest cover. This complements previous work that considers the contribution of the forest only through those of the trunks. Here we show how to make provide more performance results, including branches and attenuation effects. These two applications represent a step forward in the intended applications. However, we must make a number of reservations about the results obtained for applications involving second order parameters, for example in the case of dense crowns.

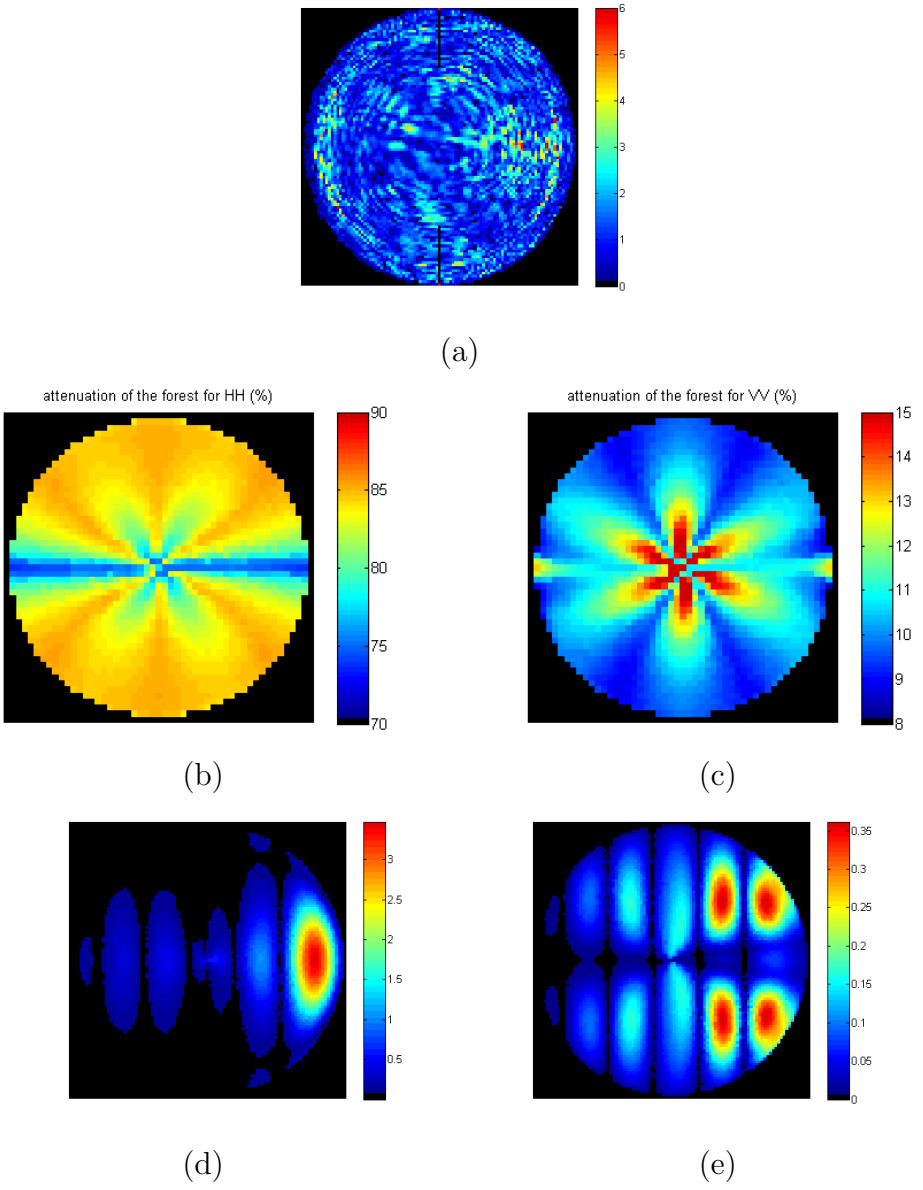

FIGURE 8.8: *(a) the total intensity of the forest with random orientation branches, $\theta_e = 60°$, (b) the corresponding attenuation matrix amplitude hh (%), (c) the corresponding attenuation matrix amplitude hh (%), (*100% *means no attenuation for the target) (d) the target scattering coefficient hh without the forest attenuation. (e) the target scattering coefficient vv without the forest attenuation [dB].*

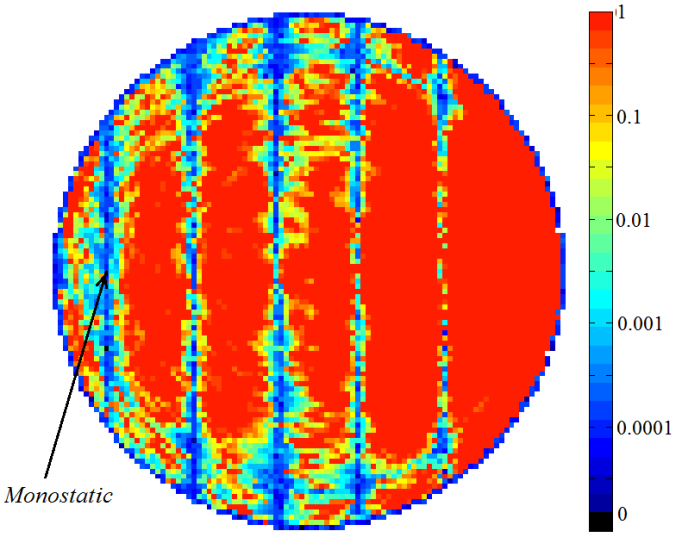

FIGURE 8.9: *Probability of detection of an attenuated horizontal metallic cylinder target under the trunk and random branch forest.*

* * *

Summary
The validation of COBISMO through the measurement of CNT forest make us confident in using it for the analysis of polarimetric sensitivity the forest structure depending on the bistatic angle. The study showed the sensitivity to the branches orientation. Simulation of three forest stands with different branch orientations where conducted. Then a distance between the Mueller matrices is proposed using the Lu and Chipman decomposition parameters. As a conclusion, we have shown that the polarimetric information brings features to distinguish forest stands and that the bistatic configuration with separated elevation angles between emission and reception leads to higher contrast between the different kind of branch orientations.
For the FoPen detection ability of radar system our simulation code is also relevant. In the precedent chapter, among other conclusions, the relevance of the circular polarization for high bistatic angles was underlined. Her in this chapter we have considered a full polarimetric system. A comparison between the bistatic configurations using the polarimetry was realized on a simple case of a metallic target among a dense forest scenario. High bistatic angle configurations seem to be very promising for the detection of man-made object in the forest. In particular, as for the contrast between forest stands, it comes that highly separated elevation angle between emission and reception enables better detection performances. In any case, other detection simulations with different targets and different emission elevation angles should be performed in future works.

Conclusion and perspectives

This PhD thesis presented a new and innovative way of measuring a forest in a full polarimetric and bistatic configuration. To this aim, an optical device has been set up in order to anticipate forest radar measurements. It can be seen as an extension of the principle of "scaled measurements", as is frequently done in an anechoic chamber, but here with higher scale ratios. Indeed our device allows a scaling factor of one million for the radar used in forestry, where an anechoic chamber measurement may propose a scale ratio up to 100. It has several advantages, including

- Its ability to measure a forest for a large set of bistatic configurations: a fixed emitter and the set of all receiving receptor positions on the whole upper hemisphere.
- The speed of acquisition. The time for the execution of a measurement for the entire bistatic and full polarimetric configuration is of the order of one hour taking into account the calibration procedure.
- It is an affordable device and the estimated price of the device is around ten kilo-euros.
- The capacity to vary the number of different scenes.

First, the relevance of carbon nanotube forest for anticipating real forest measurements at P-band has been assessed. The scale ratios are perfectly respected, between real trunk dimensions, both for radius and height, and the wavelength. The polarimetric decompositions suitable to handle bistatic configurations are then selected to be applied to two kinds of forests with different densities.

Once we have gained some confidence in the measurement tool, it is has been used to investigate the polarimetric bistatic signals. This analysis showed, among other things:

- The circular polarization is relevant for target detection when the bistatic angle is high.
- The influence of the density on the polarimetric parameters is more important in strictly bistatic configurations with respect to the monostatic configuration.
- The matrix decompositions used in optics such as the one of Lu and Chipman are well suited for the bistatic configurations. These decompositions make also possible the analysis of geometrical content with the orientation of the slow and the fast axes of the diattenuation and the retardance.

- The depolarization increases with forest densities. It is not an isotropic depolarization in the forest and its origin are the multiple interactions and the near field interactions. There are differences between the sensors at optical scale and the sensor at radar scale. While with optical device the measurement is realized directly in the Stokes formalism, in radar the Mueller matrix is estimated from an ensemble of Jones matrices. Consequently, it may induce differences in the absolute value of the depolarization but the relative behaviors in the evolution of the depolarization must be the same with the sensors of the two scales.

Along with these observations on optical measurements, simulation efforts have also been realized with the aim to be able in the future to simulate a forest scenario whatever the bistatic angle. It turns out that the measurement setup enables to validate the adaption of the simulation code for bistatic case, at least for first order polarimetric parameters. Consequently it is assessed that it is possible to simulate bistatic radar measurement at P-band on trunks and large branches.

However, a specific effort has to be made to assess the second order parameters such as entropy or depolarization. Indeed, the relevance of EM simulations for such effect is questionable. Our efforts were focused on the way to introduce an incoherent summation in order to be able to predict effects such as depolarization, and these studies has to be continued.

For measurements at the optical scale, it seems that the most representative way to retrieve the depolarization levels obtained in the measurement is that of the incoherent summation of signals on the angular range of reception. Moreover, it seems clear that in this case, the multiple interactions, coupled with an incoherent angular summation, are at the origin of this depolarization. In all cases, these considerations show that it is necessary to consider in more details the effects of multipath and associated depolarization in future bistatic SAR missions.

Traditionally, SAR images users determinate entropy with spatial averaging. These could also be coupled with the notion of temporal decorrelation. Indeed, in optics, the temporal integration enables to evaluate the depolarization effects. In SAR, a similar approach could be used to compute the entropy with a time averaging using the fact that the revisit times become shorter.

Once the simulation tool is validated in its area of use, it can be applied to develop inversion and detection algorithms. This approach constitutes the last part of this manuscript. The correspondent studies revealed that some bistatic configurations are more sensitive to the branch orientations and would also induce an higher probability of man made target detection.

In summary, this thesis is a preliminary work to offer an innovative tool for anticipation of bistatic measurements, both by optical measurements and electromagnetic

simulation. Also, even if the first results are very promising, several areas need to be developed:

- The device and the CVD technique to create the forest samples would enable a well controlled and a high variety of the forest scene, including the presence of branches via dentritic nanostructures, as represented in figure 8.10 extracted from [96] and [97].
- The influence of the permittivity of elements on the polarimetric behavior of the scene should be better mastered.

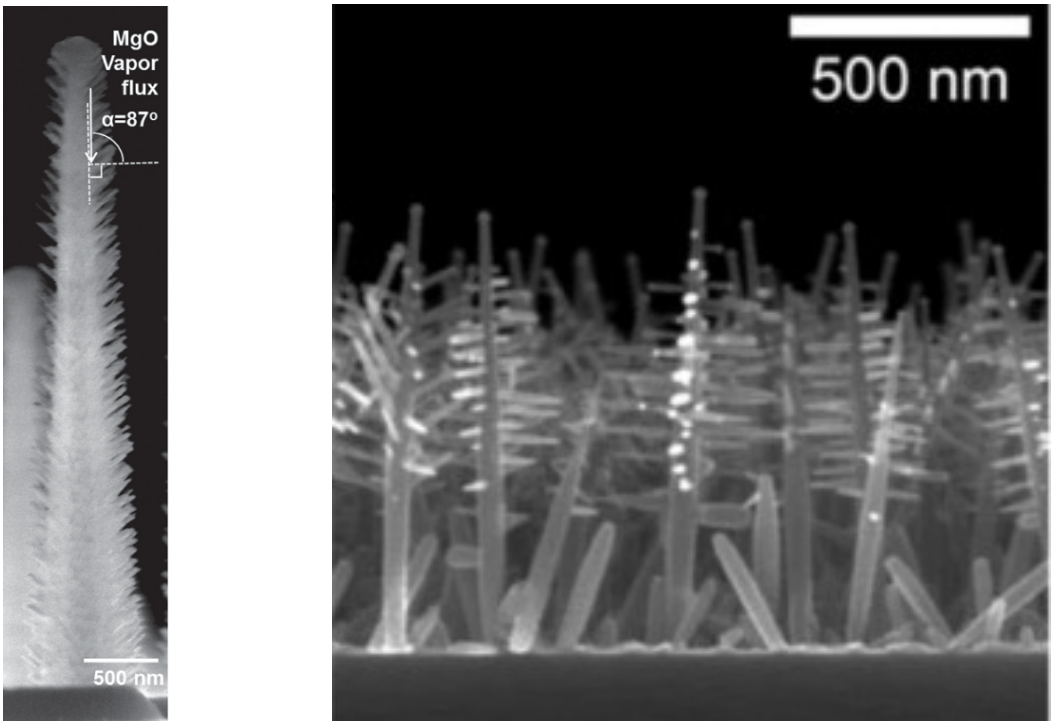

FIGURE 8.10: *Nanotree structure with oriented branches, extracted from [96] and [97].*

These further works will conclude specifically about the similarities of physical phenomena at optical scale and radar scale, and will offer, I hope, a new way to anticipate future bistatic satellite missions in the forest.

Bibliography

[1] L. Thirion-Lefevre. *Modélisation de l'interaction cohérente des ondes électromagnétiques avec des couverts forestiers*. PhD thesis, Université Paul Sabatier-Toulouse III, 2003.

[2] R. Baque, P. Dreuillet, O. Ruault du Plessis, H. Cantalloube, L. Ulander, G. Stenstrom, T. Jonsson, and A. Gustavsson. Lorambis a bistatic vhf/uhf sar experiment for fopen. In *Radar Conference, 2010 IEEE*, pages 832–837. IEEE, 2010.

[3] L. Thirion-Lefevre, E. Colin-Koeniguer, and C. Dahon. Bistatic scattering from forest components. part i: coherent polarimetric modelling and analysis of simulated results. *Waves in Random and Complex Media*, 20(1):36–61, 2010.

[4] T. Le Toan, .S Quegan, M.W.J. Davidson, H. Balzter, P. Paillou, K. Papathanassiou, S. Plummer, F. Rocca, S. Saatchi, H. Shugart, et al. The biomass mission: Mapping global forest biomass to better understand the terrestrial carbon cycle. *Remote sensing of environment*, 115(11):2850–2860, 2011.

[5] P. Dubois-Fernandez, H. Cantalloube, B. Vaizan, G. Krieger, R. Horn, M. Wendler, and V. Giroux. ONERA-DLR bistatic SAR campaign: planning, data acquistiton, and first analysis of bistatic scattering behaviour of natural and urban targets. *Radar, Sonar and Navigation, IEEE Proceedings* -, 153(3):214–223, June 2006.

[6] M. Rodriguez-Cassola, P. Prats, D. Schulze, N. Tous-Ramon, U. Steinbrecher, L. Marotti, M. Nannini, M. Younis, P. López-Dekker, M. Zink, et al. First bistatic spaceborne sar experiments with tandem-x. *Geoscience and Remote Sensing Letters, IEEE*, 9(1):33–37, 2012.

[7] A. S. Goh, M. Preiss, and N. JS. Stacy. Initial polarimetric results from the ingara bistatic sar experiment. In *Radar (Radar), 2013 International Conference on*, pages 27–32. IEEE, 2013.

[8] N. Trouve, E. Colin-Koeniguer, P. Fargette, and A. De Martino. Influence of geometrical configurations and polarization basis definitions on the analysis of bistatic

polarimetric measurements. *IEEE Transactions on Geoscience and Remote Sensing*, 49(6):2238–2250, 2011.

[9] S. Bellez, H. Roussel, C. Dahon, and J.-M. Geffrin. A rigorous forest scattering model validation through comparison with indoor bistatic scattering measurements. *Progress In Electromagnetics Research B*, 33:1–19, 2011.

[10] L. Thirion-Lefevre, C. Dahon, E. Colin-Koeniguer, and C. Titin-Schnaider. Modeling of the polarimetric bistatic scattering of a forested area at p-band. *EUSAR 2006*, 2006.

[11] E. Colin-Koeniguer and L. Thirion-Lefevre. Bistatic scattering from forest components. part II: first validation of a bistatic polarimetric forest model in the vhf-uhf band [225–475 mhz] using indoor measurements. *Waves in Random and Complex Media*, 20(1):62–85, 2010.

[12] N. Trouvé. *Comparaison des outils optique et radar en polarimétrie bistatique*. PhD thesis, Ecole Polytechnique X, November 2011.

[13] Y. K. Chan and V. C. Koo. An introduction to synthetic aperture radar (sar). *Progress In Electromagnetics Research B*, 2:27–60, 2008.

[14] L. M. H. Ulander, P. Frolind, A. Gustavsson, and G. Stenstrom. Bistatic p-band SAR signatures of forests and vehicles. In *Geoscience and Remote Sensing Symposium (IGARSS), 2012 IEEE International*, pages 311–314, 2012.

[15] F. Daout, F. Schmitt, G. Ginolhac, and P. Fargette. Multistatic and multiple frequency imaging resolution analysis-application to gps-based multistatic radar. *Aerospace and Electronic Systems, IEEE Transactions on*, 48(4):3042–3057, October 2012.

[16] C.H. Gierull. Bistatic synthetic aperture radar. *Defence R&D Canada, Ottawa, ON, Canada, Tech. Rep. DRDC-OTTAWA-TR-2004-190*, pages 31–41, 2004.

[17] J. Homer, E. Donskoi, B. Mojarrabi, J. Palmer, and K. Kubik. Three-dimensional bistatic synthetic aperture radar imaging system: spatial resolution analysis. *IEE Proceedings-Radar, Sonar and Navigation*, 152(6):391–394, 2005.

[18] I. Walterscheid, J. Klare, A. R Brenner, J. HG Ender, and O. Loffeld. Challenges of a bistatic spaceborne/airborne sar experiment. *EUSAR 2006*, 2006.

[19] B. D. Rigling. *Signal processing strategies for bistatic synthetic aperture radar*. PhD thesis, The Ohio State University, 2003.

[20] T. Zeng, M. Cherniakov, and T. Long. Generalized approach to resolution analysis in bsar. *Aerospace and Electronic Systems, IEEE Transactions on*, 41(2):461–474, 2005.

[21] A. Moccia and A. Renga. Spatial resolution of bistatic synthetic aperture radar: Impact of acquisition geometry on imaging performance. *Geoscience and Remote Sensing, IEEE Transactions on*, 49(10):3487–3503, 2011.

[22] G.P. Cardillo. On the use of the gradient to determine bistatic sar resolution. In *Antennas and Propagation Society International Symposium*, volume 2, pages 1032–1035, 1990.

[23] J. J. Gil. Review on mueller matrix algebra for the analysis of polarimetric measurements. *Journal of Applied Remote Sensing*, 8(1):081599–081599, 2014.

[24] S.-Y. Lu and R. A. Chipman. Interpretation of mueller matrices based on polar decomposition. *Journal of the Optical Society of America A*, 13(5):1106–1113, May 1996.

[25] R. A. Chipman. Depolarization index and the average degree of polarization. *Applied optics*, 44(13):2490–2495, 2005.

[26] R. Barakat. Statistics of the stokes parameters. *Journal of the Optical Society of America A*, 4(7):1256–1263, July 1987.

[27] S. L. Durden, J. J. Van Zyl, and H.A. Zebker. The unpolarized component in polarimetric radar observations of forested areas. *Geoscience and Remote Sensing, IEEE Transactions on*, 28(2):268–271, 1990.

[28] S. Cloude. *Polarisation: applications in remote sensing*. Oxford University Press, 2009.

[29] R. Ossikovski, M. Anastasiadou, S. Ben Hatit, E. Garcia-Caurel, and A. De Martino. Depolarizing Mueller matrices: how to decompose them? *Physica status solidi (a)*, 205(4):720–727, 2008.

[30] J. J. Gil and E. Bernabeu. A depolarization criterion in Mueller matrices. *Journal of Modern Optics*, 32(3):259–261, 1985.

[31] J. Morio and F. Goudail. Influence of the order of diattenuator, retarder, and polarizer in polar decomposition of mueller matrices. *Optics letters*, 29(19):2234–2236, 2004.

[32] R. Ossikovski, A. De Martino, and S. Guyot. Forward and reverse product decompositions of depolarizing mueller matrices. *Optics Letters*, 32(6):689–691, March 2007.

[33] R. Ossikovski. Analysis of depolarizing mueller matrices through a symmetric decomposition. *JOSA A*, 26(5):1109–1118, 2009.

[34] F. T. Ulaby and C. Elachi. Radar polarimetry for geoscience applications. *Norwood, MA, Artech House, Inc., 1990, 376 p. No individual items are abstracted in this volume.*, 1, 1990.

[35] E. Krogager. New decomposition of the radar target scattering matrix. *Electronics Letters*, 26(18):1525–1527, 1990.

[36] N. Trouve, E. Colin-Koeniguer, P. Fargette, and A. De Martino. Influence of geometrical configurations and polarization basis definitions on the analysis of bistatic polarimetric measurements. *IEEE Transactions on Geoscience and Remote Sensing*, 49(6):2238–2250, 2011.

[37] C. R. Schumacher. Electrodynamic similitude and physical scale modeling of nondispersive targets. *Journal of applied physics*, 62(7):2616–2625, 1987.

[38] M. I. Mishchenko. Scale invariance rule in electromagnetic scattering. *Journal of Quantitative Spectroscopy and Radiative Transfer*, 101(3):411–415, October 2006.

[39] D. Colton and R. Kress. *Integral equation methods in scattering theory*, volume 72. SIAM, 2013.

[40] A. Doicu. Acoustic and electromagnetic scattering analysis using discrete sources. *Acoustic and Electromagnetic Scattering Analysis Using Discrete Sources, ISBN: 978-0-12-219740-6, p. ix-xi.*, 1, 2000.

[41] J. A. Stratton. *Electromagnetic theory*, volume 33. John Wiley & Sons, 2007.

[42] Z. Wu and B. Liu. Electromagnetic similitude and inconsistency of laser scattering for scale model. *International journal of infrared and millimeter waves*, 16(7): 1249–1259, 1995.

[43] C.S. Cojocaru, D. Kim, and J.-E. Pribat, D.and Bourée. Synthesis of multi-walled carbon nanotubes by combining hot-wire and dc plasma-enhanced chemical vapor deposition. *Thin Solid Films*, 501(1):227–232, 2006.

[44] M.P. Siegal, D.L. Overmyer, and F.H. Kaatz. Controlling the site density of multiwall carbon nanotubes via growth conditions. *Applied physics letters*, 84 (25):5156–5158, 2004.

[45] C.S. Cojocaru, D. Kim, D. Pribat, J.-E. Bourée, E. Minoux, and P. Gangloff, L.and Legagneux. Study of electron field emission from arrays of multi-walled carbon nanotubes synthesized by hot-wire dc plasma-enhanced chemical vapor deposition. *Journal of non-crystalline solids*, 352(9):1352–1356, 2006.

[46] D. Kim, J.E. Bourée, and S.Y. Kim. Numerical study on the field emission properties of aligned carbon nanotubes using the hybrid field enhancement scheme. *Applied Physics A*, 83(1):111–114, 2006.

[47] S. Ben Hatit. *Polarimétrie de Mueller résolue en angle*. PhD thesis, Ecole Polytechnique X, January 2009.

[48] B. Laude-Boulesteix. *Développements instrumentaux en imagerie tomographique et polarimétrique.* PhD thesis, Ecole Polytechnique X, June 2004.

[49] C. Fallet. *Polarimétrie de Mueller résolue angulairement et applications aux structures périodiques*. PhD thesis, Ecole Polytechnique X, October 2011.

[50] J. J. Gil and I San José. Polarimetric subtraction of mueller matrices. *Journal of the Optical Society of America A*, 30(6):1078–1088, June 2013.

[51] S. Ben Hatit. Polarimétrie de mueller résolue en angle, January 2009.

[52] J. Praks, E. Colin-Koeniguer, and M. T. Hallikainen. Alternatives to target entropy and alpha angle in sar polarimetry. *Geoscience and Remote Sensing, IEEE Transactions on*, 47(7):2262–2274, 2009.

[53] R. Ossikovski, A. De Martino, and S. Guyot. Forward and reverse product decompositions of depolarizing mueller matrices. *Optics letters*, 32(6):689–691, 2007.

[54] L. Thirion-Lefevre, E. Colin-Koeniguer, and C. Dahon. Capabilities of a forest coherent scattering model applied to radiometry, interferometry, and polarimetry at p- and l-band. *IEEE Transactions on Geoscience and Remote Sensing*, 44(4): 849–862, April 2006.

[55] S. Bellez, H. Roussel, and C. Dahon. Full wave analysis of vhf-uhf forest bistatic scattering mechanisms an investigation on the influence of electromagnetic coupling. In *Geoscience and Remote Sensing Symposium (IGARSS), 2010 IEEE International*, pages 2547–2550. IEEE, 2010.

[56] V. LY Loke, M. Pinar Mengüç, and T. A. Nieminen. Discrete-dipole approximation with surface interaction: Computational toolbox for matlab. *Journal of Quantitative Spectroscopy and Radiative Transfer*, 112(11):1711–1725, 2011.

[57] L. Thirion, P. Borderies, I. Chenerie, E. Mougin, and C. Proisy. Modelling of interferometric phase for forested areas. In *Geoscience and Remote Sensing Symposium, 2001. IGARSS'01. IEEE 2001 International*, volume 1, pages 401–403. IEEE, 2001.

[58] P. Liang, L. E. Pierce, and M. Moghaddam. Radiative transfer model for microwave bistatic scattering from forest canopies. *Geoscience and Remote Sensing, IEEE Transactions on*, 43(11):2470–2483, 2005.

[59] A. A. Kononov, A. Wyholt, G. Sandberg, and L. MH Ulander. Statistical analysis of vhf-band tree backscattering using forest ground truth data and po scattering model. *Geoscience and Remote Sensing, IEEE Transactions on*, 49(8):3035–3046, 2011.

[60] P. Ferrazzoli, L. Guerriero, and D. Solimini. Simulating bistatic scatter from surfaces covered with vegetation. *Journal of electromagnetic waves and applications*, 14(2):233–248, 2000.

[61] H. Nguyen, H. Roussel, and W. Tabbara. A coherent model of forest scattering and sar imaging in the vhf and uhf-band. *Geoscience and Remote Sensing, IEEE Transactions on*, 44(4):838–848, 2006.

[62] S. Bellez, H. Roussel, C. Dahon, J. C. Castelli, and A. Cheraly. Full polarimetric bistatic radar imaging experiments on sets of dielectric cylinders above a conductive circular plate. *IEEE transactions on geoscience and remote sensing*, 51(7): 4164–4176, 2013.

[63] L. Villard, P. Borderies, P. Dubois-Fernandez, and J. Nouvel. Bistatic border effects modelling in forest scattering. In *Geoscience and Remote Sensing Symposium, 2007. IGARSS 2007. IEEE International*, pages 2354–2357. IEEE, 2007.

[64] L. Thirion-Lefevre and E. Colin-Koeniguer. First polarimetric validation and results on the bistatic scattering by a set of cylinders using a forest scattering model. In *Synthetic Aperture Radar (EUSAR), 2008 7th European Conference on*, pages 1–4. VDE, 2008.

[65] L. Thirion-Lefevre, E. Colin-Koeniguer, and C. Dahon. Bistatic scattering from forest components. part I: coherent polarimetric modelling and analysis of simulated results. *Waves in Random and Complex Media*, 20(1):36–61, 2010.

[66] K. P. Papathanassiou and S. R. Cloude. Single-baseline polarimetric sar interferometry. *Geoscience and Remote Sensing, IEEE Transactions on*, 39(11):2352–2363, 2001.

[67] M. I. Mishchenko. Multiple scattering, radiative transfer, and weak localization in discrete random media: unified microphysical approach. *Reviews of Geophysics*, 46(2), 2008.

[68] L. Tsang and JA Kong. Multiple scattering of electromagnetic waves by random distributions of discrete scatterers with coherent potential and quantum mechanical formalism. *Journal of Applied Physics*, 51(7):3465–3485, 1980.

[69] F. Brigui, L. Thirion-Lefevre, G. Ginolhac, and P. Forster. Contribution of the polarimetric information in order to discriminate target from interference subspaces. application to fopen detection with sar processing. In *Geoscience and Remote Sensing Symposium (IGARSS), 2011 IEEE International*, pages 138–141. IEEE, 2011.

[70] H. Butt, T. D. Wilkinson, and G. AJ Amaratunga. Fem modeling of periodic arrays of multiwalled carbon nanotubes. *Progress In Electromagnetics Research M*, 22:1–12, 2012.

[71] E. Lidorikis and A. C. Ferrari. Photonics with multiwall carbon nanotube arrays. *ACS nano*, 3(5):1238–1248, 2009.

[72] A. B. Djurišić and E. H. Li. Optical properties of graphite. *Journal of applied physics*, 85(10):7404–7410, 1999.

[73] E. D. Palik. *Handbook of optical constants of solids*, volume 3. Academic press, 1998.

[74] E. L. Malus. *Théorie de la double réfraction de la lumière dans les substances cristallisés: mémoire couronné par l'Institut, dans la séance publique du 2 janvier 1810*. Garnery, 1810.

[75] D. Brewster. On the laws which regulate the polarisation of light by reflexion from transparent bodies. *Philosophical Transactions of the Royal Society of London*, 105:125–159, 1815.

[76] Q. Zhao and R. H. Lang. Fresnel double scattering from tree branches. *Geoscience and Remote Sensing, IEEE Transactions on*, 50(10):3640–3647, 2012.

[77] F.C. MacKintosh, J.X. Zhu, D.J. Pine, and D.A. Weitz. Polarization memory of multiply scattered light. *Physical Review B*, 40(13):9342, 1989.

[78] M. I. Mishchenko. Radiative transfer: a new look of the old theory. *ICHMT DIGITAL LIBRARY ONLINE*, 17, 2007.

[79] A.A. Ibrahim and K. Sarabandi. Simulation of long distance wave propagation in 2-d sparse random media: A statistical s-matrix approach in spectral domain. *IEEE Transactions on Antennas and Propagation*, 62(5):2708–2720, May 2014.

[80] L. Tsang, K-H Ding, G. Zhang, C.C. Hsu, and J. A Kong. Backscattering enhancement and clustering effects of randomly distributed dielectric cylinders overlying a dielectric half space based on monte-carlo simulations. *Antennas and Propagation, IEEE Transactions on*, 43(5):488–499, 1995.

[81] N. Ortega-Quijano, F. Fanjul-Vélez, I. Salas-García, and J. L. Arce-Diego. Polarized light monte carlo analysis of birefringence-induced depolarization in biological tissues. volume 8803, pages 88030T–88030T–8, 2013.

[82] A. J. Brown and Y. Xie. Symmetry relations revealed in mueller matrix hemispherical maps. *Journal of Quantitative Spectroscopy and Radiative Transfer*, 113 (8):644–651, 2012.

[83] L. L. Foldy. The multiple scattering of waves. i. general theory of isotropic scattering by randomly distributed scatterers. *Physical Review*, 67(3-4):107, 1945.

[84] A. Ishimaru. Wave propagation and scattering in random media and rough surfaces. *Proceedings of the IEEE*, 79(10):1359–1366, 1991.

[85] G. Puentes, D. Voigt, A. Aiello, and J.P. Woerdman. Depolarizing power and polarization entropy of light scattering media: experiment and theory. *arXiv preprint physics/0412096*, 2004.

[86] A. Ishimaru. *Wave propagation and scattering in random media*, volume 2. Academic press New York, 1978.

[87] D. G. Goebel. Generalized integrating-sphere theory. *Applied Optics*, 6(1):125–128, 1967.

[88] D. Bicout and C. Brosseau. Multiply scattered waves through a spatially random medium: entropy production and depolarization. *Journal de Physique I*, 2(11): 2047–2063, 1992.

[89] Ø. Svensen, M. Kildemo, J. Maria, J. J Stamnes, and Ø. Frette. Mueller matrix measurements and modeling pertaining to spectralon white reflectance standards. *Optics express*, 20(14):15045–15053, 2012.

[90] M. L. Imhoff. A theoretical analysis of the effect of forest structure on synthetic aperture radar backscatter and the remote sensing of biomass. *Geoscience and Remote Sensing, IEEE Transactions on*, 33(2):341–352, 1995.

[91] S.R. Cloude. On the status of bistatic polarimetry theory. In *Geoscience and Remote Sensing Symposium, 2005. IGARSS '05. Proceedings. 2005 IEEE International*, volume 3, pages 2003–2006, July 2005.

[92] Mark E Davis. Developments in foliage penetration radar. In *Inter. Radar Conf.-Surveillance for a Safer World*, pages 1–6, 2009.

[93] L. MH Ulander and T. Martin. Bistatic ultra-wideband sar for imaging of ground targets under foliage. In *Radar Conference, 2005 IEEE International*, pages 419–423. IEEE, 2005.

[94] L. MH Ulander, A. Gustavsson, T. Jonsson, R. Ragnarsson, and G. Stenstrom. Development of carina bistatic vhf-band sar. In *Radar Conference (Radar), 2014 International*, pages 1–4. IEEE, 2014.

[95] E. Jay, J.P. Ovarlez, D. Declercq, and P. Duvaut. Bord: Bayesian optimum radar detector. *Signal Processing*, 83(6):1151–1162, 2003.

[96] B.U. Ye, B. J. Kim, J. Park, H. Y. Jeong, J. Y. Park, J. K. Kim, J.-H. Hur, M. H. Kim, J.-L. Lee, and J. M. Baik. Three-dimensional branched nanowire heterostructures as efficient light-extraction layer in light-emitting diodes. *Advanced Functional Materials*, 24(22):3384–3391, 2014.

[97] A. L. Beaudry, J. M. LaForge, R. T. Tucker, J.B. Sorge, N. L. Adamski, P. Li, M. T. Taschuk, and M. J. Brett. Directed branch growth in aligned nanowire arrays. *Nano letters*, 14(4):1797–1803, 2014.

Résumé

Les systèmes radar permettent de couvrir de larges zones et grâce à la capacité qu'ont les ondes électromagnétiques qu'ils utilisent de passer à travers les milieux, le radar est un des outils les plus approprié pour la télédétection dans la forêt. Mais pour une utilisation efficace, il est important de choisir de bonne configuration d'acquisition. À trop haute fréquence l'onde ne pénètre pas, c'est pourquoi nous limitons notre étude aux bandes UHF, P et L. De plus, un système radar qui utilise une diversité de polarisations d'émission et de réception peut récolter plus d'information de la scène, car la polarisation est sensible à la structure de la forêt. Avec un récepteur radar dissocié de l'émetteur, la polarimétrie a encore plus de potentiel car la symétrie entre les trajets aller et retour du monostatique est évité. Le but de cette thèse est d'anticiper des mesures réelles bistatiques en bande P sur la forêt. Cela permet de donner des paramètres clés pour choisir la meilleure configuration que ce soit pour une application dans l'inversion des paramètres physiques de la forêt ou la détection d'objets artificiels dans la forêt. La solution que nous proposons consiste en l'utilisation d'un polarimètre à l'échelle optique et qui permet de faire des mesures sur un ensemble de configurations bistatiques à la fois. Les scènes utilisées sont constituées de nanotubes de carbone qui reproduisent les caractéristiques structurelles et diélectriques de forêts de troncs à l'échelle radar. Nous démontrons que ces mesures peuvent être utilisées pour anticiper la mesure bistatique radar mais elles permettent également la validation des codes de simulation existants. Le code COBISMO développé pour le radar peut reproduire les mesures de nanotubes. En utilisant les résultats de comparaison, le code de simulation est ensuite appliqué pour étudier les configurations et les polarisations les plus à même de retrouver l'orientation des branches et pour la détection sous le couvert forestier.

Summary:

Due to penetration capabilities of electromagnetic waves and the possibility to cover large areas, radar is one of the most appropriate tool for remote sensing of forest. To use radar images for forestry, it is crucial to select and optimize the best configurations of acquisition. If the frequency is too high, no penetration occurs and only the top leafs will play a role in the scattering events. Large wavelengths used in radar are more able to penetrate the forest elements and to interact also with the ground below. For this reason, we limit this thesis to the use of UHF, P-band and L-band. By emitting and receiving several couples of polarizations, several images can be collected. The polarimetry is sensitive the structure information and consequently, it can bring a diversity of information. A radar system which comprises a transmitter and receiver which are spatially separated is an opportunity to supply additional information to classical polarimetric radar, because it breaks symmetry observed in the monostatic case. The aim of the thesis is to anticipate real P-band bistatic radar measurements on forest and to give keys to choose more appropriate configuration for a given application: physical parameter retrieval or target detection. The solution we propose is to construct an optical scale device that is full polarimetric and that handle the bistatic configurations, and to measure scene having a structure comparable to a real forest. We demonstrate that the optical scale measurement can be used to anticipate polarimetric behavior of forest and jointly to validate our simulation code. Polarization and configuration are studied to discriminate branch orientation and to detect man-made objects in the forest.